Relationships between the macroscale sedimentology and micromorphology of glacigenic diamictons in south-central British Columbia

by

Christina M. Neudorf
B.Sc. (Hons), University of Saskatchewan

THESIS SUBMITTED IN PARTIAL FULFILLMENT OF THE REQUIREMENTS FOR THE DEGREE OF

MASTER OF SCIENCE

In the Department of Geography

SIMON FRASER UNIVERSITY
Summer 2008

APPROVAL

Name: **Christina Neudorf**

Degree: **Master of Science**

Title of Thesis: **Relationships between the macroscale sedimentology and micromorphology of glacigenic diamictons in south-central British Columbia**

Examining Committee:

Chair: **Dr. N.K. Blomley**, Professor

Dr. Tracy A. Brennand
Associate Professor
Senior Supervisor

Dr. Olav Lian
Adjunct Professor, Department of Geography, SFU
Instructor, University of the Fraser Valley
Committee Member

Dr. Dan Smith, Professor
Chair, Department of Geography
University of Victoria
External Examiner

Date Approved: May 14, 2008

ABSTRACT

This research explores relationships between the macroscale sedimentology and micromorphology of glacigenic diamictons associated with the last Cordilleran Ice Sheet in south-central B.C., and tests the hypothesis that diamictons classified using traditional definitions and sedimentological criteria have unique micromorphologies. Cluster analyses suggest that diamicton types cannot be differentiated by the relative abundances of particular microstructures. Qualitative analyses suggest that microfabrics may be less consistent with macrofabrics in deformation tills and gravity flow diamictons than in undeformed or partially deformed lodgement tills, and evidence of water sorting at the microscale may be more prevalent in gravity flow diamictons than in primary tills. This suggests that though microstructures and microfabrics are not *diagnostic* to any one diamicton type, depositional processes express themselves at the microscale. Therefore diamicton micromorphology may be used to elaborate on diamicton depositional mechanics and post-depositional modification; however, interpretations are best made within the context of macroscale sedimentological inferences.

ACKNOWLEDGEMENTS

Thanks to Drs Olav Lian and Tracy Brennand for their invaluable support, encouragement and guidance. Thanks for Dan Smith for agreeing to be my external examiner on such short notice. Thanks to my field and lab assistant, Robert Price, for his never-ending patience, stamina and hard work. You are responsible for half of the clast fabrics presented in this thesis! – (and for getting the departmental truck out of the ditch…). Thanks to Dr. Dan Gibson (SFU) for allowing me access to his macroscope and digital imaging system and to Candace Kramer (Brock University) for preparing the thin sections.

The subject of till is long and complicated, and in making sense of it, I have benefited enormously from input from the following people: Drs Olav Lian (SFU and UFV), Neal Iverson (Iowa State University), Aleksis Dreimanis (University of Western Ontario), Slawek Tulaczkyk (University of California), Daniel Lawson (Cold Regions Research and Engineering Laboratory, New Hampshire), Jason Thomason (Illinois State Geological Survey), John Menzies (Brock University), Jaap van der Meer (Queen Mary, University of London), Mark Tarplee (Queen Mary, University of London), and Aoibheann Kilfeather (Queen Mary, University of London).

Very helpful statistical advice has come from SFU graduate student Simon Goring, who was the first to suggest cluster analysis as a useful approach, and who introduced me to the wonderful world of R. Special thanks to Drs Carl Schwartz (SFU), Tim Swartz (SFU) and MartÍn Fernández (Universitat de Girona), for helping me refine my statistical approach.

Somehow, throughout the duration of this project I've managed to keep my sanity, and I attribute this first and foremost to Keith, my healthy reminder that there is life outside of work. Your love, support (and of course, your Photoshop expertise) will not be forgotten. Thanks so much to Kerry, for the girl talk, card nights, guitar hero, intellectual debates, and for listening to my emotional rants. Grad school hasn't been the same since you left, and you are sorely missed!

TABLE OF CONTENTS

APPROVAL ii
ABSTRACT iii
ACKNOWLEDGEMENTS iv
TABLE OF CONTENTS v
LIST OF TABLES ix
LIST OF FIGURES x
Chapter 1: Research objectives and rationale 1
1.1 Introduction 1
1.2 Research objectives 3
Chapter 2: Literature review 4
2.1 The ever-changing classification scheme of tills 4
2.2 Geological criteria for till classification 7
2.3 Glacial micromorphology: principles and microstructure classification 11
2.4 Microstructures, plasmic fabrics, microfabrics and “macro”-processes 13
2.4.1 Microstructures 13
2.4.2 Plasmic fabrics 14
2.4.3 Microfabrics 14
2.4.4 The scaling issue 15
2.5 Past uses of glacial micromorphology 16
2.5.1 Supplementary data 16
2.5.2 Diagnostic criteria 17
2.6 Summary 20
Chapter 3: Study area and methodology 21
3.1 Study area 21
3.1.1 Regional geology and topography 21
3.1.2 Inferred recent glacial history 24
3.2 Geological criteria for till classification in south-central B.C. 25
3.2.1 Till clast fabric and wear features 25
3.2.2 Macroscale properties of lodgement till 26
3.2.3 Macroscale properties of deformation till 27
3.2.4 Macroscale properties of deformed lodgement till 28
3.2.5 Macroscale properties of gravity flow till 28
3.3 Methodology 29
3.3.1 Field observation 29
3.3.2 Diamicton sampling 32
3.3.3 Thin section preparation and grain size analysis 33
3.3.4 Laboratory observation 34

Chapter 4: Macroscale and microscale observations....39
4.1 Introduction....39
4.2 Site 23....39
4.2.1 Macroscale sedimentology and structural geology....39
4.2.2 Micromorphology....45
4.2.3 Interpretation....52
4.3 Site 20....55
4.3.1 Macroscale sedimentology and structural geology....55
4.3.2 Micromorphology....58
4.3.3 Interpretation....61
4.4 Site 44....63
4.4.1 Macroscale sedimentology and structural geology....63
4.4.2 Micromorphology....67
4.4.3 Interpretation....70
4.5 Site 6....75
4.5.1 Macroscale sedimentology and structural geology....75
4.5.2 Micromorphology....76
4.5.3 Interpretation....85
4.6 Site 60....87
4.6.1 Macroscale sedimentology and structural geology....87
4.6.2 Cobble and boulder striae measurements....94
4.6.3 Micromorphology....96
4.6.4 Interpretation....105
4.7 Site 48....110
4.7.1 Macroscale sedimentology and structural geology....110
4.7.2 Micromorphology....114
4.7.3 Interpretation....126
4.8 Site 27....128
4.8.1 Macroscale sedimentology and structural geology....128
4.8.2 Micromorphology....132
4.8.3 Interpretation....135
4.9 Sites 25 & 26....139
4.9.1 Macroscale sedimentology and structural geology....139
4.9.2 Micromorphology....144
4.9.3 Interpretation....149
4.10 Site 57....151
4.10.1 Macroscale sedimentology and structural geology....151
4.10.2 Micromorphology....155
4.10.3 Interpretation....160
4.11 Site 22....161
4.11.1 Stratigraphic context of site 22....161

4.11.2 Macroscale sedimentology and structural geology....163
4.11.3 Micromorphology....163
4.11.4 Interpretation....166
4.12 Summary and discussion....169
4.12.1 Macroscopic evidence for lodgement till....170
4.12.2 Macro-micro comparisons....174
Chapter 5: Intra- and inter-site micromorphological comparisons - a clustering approach....184
5.1 Purpose and methodology....184
5.2 Results and discussion....189
5.2.1 Microstructure association and diamicton type....189
5.2.2 Microstructure association and bedrock lithology....190
5.2.3 Microstructure association and number of microstructures....190
5.2.4 Microstructure association and diamicton texture....193
5.2.5 Microstructure association and topographic position....194
5.2.6 Microstructure association and ice/sediment provenance....196
5.3 Summary....197
Chapter 6: Discussion and conclusions....198
6.1 Objective 1: The relationship between diamicton micromorphology and macroscale sedimentology....198
6.2 Objective 2: Do different diamicton types contain diagnostic micromorphologies?....199
6.3 Objective 3: The relationship between diamicton micromorphology and environmental variables....200
6.4 Recommendations for future research....201
Appendix A....203
Site latitude and longitude coordinates....203
Appendix B....204
Clast shape data....204
Appendix C....210
Rectified photographs of diamictons for clast concentration measurements....210
Appendix D....212
Thin section preparation protocol....212
Appendix E....213
Grain size data....213
Appendix F....214
Criteria for identification of discrete microstructures....214
Turbates....214
Necking Structures....214

Grain Lineations 215
Grain Stacks 215
Crushed grains 215
Appendix G 216
Annotated 2400 dpi vertical thin section scans 216
Appendix H 218
2400 dpi horizontal thin section scans 218
Appendix I 219
Hierarchical clustered microstructure association data 219
References 228

LIST OF TABLES

Table 2.5-1. Micromorphological characteristics of "para-tills" and "ortho-tills" after Seret (1993). 18

Table 2.5-2. Micromorphological characteristics of glaciomarine and subglacial sediments adapted from Carr (2001), by permission. © 2001 Elsevier Science Ltd. 19

Table 4.2-1. Macrofabric eigenstatistics, randomness test results and modalities, and diamicton clast concentration and macroscale structures. Sites are sorted according to the inferred genesis (G) of the unit in question. 43

Table 4.2-2. Mode statistics for bimodal/multimodal macrofabrics and macrofabrics with outliers. Sites are ordered according to the inferred diamicton genesis (G) 44

Table 4.2-3. Clast wear features for all diamicton types. Sites are ordered according to the inferred genesis (G) of the unit in question. 46

Table 4.12-1. Microstructure association data displayed in a 23 x 5 matrix. Sites are sorted according to inferred diamicton genesis (G) 175

Table 4.12-2. Vertical microfabric statistics and relationships with planar voids in vertical thin sections. Thin sections are sorted according to inferred diamicton genesis (G) 176

Table 4.12-3. Macrofabric and horizontal microfabric statistics. Sites are sorted first according to inferred diamicton genesis (G), then according to macrofabric modality (M). 178

Table 5.2-1. Pearson-product moment correlation coefficients describing the strength and direction of the linear relationship between microstructure relative abundance and grain size fraction. See Figure 5.2-4 for scatterplots. 195

Table A-1. Site latitude and longitude coordinates. 203

Table E-1. Grain size data for each diamicton matrix sample. Sites are arranged in numerical order. 213

LIST OF FIGURES

Figure 2.1-1. The 'Genetic Till Prism' (Source: Hicock 1990, by permission. © 1990 Geological Society of America) based on the classification scheme of the INQUA Commission on the Genesis and Lithology of Glacial Quaternary Deposits (Dreimanis 1989). 4

Figure 2.2-1. Sedimentological evidence used to constrain the depth of deformation within subglacial tills and underlying sediments. A) Laterally continuous intra-till sorted sediment layers thought to record decoupling of ice from the substrate (Source: Piotrowski *et al.* 2006, by permission. © 2005 International Association of Sedimentologists). B) Preserved undeformed peat clast with sharply defined edges used as evidence against pervasive deformation of the surrounding till (Source: Larsen *et al.* (2004), by permission. © John Wiley & Sons Limited). C) Grooves parallel to ice flow direction preserved on till surfaces below intra-till sand layers (such as that shown in A) suggestive of lodgement and ploughing processes (Source: Piotrowski *et al.* 2006, by permission. © 2005 International Association of Sedimentologists). D) Undeformed sub-till Nye channels preserved at the lower till contact precluding the possibility of the deforming layer extending below this level (Source: Larsen *et al.* 2004, by permission. © 2004 John Wiley & Sons Limited). E) Ploughed striated and faceted (on top) boulder showing evidence of abrasion of upper surface while stationary (Source: Piotrowski *et al.* 2001, by permission. © 2001 Elsevier Science Ltd and INQUA). F) Heavily weathered boulder with tongue smeared into till from it's upper surface indicative of erosion while in situ (Source: Piotrowski *et al.* 2001, by permission. © 2001 Elsevier Science Ltd and INQUA). 9

Figure 2.2-2. March (1932) and Jeffery (1922) styles of particle rotation associated with plastically and viscously deforming materials, respectively. Jeffery style rotation graphics adapted from Carr and Rose (2003), by permission. © 2003 Elsevier Science Ltd. 10

Figure 2.3-1. Preliminary taxonomy of microfabrics and microstructures within the plasma and S-matrix of glacial sediments (Source: Menzies 2000, by permission. © 2000 The Geological Society of London). 12

Figure 3.1-1. Jesmond valley-Pavilion plateau area and till types identified by Lian (1997) and Lian and Hicock (2000) on a hillshaded and classed TRIM I digital elevation model (DEM) (Projection: Albers Conical Equal Area, Datum: NAD 83. Source: Government of British Columbia 2007. © Province of British Columbia). Last glacial maximum ice flow directions are based on those deduced by Lian and Hicock (2000). 22

Figure 3.1-2. Bedrock geology map (based on Roddick *et al.* 1976) and till types identified by Lian (1997) and Lian and Hicock (2000) superimposed on a hillshaded TRIM I digital elevation model of the study area (Projection: Albers Conical Equal Area, Datum: NAD 83. Source: Government of British Columbia 2007. © Province of British Columbia). 23

Figure 3.3-1. Legend for macrofabric scatterplots (A) and contoured stereograms (B). The principal eigenvectors in A point in the direction of maximum clustering within each mode. The principal eigenvector in B points in the

direction of maximum clustering for all clasts in the sample. All modes are significant to the 95% confidence interval. Measurements that do not fall inside a statistically significant mode are considered to be outliers. Structural data (shear, fracture and fissility planes) are plotted on the stereograms as poles to planes. 30

Figure 3.3-2. Rectified photograph of 45 x 35 cm grid overlying exposed diamicton by F17, site 48. Clasts have been traced (pink lines) using the image processing software, ImageJ (Rasband 1997-2007). 31

Figure 3.3-3. Bulk diamicton samples were carved out of the face (A), coated with plaster of paris to preserve internal structures (B), labelled on a flat horizontal surface (e.g., TN = true north, 197 = 197° azimuth) (C & D), and transported upside down in small plastic containers lined with bubble wrap (E) to the Micromorphology Lab at Brock University. The volume of the sample above (encased in plaster of paris) is ~12 cm x 10 cm x 10 cm. 32

Figure 3.3-4. Microfabric diagrams for vertically (A) and horizontally (B) oriented thin sections. Both horizontal and vertical microfabrics are plotted as 2D bi-directional rose diagrams (10° class interval). The peak(s) (or 10° class(es) with the highest number of observations) of the vertical microfabrics is (are) highlighted with cross-hatching. Horizontal microfabrics are superimposed on the contoured stereogram of the associated macrofabric (in this case F31) for comparison. The peak of what is visually estimated to be the tightest cluster is highlighted with cross-hatching, and the peak(s) of what is visually estimated to be the second tightest cluster is filled in black. Concentric circles are numbered as percentages of the total number of sand grains measured (N). Purple bidirectional arrows show the orientation of the 2D principal eigenvectors for each microfabric. Red unidirectional arrows show the direction of the 3D principal eigenvector for the macrofabric (for unimodal, spread unimodal, and multimodal/girdled macrofabrics), or for macrofabric modes (for bimodal and spread bimodal macrofabrics) (see Fig. 3.3-1). 35

Figure 3.3-5. A 'discrete microstructure map' including a legend for symbols, and associated frequency histogram. Each vertical thin section is divided into six 2.5 cm x 2.5 cm cells to facilitate counting. On the microstructure map, the orientation of the plane of the vertical thin section is indicated with black arrows. Crushed grains are labelled as ms for metasedimentary, cr for crystalline, ls for limestone, v for volcanic, and u for unknown. On the frequency histogram, T=turbates, N=necking structures, GL=grain lineations, GS=grain stacks, and CG=crushed or broken grains. 37

Figure 3.3-6. Microstructure identification subjectivity tests for thin sections S6F26v, S23F30v, S27F2v, and S48F18v. Each thin section was counted twice, with five days between each counting session. T=turbates, N=necking structures, GL=grain lineations, GS=grain stacks, CG=crushed/broken grains. 38

Figure 4.2-1. Site 23, F30 and F31. The stereogram for fabric 23 (fab-23) is adapted from Lian and Hicock (2000) with permission; the exact location of this fabric is unknown. See Figure 3.3-1 for stereogram legend. 40

Figure 4.2-2. Textural composition of the matrix of glacigenic diamictons. Particle size analysis was conducted on samples collected from all clast fabric measurement sites by laser diffraction at the University of Calgary (Mullins and Hutchison 1982; Anonymous 1998). See Table E-1, Appendix E for the raw data. 40

Figure 4.2-3. Units 1 and 2 and F30, site 23. See Figure 3.3-1 for stereogram legend. Metre stick with decimetre subdivisions for scale. 41

Figure 4.2-4. F31 and carbonate coated fissility planes in the diamicton at site 23. See Figure 3.3-1 for stereogram legend. Metre stick with decimetre subdivisions for scale. 42

Figure 4.2-5. Thin section S23F30v. A) A 2400 dpi scan of the thin section showing planar voids (yellow arrows). Large grains (blue arrows) are oriented sub-parallel to planar voids and smaller grains (green arrows) are oriented oblique to planar voids. The locations of microphotographs B, C, D, E, F and G are indicated by red squares. Microphotographs show planar voids (B), vughs (C), rounded sand sized grains (D, E), a broken grain (E), calcium carbonate precipitate (G) and a reddish-brown residue encircling grains (F). 47

Figure 4.2-6. Thin section S23F31v. A) A 2400 dpi scan of the thin section showing planar voids (yellow arrows) and the orientation of large (blue arrows) and small (green arrows) grains relative to the planar voids. The locations of microphotographs B, C, D, E, F and G are indicated by red squares. Microphotographs show planar voids (B), vughs (B, C), calcite/clay patches (B, D), calcium carbonate precipitate (F) and a reddish residue (G) lining grains. 48

Figure 4.2-7. Microfabrics S23F30v-1, S23F30h-1 and S23F30h-2, and microstructure map and frequency histogram for thin section S23F30v. See Figures 3.3-4 and 3.3-5 for legends. 50

Figure 4.2-8. Microfabrics S23F31v-1, S23F31h-1 and S23F31h-2, and microstructure map and frequency histogram for thin section S23F31v. See Figures 3.3-4 and 3.3-5 for legends. 51

Figure 4.3-1. F7 and fractures (solid lines) and shears (dashed lines) in the diamicton at site 20. The stereogram of fabric 20 (fab-20) reported by Lian and Hicock (2000) is reprinted with permission. Fabric 20 was collected from the same exposure as F7. Clast fabric data collected in this study is shown to the left. See Figure 3.3-1 for stereogram legend. Metre stick with decimetre subdivisions for scale. 56

Figure 4.3-2. F8 and fissility planes in the diamicton at site 20. The orientation of fissility planes is similar to that exposed at F7. See Figure 3.3-1 for stereogram legend. Metre stick with decimetre subdivisions for scale. 57

Figure 4.3-3. Thin section S20F7v. A) A 2400 dpi scan of thin section showing planar voids (yellow arrows). Large grains (blue arrows) are oriented subparallel to planar voids and smaller grains (green arrows) are oriented oblique to planar voids. The locations of microphotographs B, C, D, E, F and G are indicated by red squares. Microphotographs show planar voids and grains with darkened walls (B, C), vughes (B, C, E), a broken

grain (D), a grain stack (D), a necking structure (F), a crushed grain (F) and a turbate (G). 59

Figure 4.3-4. Microfabrics S20F7v-1, S20F7h-1 and S20F7h-2, and microstructure map and frequency histogram for thin section S20F7v. See Figures 3.3-4 and 3.3-5 for legends. 60

Figure 4.4-1. Site 44, units 1 (sandy gravel), 2 (diamicton), 3 (boulder-cobble pavement), and 4 (silt and clay rhythmites). The location of F5 and F6 within unit 2 is indicated with black dots. The stereogram for fabric 44 (fab-44) (measured in unit 2 - exact location unknown) is adapted from Lian (1997) with permission. Striae measurements reported by Lian (1997), coloured red on the fab-44 stereogram, were taken from the tops of cobbles and boulders in unit 3. Fractured ends reported by Lian (1997) from clasts in unit 2 are shown in black, and fractured ends reported by Lian (1997) from the cobble-boulder pavement are shown in red on the stereogram of fab-44. F36 is the boulder-cobble pavement fabric measured in this study from unit 3. See Figure 3.3-1 for stereogram legend. Metre stick with decimetre subdivisions for scale. 64

Figure 4.4-2. F6 and units 1 (sandy gravel), 2 (diamicton), 3 (boulder-cobble pavement) and 4 (silt and clay rhythmites) at site 44. See Figure 3.3-1 for stereogram legend. Metre stick with decimetre subdivisions for scale. 65

Figure 4.4-3. F5 and units 1 (sandy gravel), 2 (diamicton) and 4 (silt and clay rhythmites), site 44. See Figure 3.3-1 for stereogram legend. Metre stick with decimetre subdivisions for scale. 66

Figure 4.4-4. Thin section S44F5v. A) A 2400 dpi scan of thin section S44F5v showing subvertically and subhorizontally oriented fractures (yellow arrows). The locations of microphotographs B, C, D, E, F and G are indicated by red squares. Microphotographs show interfingering coarse (light coloured) and fine (dark coloured) textured domains (B, C), a skeletal grain-rich area of the thin section containing imbrication (D), soft sediment grains (E), a fuzzy grey patch inferred to be an area of calcium carbonate deposition (E), thin partings in a clay-rich area of the matrix (F) and a broken grain (G). 68

Figure 4.4-5. Microfabrics S44F5v-1, S44F5h-1 and S44F5h-2, and microstructure map and frequency histogram for thin section S44F5v. See Figures 3.3-4 and 3.3-5 for legends. 69

Figure 4.4-6. The formation of soft sediment grains. Silt and clay rich areas of the matrix (ellipse) fracture and divide into discrete mobile soft sediment grains (arrows) that become more rounded during transport. 72

Figure 4.5-1. F26 and F27 (exposure 1) and F33 (exposure 2), site 6 in a valley tributary to Jesmond valley (Fig. 3.1-1). The stereogram for fabric 6 (fab-6) reported by Lian and Hicock (2000) is reprinted with permission and shown in the bottom right. The exact location of this fabric is unknown. See Figure 3.3-1 for stereogram legend 75

Figure 4.5-2. F26 and F27 in unit 1, exposure 1, site 6. A shear plane and a fold are annotated on the photograph. The southeast dipping and northwest dipping limbs of the fold are represented by upright and inverted triangles,

respectively on the contour stereogram of F27. The strike and dip of the shear plane could not be measured. Metre stick with decimetre subdivisions for scale. See Figure 3.3-1 for stereogram legend. 77

Figure 4.5-3. F33, exposure 2, site 6. Metre stick with decimetre subdivisions for scale. See Figure 3.3-1 for stereogram legend. 77

Figure 4.5-4. Thin section S6F26v. A) 2400 dpi scan of thin section showing subparallel planar voids (yellow arrows). The locations of microphotographs B, C, D, E, F and G are indicated by red squares. Microphotographs show planar voids with clean walls (B), similarly aligned grains (C), a grain lineation (D), dark matrix/residue surrounding a grain (E), a grain stack (F), a vugh (F) and a turbate (G). 79

Figure 4.5-5. Thin section S6F27v. A) 2400 dpi scan of thin section showing large vughs and planar voids (yellow arrows). The locations of microphotographs B, C, D, E, F and G are indicated by red squares. Microphotographs show vughs (B), a necking structure (C), heavily weathered grains (D), similarly aligned grains (E), calcium carbonate precipitate (F), a grain stack (G) and a turbate (G). 80

Figure 4.5-6. Thin section S6F33v. A) A 2400 dpi scan of the thin section showing subparallel planar voids (yellow arrows). The locations of microphotographs B, C, D, E, and F are indicated by red squares. Microphotographs show a broken grain (B), calcium carbonate precipitate (B, C, D), a necking structure (E), vughs (E), and a turbate (F). 81

Figure 4.5-7. Microfabrics S6F26v-1, S6F26h-1 and S6F26h-2, and microstructure map and frequency histogram for thin section S6F26v. See Figures 3.3-4 and 3.3-5 for legends. 82

Figure 4.5-8. Microfabrics S6F27v-1, S6F27h-1 and S6F27h-2, and microstructure map and frequency histogram for thin section S6F27v. See Figures 3.3-4 and 3.3-5 for legends. 83

Figure 4.5-9. Microfabrics S6F33v-1, S6F33h-1 and S6F33h-2, and microstructure map and frequency histogram for thin section S6F33v. See Figures 3.3-4 and 3.3-5 for legends. 84

Figure 4.6-1. Site 60, exposure 1 (site 4 in Lian 1997) showing unit 4. The diamicton in this exposure is considered to be equivalent to unit 4 in exposure 2. ‘a’ points to shears previously measured to be dipping to the SW, ‘b’ points to imbricated sandstone blocks from the Jesmond valley formation (JRF) that have been entrained into the overlying diamicton, and ‘c’ points to folds in the JRF. SW dipping shears are plotted as poles to planes in the stereogram (Photograph and stereogram data source: Lian and Hicock 2000, by permission. © 2000 Elsevier Science Ltd. and INQUA.) 88

Figure 4.6-2. Site 60, exposure 2 showing units 1 (horizontally bedded and rippled sand), 2 (interbedded pebbly sand and gravel), 3 (massive, clast-poor diamicton), 4 (massive, clast-rich diamicton) and 5 (sandy gravel). Shears and fractures are annotated on the photograph and plotted on the contour stereogram of the fabric they are closest to on the exposure. The contact between units 3 and 4 was measured and plotted as a shear

plane on the stereogram of F25 (black triangle). The positions of indurated sediment clasts A, B, C and D (shown in Fig. 4.6-2) are indicated with a blue dashed circle. The approximate position of Lian's (1997) fab-60a and fab-60b (stereograms reprinted with permission) is indicated by white boxes. The red squares on the stereogram of fabric 60b represent a group of fractures (red lines) measured by Lian (1997, p. 204). See Figure 3.3-1 for stereogram legend. 89

Figure 4.6-3. Indurated sediment clasts found in unit 4, site 60. Photographs A-D correspond to clasts A-D labelled in Figure 4.6-2. Sediment clasts A and C are composed of a light yellow massive pebbly silt. Sediment clast B is composed of laminated silt and sand. Sediment clast D consists of pebble-sized clasts suspended in massive, partially oxidized sand. The head of the geologic hammer is 6 cm wide. The right margin of the ruler in photograph C is subdivided into centimetre subdivisions. The metre stick in photograph D is subdivided into red and white decimetre subdivisions. 91

Figure 4.6-4. Striae measurements from two groups of boulder and cobble-sized clasts in unit 4, site 60 (exposure 2) . Striae sets are plotted both as raw data (one line per striae set) (a), and as a circular frequency distribution with a 10° class interval (b). Purple bidirectional arrows represent principal eigenvectors (V1). Concentric circles on the rose diagrams are numbered as percentages of the total number of striae sets measured (N). Rose diagrams are shaded to match the circles on the photograph, which indicate individual stone locations in the face. Stones located below (group 1) and above (group 2) the shear plane above F13 (annotated) are plotted separately and show no differences in boulder-cobble striae orientation. 95

Figure 4.6-5. Thin section S60F15v. A) A 2400 dpi scan of the thin section. The locations of microphotographs B, C, D, E, F and G are indicated by red squares. Microphotographs show vughs (B), an opaque residue creating a patchy matrix (C), steeply dipping fractures (D), a necking structure (E), a grain stack (F), and a broken grain (G). 97

Figure 4.6-6. Thin section S60F11v. A) A 2400 dpi scan of the thin section. The locations of microphotographs B, C, D, E, F and G are indicated by red squares. Microphotographs show similarly aligned grains (B), a grain lineation (C), a grain stack (D), a turbate (E) a necking structure (F) and a broken grain (G). 98

Figure 4.6-7. Thin section S60F13v. A) A 2400 dpi scan of the thin section. The locations of microphotographs B, C, D, E, F and G are indicated by red squares. Microphotographs show a sand inclusion (B), calcium carbonate precipitate in the matrix (C), calcium carbonate coating a grain (D), a turbate (E) a grain lineation (F) and a broken grain (G). 99

Figure 4.6-8. Thin section S60F14v. A) A 2400 dpi scan of the thin section. The locations of microphotographs B, C, D, E, F and G are indicated by red squares. Microphotographs show a broken grain (B), a grain stack (C), a grain lineation (D), vughs (E), a turbate (F) and small grains that are aligned to the edges of a large grain (G). 100

Figure 4.6-9. Microfabrics S60F15v-1, S60F15h-1 and S60F15h-2, and microstructure map and frequency histogram for thin section S60F15v. See Figures 3.3-4 and 3.3-5 for legends. 101

Figure 4.6-10. Microfabrics S60F11v-1, S60F11h-1 and S60F11h-2, and microstructure map and frequency histogram for thin section S60F11v. See Figures 3.3-4 and 3.3-5 for legends. 102

Figure 4.6-11. Microfabrics S60F13v-1, S60F13h-1 and S60F13h-2, and microstructure map and frequency histogram for thin section S60F13v. See Figures 3.3-4 and 3.3-5 for legends. 103

Figure 4.6-12. Microfabrics S60F14v-1, S60F14h-1 and S60F14h-2, and microstructure map and frequency histogram for thin section S60F14v. See Figures 3.3-4 and 3.3-5 for legends. 104

Figure 4.7-1. Site 48, units 1 (diamicton) and 2 (sandy gravel). Zones A and B mark zones of increased boulder-cobble concentration within unit 1. Fractures and shears are annotated on the photograph. Due to accessibility issues, only four shear planes were measured in the field. These are plotted as poles to planes on the contoured stereogram of the fabric they are closest to. The stererogram of fabric 48 (fab-48) is adapted from Lian and Hicock (2000) with permission. See Figure 3.3-1 for stereogram legend. 111

Figure 4.7-2. Sedimentological and structural features within the diamicton (unit 1) at site 48. A) Stacked cobbles and boulders. The ruler is 15 cm long. B) A faceted and striated boulder located at F17. C) A sand filled shear plane measured above F10. The metre stick in B & C has red and white decimetre subdivisions. Photograph locations are indicated in Fig. 4.7-1. 113

Figure 4.7-3. Thin section S48F32v. A) A 2400 dpi scan of the thin section showing steeply dipping narrow planar voids (yellow arrows). The locations of microphotographs B, C, D, E, F and G are indicated by red squares. Microphotographs show voids that previously housed grains (B), a grain lineation (B), mottled matrix (C), a close-up of darkened matrix (D), darkened matrix encircling a grain (E), opaque residue in the matrix and lining the walls of voids (F) and a turbate (G). 116

Figure 4.7-4. Thin section S48F17v. A) A 2400 dpi scan of the thin section showing steeply dipping planar voids (yellow arrows). The locations of microphotographs B, C, D, E, F and G are indicated by red squares. Microphotographs show turbates (B, D), grain stacks (B, G), opaque residue creating dark coloured patches in the matrix (C, D, E) and a broken grain (F). 117

Figure 4.7-5. Thin section S48F9v. A) A 2400 dpi scan of the thin section showing NE and SW dipping planar voids (yellow arrows). The locations of microphotographs B, C, D, E, F and G are indicated by red squares. Microphotographs show vughs (B), an opaque residue (C, D), grain lineations (E), a necking structure (F) and a turbate (G). 118

Figure 4.7-6. Thin section S48F10v. A) A 2400 dpi scan of the thin section. The location of microphotographs B, C, D, E, F and G are indicated by red squares. Microphotographs show mottled areas of the matrix (B), a close-

up of a dark patch (C), a grain lineation (D), a grain stack (E), a broken grain (F), and an opaque residue (G). 119

Figure 4.7-7. Thin section S48F18v. A) A 2400 dpi scan of the thin section. The locations of microphotographs B, C, D, E, F and G are indicated by red squares. Microphotographs show vughs (B), an opaque residue (C), similarly aligned grains (D), a grain lineation (E) a turbate (F) and broken grains (G). 120

Figure 4.7-8. Microfabrics S48F32v-1, S48F32h-1 and S48F32h-2, and microstructure map and frequency histogram for thin section S48F32v. See Figures 3.3-4 and 3.3-5 for legends. 121

Figure 4.7-9. Microfabrics S48F17v-1, S48F17h-1 and S48F17h-2, and microstructure map and frequency histogram for thin section S48F17v. See Figures 3.3-4 and 3.3-5 for legends. 122

Figure 4.7-10. Microfabrics S48F9v-1, S48F9h-1 and S48F9h-2, and microstructure map and frequency histogram for thin section S48F9v. See Figures 3.3-4 and 3.3-5 for legends. 123

Figure 4.7-11. Microfabrics S48F10v-1, S48F10h-1 and S48F10h-2, and microstructure map and frequency histogram for thin section S48F10v. See Figures 3.3-4 and 3.3-5 for legends. 124

Figure 4.7-12. Microfabric S48F18v-1, microstructure map and frequency histogram for thin section S48F18v. See Figures 3.3-4 and 3.3-5 for legends. 125

Figure 4.8-1. Site 27, exposures 1 (A) and 2 (B), showing units 1 (interbedded pebble-boulder gravel and diamicton), 2 (sandy silt clast-poor diamicton) and 3 (sandy silt clast-rich diamicton). The stereogram of fabric 27 (fab-27) is adapted from Lian and Hicock (2000) with permission. Fabric 27 was collected near the centre of unit 2 in exposure 1 (the exact location is unknown). The location of F1 and F2 (this study) are shown in ‘A’ and ‘B’ respectively. Blue banding (C) can be seen near the lower contact of unit 2, exposure 2. Metre stick with red and white decimetre subdivisions for scale. See Figure 3.3-1 for stereogram legend. 129

Figure 4.8-2. Sedimentological features near the upper contact of unit 2 at exposure 1, site 27. A) Heterogenous diamicton matrix showing dark grey and light grey patches. B & C) Imbricated and striated (arrow) pebbles. Left margin of ruler shows numbered centimetre intervals for scale. Field book is 18 cm tall. 131

Figure 4.8-3. Thin section S27F1n. A) A 2400 dpi scan of the thin section showing dark grey and brown matrices. The locations of microphotographs B, C, D, E, F and G are indicated by red squares. Microphotographs show vughs (B), patches of dark grey matrix with diffuse and sharp edges (B, C, D), fractures with clean walls (B, C), a grain lineation (C), a necking structure (D), a close-up of the grey diamicton (E), fractures following paths restricted to the brown diamicton (F), and a dark opaque residue (G). 133

Figure 4.8-4. Thin section S27F2v. A) A 2400 dpi scan of the thin section. The locations of microphotographs B, C, D, E, F and G are indicated by red

squares. Microphotographs show vughs (B), a grain stack (B), fractures with clean walls (C), similarly aligned skeletal grains (D, E), an opaque residue around a skeletal grain (D) and a broken grain (G). 134

Figure 4.8-5. Microstructure map and frequency histogram for thin section S27F1n. See Figure 3.3-5 for legend. Because this thin section was not oriented, microfabrics were not measured. 136

Figure 4.8-6. Microfabrics S27F2v-1, S27F2h-1 and S27F2h-2, and microstructure map and frequency histogram for thin section S27F2v. See Figures 3.3-4 and 3.3-5 for legends. 137

Figure 4.9-1. Site 26 showing two diamicton units (1 and 2), and the location of F29. Unit 1 is restricted to the bedrock depression and overlies the bedrock (Fig. 4.9-2). Unit 2 overlies unit 1 in the depression, and bedrock on either side of the depression. F28, site 25 (Fig. 4.9-3) is located ~20 m NW of F29 within the unit 2 diamicton (black arrow). The shear plane separating diamicton units 1 and 2 (Fig. 4.9-2) is plotted as a pole to plane on the contour stereogram of F29 (black triangle). The red squares and triangles on the contour stereogram of F29 record fractures (squares) and shear planes (triangles) measured by Lian (1997) in the underlying bedrock. These fractures and shears have since been covered by colluvium. The stereograms of Lian and Hicock's (2000) fabrics (fab-26a and fab-26b) are reprinted with permission and the approximate location of these fabrics are shown. See Figure 3.3-1 for stereogram legend..... 140

Figure 4.9-2. Close-up of the bedrock depression at site 26, showing argillite bedrock, and diamicton units 1 and 2. The orientations of striae sets were measured on the tops of seven cobble to boulder-sized stones (delineated in yellow) in unit 1 and are plotted as lines on stereograms (see Fig. 3.3-1 for stereogram legend). A subtle reddish layer is visible at the base of unit 2 (white dotted line), and a grey streak follows the shear zone between units 1 and 2. Metre stick with decimetre subdivisions for scale. 141

Figure 4.9-3. F28, site 25. The stereogram of fabric 25 (fab-25) is adapted from Lian and Hicock (2000) with permission. Fabric 25 was measured from the same exposure as F28. The shear plane and tension fracture measurements recorded in the fabric 25 stereogram were obtained from the bedrock that underlies unit 2 between the locations of F28 and the bedrock depression shown in Figure 4.9-2. These shear planes and tension fractures are now covered. See Figure 3.3-1 for stereogram legend. Metre stick with decimetre subdivisions for scale. 142

Figure 4.9-4. Thin section S25F28v. A) A 2400 dpi scan of the thin section showing planar voids (yellow, wide arrows) and skeletal grains (blue, narrow arrows) aligned parallel to them. The locations of microphotographs B, C, D, E, F and G are indicated by red squares. Microphotographs show sand grains oriented parallel to fractures (B), calcium carbonate patches (C, D), a necking structure (E), a grain lineation (F), and a broken grain (G). 145

Figure 4.9-5. Thin section S25F29v. A) A 2400 dpi scan of the thin section showing skeletal grains (blue arrows) aligned with planar voids. The

locations of microphotographs B, C, D, E, and F are indicated by red squares. Microphotographs show grain lineations (B), small grains aligned with the edges of a large grain (C), minor fractures with variable orientations (D), a heavily fractured matrix (E), and a broken grain (F). 146

Figure 4.9-6. Microfabrics S25F28v-1, S25F28h-1 and S25F28h-2, and microstructure map and frequency histogram for thin section S25F28v. See Figures 3.3-4 and 3.3-5 for legends. 147

Figure 4.9-7. Microfabrics S26F29v-1, S26F29h-1 and S26F29h-2, and microstructure map and frequency histogram for thin section S26F29v. See Figures 3.3-4 and 3.3-5 for legends. 148

Figure 4.10-1. F19 and F20, site 57. The stereogram of fabric 57 (fab-57) is adapted from Lian (1997). Metre stick with decimetre subdivisions for scale. See Figure 3.3-1 for stereogram legend. 152

Figure 4.10-2. Sedimentology of site 57 around F19. Unit 1 is over-consolidated clast poor glacigenic diamicton, the darkest part of which has been recently exposed at the time this photograph was taken. Unit 2 is stoney colluvium. Fractures in unit 1 (not visible in the photograph) are plotted as poles to planes on the contour stereogram. See Figure 3.3-1 for stereogram legend. Metre stick with decimetre subdivisions for scale. 153

Figure 4.10-3. Sedimentology of site 57 around F20. Unit 1 is over-consolidated clast poor glacigenic diamicton. Unit 2 is stoney colluvium. Fractures in unit 1 (not visible in photograph) are plotted as poles to planes on the contour stereogram. See Figure 3.3-1 for stereogram legend. Metre stick with decimetre subdivisions for scale. 154

Figure 4.10-4. Thin section S57F19v. A) A 2400 dpi scan of the thin section. Yellow arrows point to a brown residue on the edges of 2 large skeletal grains. The locations of microphotographs B, C, D, E and F are indicated by red squares. Microphotographs show vughs (B), fractures (C), dark residue lining a vugh (D), a grain lineation (E) and a turbate (F)..... 156

Figure 4.10-5. Thin section S57F20v. A) A 2400 dpi scan of the thin section. The locations of microphotographs B, C, D, E, F and G are indicated by red squares. Microphotographs show a coarse textured domain forming a band (B), necking structures (C, E), broken grains (C, G), a grain stack (F) and a turbate (D). 157

Figure 4.10-6. Microfabrics S57F19v-1, S57F19h-1 and S57F19h-2, and microstructure map and frequency histogram for thin section S57F19v. See Figures 3.3-4 and 3.3-5 for legends. 158

Figure 4.10-7. Microfabric S57F20v-1, and microstructure map and frequency histogram for thin section S57F20v. See Figures 3.3-4 and 3.3-5 for legends. 159

Figure 4.11-1. Composite stratigraphic log summarizing the Fraser River valley stratigraphy and associated interpretation near Clinton, B.C. (after Lian and Hicock 2001). Unit thicknesses shown in the log are general approximations; unit thicknesses vary widely from site to site. OSL stands for optically stimulated luminescence. C=clay, Si=silt, S=sand, G=gravel and D=diamicton. 162

Figure 4.11-2. Site 22 showing units II (sandy silt diamicton) and III (clast- and matrix-supported pebble gravel and sand) of Lian and Hicock (2001) and the locations of F34 and F35. Fractures in unit II (not visible in photograph) dip toward Fraser River and are plotted as poles to planes on the contour stereogram of the closest fabric. The stereogram of fabric 22 (fab-22) is adapted from Lian (1997) with permission, and was collected from unit II at the same exposure (the exact location is uncertain). Metre stick with decimetre subdivisions for scale. See Figure 3.3-1 for stereogram legend. 164

Figure 4.11-3. Thin section S22F34v. A) A 2400 dpi scan of the thin section showing orthogonal fractures (yellow, wide arrows) and a fine grained sorted domain. Some grains are oriented subparallel to the fractures (blue, narrow arrows). The locations of microphotographs B, C, D, E, F and G are indicated by red squares. Microphotographs show the sorted domain (B), residue along fracture walls (C), a grain lineation (D), subvertically oriented grains (E), residue patches (F) and a grain stack (G). 165

Figure 4.11-4. Microfabrics S22F34v-1, S22F34h-1 and S22F34h-2, and microstructure map and frequency histogram for thin section S22F34v. See Figures 3.3-4 and 3.3-5 for legends. 167

Figure 4.12-1. The positions of facets and keels on clasts in all fabric samples. N = the total number of clasts in a fabric sample. Fabric samples (recorded as site #/fabric # on the x-axis) are sorted according to inferred diamicton genesis (this study), where L = mainly lodgement, DL = deformed lodgement, D = deformation, G = gravity flow and M = melt-out. Facet data (a) is reported in percent. Keel data (b) is reported in absolute numbers. The absolute numbers of clasts that have both a facet on their top and a keel on their bottom is shown in 'b' as an orange line. All fabric samples are obtained from diamictons, except for F36, site 44, (S44/F36*) which was measured from a cobble-boulder pavement (see Section 4.4). 172

Figure 4.12-2. Primary till horizontal microfabric eigenvalues (S_1) for grains less than 1 mm in apparent length, and grains greater than 1 mm in apparent length. N=the total number of grains counted in a microfabric. Horizontal thin sections are sorted according to inferred genesis (this study), where L=mainly lodgement, DL=deformed lodgement, and D=deformation. 181

Figure 5.1-1. A dendrogram showing the results of hierarchical cluster analysis of micromorphological data from all vertical thin sections using the average linkage method. rx,y = the cophenetic correlation coefficient. Coloured boxes delineate groups that have been superimposed on a map of the study area in Figure 5.1-2. Red = group 1, blue = group 2, green = group 3, yellow = group 4, purple = group 5, and pink = group 6. The inferred diamicton genesis (this study) and clast concentration (clast c.) associated with each thin section is included below the dendrogram. L/DL = lodgement or deformed lodgement, DL = deformed lodgement, D = deformation, and G = gravity flow. N is the absolute number of discrete microstructures counted in the thin section. 187

Figure 5.1-2. Geographic distribution of microstructure association clusters (groups) derived using the average linkage clustering method (see Figure 5.1-1 for dendrogram). Site locations are marked with coloured circles indicating the inferred diamicton genesis according to Neudorf (this study), where L/DL = lodgement or deformed lodgement, DL = deformed lodgement, D = deformation, and G = gravity flow. Ice flow directions (white arrows) for the early part of the last glaciation (A), and the last glacial maximum (B) are from Lian and Hicock (2000). Both maps are superimposed on a hillshaded and classed TRIM I digital elevation model (Projection: Albers Conical Equal Area, Datum: NAD 83. Source: Government of British Columbia 2007. © Province of British Columbia)..... 188

Figure 5.2-1. Stacked bar plots for each of the 6 groups identified by the average linkage clustering procedure. The microstructure association of each vertical thin section is represented by one layer in the stack. The value above each stack represents the average proportion (%) each microstructure represents in thin sections of that group. N is the total number of thin sections in each group..... 190

Figure 5.2-2. Average diamicton texture (pie charts, beige=sand, brown=silt, black=clay), and microstructure association clusters (average linkage clustering method) superimposed on a map of bedrock lithology (based on Roddick *et al.* 1976) overlaying a hillshaded TRIM I digital elevation model (Projection: Albers Conical Equal Area, Datum: NAD 83. Source: Government of British Columbia 2007. © Province of British Columbia). Site locations are marked with symbols indicating the inferred diamicton genesis according to Neudorf (this study), where L/DL = lodgement or deformed lodgement, DL = deformed lodgement, D = deformation, and G = gravity flow. 191

Figure 5.2-3. Proportion of brittle and ductile structures in each thin section, sorted by increasing number of microstructures (N) per thin section (top to bottom). The average linkage method group each thin section belongs to is indicated on the right side of the bar graph..... 192

Figure 5.2-4. Scatterplots of microstructure relative abundance (%) against diamicton matrix texture. No clear correlation between and the size of sand, silt or clay fractions and the relative abundance of particular microstructures is discernable. 195

Figure B-1. Fabric scatterplots showing principal eigenvectors for all modes (left) adjacent to fabric scatterplots with symbols representing clast shapes according to Sneed and Folk (1958) (right). Sites are arranged in ascending numerical order (pages 204 to 209). 204

Figure D-1. General thin section preparation procedure based on protocol after Lee and Kemp (1992). 212

Figure F-1. Criteria for identifying turbates. ‘a’-‘c’ have smaller grains surrounding a core stone with four sides labelled 1, 2, 3 and 4. ‘a’ and ‘b’ are counted as turbates, but ‘c’ is not because only 2 sides of the core stone (2 & 3) have grains oriented with their long axes subparallel to the core stone edge. ‘d’ is a turbate with no core stone. 214

Figure F-2. Criteria for identifying necking structures. ‘a’ is considered to be a necking structure, ‘b’ considered to be part of a turbate. 214

Figure F-3. Criteria for identifying grain lineations. ‘a’ is considered to be a grain lineation, ‘b’ is not. 215

Figure F-4. Criteria for identifying grain stacks. ‘a’ is considered to be a grain stack, ‘b’ is not. 215

Figure F-5. Criteria for identifying crushed/broken grains. ‘a’ is considered to be a crushed/broken grain, ‘b’ is not. 215

Figure I-1. A dendrogram showing the results of hierarchical cluster analysis of micromorphological data from all vertical thin sections using Ward’s linkage method. rx,y = the cophenetic correlation coefficient. Coloured boxes delineate groups that have been superimposed on a map of the study area in Figure F-5. Red = group 1, blue = group 2, green = group 3, yellow = group 4, purple = group 5, and pink = group 6. The inferred diamicton genesis (this study) associated with each thin section is included below the dendrogram. L/DL = lodgement or deformed lodgement, DL=deformed lodgement, D=deformation, and G=gravity flow. N is the absolute number of discrete microstructures counted in the thin section. 220

Figure I-2. A dendrogram showing the results of hierarchical cluster analysis of micromorphological data from all vertical thin sections using the single linkage method. rx,y = the cophenetic correlation coefficient. Coloured boxes delineate groups that have been superimposed on a map of the study area in Figure F-6. Red = group 1, blue = group 2, green = group 3, yellow = group 4, purple = group 5, and pink = group 6. The inferred diamicton genesis (this study) associated with each thin section is included below the dendrogram. L/DL = lodgement or deformed lodgement, DL = deformed lodgement, D = deformation, and G = gravity flow. N is the absolute number of discrete microstructures counted in the thin section. 221

Figure I-3. A dendrogram showing the results of hierarchical cluster analysis of micromorphological data from all vertical thin sections using the complete linkage method. rx,y = the cophenetic correlation coefficient. Coloured boxes delineate groups that have been superimposed on a map of the study area in Figure F-7. Red = group 1, blue = group 2, green = group 3, yellow = group 4, purple = group 5, and pink = group 6. The inferred diamicton genesis (this study) associated with each thin section is included below the dendrogram. L/DL = lodgement or deformed lodgement, DL = deformed lodgement, D = deformation, and G = gravity flow. N is the absolute number of discrete microstructures counted in the thin section. 222

Figure I-4. A dendrogram showing the results of hierarchical cluster analysis of micromorphological data from all vertical thin sections using McQuitty’s linkage method. rx,y = the cophenetic correlation coefficient. Coloured boxes delineate groups that have been superimposed on a map of the study area in Figure F-8. Red = group 1, blue = group 2, green = group 3, yellow = group 4, purple = group 5, and pink = group 6. The inferred

diamicton genesis (this study) associated with each thin section is included below the dendrogram. L/DL = lodgement or deformed lodgement, DL = deformed lodgement, D = deformation, and G = gravity flow. N is the absolute number of discrete microstructures counted in the thin section. 223

Figure I-5. Geographic distribution of microstructure association clusters (groups) derived using Ward's linkage clustering method (see Figure I-1 for dendrogram). Site locations are marked with coloured circles indicating the inferred diamicton genesis according to Neudorf (this study), where L/DL = lodgement or deformed lodgement, DL = deformed lodgement, D = deformation, and G = gravity flow. Last glacial maximum ice flow directions (white arrows) are from Lian and Hicock (2000). The map is superimposed on a hillshaded and classed TRIM I digital elevation model (Projection: Albers Conical Equal Area, Datum: NAD 83. Source: Government of British Columbia 2007. © Province of British Columbia)..... 224

Figure I-6. Geographic distribution of microstructure association clusters (groups) derived using the single linkage clustering method (see Figure I-2 for dendrogram). Site locations are marked with coloured circles indicating the inferred diamicton genesis according to Neudorf (this study), where L/DL = lodgement or deformed lodgement, DL = deformed lodgement, D = deformation, and G = gravity flow. Last glacial maximum ice flow directions (white arrows) are from Lian and Hicock (2000). The map is superimposed on a hillshaded and classed TRIM I digital elevation model (Projection: Albers Conical Equal Area, Datum: NAD 83. Source: Government of British Columbia 2007. © Province of British Columbia)..... 225

Figure I-7. Geographic distribution of microstructure association clusters (groups) derived using the complete linkage clustering method (see Figure I-3 for dendrogram). Site locations are marked with coloured circles indicating the inferred diamicton genesis according to Neudorf (this study), where L/DL = lodgement or deformed lodgement, DL = deformed lodgement, D = deformation, and G = gravity flow. Last glacial maximum ice flow directions (white arrows) are from Lian and Hicock (2000). The map is superimposed on a hillshaded and classed TRIM I digital elevation model (Projection: Albers Conical Equal Area, Datum: NAD 83. Source: Government of British Columbia 2007. © Province of British Columbia)..... 226

Figure I-8. Geographic distribution of microstructure association clusters (groups) derived using McQuitty's linkage clustering method (see Figure I-4 for dendrogram). Site locations are marked with coloured circles indicating the inferred diamicton genesis according to Neudorf (this study), where L/DL = lodgement or deformed lodgement, DL = deformed lodgement, D = deformation, and G = gravity flow. Last glacial maximum ice flow directions (white arrows) are from Lian and Hicock (2000). The map is superimposed on a hillshaded and classed TRIM I digital elevation model (Projection: Albers Conical Equal Area, Datum: NAD 83. Source: Government of British Columbia 2007. © Province of British Columbia)..... 227

Chapter 1: Research objectives and rationale

1.1 Introduction

In order to understand the behaviour of both ancient and present day ice sheets and their response to climate change, it is imperative that we understand processes that occur at the glacier bed. These processes are influenced not only by ice sheet geometry, thickness and thermal regime, but also by substrate permeability, strength and deforming behaviour. Because of the inaccessibility of the beds of contemporary ice sheets, sedimentologists, structural geologists and geomorphologists look to sediments and landforms on the beds of former continental ice sheets to elucidate subglacial processes that may have influenced past ice flow velocities and ice sheet stabilities. These investigations often rely heavily on sedimentological and structural observations of nearly massive, enigmatic diamictons perceived to be subglacial tills.

A *diamicton* is a non-genetic term for an unsorted or poorly sorted unconsolidated sediment typically consisting of pebbles, cobbles or boulders set within a fine-grained matrix of sand, silt and clay (Lundqvist 1989; Bennett and Glasser 1996). *Till* is a type of diamicton that has been transported and deposited by or from glacier ice, with little or no sorting by water (Dreimanis and Lundqvist 1984; Dreimanis 1989).

Because of the difficulties involved in interpreting diamictons in the field, micro-scale sedimentological observations (i.e., observations and measurements made from thin sections using a microscope) are now being used alongside macroscale observations (i.e., observations and measurements made from an exposure in the field) to infer subglacial processes and conditions (e.g., Menzies *et al.* 1997). The microscale analysis of glacial sediments is now termed 'glacial micromorphology' (Menzies 2000).

Traditionally tills have been classified according to their macroscale sedimentological and structural characteristics using definitions proposed by the International Quaternary Association (INQUA) Commission on the Genesis and Lithology of Glacial Quaternary Deposits (Dreimanis 1989). Macroscale sedimentological and structural criteria typically include the type and orientation of brittle/ductile structures, the nature of lower contacts (i.e., gradational vs sharp), the level of consolidation, the type and position of wear features on clasts, and the strength, shape and orientation of clast fabrics (e.g., Dreimanis 1989; Hart and Roberts 1994; Hicock *et al.* 1996). More recently, authors have criticized traditional methods of till classification, stating that macroscale sedimentological and structural criteria are often

unable to differentiate between diamicton types as defined by the INQUA Commission (van der Meer *et al.* 2003; Menzies *et al.* 2006). These authors have proposed to modify the existing classification scheme in light of micromorphological observations (van der Meer *et al.* 2003; Menzies *et al.* 2006). In the last 30 years, micromorphological observations have been used by some glacial geologists to support inferences regarding subglacial depositional processes and conditions that may influence ice sheet behaviour (Menzies and Maltman 1992; van der Meer 1993; Menzies *et al.* 1997; van der Meer 1997; Menzies 1998; O'Cofaigh *et al.* 2005). These observations are made at the millimetre to micrometre scale, however, and their significance with respect to larger scale glacial depositional processes and environments is hard to evaluate. The general assumption is that different glacial lithofacies types should exhibit diagnostic micromorphologies (Menzies 2000), but this has yet to be demonstrated for a range of subglacial till types that provide insight into subglacial conditions and paleo-ice flow velocities. Therefore, the relationship between depositional/deformation processes (implied by diamicton macroscale sedimentology and structural geology), and microscale depositional/deformational processes (implied by diamicton micromorphology) is unclear, and must be clarified before a consensus can be reached regarding reliable sedimentological and structural criteria with which to classify glacigenic diamictons.

Past macroscale sedimentological and structural work has identified a range of glacigenic diamicton types in a small open-ended valley and adjacent plateau in south-central British Columbia (Lian 1997; Lian and Hicock 2000). These diamicton types have been classified using the definitions of the INQUA Commission of 1989 and have been inferred to represent a range of glacial processes and conditions. Additional macroscale and microscale sedimentological analyses have been conducted in this area to determine the relationship between till micromorphology and macroscale sedimentology. This relationship must be clarified for two reasons:

1) to determine whether or not we can use micromorphological observations as we do macroscale observations to support inferences regarding glacial processes, environments and consequent ice flow dynamics, and
2) to understand the implications of using either microscale or macroscale observations as criteria for till classification.

1.2 Research objectives

The purpose of this project is three fold:

1) to investigate the relationship between diamicton micromorphology and macroscale sedimentology,
2) to test the hypothesis that diamictons classified using macroscale sedimentological criteria and definitions proposed by the INQUA Commission (Dreimanis 1989) contain diagnostic micromorphologies, and
3) to investigate the relationship between diamicton micromorphology and local environmental variables such as topographic position, diamicton texture, and local bedrock lithology.

Chapter 2: Literature review

2.1 The ever-changing classification scheme of tills

Tills have been identified based on their macroscale sedimentological and structural characteristics in field exposures and classified according to the classification scheme of the International Quaternary Association (INQUA) Commission on the Genesis and Lithology of Glacial Quaternary Deposits (Fig. 2.1-1) (Dreimanis 1989; Hicock 1990; Hicock and Lian 1999; Lian and Hicock 2000; Lian *et al.* 2003; Ruszczyńska-Szenajch *et al.* 2003). Under this scheme, the category under which a till falls is named according to the process by which the till was emplaced. Melt-out tills, lodgement tills and deformation tills are recognized as the products of end-member processes by which sediment is deposited directly by glacial ice (primary tills), while gravity flow tills result from subsequent minor remobilization of primary tills by gravity (secondary tills) (Fig. 2.1-1) (Dreimanis 1989; Hicock 1990).

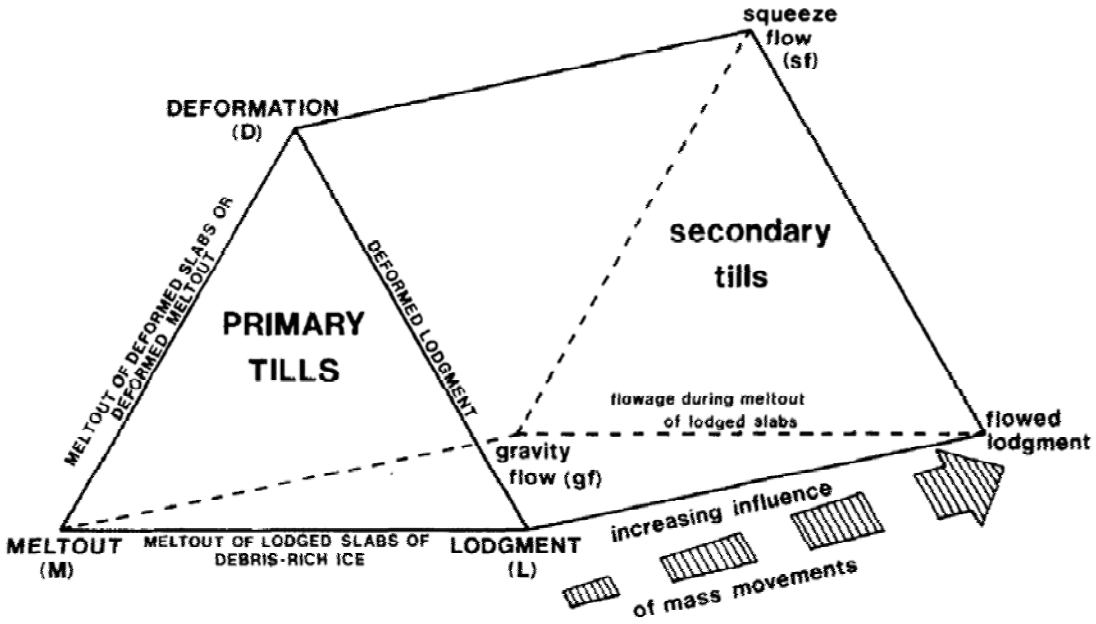

Figure 2.1-1. The 'Genetic Till Prism' (Source: Hicock 1990, by permission. © 1990 Geological Society of America) based on the classification scheme of the INQUA Commission on the Genesis and Lithology of Glacial Quaternary Deposits (Dreimanis 1989).

Melt-out till is deposited by the "gradual release of glacial debris from ice that is not sliding or deforming internally" (Dreimanis 1989, p. 45). Lodgement till is deposited by "plastering of glacial debris from the sliding base of a moving glacier by pressure melting and (or) other mechanical processes" (Dreimanis 1989, p. 43) where mechanical processes include clast ploughing into the substrate, and clast collisions and pile-ups (Boulton *et al.* 1974; Clark and Hansel 1989). Deformation till is "weak rock or unconsolidated sediment that has been detached from its source, the primary structures destroyed, and foreign material admixed" (Elson 1989, p. 85). Originally this term was used to describe a range of sediment types including:

> 1) thoroughly homogenized, previously deposited stratified sediment, in which all primary sedimentary structures have been destroyed, with a few clasts of different origin, 2) breccia of disoriented fragments retaining some of the original sedimentary structures in a matrix of the same material in a homogenized state, and 3) strongly contorted and displaced sediment containing sparse foreign clasts that has moved only a short distance (Elson 1989, p. 86).

The distinction between sediment type 3) and glacially deformed (glaciotectonic) bedrock "is arbitrary, and should be based on the presence of foreign clasts and evidence that the material, if it is till, has no attachment to its undisturbed source" (Elson 1989, p. 86). According to Elson (1989), deformation till is the 'deforming bed' of Boulton and Jones (1979) and commonly forms in undrained basins (such as lake basins), or where the glacier is flowing upslope, incorporating weak and (or) saturated sediments.

Deformed lodgement till falls between the lodgement and deformation till end-members and is "resedimented subglacial till deposited by the same glacier that subsequently deformed it" (Dreimanis 1989, p. 50). Gravity flow tills "may [be] derive[d] from any glacial debris upon its release from glacier ice or from a freshly deposited till, in direct association with glacier ice" (Dreimanis 1989, p. 48). The till may be derived from debris on the ice surface or the ice base, and its final deposition is through gravitational processes.

Many more terms have evolved over the years in attempts to describe subglacial till depositional histories. Some include "hard" and "soft" lodgement till (Ruszczyńska-Szenajch 2001), "soft bed till" (Hart 1994), "constructional" and "excavational" deformation till (Hart *et al.* 1990), and "non-deformable" till (Muller and Schluchter 2000). Often, tills with similar macroscale characteristics are classified differently by different authors. For example, the inferred A (upper, dilated and rapidly deforming) and B (lower, rigid and slowly deforming) layers found in subglacial tills associated with modern

Icelandic glaciers (Boulton and Hindmarsh 1987) have been classified as two layers within a 'soft bed till' (Hart 1994), two layers within a 'deformation till' (Benn 1995), and two layers corresponding to a 'deformed lodgement till' and an 'undeformed lodgement till', respectively (Dowdeswell and Sharp 1986).

In response to the growing mass of terms and overlapping definitions, recent publications have proposed a complete revamping of the traditional till classification scheme to acknowledge that most subglacial tills are hybrids formed in a spatially and temporally dynamic subglacial environment (e.g., Piotrowski *et al.* 2004) where till deposition and deformation processes are virtually inseparable in the geological record (van der Meer *et al.* 2003; Evans *et al.* 2006). Evans *et al.* (2006) are convinced that glacial geologists can confidently differentiate only between glaciotectonites, or "rock or sediment that has been deformed by subglacial shearing but retains some of the structural characteristics of the parent material" (Benn and Evans 1998, p. 387), and subglacial traction till, that is "sediment deposited by a glacier sole either sliding over and (or) deforming it's bed, the sediment having been released directly by the ice by pressure melting and (or) liberated from the substrate and then disaggregated and completely or largely homogenized by shearing" (Evans *et al.* 2006, p. 169). In their classification scheme, subglacial traction till encompasses the previously defined lodgement, deformed lodgement and deformation tills, and melt-out tills are redefined as "sediment released by the melting or sublimation of stagnant *or slowly moving* debris-rich glacier ice and directly deposited without subsequent transport or deformation" (Evans *et al.* 2006, p. 169). Due to their poor preservation potential it was suggested that melt-out tills will rarely inherit or replicate the foliation or structure of the parent ice, and most melt-out tills will be preserved as both crudely stratified and macroscopically massive diamictons displaying a variety of gravity induced structures (Evans *et al.* 2006). Thus, it could be difficult to differentiate them from the previously defined gravity flow tills (Dreimanis 1989; Lian 1997).

van der Meer *et al.* (2003) and Menzies *et al.* (2006) have suggested that lodgement and melt-out tills *senso stricto* are not preserved at all in the geological record and that all primary tills are products of a subglacial deforming bed (van der Meer *et al.* 2003; Menzies *et al.* 2006). They assert that at the microscale, subglacial diamictons are dominated by deformation structures, and primary (or depositional) structures are rare. From this perspective, ice dynamics over a soft sediment substrate are largely controlled by the deformation mechanics and thickness of the deforming layer, both of

which are heavily influenced by the substrate granulometry, heterogeneity, permeability, porewater pressure, and pre-existing macro and microstructures (van der Meer *et al.* 2003). They have proposed the term 'tectomict' to describe all subglacial tills because they are the products of structural, tectonic (kinetic) processes as opposed to depositional processes (van der Meer *et al.* 2003), and may be differentiated from other diamictons (i.e., subaerial debris flows) according to the presence or absence of certain microstructures (Menzies *et al.* 2006).

Other authors maintain that the tills should continue to be classified according to *sedimentary* processes, and not according to the deformation structures superimposed on them, because much of the till sediment is derived from the ice, not just the substrate (Ruszczyńska-Szenajch 2001; Lian *et al.* 2003). These authors assert that deformation only causes a redeposition or reorganization of already existing deposits and that syndepositional deformation during the lodgement processes is inevitable. Purely tectonic terms, such as *glaciotectonic melange* or *tectomict*, for example, should be reserved for sediments of the substrate, which have been deformed and (or) redeposited by glacial tectonics only (Ruszczyńska-Szenajch 2001; Lian *et al.* 2003). True *deformation till* should be a till that forms primarily from the glacial erosion and direct sedimentation of till and (or) sub-till sediment, with only a minor input of material from the ice itself (Lian *et al.* 2003). For example, a deformation till could form if porewater pressure in a lodgement till increased to the point where the till undergoes ductile flow under the stress of the overriding glacier and locally erodes and entrains substrate material. The new till resulting from this process is formed mainly from substrate material, rather than material melting out from the overriding ice (Lian *et al.* 2003).

2.2 Geological criteria for till classification

Part of the difficulty involved in classifying tills in terms of the subglacial processes they represent is due to a lack of consensus in the scientific community regarding reliable sedimentological and structural criteria with which to identify those processes (Hooke and Iverson 1995; Bennett *et al.* 1999; Hooyer and Iverson 2000b; Benn and Gemmell 2002; Carlson 2004). For example, if we recognize lodgement and deformation processes as end-members of a continuum (Hicock 1990), and that deformation occurs during the lodgement of clasts into a soft substrate (Clark and Hansel 1989), then distinguishing 'undeformed' lodgement tills from 'deformed' lodgement tills and 'deformation' tills in the field requires sedimentological evidence that

tells us the maximum depth of deformation at any given time when the ice is coupled to the substrate.

How the maximum depth of deformation is inferred from subglacial sediments, however, is the subject of much controversy (Piotrowski 1994; Hart *et al.* 1996; Hart *et al.* 1997; Piotrowski *et al.* 1997; Boulton *et al.* 2001; Piotrowski *et al.* 2002), and is most difficult to ascertain from macroscopically massive diamictons. Some sedimentological and structural evidence that has been used to constrain the thickness of deformation includes preserved sand, clay and peat intra-clasts or sand stringers showing limited deformation, strain proxies (clast fabrics, CI-indices, microshear geometry, S-matrix microstructures (Larsen 2006)) that deviate from the expected vertical trend of increasing strain in a deforming bed (e.g., van der Meer 1993), as well as features thought to represent a paleo-ice-bed interface, such as sharp lower till contacts with underlying sediment, laterally continuous intra-till sorted sediment layers suggestive of ice-bed decoupling, intra-till ploughing marks, sub-till Nye channels, and striated and faceted clasts with long axes aligned parallel to ice flow direction (Lian and Hicock 2000; Piotrowski *et al.* 2001; Larsen *et al.* 2004; Larsen 2006; Piotrowski *et al.* 2006) (Fig. 2.2-1).

Accompanying the debate regarding the spatial extent and thickness of the deforming bed under present day and Pleistocene glaciers and ice sheets, is the debate regarding the deforming behaviour of subglacial till and thus, how glacial geologists should interpret till clast fabrics. Till clast fabrics typically consist of the trends and plunges of the long axes of 25 to 50 clasts sampled within a ~0.6 m x 0.6 m area of exposed diamicton. How till clast fabrics are interpreted is related to whether or not the till in question is thought to have deformed plastically (Iverson and Iverson 2001; Piotrowski et al. 2004), in a ductile or viscous manner (Hicock and Dreimanis 1992), or if the inferred subglacial conditions are such that the mechanism of till deformation changes over time (Lian 1997; Lian and Hicock 2000; Benn 2002). For example, if till is expected to behave plastically as suggested by ring shear experiments, then clasts are expected to behave as passive markers according to the March (1932) model of rotation (Fig. 2.2-2) (Hooyer and Iverson 2000b), till fabrics will increase in strength with increasing strain (Iverson et al. 2003), and longer clasts may align closer to the shear direction than shorter clasts (Drake 1974).

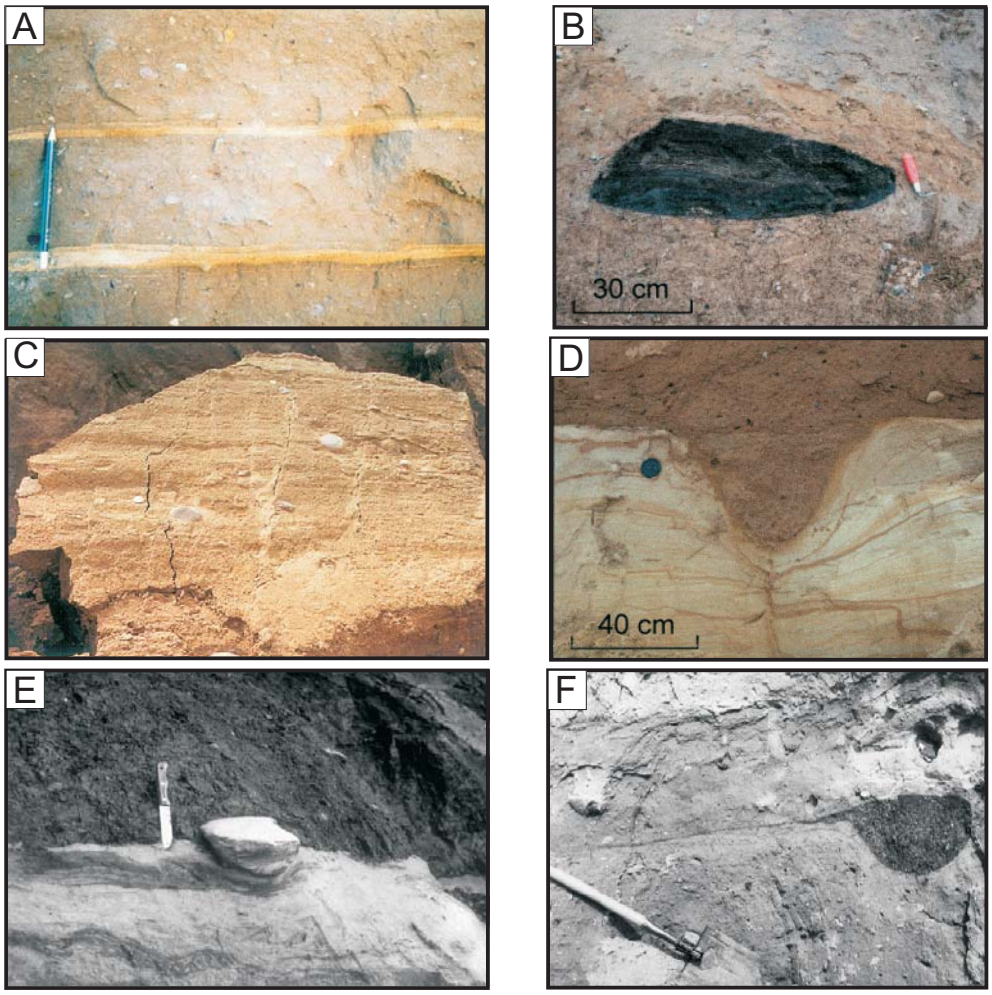

Figure 2.2-1. Sedimentological evidence used to constrain the depth of deformation within subglacial tills and underlying sediments. A) Laterally continuous intra-till sorted sediment layers thought to record decoupling of ice from the substrate (Source: Piotrowski *et al.* 2006, by permission. © 2005 International Association of Sedimentologists). B) Preserved undeformed peat clast with sharply defined edges used as evidence against pervasive deformation of the surrounding till (Source: Larsen *et al.* 2004, by permission. © 2004 John Wiley & Sons Limited). C) Grooves parallel to ice flow direction preserved on till surfaces below intra-till sand layers (such as that shown in A) suggestive of lodgement and ploughing processes (Source: Piotrowski *et al.* 2006, by permission. © 2005 International Association of Sedimentologists). D) Undeformed sub-till Nye channels preserved at the lower till contact precluding the possibility of the deforming layer extending below this level (Source: Larsen *et al.* 2004, by permission. © 2004 John Wiley & Sons Limited). E) Ploughed striated and faceted (on top) boulder showing evidence of abrasion of upper surface while stationary (Source: Piotrowski *et al.* 2001, by permission. © 2001 Elsevier Science Ltd and INQUA). F) Heavily weathered boulder with tongue smeared into till from it's upper surface indicative of erosion while in situ (Source: Piotrowski *et al.* 2001, by permission. © 2001 Elsevier Science Ltd and INQUA).

On the other hand, if till is expected to behave as a viscous material with limited slip between clast surfaces and the till matrix, then clasts are expected to exhibit a Jeffery (1922) style rotation (Fig. 2.2-2) (Hicock *et al.* 1996; Iverson *et al.* 2003), fabrics may weaken with increased strain as more clast long axes become oriented in the transverse direction with respect to shear (Hart 1994; Carr and Rose 2003), and longer clasts may become oriented in the transverse direction before shorter clasts (Glen *et al.* 1957). All other factors being equal, fabric strengths are expected to be weaker in thick deforming layers than in thin deforming layers (Hart 1994). Thus, different assumptions and (or) inferences regarding till deformation mechanisms and the thickness of the deforming layer can lead to quite contrasting interpretations of till clast fabrics.

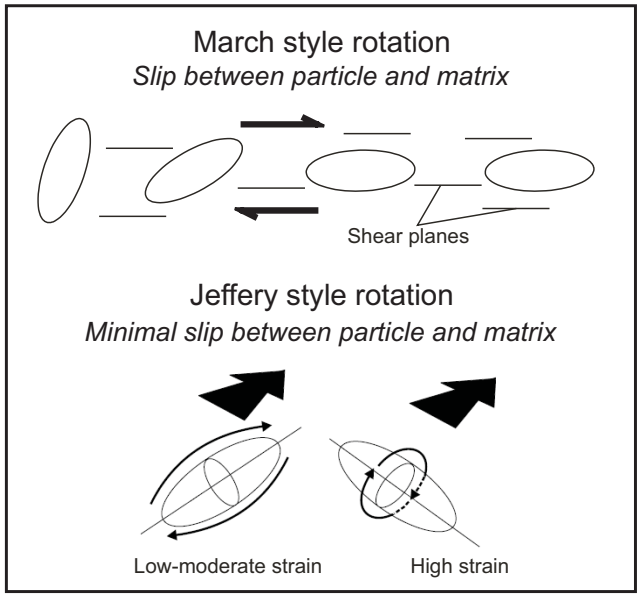

Figure 2.2-2. March (1932) and Jeffery (1922) styles of particle rotation associated with plastically and viscously deforming materials, respectively. Jeffery style rotation graphics adapted from Carr and Rose (2003), by permission. © 2003 Elsevier Science Ltd.

Although till was originally thought to deform as a viscous medium (Boulton and Hindmarsh 1987), more recent laboratory experiments (Iverson and Iverson 2001), measurements below contemporary glaciers (Hooke *et al.* 1997; Tulaczyk 2006), and sedimentological evidence from basal tills (Larsen and Piotrowski 2003) have suggested that subglacial till approximates a plastically deforming medium. The possibility that local increases in porewater pressure can compromise the shear strength of underlying sediments to the point of ductile or viscous-like deformation has not been ruled out however (Benn 2002), and many authors have reported evidence for this in the geological record (Hart *et al.* 1990; Hicock 1990; Hicock and Dreimanis 1992; Benn 1995; Hicock and Fuller 1995; Boulton *et al.* 1996; Hart 1997; Lian and Hicock 2000). Unfortunately, in the field, it is not possible to use clast fabric data alone to distinguish between clasts which have experienced Jeffrey-style rotation and those which have experienced March-style rotation within deforming till. Independent evidence for either

viscous, ductile or plastic-type deformation (in the form of deformation structures, for example), or, better yet, an independent measure of strain magnitude and direction (Iverson *et al.* 2008) is required to inform interpretations regarding clast rotation in response to strain.

The lack of consensus among glaciologists and glacial geologists concerning the spatial extent and thickness of deforming beds, the deforming behaviour of subglacial till, and the sedimentological criteria with which to identify past subglacial depositional and deformational processes is ultimately due to the difficulty in obtaining geophysical, sedimentological and structural measurements from the beds of contemporary glaciers and ice sheets, and the difficulties in reproducing subglacial conditions in the laboratory (Watts and Carr 2002). The enigmatic nature of subglacial sediments therefore demands that researchers use multiple lines of evidence to support their inferences of past subglacial processes and consequent ice flow dynamics (e.g., Larsen 2006). One method of inquiry that is becoming increasingly popular is glacial micromorphology.

2.3 Glacial micromorphology: principles and microstructure classification

Micromorphology is the analysis of structures and textures in undisturbed sediment, typically at the millimetre to micrometre scale. The roots of this technique lie in soil science (Brewer 1976), however, within the last 30 years it has been incorporated into glacial sedimentology to infer depositional and deformational processes from glacigenic sediments (Menzies *et al.* 1997; Carr 1999; Carr *et al.* 2000; Roberts and Hart 2005). Proponents of glacial micromorphology state that not only is the method a valuable resource when sediment exposures are lacking, but detailed information about depositional processes can be obtained from microstructures in diamictons that look homogenous at the macroscale (van der Meer 1987). Micromorphology is considered to be particularly valuable in research towards understanding subglacial environments (van der Meer 1987; Menzies and Maltman 1992; van der Meer 1993; van der Meer 1996; van der Meer 1997; Menzies 2000; O'Cofaigh *et al.* 2005).

Microstructures prevalent in glacial sediments have been classified according to the type of deformation involved (ductile vs brittle), as well as the relative role of porewater in the sediment during or after deposition (Fig. 2.3-1) (Menzies 2000). The focus on deformational process as opposed to depositional process is attributed to the

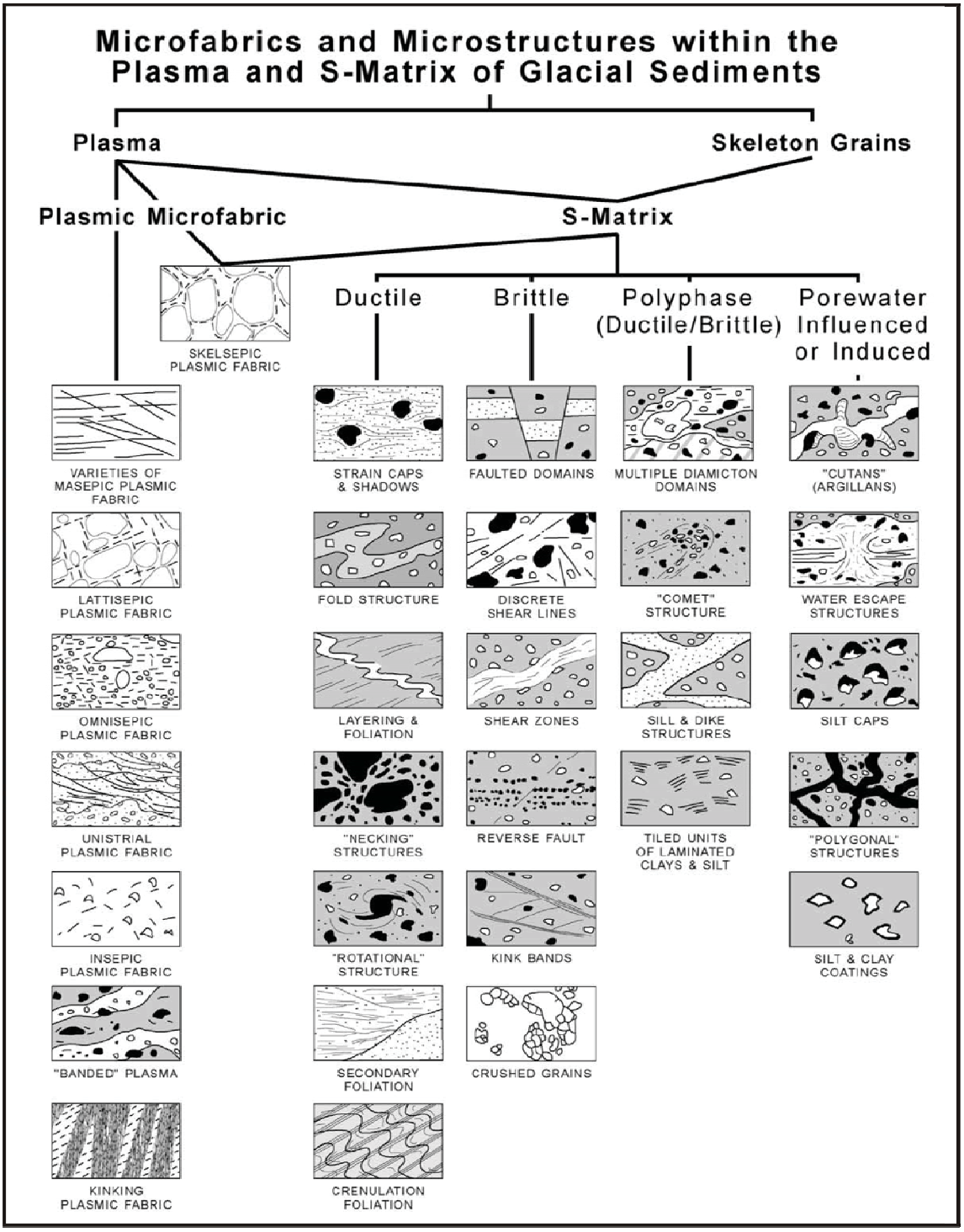

Figure 2.3-1. Preliminary taxonomy of microfabrics and microstructures within the plasma and S-matrix of glacial sediments (Source: Menzies 2000, by permission. © 2000 The Geological Society of London).

assertion that preserved depositional features are rare in glacigenic diamictons (van der Meer 1987; van der Meer *et al.* 2003).

The term “ductile” deformation in glacial sedimentology usually refers to the continuous flow due to grain-boundary sliding and failure of unlithified over-pressurized sediment. “Brittle” deformation refers to the grain-boundary sliding of dewatered sediment showing dislocation of sedimentary fabric along discrete planes (Passchier 2000). It occurs when stress applied to sediment is so rapid and (or) sufficiently large that the sediment particulates and matrix cannot adjust in sufficient time, causing fracturing (Menzies 2000).

All microstructures form in what is called the S-matrix, which constitutes the skeletal grains, matrix, and voids within the sediment (Fig. 2.3-1) (Brewer 1976; Menzies 2000). Patterns of grain alignment, fractures or shears within the plasma (i.e., all grains < 2 μm in diameter) constitute the plasmic fabric (Fig. 2.3-1). The identification and classification of plasmic fabrics depends on the presence of birefringent clay particles that are only visible under crossed polarized light (van der Meer and Menzies 2006). Each microstructure and plasmic fabric is interpreted as a local response of the sediment to some external stress (van der Meer 1987; Menzies 2000). Deformational processes and specific strain orientations have been inferred from combinations of these structures and fabrics (Menzies *et al.* 1997; Carr *et al.* 2000; Lachniet *et al.* 2001; Ruszczyńska-Szenajch *et al.* 2003; Hiemstra *et al.* 2005)

2.4 Microstructures, plasmic fabrics, microfabrics and “macro”-processes

2.4.1 Microstructures

> [an] advantage of micromorphological analyses is that they provide easy up-scaling from the microscope to the field outcrop as most of the phenomena that have been identified in thin-sections of subglacial sediments [cf. van der Meer 1993; Menzies 2000] seem to have equivalents at the outcrop-scale (structural isomorphism). (Hiemstra and Rijsdijk 2003, p. 374)

Microstructures are generally treated as microscale versions of macroscale sedimentological features, and as a result, are associated with similar processes. Thus, normal microfaulting is associated with brittle failure due to tension, microfolding to ductile deformation due to compression, and ‘galaxy’ or turbate structures to grain rotation within the matrix (van der Wateren *et al.* 2000; Phillips *et al.* 2007). The origin of plasmic fabrics and microfabrics, however, are less intuitive.

2.4.2 Plasmic fabrics

Plasmic fabrics, though described repeatedly in the literature, are enigmatic in terms of how they are formed. Horizontally aligned omnisepic fabrics are attributed to consolidation by a force perpendicular to the alignment, or settling through fluids (Evans 1998). Lattisepic plasmic fabrics have been associated with the shrink-and-swell of clays, or the rotation of sediment blocks under shear (van der Meer 1987; 1993). Skelsepic plasmic fabric is now typically associated with skeletal grain rotation (van der Meer 1993; Hiemstra and Rijsdijk 2003; Menzies and Zaniewski 2003; Roberts and Hart 2005), however, sediment consolidation and clay swelling should not be ruled out as possible causes (van der Meer 1987). Depositional and deformational processes, as well as the electrostatic charge of clay particles influence plasmic fabric formation, therefore it is likely that more than one process is responsible for each type (Evans 1998).

2.4.3 Microfabrics

Microfabrics are measurements of the apparent a- (long) axis orientations of sand sized particles in thin section. Because sand size particles have smaller masses and are largely influenced by neighbouring skeletal grains of an equal size or larger, they are not expected to reflect strain histories in the same manner as pebble, cobble, or boulder sized stones (Benn 1994; Carr and Rose 2003; Thomason and Iverson 2006). How microfabrics are interpreted, again, depends on the researcher's pre-conceived idea or pre-obtained knowledge concerning the deformation mechanism or rheology of the till (Fig. 2.2-2).

Some studies have shown a close correlation between macro- and microfabrics which has been attributed to shear plane development in response to overriding ice (Evenson 1971). Ring shear experiments with tills have shown sand sized grains to align in the direction of shear due to slip at the particle-matrix interface (Thomason and Iverson 2006).

Other studies showing inconsistent relationships between macro- and microfabrics in the field have attributed this to the Jeffrey (1922) style rotation of grains in a viscously deforming till where particles of different masses respond differently to strain, local shear zone thicknesses, and sediment heterogeneity (Carr and Rose 2003; Hart 2006). Carr and Rose (2003) integrated macrofabrics (using pebble sized grains) and microfabrics to differentiate between till that had experienced high strain from till that

had experienced low strain. This method was based on the assumption that the till experienced viscous deformation, and particles with small masses would begin to rotate along their long axes before particles with larger masses. Thomason and Iverson (2006) have stated that the assumption that particle rotation in deforming till is dependent on its mass is flawed, however, because particles in till are not isolated. Rather, they say, rotation is resisted by friction against adjacent particles. Thus, for sizes of particles studied in thin section, inertial resistance to rotation will be negligible relative to this frictional resistance (Thomason and Iverson 2006).

2.4.4 The scaling issue

The deformation style of unconsolidated sediments beneath ice sheets has important implications in terms of ice velocity (Boulton and Hindmarsh 1987), thus 'good' geological data is required to accurately model ice sheet dynamics. Microstructures, plasmic fabrics and microfabrics have been used to substantiate the deforming bed model of till deposition (O'Cofaigh *et al.* 2005; Menzies and Brand 2007), and to describe the viscous or plastic nature of sediment deformation (Roberts and Hart 2005).

How the micromorphology of 'deformable bed' tills compares with that of 'lodgement' tills or 'melt-out' tills, however, is unclear (see Section 2.5.2*)*. Lodgement processes should include syndepositional deformation (Ruszczyńska-Szenajch 2001), so microscale differences may not exist.

Substantiating a viscous or plastic rheological interpretation with micromorphological evidence is also problematic. Hindmarsh (1997) has suggested that the cross-over scale between viscous and plastic deformation of sediment under an ice sheet occurs at a much larger scale than the grain-to-grain interaction previously thought to be appropriate to deforming till. He suggests that what appears to be viscous deformation at the scale of an ice sheet (10-1000km) may actually be a series of small-scale plastic-type failure events visible on the centimetre to metre scale. The question of whether or not till rheology is scale dependent is an ongoing debate (c.f. Hindmarsh 1997; Tulaczyk 2006). The scale dependence of structural features, however, is not (Passchier and Trouw 2006). Ductile structures may be manifest at the macroscale, while brittle structures appear at the micro-scale and vice versa (Menzies 2000; Passchier and Trouw 2006). Cross-cutting relationships may show that different phases of deformation occurred at different times, and it is also possible for both types of deformation to occur simultaneously (Menzies 2000).

2.5 Past uses of glacial micromorphology

In glacial studies, micromorphology is used to supplement sedimentological and structural observations at the macroscale (Ruszczyńska-Szenajch *et al.* 2003; Roberts and Hart 2005), and to define diagnostic criteria for the purposes of ascribing genesis to sediments of unknown origin, particularly in the absence of field exposures (i.e., using deep oceanic drill cores) (Seret 1993; Carr 2001; Menzies and Zaniewski 2003). The implications of each application are discussed below.

2.5.1 Supplementary data

More often than not, thin section analysis is pursued *after* macroscale sedimentological analyses have been performed. In these cases, the sampling strategy for thin section analysis is determined by the macroscale sedimentology, and micromorphological interpretations are made within the context of macroscale inferences. For example, coastal exposures in north Norfolk, West Runton, UK are considered to be a type site for glaciotectonic deforming bed sediments (Roberts and Hart 2005). Roberts & Hart (2005) used thin section analysis to record evidence of brittle and ductile failure to infer the relative importance of viscous and plastic modes of deformation within a rheologically heterogeneous deforming bed. Macroscale sedimentological analyses of another diamicton in Dębe, Poland lead to its classification as a lodgement till (Ruszczyńska-Szenajch *et al.* 2003). As such, further microscopic analysis was used to understand the mechanics of lodgement, and to distinguish between 'hard' lodgement and 'soft' lodgement phases within the profile (Ruszczyńska-Szenajch *et al.* 2003).

It is always beneficial to interpret microstructures within the context presented by macroscale observations, if only because the size of even the largest of thin sections provides such a spatially restricted view. However, using micromorphological data as supplementary information to macroscale analyses can be problematic, particularly in the case of glacigenic diamictons. This is because the macroscale interpretations may be incorrect. Microscale interpretations, influenced by preconceived notions of sediment depositional processes or environments, can yield misleading information in terms of the processes responsible for microstructure or microfabric formation. For example, a macroscale sedimentological examination of diamictons within drumlins in New York State revealed diamictons that exhibited intraclasts, intercalated stringers and lenses of stratified sand and gravel, and multiple macroscale deformation structures (Menzies *et*

al. 1997). These diamictons were thought to record mélange-style deposition of sediment under subglacial deformable bed conditions (Menzies *et al.* 1997). Thin sections extracted from the diamictons revealed a suite of brittle-type structures (faults, shear lines, planes and zones) and ductile-type structures (folds, boudins, shadows, rotational structures, squeeze flow forms and diffusive boundaries), which were used to support the macroscale interpretation of a subglacial deforming bed (Menzies *et al.* 1997). These microscale interpretations, however, suggest that similar ductile and brittle-type microstructures would not form during lodgement processes, despite more recent evidence for the contrary (Ruszczyńska-Szenajch *et al.* 2003). For example, in central Poland, microstructures in the form of circular structures, deformed intraclasts, discrete shears, and plasmic fabrics have been described in diamictons that have been classified as lodgement tills based on macroscale sedimentological and structural characteristics (Ruszczyńska-Szenajch *et al.* 2003).

2.5.2 Diagnostic criteria

Despite the paucity of research behind the physics of microstructure formation (Hiemstra and van der Meer 1997; Evans 1998; Muller and Schluchter 2000; Khatwa and Tulaczyk 2001; Hiemstra and Rijsdijk 2003; Larsen *et al.* 2005; Thomason and Iverson 2006) efforts have been made to identify microstructure associations indicative of particular depositional environments in order to guide genetic interpretations of sedimentary sequences of unknown origin. For example, a large scale study involving 208 thin sections cut from diamictons obtained in six different European countries described the micromorphological characteristics of four different till types (Table 2.5-1) (Seret 1993). Seret (1993) states that tills were classified according to the INQUA Commission, citing the Till Work Group Circular no. 25 of the INQUA Commission on Genesis and Lithology of Quaternary Deposits (Dreimanis 1984). It should be noted, however, that Seret's (1993) definition of melt-out till as till "deposited under the movement and pressure of the glacier" conflicts with the definition posed by the final report of the INQUA Commission, which states that melt-out till is deposited under stagnant ice (Dreimanis 1989). Despite the large amount of data analyzed in this study, methods of analysis and (or) quantification of data were not included in the publication (in fact the publication itself is only five pages long), and the resulting micromorphological criteria have yet to be successfully applied in the field. Also, deformation tills were not discussed.

Table 2.5-1. Micromorphological characteristics of "para-tills" and "ortho-tills" after Seret (1993).

PARA-TILLS (SECONDARY TILLS) Mass wasted till deposit	**ORTHO-TILLS (PRIMARY TILLS) Mechanically deposited by glacial ice**		
Flow/waterlain tills	**Lodgement tills**	**Melt-out tills** Melting occurs by the movement and by the pressure of the glacier	**Dislodgement tills** The glacial floor breaks along natural joints in the bedrock and blocks of dislocated bedrock become incorporated into the basal till
• Evidence of sorting • Periglacial-like segregation structures • Original structures partially or wholly obliterated	Clast by clast lodgement: • Mud injections penetrating clasts • Microfolds/faults downstream of lodged clasts • Skelsepic plasmic fabric Set by set lodgement (ice-cemented clasts are plucked, transported and lodged by glacier): • Primary structures - mainly lacustrine and fluviatile – are intensively folded and faulted • Injected trails of mud penetrate the clasts • Strings of splinters of cemented clasts left behind upstream	• Injections of sand grains into silty lenses • Injections of trails of mud • Micro-load cast-like structures • Intensively folded thin and short sorted lenses	• Microstructures indicative of injection in the mud filling bedrock joints • Softer grains are broken into splinters aligned along the direction of injection

A more recent field study conducted in west-central Wisconsin concluded that microstructures are not able to differentiate between tills whose genesis had been suggested by other means, such as till fabric, stratigraphic setting, and geomorphic occurrence (Svard and Johnson 2003). Unfortunately, published data on this work is restricted to a single abstract, however, and a detailed account of methods of analysis and results have yet to be made available to the scientific community.

Distinguishing between proglacial and subglacial deformation in glacigenic sediments among a series of glaciotectonically deformed sequences in Scotland using micromorphology has proven difficult (Phillips *et al.* 2007). Kinematic indicators (van der Wateren *et al.* 2000) observed at both the macroscale and micro-scale within sub-till glaciolacustrine and glaciofluvial/deltaic sediments seem to follow general paleo-ice flow directions, and appear to be heavily influenced by spatial and temporal fluctuations in

porewater content and sediment composition. Which deformation structures were formed in a proglacial setting and which were formed in a subglacial setting was difficult to discern without other geomorphological and sedimentological evidence (Phillips *et al.* 2007). The micromophology of subglacial tills was not studied in detail.

Other studies have demonstrated that subglacial deposits can be distinguished from other types of sediment using micromorphological criteria in a marine setting (Carr 2001; Hiemstra *et al.* 2005). For example, based on exposures in a fjord on the west coast of Spitsbergen, researchers have been able to define micromorphological criteria that distinguish between glaciomarine sediments and subglacial diamictons (Table 2.5-2). These authors anticipate the application of these criteria to oceanic drill-cored sediments in order to map the spatial extent of pre-existing grounded ice in offshore areas (Carr 1999).

Microscopic comparisons between primary tills and debris flows derived from them have suggested that the relative abundance of specific microstructures may vary between these two diamicton types (Lachniet *et al.* 2001; Menzies and Zaniewski 2003). For example laminar flow fabrics, flow structures, marbling, tiling and banding appear more frequently in debris flow diamictons than in their *in situ* primary till counterparts (Lachniet *et al.* 2001; Menzies and Zaniewski 2003).

Table 2.5-2. Micromorphological characteristics of glaciomarine and subglacial sediments adapted from Carr (2001), by permission. © 2001 Elsevier Science Ltd.

Subglacial sediments	**Glacimarine sediments**
General features: • crushed quartz grains • edge rounding • 'non-winnowed' matrix Planar 'brittle' deformation Associations of: • grain lineations • symmetrical pressure shadows • augen shaped intra-clasts • unistrial and masepic fabric domains Rotational 'ductile' deformation Associations of: • rotation features: circular alignments; galaxy structures; asymmetric pressure shadows • rounded soft sediment pebbles • pervasive masepic fabrics and –sepic fabrics • non-associated planar features Microfabric characteristics: • unidirectional vertical microfabric	General features: • coarse, winnowed plasma texture • dropstone structures • common, *in situ* marine microfossils • lack of deformation associations • graded bedding structures • lack of edge rounding of grains? • lack of plasmic fabric development Microfabric characteristics: • distinct vertical or near vertical microfabrics in vertical plane

2.6 Summary

Past research has demonstrated that till micromorphology may help us understand how till microstructure, particle size and heterogeneity may influence it's behaviour under shear stresses and hydraulic regimes typical of a subglacial environment (Evans 1998; Khatwa and Tulaczyk 2001; van der Meer *et al.* 2003; Phillips *et al.* 2007; Kilfeather and van der Meer 2008). However, what we can glean from microstructures commonly observed in ancient subglacial tills (i.e., turbates, necking structures, lineations, grain stacks, crushed grains, plasmic fabrics, precipitates, fractures and voids) in terms of till deforming behaviour, porewater pressure, large scale deformation mechanics and depositional processes under a paleo-ice sheet has yet to be adequately quantified. It is necessary to do so if we are to agree on sedimentological criteria with which to classify glacigenic diamictons. Therefore more work is required to 'calibrate' the micromorphological technique as it were, before it can be used to support or negate inferences regarding subglacial processes and consequent ice flow dynamics (e.g. Carr and Rose 2003; O'Cofaigh *et al.* 2005).

Chapter 3: Study area and methodology

3.1 Study area

Field work for this research was conducted in an area where previous macroscale sedimentological analysis has identified glacigenic diamictons resulting from a range of depositional and deformational/tectonic processes (Lian 1997; Lian and Hicock 2000). The study area consists of a small open-ended valley and adjacent plateau in south-central British Columbia, informally named Jesmond valley and Pavilion plateau, respectively (Fig. 3.1-1). While the majority of study sites are situated in the valley and on the plateau, site 22 is located adjacent to the Fraser River on the western side of the Edge Hills, and site 57 is located on the Fraser Plateau on the eastern side of the Marble Range (Fig. 3.1-1). See Appendix A for site coordinates.

3.1.1 Regional geology and topography

Jesmond valley trends NW-SE, roughly parallel to the Fraser River to the west. The valley is situated between the Marble Range (> 2000 m asl), which is composed of the Marble Canyon formation (predominantly Permian limestone), and the Edge Hills (up to 2000 m asl), which are composed of the Pavilion Group rocks (an agglomeration of chert, argillite, siltstone, basalt and andesite of Paleozoic and Triassic age) (Roddick *et al.* 1976) (Figs 3.1-1, 3.1-2). The valley floor lies at ~1100 m asl where it intersects Cutoff Valley at its southern-most end, and rises ~300 m for 11 km to the northwest, after which it decends ~200 m over a similar distance (Fig. 3.1-1). Jesmond valley contains a sediment fill at least 15 m thick that consists of a magnetically reversed deformed sand and gravel unit (informally named the Jesmond Road formation) (Lian *et al.* 1999) that is overlain by Kamloops Lake drift (Lian and Hicock 2000). The Kamloops Lake drift consists of advance phase glaciofluvial outwash sand, up to 5 m of diamicton referred to as Kamloops Lake till, and retreat phase glaciofluvial gravel and sand (Lian 1997; Lian and Hicock 2000).

The Pavilion plateau flanks the western side of Pavilion Mountain and has a surface that slopes gently toward the SW from ~1600 m to ~1000 m asl (Fig. 3.1-1). It is composed of the Cache Creek Group rocks (Pennsylvanian and Permian argillite, basal, chert and limestone) (Roddick *et al.* 1976) (Fig. 3.1-2). Three diamicton units have been identified on the plateau, the youngest of which is the Kamloops Lake till (Lian *et al.* 1999).

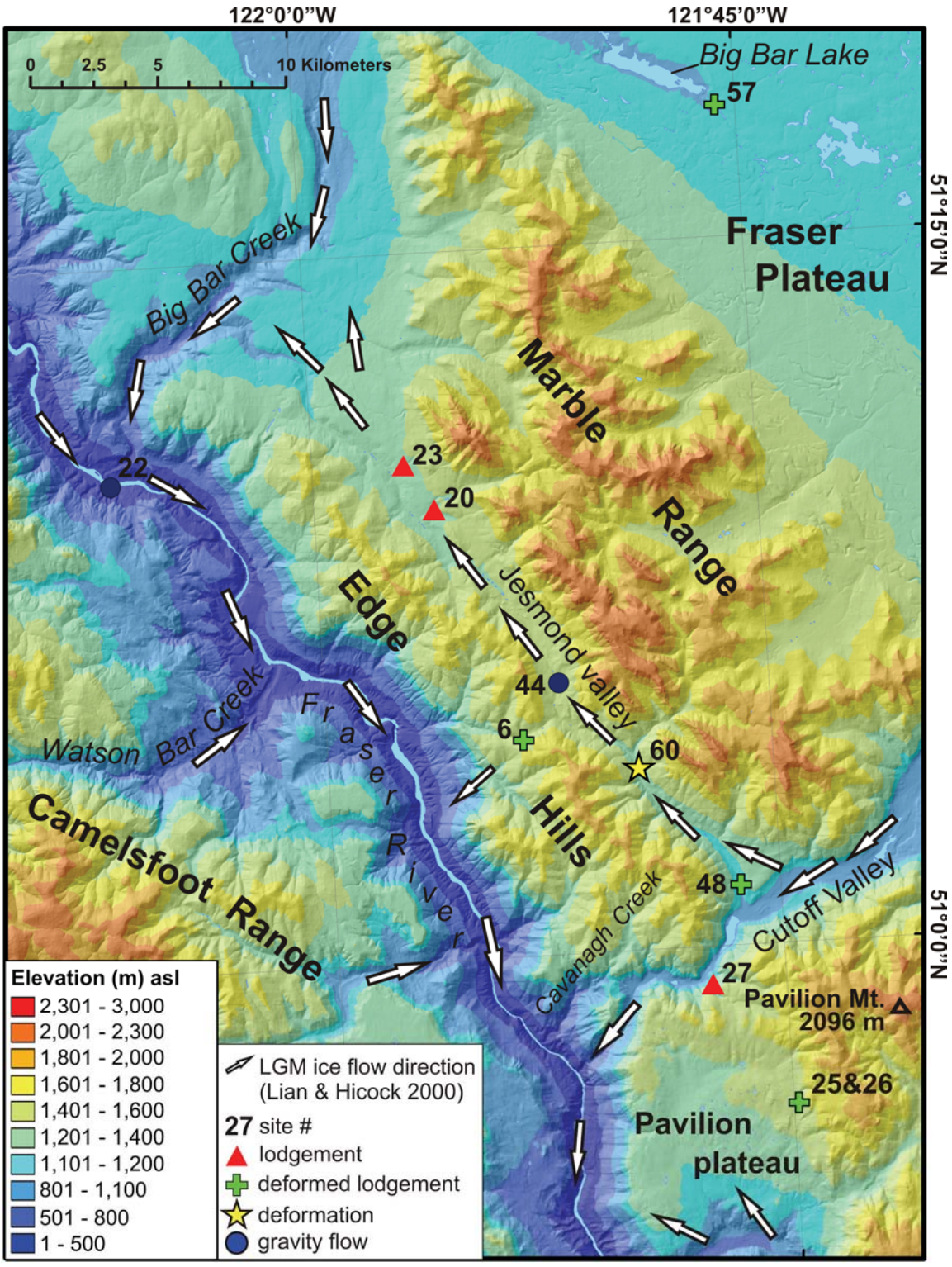

Figure 3.1-1. Jesmond valley-Pavilion plateau area and till types identified by Lian (1997) and Lian and Hicock (2000) on a hillshaded and classed TRIM I digital elevation model (DEM) (Projection: Albers Conical Equal Area, Datum: NAD 83. Source: Government of British Columbia 2007. © Province of British Columbia). Last glacial maximum ice flow directions are based on those deduced by Lian and Hicock (2000).

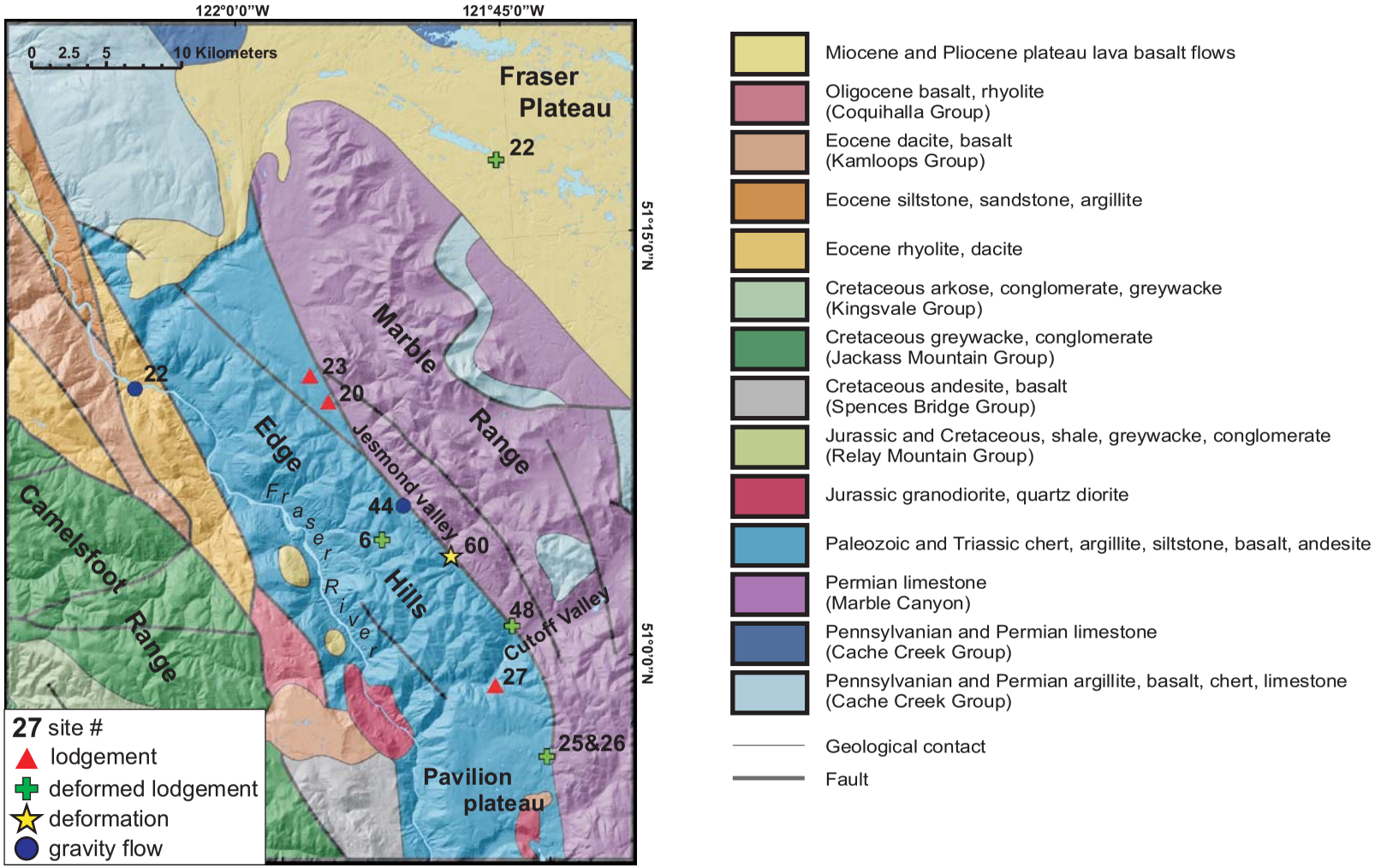

Figure 3.1-2. Bedrock geology map (based on Roddick *et al.* 1976) and till types identified by Lian (1997) and Lian and Hicock (2000) superimposed on a hillshaded TRIM I digital elevation model of the study area (Projection: Albers Conical Equal Area, Datum: NAD 83. Source: Government of British Columbia 2007. © Province of British Columbia).

East and north of the Marble Range lies the Fraser Plateau ~1100 m asl (Fig. 3.1-1). The Fraser Plateau is characterized by hummocks, swamps and depressions and is composed largely of Miocene and Pliocene basalt flows (Fig. 3.1-2). The surficial cover is generally thin (less than 10 m), and comprises landforms such as hills and hummocks consisting of glaciofluvial sand and gravel, glacigenic diamicton, aeolian silt, or a combination of all three (Lian 1997). Northwest-southeast trending streamlined hills and troughs are visible in aerial photographs (Lian 1997, p. 161).

West of the Edge Hills on the opposite side of the Fraser River lies the Camelsfoot Range reaching elevations above 2000 m asl (Fig. 3.1-1). The Camelsfoot Range is composed of Eocene rhyolite and dacite in the north, and lower Cretaceous greywacke and conglomerate in the south (Roddick *et al.* 1976) (Fig. 3.1-2). The highest peaks contain arêtes and cirques, and high structurally-controlled valleys are U-shaped (Lian 1997).

3.1.2 Inferred recent glacial history

During the onset of the Fraser Glaciation (MIS 2), ice advanced from the eastern and western mountain systems into the low-lying interior of south-central B.C. (Clague *et al.* 1989). At glacial maximum, the Cordilleran Ice Sheet is thought to have consisted of localized ice divides, domes, saddles, and coalescent glaciers (Tipper 1971) obtaining a maximum thickness of over 2000 m over major valleys, and several hundred metres over inland plateaus (Clague *et al.* 1989). Glaciotectonic structures and till clast fabrics measured from the Kamloops Lake till suggest that early ice spilled into the northern end of the Jesmond valley from the Fraser Plateau, and into the southern end of Jesmond valley from Cutoff Valley (Lian 1997). At glacial maximum the dominant ice flow direction in Jesmond valley and on Pavilion plateau was inferred to be from the southeast, while in the Fraser Valley ice flow was inferred to be from the northwest (Fig. 3.1-1) (Lian 1997; Lian and Hicock 2000).

In the study area, the style of till deposition beneath the Cordilleran Ice Sheet was inferred to be influenced largely by topography and substrate permeability. Where drainage was poor, such as the more constricted, southern part of Jesmond valley (Fig. 3.1-1), porewater pressures in the subglacial sediments increased, leading to a decrease in their strength and subsequent ductile deformation. Where drainage was improved, such as in the less constrained, northern end of the valley or on the plateaus (Fig. 3.1-1), till deposition occurred primarily through lodgement, leading to the

preservation of lodgement till (Lian 1997; Lian and Hicock 2000). On the basis of macroscale sedimentological analyses (below), four major glacigenic diamicton types have been identified and classified according to the classification scheme of the INQUA Commission (Dreimanis 1989): lodgement till, deformed lodgement till, deformation till and gravity flow till (Fig. 3.1-1) (Lian 1997; Lian and Hicock 2000).

3.2 Geological criteria for till classification in south-central B.C.

Diamictons in the study area have been classified according to their macroscale sedimentological and structural characteristics. These include till clast fabrics and wear features (the positions of striae, facets, keels, and stoss-lee features), the type and orientation of glaciotectonic structures, the nature (sharp vs gradational) of visible sub-till contacts, and the position of the diamicton within the stratigraphic sequence (Lian 1997; Lian and Hicock 2000). All diamicton units of interest in this study are thought to have been deposited during or shortly after the last (Fraser) glaciation (Lian 1997; Lian and Hicock 2001).

3.2.1 Till clast fabric and wear features

The orientation of clast fabrics and clast wear features were used extensively by Lian (1997) and Lian and Hicock (2000) in order to aid interpretations regarding till depositional history and environment. Pebble a-axis trend and plunge angles were measured on 30 to 50 stones with an a:b axis ratio of about 2:1 to 3:2, and a length greater than or equal to 1 cm. Care was taken not to measure clasts next to large boulders. Fabric strengths and orientations were measured using the eigenstatistics of Mark (1973), and individual modes were identified following the criteria outlined by Hicock *et al.* (1996), and tested against randomness using the procedure outlined by Woodcock and Naylor (1983). At the end of each day in the field, the fabric stereonet plots and associated statistics were analyzed. If outliers on the scatterplot suggested the existence of one or more additional modes, then more clasts were measured at the same location during the following season and (or) by another operator (Lian 1997).

The orientations of clast wear features were also measured within each diamicton unit on 10-20 clasts. Sometimes these clasts were part of the clast fabric sample, and sometimes the a-axis orientations of these clasts were not measured. Clast wear feature data included the orientation of the most recent striae on the upper surfaces of clasts, facets, keels, and stoss-lee features (bullet noses and fractured ends)

(Lian 1997; Lian and Hicock 2000). The significance of these features in relation to till genesis is discussed below.

3.2.2 Macroscale properties of lodgement till

Lodgement till clast fabrics are expected to be aligned mainly in the direction of paleo-ice flow with a gentle plunge upglacier and a possible minor transverse mode (Hicock *et al.* 1996; Lian and Hicock 2000). Drag effects of the sliding glacier sole, the substrate, and the matrix flowing around clasts tend to align prolate clasts in the direction of subglacial shear (Hicock *et al.* 1996 and references therein). Ploughing and lodging processes are expected to deposit clasts with a gentle upglacier plunge (Lian 1997; Lian and Hicock 2000). Stone collisions and local compressive flow may cause some clasts to become oriented transverse to shear (Hicock *et al.* 1996 and references therein).

Weathering, plucking and abrasion of clasts that are lodged into the substrate by the sliding glacier sole is expected to form ice flow parallel striae and facets on the upper surfaces of clasts, tapered clast ends (bullet noses) pointing up-glacier, fractured ends pointing down glacier on the upper-side of clasts, and (or) fractured ends pointing upglacier on the underside of clasts (double stoss-lee forms) (Kruger 1984; Clark and Hansel 1989; Lian 1997). Clasts that have been deposited quickly are expected to have irregular bottoms, and clasts that are dragged for a period of time by the glacier sole before becoming lodged are expected to develop boat-shaped bottoms (keels) which can be accompanied by ice flow-parallel striae (Lian 1997; Lian and Hicock 2000).

Previous authors have assumed that facets, keels, bullet noses and stoss-lee ends found in diamictons in the study area were formed during lodgement processes (Lian 1997; Lian and Hicock 2000). Ring shear experiments have demonstrated, however, that clasts can become abraded, developing striae parallel to their long axes within shear zones in plastically deforming diamicton (Iverson 2007, pers. comm.), and Benn (1995) has presented field evidence to suggest that facets and fractured ends can form along shear zones at depth within the till. Some authors have even proposed mechanisms by which striae and stoss-lee forms develop on pebbles and boulders along shear zones within glacier ice (Mickelson *et al.* 1992).

To this author's knowledge, the possibility that facets and fractured ends can develop within plastically deforming till at some depth below the ice-till interface has yet to be disproven. This scenario, however, requires that clasts be situated along a shear

zone long enough for these features to form. The temporal and spatial complexity of subglacial environments makes this scenario unlikely, because fluctuating porewater pressures and effective stresses cause shear zones to migrate over short (even diurnal) time cycles (Boulton *et al.* 2001). Clast wear feature development within glacial ice requires adequate debris concentrations to allow the abrasion of clasts, and clast proximity to englacial shear zones. Therefore, unless field evidence suggests otherwise, this study will treat clast facets, bullet noses, fractured ends (observed on the upper-sides of clasts) and keels as features that develop on clasts when they are ploughed and (or) lodged into the substrate at the ice-bed interface.

Lodgement till is expected to be highly consolidated, have a sharp, erosional lower contact, and is commonly associated with deformation structures related to the stress of overriding ice that can penetrate into underlying sediments (Lian 1997). These include subhorizontal fissility, steeply dipping (downglacier) tension fractures, and gently dipping (upglacier) shear planes (Hicock *et al.* 1996, table 1).

3.2.3 Macroscale properties of deformation till

The macroscale sedimentological properties of deformation till depends on: 1) the depth of deformation, 2) the intensity of deformation (or strain magitude experienced by the deforming sediment), 3) the porewater pressure of the sediment during deformation, and 4) the lithology and granulometry of the material deposited by the ice, and the material entrained from sub-till sediments. Subglacial tills in the study area were thought to be initially deposited by lodgement, with deformation tills only forming in areas where subglacial porewater pressures severely compromised the strength of the subglacial sediments. This lead to ductile and (or) simple shear deformation of a soft deformable layer under the glacier, which then eroded and entrained substrate materials (Lian 1997; Lian and Hicock 2000). Thus, a till is classified as 'deformation till' if there is evidence of ductile and (or) simple shear deformation and entrainment of sub-till sediments into the till layer.

Ductile or viscous deformation is associated with Jeffery (1922) style-like rotation of clasts (Fig. 2.2-2) within a deforming matrix leading to a spread unimodal, multimodal, girdled, or transverse fabric (the fabric type depending on strain magnitude, and thickness of the deforming layer as discussed in Section 2.2) (Hicock *et al.* 1996; Lian 1997). Clasts are expected to exhibit short striae, oriented in various directions, on both concave and convex surfaces (Hicock 1991; Benn 1995; Lian *et al.* 2003). Clast wear

features associated with earlier lodgement processes are expected to be re-oriented during the deformation process (Lian 1997).

Simple shear deformation is associated with subhorizontal shear planes, folding, attenuation, boudinage, brecciation, pressure shadows, and diamicton banding (Hicock *et al.* 1996 and references therein). Clasts located along shear planes are expected to orient themselves with their long (a) axis in the direction of shear, leading to strong parallel fabrics (Hicock *et al.* 1996).

At outcrop, deformation tills can exhibit ductile and (or) brittle deformation structures or they can be massive, suggesting complete homogenization under high strain magnitudes (Hart and Boulton 1991; Benn and Evans 1996). Because soft deformable layers are capable of absorbing shear strains more efficiently than rigid beds (Boulton 1996), brittle glaciotectonic structures are not expected to penetrate the underlying bedrock as they might during the deposition of lodgement tills (Lian 1997).

3.2.4 Macroscale properties of deformed lodgement till

A diamicton is classified as a 'deformed lodgement till' if it contains evidence of lodgement (usually in the form of clast wear features), but also shows evidence of post-depositional deformation by the same glacier that deposited it (Lian 1997). Deformed lodgement tills commonly have spread unimodal, bimodal or multimodal fabrics with misaligned clast wear features, and no significant evidence of sub-till erosion and entrainment of the bedrock (Lian 1997; Lian and Hicock 2000).

3.2.5 Macroscale properties of gravity flow till

In contrast to primary tills, gravity flow tills are expected to be normally consolidated. They are associated with structures related to sorting and settling processes, bulk density, shear stress and flow duration, and can exhibit large variations in granulometry and clast fabric over very short lateral and vertical distances (Broster and Hicock 1985; Eyles and Kocsis 1988). Deformation structures and fabrics should reflect the local slope direction and viscosity of the deposit during emplacement, and should have no consistent relationship to paleo-ice flow direction (Lian 1997). Gravity flow tills should consist of remobilized glacigenic material transported over short distances, which may include clasts with wear features inherited from subglacial depositional processes.

3.3 Methodology

The research approach of this project included field observation and measurement, diamicton sampling, thin section preparation and grain size analysis, laboratory observation and measurement, and data analysis. Each of the previously identified diamicton types in the study area were studied and sampled at a minimum of two different locations (Fig. 3.1-1).

3.3.1 Field observation

In the field, macroscale sedimentological data was collected to confirm and (or) modify previous interpretations and to establish effective sampling strategies for the purpose of thin section analysis. Data collection entailed photographs of exposures, descriptions of diamicton architecture, quantification of texture and sedimentary structures, as well as the measurement of clast fabrics (named F1, F2, etc.) and the orientation of clast wear features.

Clast fabric data collection and analysis followed the protocol of Lian (1997) and Lian and Hicock (2000) (Section 3.2.1) with minor modifications. Where possible, 60+ pebble-sized clasts (with a:b axis ratios of 3:2 to 2:1 and minimum a-axis lengths of 1 cm) were measured at a given sampling site in contrast to 30-50 pebble-sized clasts. This relatively high number of clasts was collected in order to detect any subtle modes that may have been missed previously. For each diamicton unit, a minimum of two (but occasionally three to five) clast fabrics was obtained to detect lateral and (or) vertical variations in fabric strength, shape and orientation within a unit.

Clast fabric data are plotted on lower hemisphere, equal area (Schmidt) diagrams, and contoured at 1, 2, 3, etc. points per 100/N% of the projected area, where N is the number of measurements (Starkey 1977) (Fig. 3.3-1). Fabrics were contoured at a grid resolution of 45 points to yield relatively smooth contours using StereoNet for Windows (version 1.41), created and sold by Per Ivar Steinsund (Varden 94, N-9018, Tromsø, Norway). Modes were identified visually from the fabric scatterplots and tested against randomness using the critical values and statistical protocol of Woodcock and Naylor (1983). Only modes that are significant to the 95% confidence level (Woodcock and Naylor 1983) are labelled as such on the scatterplots (Fig. 3.3-1). Because Woodcock and Naylor (1983) do not provide critical values for modes with less than five measurements (i.e., they are not testable), the measurements in these modes are considered to be outliers. In distributions with more than one mode, the mode with the

highest number of clasts is considered to be the primary or main mode (M1), and the mode with fewer clasts is considered to be the secondary mode (M2) (Fig. 3.3-1). Principal eigenvectors (of the entire fabric sample and individual modes) are represented as red arrows on fabric stereograms. Structures such as shear, fracture and fissilty planes are plotted on the stereograms as poles to planes (Fig. 3.3-1).

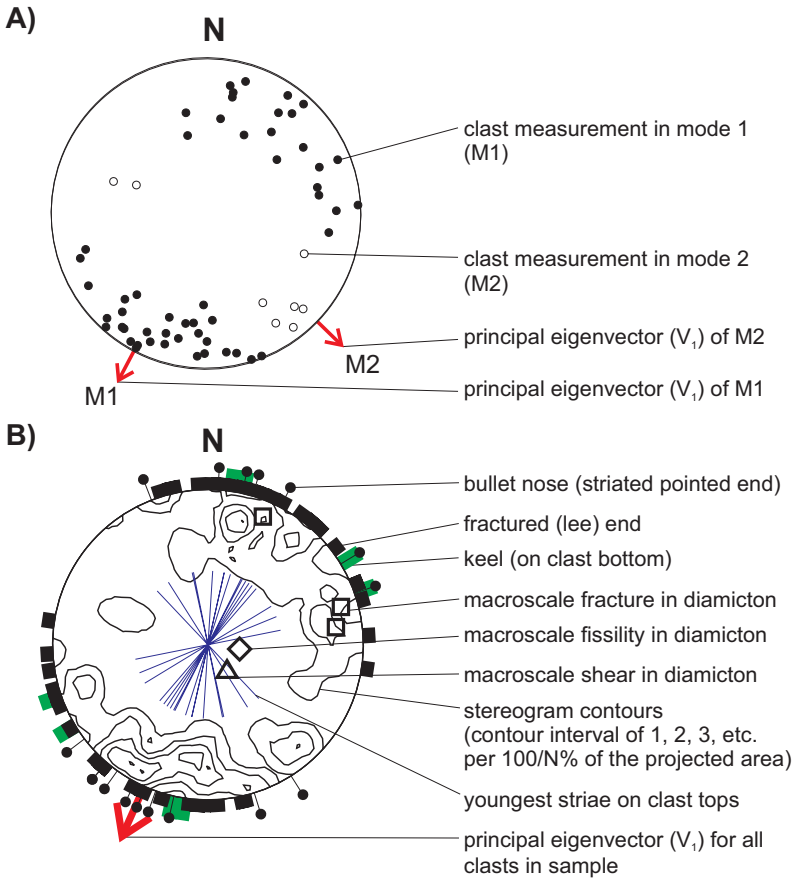

Figure 3.3-1. Legend for macrofabric scatterplots (A) and contoured stereograms (B). The principal eigenvectors in A point in the direction of maximum clustering within each mode. The principal eigenvector in B points in the direction of maximum clustering for all clasts in the sample. All modes are significant to the 95% confidence interval. Measurements that do not fall inside a statistically significant mode are considered to be outliers. Structural data (shear, fracture and fissility planes) are plotted on the stereograms as poles to planes.

Clast wear features were measured on the same clasts used for fabric measurements, rather than on the occasional separate clast as in the protocol of Lian (1997) and Lian and Hicock (2000). This was done in order to collect more clast wear feature data per clast fabric, and to establish relationships between individual clast orientations and the orientation of clast upper surface striae. Clast wear features measured included the presence or absence of striae, the orientation of the youngest (or

faintest) striae on clast tops, the presence or absence of striae following clast convexities/concavities, the orientation of keels on clast bottoms, the direction of bullet noses (or striated pointed ends), the direction of freshly fractured (lee) ends, and the positions (top, bottom or side) of facets and keels on each clast. Symbols were added to each fabric stereogram to show the direction of bullet noses and fractured ends, and the orientation of clast surface striae (the youngest on clast tops only), and keels (on clast bottoms only) (Fig. 3.3-1).

Additional clast measurements and observations were made to gauge the relationship between clast fabrics and clast shape as well as concentration. The a, b, and c-axis lengths of each clast were measured in order to classify pebble shapes following the scheme of Sneed and Folk (1958). Shape data was then superimposed onto clast fabric scatterplots to visualize any trends between clast orientation and clast shape (Appendix B).

Clast concentration data was collected at all macrofabric sites. Immediately adjacent to each fabric site, a 45 cm x 35 cm grid was held against the cleaned face and photographed using a 4 megapixel digital camera (Fig. 3.3-2). Photographs (Appendix C) were rectified using GIS software to remove parallax effects. All clasts visible in the photographs (with long axes generally greater than or equal to 0.5 cm) were then digitally traced. The area of each clast was calculated using the image processing

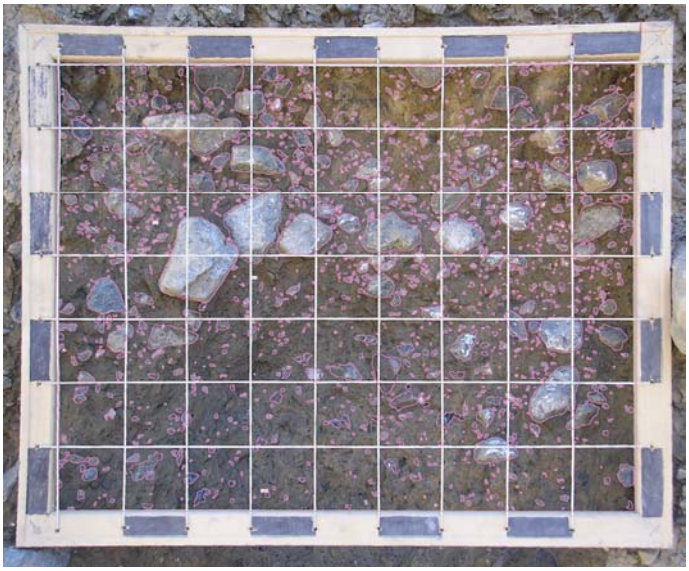

Figure 3.3-2. Rectified photograph of 45 x 35 cm grid overlying exposed diamicton by F17, site 48. Clasts have been traced (pink lines) using the image processing software, ImageJ (Rasband 1997-2007).

software package, “ImageJ” (Rasband 1997-2007) (Fig. 3.3-2). The sum of all clast areas was then divided by the total area of the face covered by the grid in order to calculate clast concentration in percent.

3.3.2 Diamicton sampling

At each clast fabric sampling site within a diamicton unit, two samples were removed; one for particle size analysis (~1kg of sediment), and one for thin section preparation (see below). This allowed a preliminary assessment of: 1) the at-a-site spatial micromorphological variability of each diamicton unit, 2) the between-site micromorphological variability of each diamicton type, 3) the between-diamicton type micromorphological variability in the study area, and 4) the influence of particle size on diamicton micromorophology (see Chapter 5).

Due to the well consolidated and stoney nature of the diamictons, traditional sample extraction using Kubiena tins (e.g. van der Meer 1996) was impractical, and larger bulk sample blocks (Fig. 3.3-3) had to be carved out of the face with a pick ax. The top and sides of each extracted sample were coated in the field with plaster of paris

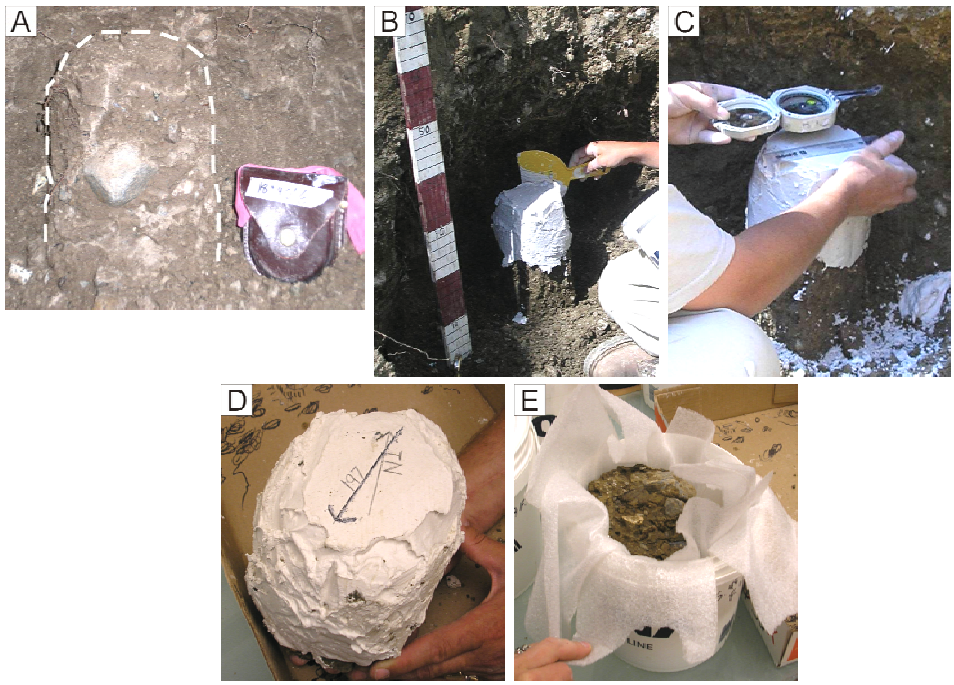

Figure 3.3-3. Bulk diamicton samples were carved out of the face (A), coated with plaster of paris to preserve internal structures (B), labelled on a flat horizontal surface (e.g., TN = true north, 197 = 197° azimuth) (C & D), and transported upside down in small plastic containers lined with bubble wrap (E) to the Micromorphology Lab at Brock University. The volume of the sample above (encased in plaster of paris) is ~12 cm x 10 cm x 10 cm.

and left to dry for 20 minutes. The top of each sample was then shaved with a trowel and measured with a level to create a horizontal surface, on which the orientation of the sample was marked. Each sample was then transported to the laboratory in a small plastic container lined with bubble wrap for impregnation and thin section preparation (Fig. 3.3-3).

3.3.3 Thin section preparation and grain size analysis

The diamicton samples for thin sectioning were shipped to the Micromorphology Lab at Brock University, St. Catherines, Ontario where thin section production techniques have been developed for unconsolidated, glacigenic sediments (Lee and Kemp 1992; Carr and Lee 1998; van der Meer and Menzies 2006) (Fig. D-1, Appendix D). Out of 28 samples shipped to the laboratory, 24 survived the thin section preparation process (four fissile samples collapsed before impregnation). From each diamicton sample, one vertically-oriented and one horizontally-oriented thin section were cut, where possible; (two samples were either too fissile or too small to obtain more than one thin section). In total, 43 thin sections were produced (20 horizontal, 23 vertical). Each thin section is named according to the site and clast fabric location from which the diamicton sample was retrieved, and according to the orientation of the thin section plane (i.e., vertical or horizontal). For example, thin section S6F33h is a horizontally-oriented (h) thin section cut from a diamicton sample obtained from the sample site of fabric 33 (F33), site 6 (S6).

The planes of all vertically-oriented thin sections were intended to follow the principal eigenvector of the macrofabric measured at the sampling site in order to approximate the orientation of shear. Unfortunately an error was made while correcting macrofabric data for magnetic declination (this was later corrected), and consequently the planes of all vertical thin sections are oriented ~37° W of the associated macrofabric eigenvectors. Therefore, the reader should keep in mind that the true sense of shear within the diamictons may not follow the plane of the vertical thin section. For this reason, microscopic observations and measurements were not used to infer shear sense or strain magnitude (Larsen *et al.* 2006; Thomason and Iverson 2006).

Grain size analysis was conducted on the diamicton matrix for the particle size range including clay to very coarse sand (Wentworth 1922) (Appendix E). These samples were processed at the University of Calgary using laser diffraction (Mullins and Hutchison 1982; Anonymous 1998).

3.3.4 Laboratory observation

Microscopic textures, structures and fabrics were observed and photographed at 10-40x magnification, using a Leica M420 binocular polarizing microscope and imaging system. Qualitative observations were recorded from the vertically-oriented thin sections and include: skeletal grain lithology and roundness, matrix colour, texture and heterogeneities (including domains and precipitates), and the shape and orientation of fractures and voids (Kilfeather and van der Meer 2008). Qualitative observations were annotated on microphotographs and scanned images of each thin section. Plasmic fabrics were not described or classified in this study because birefringent clays were not observed in thin sections from any of the diamictons sampled in the study area, except for those sampled at sites 25 and 26 on Pavilion plateau. Birefringent clays in the diamicton at sites 25 and 26 were too faint to allow a confident classification of the plasmic fabric. In the Jesmond valley, the lack of visible plasmic fabrics can be attributed to the carbonate contents of the diamicton (11-18%, Table II.3 of Lian 1997) as carbonates are known to mask clay birefringence (van der Meer 1987). The lack of birefringent clay in the diamicton at site 57 on the Fraser Plateau is likely due to its low clay content (<1%, Table E-1, Appendix E). The lack of birefringent clay in the diamicton at site 22 in the Fraser Valley may be due to a low clay content (~12%), or the mineralogy of the clay grains (van der Meer 1987).

Quantitative observations include microfabrics measured on both vertically- and horizontally-oriented thin sections (e.g., Carr and Rose 2003), and the relative percentages of discrete brittle and ductile type microstructures counted on vertically-oriented thin sections. The relative percentages of discrete microstructures were not counted on horizontal thin sections because of time constraints. Microfabrics are plotted as two-dimensional rose diagrams (Fig. 3.3-4). These are statistically described using the eigenvalue method of Mark (1973) adjusted for two dimensional data where maximum clustering yields an S_1 value of 1.0 and an S_2 value of 0, and a perfectly isotropic distribution yields S_1 and S_2 values of 0.5 (e.g., Thomason and Iverson 2006).

Vertical microfabrics were measured to determine the relative frequency of steeply plunging or gently plunging grains in different diamicton types. Labels for vertical microfabrics include the thin section they were measured from, followed by “-1” (e.g., S23F31v-1, Fig. 3.3-4). Grains with apparent long axes less than 2 mm in length were measured. In vertical microfabric rose diagrams, all peak(s) (or 10° class(es) with the highest number of observations) is (are) highlighted with cross-hatching (Fig. 3.3-4).

Because vertical thin sections from primary tills only roughly approximate the orientation of subglacial shear (see explanation in Section 3.3.3), vertical microfabrics are interpreted with caution, and inferred to reflect subglacial stress regimes or depositional processes only when other macro- and (or) microscopic evidence supports this view.

Horizontal microfabrics were compared with pebble macrofabrics to see if sand sized grains and pebbles were similarly aligned at each fabric site. In order to measure the change in microfabric strength and orientation with grain size, two rose diagrams are presented for horizontal microfabrics; one for grains less than an arbitrarily chosen value of 1 mm in apparent length, and one for grains greater than 1 mm in apparent length (Fig. 3.3-4). Labels for horizontal microfabrics include the thin section they were measured from, followed by "-1" for grains less than 1 mm in apparent length, and "-2"

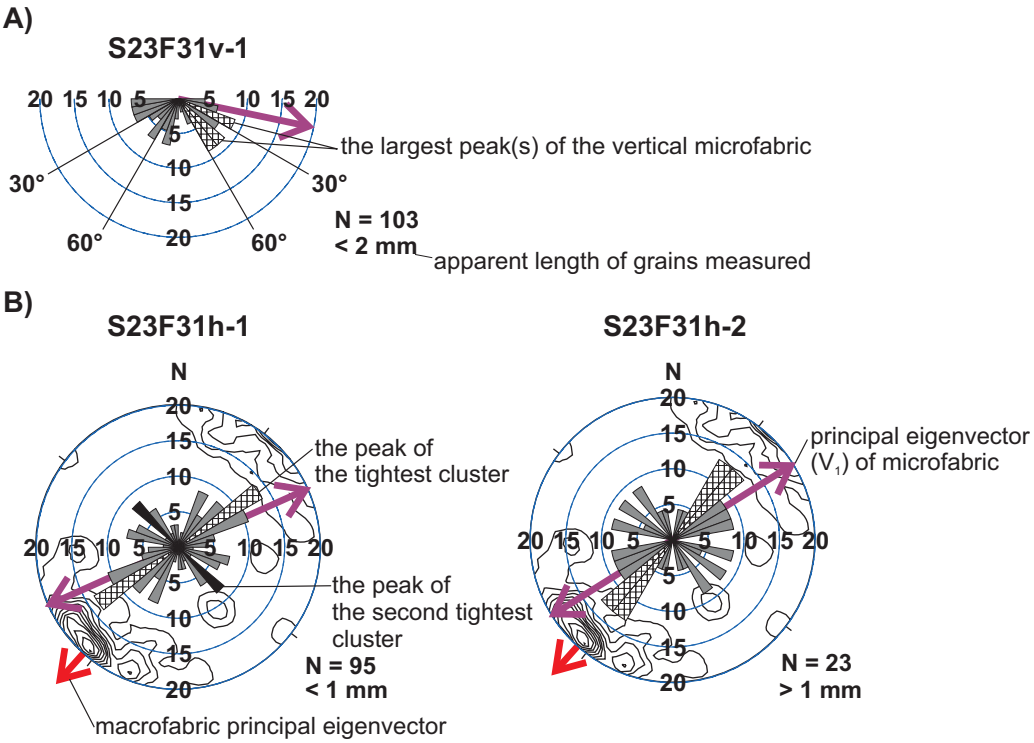

Figure 3.3-4. Microfabric diagrams for vertically (A) and horizontally (B) oriented thin sections. Both horizontal and vertical microfabrics are plotted as 2D bi-directional rose diagrams (10° class interval). The peak(s) (or 10° class(es) with the highest number of observations) of the vertical microfabrics is (are) highlighted with cross-hatching. Horizontal microfabrics are superimposed on the contoured stereogram of the associated macrofabric (in this case F31) for comparison. The peak of what is visually estimated to be the tightest cluster is highlighted with cross-hatching, and the peak(s) of what is visually estimated to be the second tightest cluster is filled in black. Concentric circles are numbered as percentages of the total number of sand grains measured (N). Purple bidirectional arrows show the orientation of the 2D principal eigenvectors for each microfabric. Red unidirectional arrows show the direction of the 3D principal eigenvector for the macrofabric (for unimodal, spread unimodal, and multimodal/girdled macrofabrics), or for macrofabric modes (for bimodal and spread bimodal macrofabrics) (see Fig. 3.3-1).

for grains greater than 1 mm in apparent length (e.g., S23F31h-1, S23F31h-2, Fig. 3.3-4). These rose diagrams are superimposed on the contoured stereogram of the macrofabric measured at the same fabric site (Fig. 3.3-4). In each rose diagram, the largest peak(s) in what is visually estimated to be the tightest cluster and the second tightest cluster are filled with cross-hatching and black, respectively (Fig. 3.3-4). (In some horizontal microfabrics only one cluster could be identified due to considerable spread among observations outside the tightest cluster).

Discrete microstructures that were counted include turbates, necking structures, grain lineations, stacked grains, and crushed grains (e.g. Larsen 2006) (see criteria for identification in Appendix F). These were identified under the microscope, mapped on high-resolution (2400 dpi) scans of each vertical thin section (Appendix G), and statistically summarized using normalized frequency histograms (Fig. 3.3-5). In order to assess the level of subjectivity involved in quantifying discrete microstructures, 4 thin sections were counted twice in the spring of 2007 with a minimum of five days between each counting session. The results are displayed in Figure 3.3-6, and show that the relative distributions obtained after subsequent counting sessions appear generally consistent. Thus, the level of subjectivity was considered acceptable. More in-depth studies on the subjectivity of till micromorphology are pending. As previously mentioned, discrete microstructures were not counted on horizontal thin sections, however, high resolution (2400dpi) scans of these are included on DVD in Appendix H.

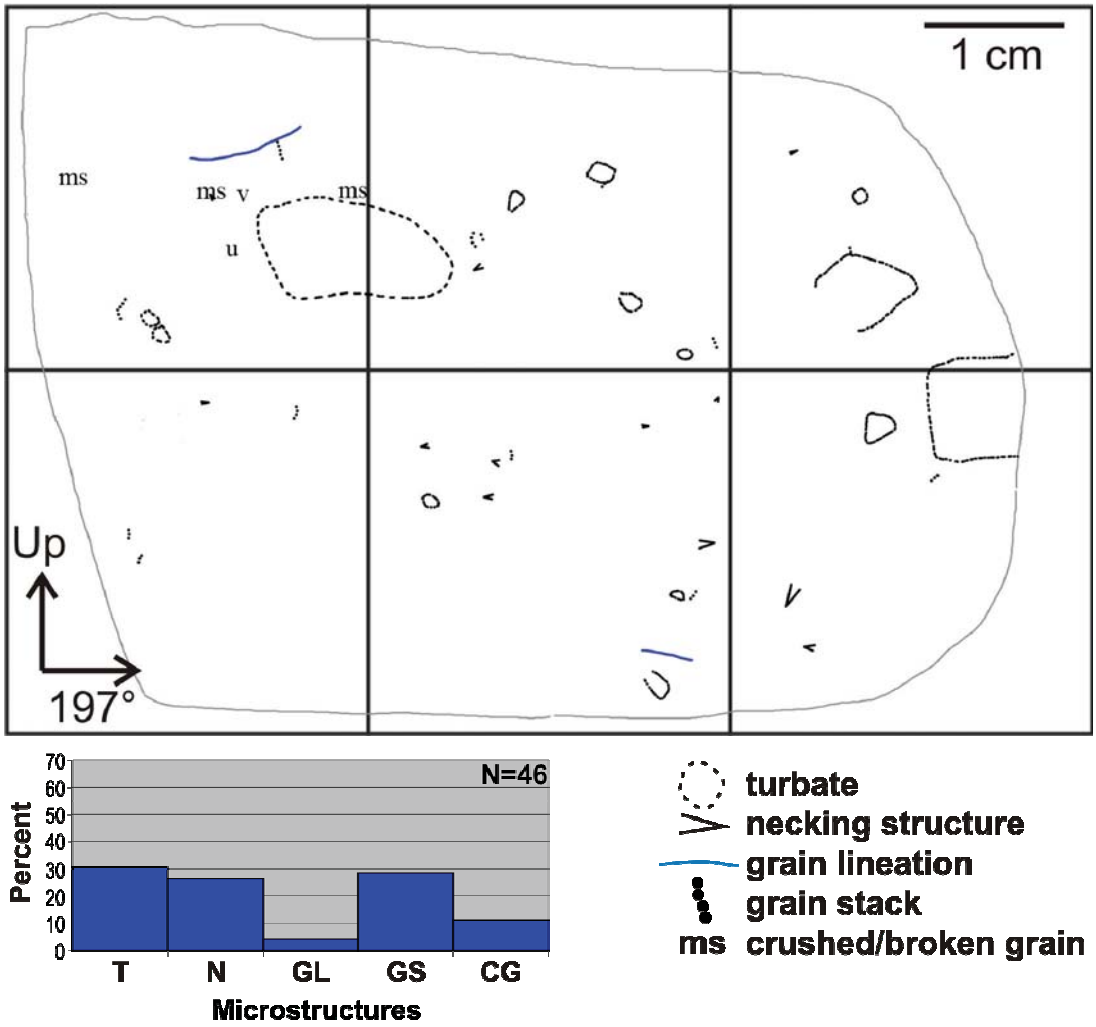

Figure 3.3-5. A 'discrete microstructure map' including a legend for symbols, and associated frequency histogram. Each vertical thin section is divided into six 2.5 cm x 2.5 cm cells to facilitate counting. On the microstructure map, the orientation of the plane of the vertical thin section is indicated with black arrows. Crushed grains are labelled as ms for metasedimentary, cr for crystalline, ls for limestone, v for volcanic, and u for unknown. On the frequency histogram, T=turbates, N=necking structures, GL=grain lineations, GS=grain stacks, and CG=crushed or broken grains.

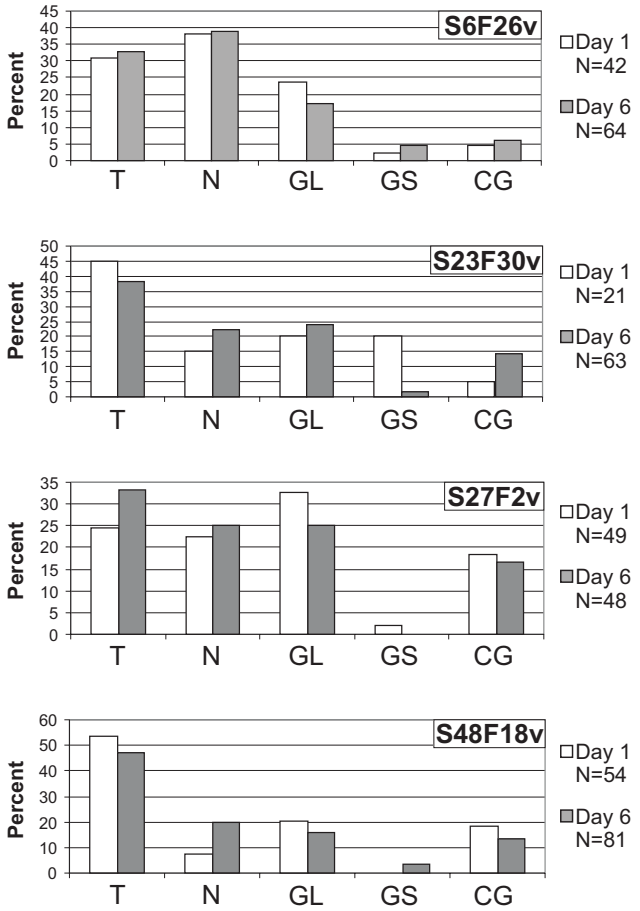

Figure 3.3-6. Microstructure identification subjectivity tests for thin sections S6F26v, S23F30v, S27F2v, and S48F18v. Each thin section was counted twice, with five days between each counting session. T=turbates, N=necking structures, GL=grain lineations, GS=grain stacks, CG=crushed/broken grains.

Chapter 4: Macroscale and microscale observations

4.1 Introduction

In this chapter, the macroscale sedimentology and micromorphology of relevant diamictons at each study site are described and interpreted in detail. Sites in the Jesmond valley will be discussed first (starting from the northern-most site, site 23). These will be followed by site 27 on the south side of Cutoff Valley, sites 25 and 26 on Pavilion plateau, site 57 on the Fraser Plateau, east of the Marble Range, and lastly, site 22 in Fraser Valley.

In Sections 4.2-4.11, macroscale sedimentological observations are used to verify and (or) refine existing interpretations of diamicton genesis. Interpretations regarding microscale depositional and deformational processes are made from diamicton microstructures and microfabrics within the context of macroscale inferences. In Section 4.12, relationships between diamicton microscale structures and fabrics and macroscale structures and (clast) fabrics are explored, and the implications (and possible limitations) of the results of this chapter are discussed.

4.2 Site 23

4.2.1 Macroscale sedimentology and structural geology

Site 23 is located within gently undulating terrain along a road cut at the northern end of Jesmond valley (Fig. 3.1-1). Two exposures, ~45 m apart on the north side of a logging road (F30 and F31, Fig. 4.2-1), were cleaned, sampled and photographed. Both exposures contain overconsolidated, macroscopically massive, matrix-supported, sandy silt diamicton (Fig. 4.2-2) (unit 1) overlain by less consolidated diamicton of a similar texture (unit 2) (Figs 4.2-3, 4.2-4). The contact between units 1 and 2 is marked by a sharp but subtle change in colour and texture. Clast concentration in unit 1 is between 18% (F30) and 9% (F31) (Table 4.2-1). Subhorizontal fissility planes (6° dip down to the SE) lined with calcium carbonate are visible at F31 near the upper contact of the diamicton (Fig. 4.2-4). Due to the lack of carbonates, these fissility planes, if present, were not visible ~50 cm below the upper contact where the micromorphology sample was extracted.

One fabric was measured from each exposure ~0.65 m below the surface and in unit 1 (F30 and F31). F30 is spread bimodal, with a primary mode oriented SW and a secondary (n=8) statistically significant transverse mode (Fig. 4.2-3, Table 4.2-2). The

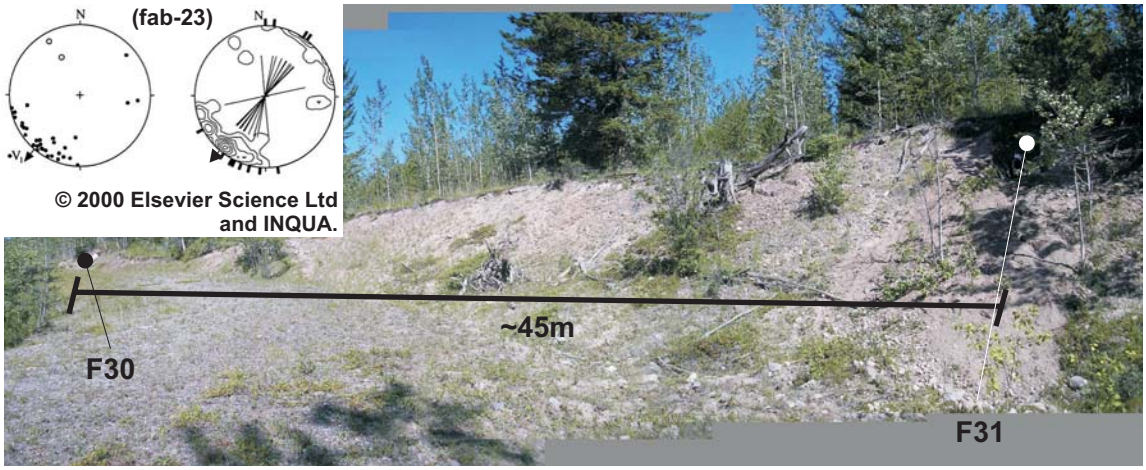

Figure 4.2-1. Site 23, F30 and F31. The stereogram for fabric 23 (fab-23) is adapted from Lian and Hicock (2000) with permission; the exact location of this fabric is unknown. See Figure 3.3-1 for stereogram legend.

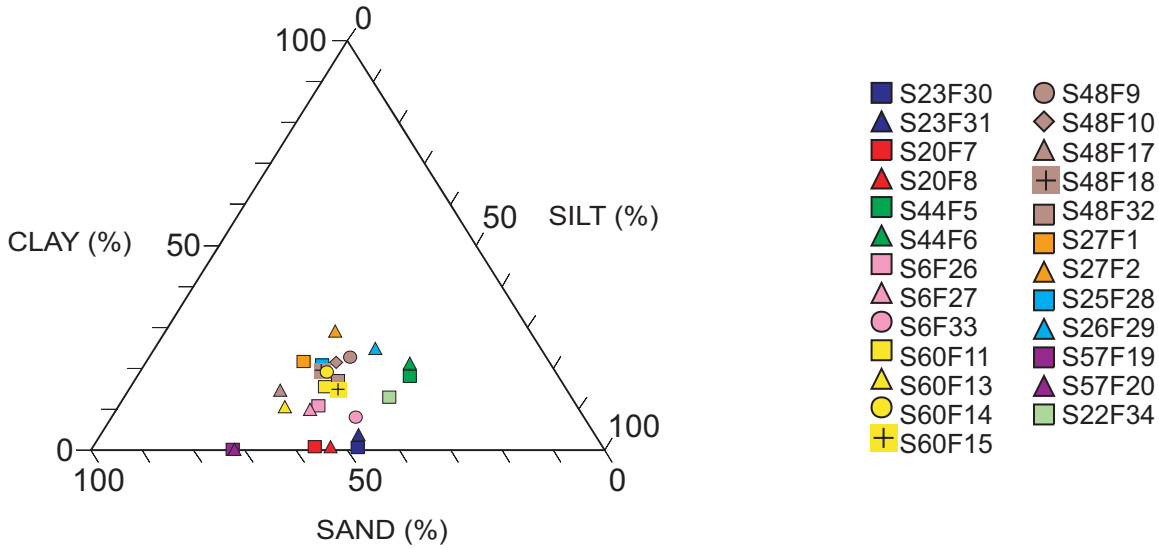

Figure 4.2-2. Textural composition of the matrix of glacigenic diamictons. Particle size analysis was conducted on samples collected from all clast fabric measurement sites using laser diffraction at the University of Calgary (Mullins and Hutchison 1982; Anonymous 1998). See Table E-1, Appendix E for the raw data.

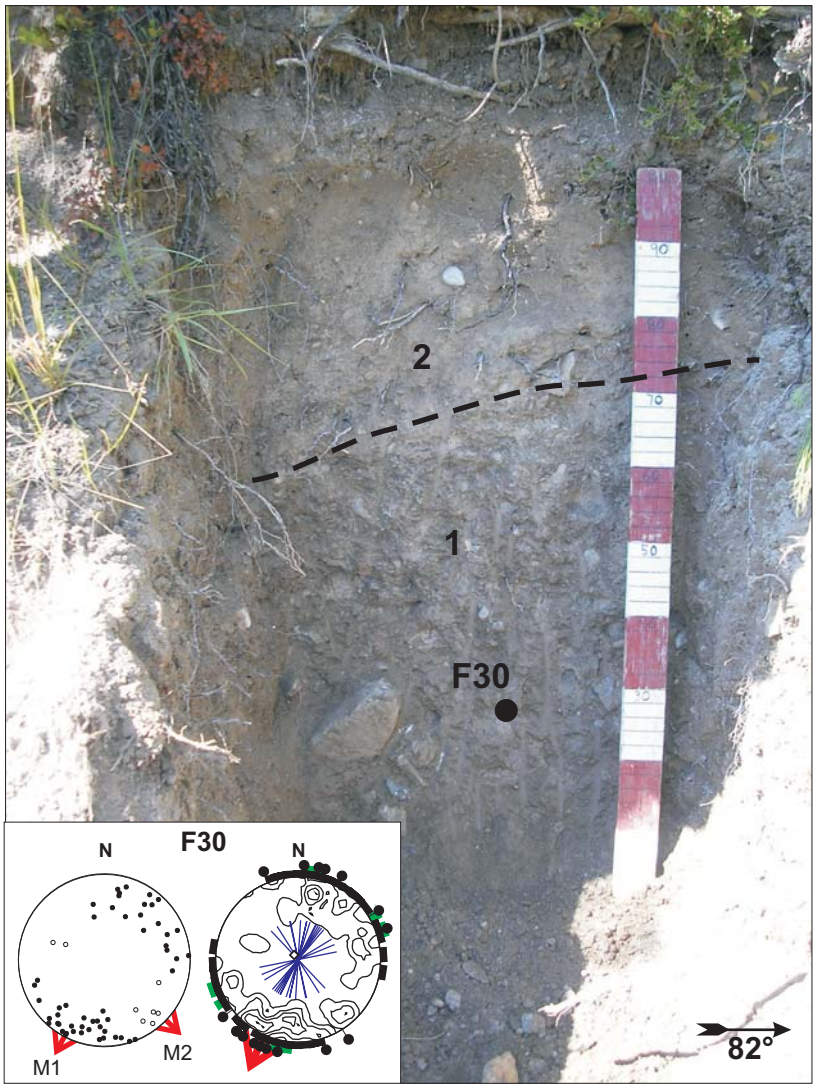

Figure 4.2-3. Units 1 and 2 and F30, site 23. See Figure 3.3-1 for stereogram legend. Metre stick with decimetre subdivisions for scale.

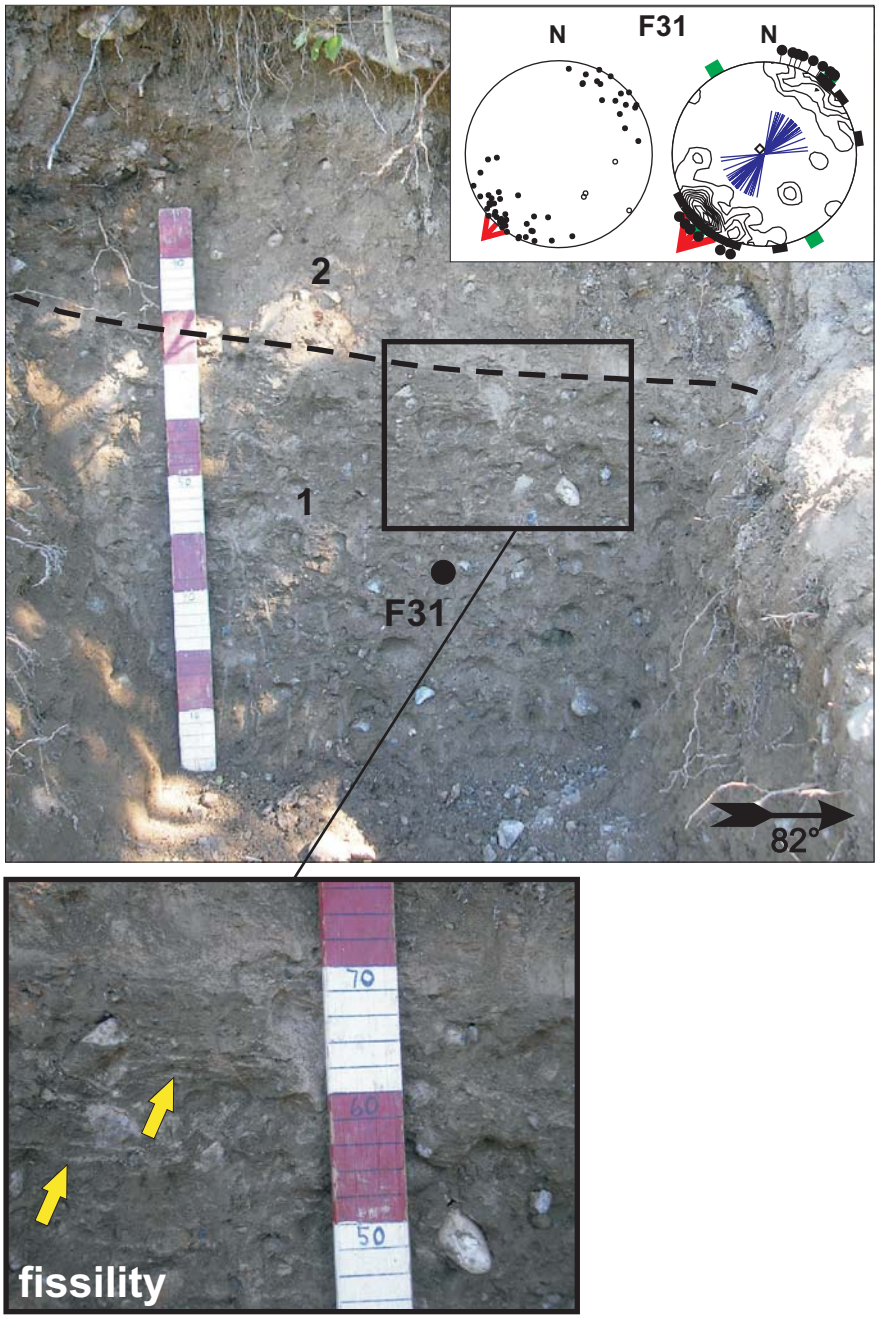

Figure 4.2-4. F31 and carbonate coated fissility planes in the diamicton at site 23. See Figure 3.3-1 for stereogram legend. Metre stick with decimetre subdivisions for scale.

Table 4.2-1. Macrofabric eigenstatistics, randomness test results and modalities, and diamicton clast concentration and macroscale structures. Sites are sorted according to the inferred genesis (G) of the unit in question.

Site/Fabric	Unit	G[1]	G[2]	N[3]	V_1[4] trend(°)/plunge(°)	S_1[4]	S_3[4]	Random?[5] N=No Y=Yes	Modality[6]	Clast Concen. (%)	Macro-scale structures in exposure[7]
S44/F36	3	M	L/M	20	161.3/10.6	0.754	0.024	N	N/A	N/A	Cobble-boulder pavement
S23/F30	1	L	L/DL	61	203.9/3.6	0.608	0.130	N	SB	18	None
S23/F31	1	L	L/DL	59	221.7/4.7	0.782	0.078	N	SU+4O	9	Fi
S20/F7	1	L	L/DL	60	320.7/8.8	0.797	0.058	N	U	8	Fi
S20/F8	1	L	L/DL	60	323.3/11.9	0.796	0.077	N	U	7	Fi
S27/F1	2	L	L/DL	60	218.1/5.7	0.724	0.070	N	SB	9	B
S27/F2	2	L	L/DL	60	199.2/6.1	0.733	0.056	N	SU	13	B
S57/F19	1	DL	DL	60	169.9/0.8	0.641	0.132	N	SB	10	Fr
S57/F20	1	DL	DL	53	185.2/10.5	0.716	0.070	N	SU+2O	6	Fr
S25/F28	2	DL	DL	60	271.6/24.4	0.475	0.151	N	SU	3	Fr
S26/F29	2	DL	DL	60	270.2/15.4	0.626	0.170	N	SB	5	Fr+Sh
S6/F26	1	DL	DL	60	245.5/6.7	0.828	0.047	N	U+3O	7	Sh+Fo
S6/F27	1	DL	DL	60	246.3/8.6	0.670	0.155	N	SB	6	Sh+Fo
S6/F33	1	DL	DL	60	59.6/3.8	0.660	0.159	N	SB	3	None
S48/F9	1	DL	DL	60	100.5/14.3	0.521	0.181	N	SB	8	Fr+Sh
S48/F10	1	DL	DL	60	73.4/28.5	0.431	0.164	N	G	19	Fr+Sh
S48/F17	1	DL	DL	60	234.4/5.3	0.696	0.114	N	B	25	Fr+Sh
S48/F18	1	DL	DL	60	205.2/2.5	0.505	0.160	N	M-G	18	Fr+Sh
S48/F32	1	DL	DL	60	213.9/2.3	0.598	0.147	N	SU	21	Fr+Sh
S60/F11	4	D	D	67	62.8/9.6	0.501	0.186	N	SB	24	Fr+Sh+S
S60/F12	4	D	D	60	162.2/7.2	0.475	0.112	N	SB-G	14	Fr+Sh+S
S60/F13	4	D	D	60	211.9/4.2	0.545	0.125	N	SU	25	Fr+Sh+S
S60/F14	4	D	D	60	209.4/10.0	0.591	0.128	N	SB	17	Fr+Sh+S
S60/F15	4	D	D	60	22.0/1.1	0.418	0.188	N	G	26	Fr+Sh+S
S60/F25	3	D	G	36	321.2/25.1	0.533	0.121	N	M-G	10	Fr+Sh+S
S44/F5	2	G	G	60	323.7/4.5	0.535	0.117	N	G	8	Pavement
S44/F6	2	G	G	60	355.6/1.4	0.542	0.075	N	G	6	Pavement
S22/F34	II	G	G	59	285.0/22.9	0.540	0.182	N	SU+5O	15	Fr
S22/F35	II	G	G	60	38.2/17.9	0.555	0.121	N	G	11	Fr

[1]Genesis of site units according to Lian (1997) and Lian and Hicock (2000): L=mainly lodgement, DL=deformed lodgement, D=deformation, G=gravity flow, and M=melt-out. Unit number scheme follows that of this study.

[2] Genesis of site units according to Neudorf (this study): L/DL=lodgement or deformed lodgement, DL= deformed lodgement, D=deformation, G=gravity flow and L/M=lodgement or melt-out. Unit number scheme follows that of this study.

[3]N is the total number of clasts measured at a fabric site.

[4]V_1 is the principal eigenvector, S_1 is the principal eigenvalue, and S_3 is the tertiary eigenvalue.

[5]Statistical test for randomness using the protocol of Woodcock & Naylor (1983).

[6]U=unimodal, B=bimodal, SU=spread unimodal, SB=spread bimodal, M=multimodal, G=girdled, O=outliers, N/A=not enough clasts measured to determine modality.

[7]Fi=fissility, Fo=fold, Fr=fractures, Sh=shears, B=banding and S=sediment clasts.

Table 4.2-2. Mode statistics for bimodal/multimodal macrofabrics and macrofabrics with outliers. Sites are ordered according to the inferred diamicton genesis (G).

Site/Fabric	Genesis[1]	N[2]	V_1[3] trend(°)/plunge(°)	S_1[3]	S_3[3]	Random?[4]
S23/F30	L/DL					
Mode 1		53	207.8/1.9	0.682	0.012	N
Mode 2		8	134.3/11.7	0.754	0.030	N
S23/F31	L/DL					
Mode 1		55	221.8/4.6	0.834	0.063	N
Outliers		4	130.0/37.2	0.839	0.061	N/A
S27/F1	L/DL					
Mode 1		52	219.7/5.7	0.810	0.075	N
Mode 2		8	320.2/9.6	0.828	0.026	N
S26/F29	L/DL					
Mode 1		51	273.4/15.6	0.716	0.095	N
Mode 2		9	197.3/9.9	0.682	0.059	N
S6/F26	DL					
Mode 1		57	245.7/6.8	0.868	0.048	N
Outliers		3	341.2/5.7	0.899	0.025	N/A
S6/F27	DL					
Mode 1		53	244.8/8.3	0.751	0.106	N
Mode 2		7	142.7/17.1	0.671	0.025	N
S6/F33	DL					
Mode 1		52	57.8/3.4	0.751	0.106	N
Mode 2		8	317.0/3.5	0.653	0.039	N
S48/F9	DL					
Mode 1		38	113.7/15.0	0.732	0.105	N
Mode 2		22	37.4/0.6	0.685	0.093	N
S48/F17	DL					
Mode 1		50	234.8/5.7	0.809	0.063	N
Mode 2		10	328.0/6.1	0.766	0.091	N
S57/F19	DL					
Mode 1		53	172.5/1.4	0.712	0.099	N
Mode 2		7	279.8/6.9	0.686	0.039	N
S57/F20	DL					
Mode 1		51	147.3/10.4	0.742	0.062	N
Outliers		2	79.0/16	0.719	0	N/A
S60/F11	D					
Mode 1		58	59.3/7.7	0.566	0.118	N
Mode 2		9	142.5/31.7	0.845	0.041	N
S60/F12	D					
Mode 1		34	194.8/22.5	0.695	0.087	N
Mode 2		26	300.6/19.6	0.780	0.077	N
S60/F14	D					
Mode 1		47	244.6/8.6	0.739	0.090	N
Mode 2		13	330.7/4.0	0.739	0.038	N
S22/F34	G					
Mode 1		50	285.6/22.5	0.582	0.121	N
Outliers		5	160.4/3.5	0.853	0.042	Y

[1]Genesis according to Neudorf (this study), where L=mainly lodgement, DL=deformed lodgement, D=deformation, and G=gravity flow.
[2]N is the number of clasts in a mode, or the number of outliers.
[3]V_1 is the principal eigenvector, S_1 is the principal eigenvalue, and S_3 is the tertiary eigenvalue.
[4]Woodcock and Naylor (1983) test for randomness. Y=random, N=not random, and N/A=not testable because number of measurements (N) is less than 5.

vast majority of striae identified on clast tops in both modes are parallel to the clast a-axis, and only one clast (in the primary mode) had upper surface striae with multiple orientations (Table 4.2-3). Keels on clast bottoms are oriented similar to the primary mode. Out of all clasts in the sample, 30% are faceted on the top, side and (or) bottom, and 7% have keels on the top, side and (or) bottom (Table 4.2-3).

F31 is spread unimodal, with a principal eigenvector oriented SW (Fig. 4.2-4, Table 4.2-1). Most clast upper surface striae are oriented parallel to clast a-axes (Table 4.2-3). Most fractured ends point to the SW, and bullet noses show no preferred direction. Out of all clasts in the sample, 54% are faceted, and two clasts have keels (Table 4.2-3). Lian's (1997) fabric 23 (fab-23, Fig. 4.2-1) is unimodal with two outliers. The principal eigenvector of fabric 23 points to the SW.

Both bladed and elongate particle shapes of various levels of compactness (Sneed and Folk 1958) characterize the modes of F30 and F31 (Fig. B-1, Appendix B). Seven out of eight clasts comprising the transverse mode of F30, however, are blades, most of which have striae parallel to clast a-axes.

4.2.2 Micromorphology

One sample was extracted from each of the fabric locations at site 23 for thin section preparation. In total, two horizontal (S23F30h and S23F31h) and two vertical (S23F30v and S23F31v) thin sections were cut from these samples. The vertical thin sections from site 23 (S23F30v, S23F31v) show that the diamicton is plasma supported at the microscale (Kilfeather and van der Meer 2008), and contains mostly limestone skeletal grains, and a smaller proportion of volcanic and metasedimentary/metamorphic grains including argillite (Figs 4.2-5, 4.2-6). Limestone grains are subangular to subrounded, volcanic grains are subrounded to rounded, and metamorphic/metasedimentary grains subangular to subrounded. At one location in S23F30v a broken grain was observed (Fig. 4.2-5E). Rounded and subrounded sand sized grains of all the above lithologies are common (Figs 4.2-5D, 4.2-5E).

The fissility planes observed in the exposure at the macroscale are expressed as subparallel planar voids in both thin sections (Figs 4.2-5, 4.2-6). In thin section S23F30v, these voids have an apparent dip ~15° down to 167° azimuth, and in S23F31v they have an apparent dip of ~50° down to 184° azimuth. In thin section S23F30v, the apparent long axes of skeletal grains whose maximum dimension approaches the distance between the planar voids are oriented in a similar direction to them while

Table 4.2-3. Clast wear features for all diamicton types. Sites are ordered according to the inferred genesis (G) of the unit in question.

Site/Fabric	Unit	G[1]	N[2]	Clasts with striae[3] (%)	Clasts with striae on top[3] (%)	Clasts with striae on top parallel to a-axis[4](%)	Clasts with striae sets on top with multiple orientations[4] (%)	Clasts with striae following convexities/ concavities[3] (%)	Faceted clasts[3] (%)	Clasts with keels[3] (%)	Bullet noses show preferred direction? Y=yes N=no N/A=none observed	Fractured ends show preferred direction? Y=yes N=no	Clast shape related to clast orientation? Y=yes N=no N/A=not recorded
S44/F36	3	L/M	20	80	75	80	0.0	0.0	50	5	N	N	N/A
S23/F30	1	L/DL	61	38	26	75	1.6	0.0	30	7	N	N	Y
S23/F31	1	L/DL	59	76	61	97	0.0	0.0	54	3	N	N	N
S20/F7	1	L/DL	60	62	43	96	3.3	1.7	37	12	N	N	Y
S20/F8	1	L/DL	60	65	50	83	6.7	0.0	45	13	Y	N	N
S27/F1	2	L/DL	60	68	50	77	8.3	0.0	32	7	N	N	N
S27/F2	2	L/DL	60	55	45	93	5.0	0.0	48	2	N	N	N
S57/F19	1	DL	60	38	23	93	1.7	0.0	42	8	N	N	N
S57/F20	1	DL	53	19	9	100	0.0	0.0	6	0	N	N	N
S25/F28	2	DL	60	40	23	79	0.0	1.7	38	3	N	N	N
S26/F29	2	DL	60	10	7	100	0.0	0.0	7	0	N/A	N	N
S6/F26	1	DL	60	58	47	89	1.7	1.7	45	7	N	N	Y
S6/F27	1	DL	60	50	33	95	0.0	0.0	32	0	Y	N	N
S6/F33	1	DL	60	52	35	95	0.0	0.0	32	7	N	N	N
S48/F9	1	DL	60	55	35	91	1.7	0.0	15	7	N	N	N
S48/F10	1	DL	60	45	28	94	3.3	1.7	18	5	N	N	N
S48/F17	1	DL	60	65	40	88	10.0	6.7	18	0	N	N	N
S48/F18	1	DL	60	53	40	96	5.0	0.0	43	7	N	N	N
S48/F32	1	DL	60	75	57	85	1.7	0.0	55	7	N	N	N
S60/F11	4	D	67	37	21	86	3.0	0.0	12	0	N	N	N
S60/F12	4	D	60	58	33	80	10.0	0.0	23	7	Y	N	N
S60/F13	4	D	60	67	48	100	5.0	5.0	35	10	N	N	N
S60/F14	4	D	60	58	45	78	5.0	0.0	38	7	N	N	N
S60/F15	4	D	60	60	32	100	5.0	6.7	27	2	N	N	N
S60/F25	3	G	36	22	14	80	0.0	0.0	42	3	Y	N	N
S44/F5	2	G	60	23	13	100	3.3	0.0	10	0	N	N	N
S44/F6	2	G	60	7	7	75	0.0	0.0	7	2	N	N	N
S22/F34	II	G	59	12	5	100	0.0	0.0	3	0	N	N	N
S22/F35	II	G	60	35	22	100	0.0	0.0	27	7	N	N	N

[1]Genesis of unit according to Neudorf (this study), where L/M= lodgement or melt-out, L/DL=lodgement or deformed lodgement, DL=deformed lodgement, D=deformation, and G=gravity flow.
[2]Number of clasts measured at a fabric sampling site.
[3]Reported as a percentage of N.
[4]Reported as a percentage of all clasts with striae on top.

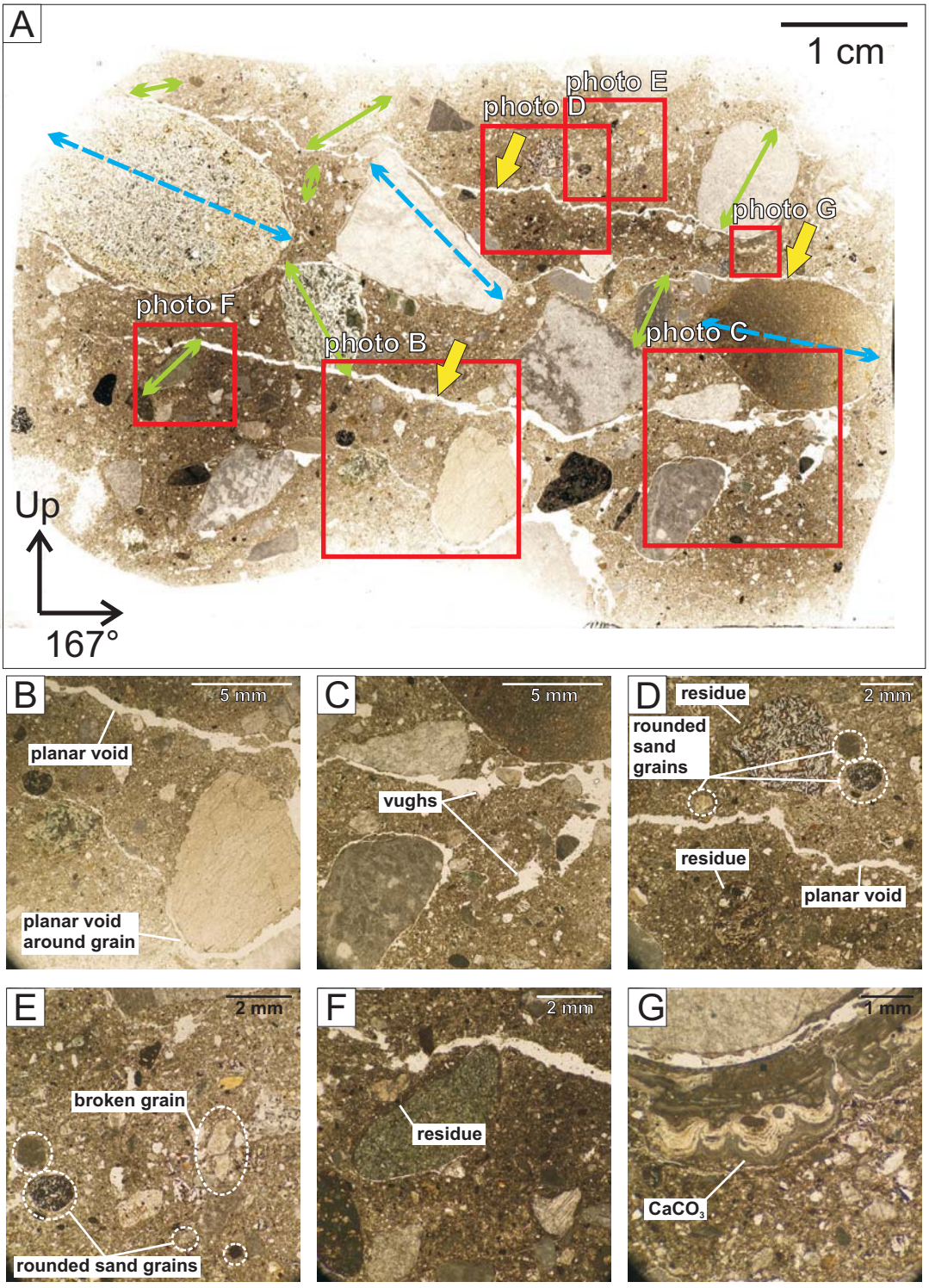

Figure 4.2-5. Thin section S23F30v. A) A 2400 dpi scan of the thin section showing planar voids (yellow arrows). Large grains (blue arrows) are oriented sub-parallel to planar voids and smaller grains (green arrows) are oriented oblique to planar voids. The locations of microphotographs B, C, D, E, F and G are indicated by red squares. Microphotographs show planar voids (B), vughs (C), rounded sand sized grains (D, E), a broken grain (E), calcium carbonate precipitate (G) and a reddish-brown residue encircling grains (F).

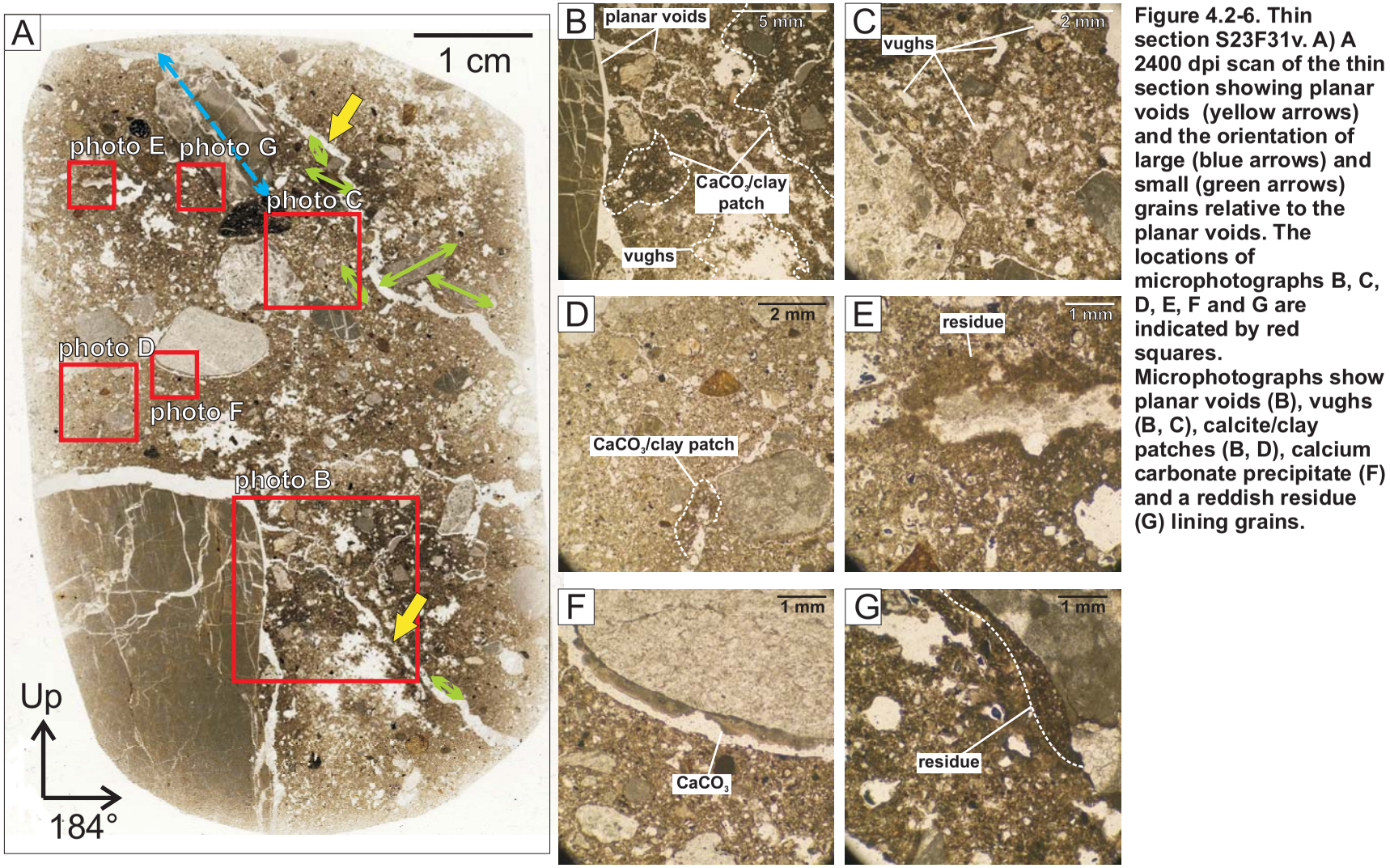

Figure 4.2-6. Thin section S23F31v. A) A 2400 dpi scan of the thin section showing planar voids (yellow arrows) and the orientation of large (blue arrows) and small (green arrows) grains relative to the planar voids. The locations of microphotographs B, C, D, E, F and G are indicated by red squares. Microphotographs show planar voids (B), vughs (B, C), calcite/clay patches (B, D), calcium carbonate precipitate (F) and a reddish residue (G) lining grains.

smaller grains are often oriented oblique to them (Fig. 4.2-5A). Many large grains and small grains that are adjacent to planar voids in thin section S23F31v are oriented subparallel to them (Fig. 4.2-6A). The apparent distance between planar voids in thin section S23F31v is ~1.5x the apparent distance between planar voids in thin section S23F30v (Figs 4.2-5A, 4.2-6A). Voids surround the edges of grains, and vughs (pores with irregular edges, Kilfeather and van der Meer 2008) of various sizes are common (Figs 4.2-5B, 4.2-5C), the largest and most frequent occurring in thin section S23F31v (Figs 4.2-6B, 4.2-6C). Both thin sections consist of what appears to be calcite precipitate and a dark red-brown residue (clay or iron/manganese oxide?). The red-brown residue appears on grains (Figs 4.2-5F, 4.2-5G, 4.2-6F, 4.2-6G), along the walls of voids (Figs 4.2-6D, 4.2-6E), and within the matrix forming dark grey or brown coloured patches (Figs 4.2-6B, 4.2-6D). Calcite precipitate found on limestone grains in both thin sections is thickest along the underside of these grains (Figs 4.2-5G, 4.2-6G), while the residue lines the upper side or entire perimeter of some grains (Figs 4.2-5D, 4.2-5F, 4.2-6G). The walls of the fissility planes in both thin sections, however, are quite clean (Figs 4.2-5B, 4.2-5D, 4.2-6B).

Discrete microstructures including turbates, necking structures, grain lineations, grain stacks, and crushed/broken grains were mapped throughout each thin section and the results displayed in Figures 4.2-7 and 4.2-8. Both thin sections S23F30v and S23F31v have relatively few visible structures in total (21 and 16 respectively) and are dominated by turbates which constitute about half of the structures counted. Only one broken grain (limestone) was identified with confidence in thin section S23F30v (Fig. 4.2-5E).

Both vertical microfabrics S23F30v-1 and S23F31v-1 have subhorizontal principal eigenvectors and spread out clusters with grains plunging from 0° to 70-80° (Figs 4.2-7, 4.2-8). The plunge direction of most sand grains in microfabric S23F30v-1 is opposite to the apparent dip of the fissility planes in thin section S23F30v, however a small peak plunging 10-20° down to 167° azimuth is parallel to the fissility planes. The plunge direction of most sand grains in microfabric S23F31v-1 follows the plunge direction of the fissility planes in thin section S23F31v and a cluster with a 20-60° plunge down to 184° azimuth approximates the apparent dip angle of the fissility planes (Fig. 4.2-8).

The tightest clusters in the microfabrics measured from horizontal thin sections, S23F30h and S23F31h, generally follow the main modes and principal eigenvectors of

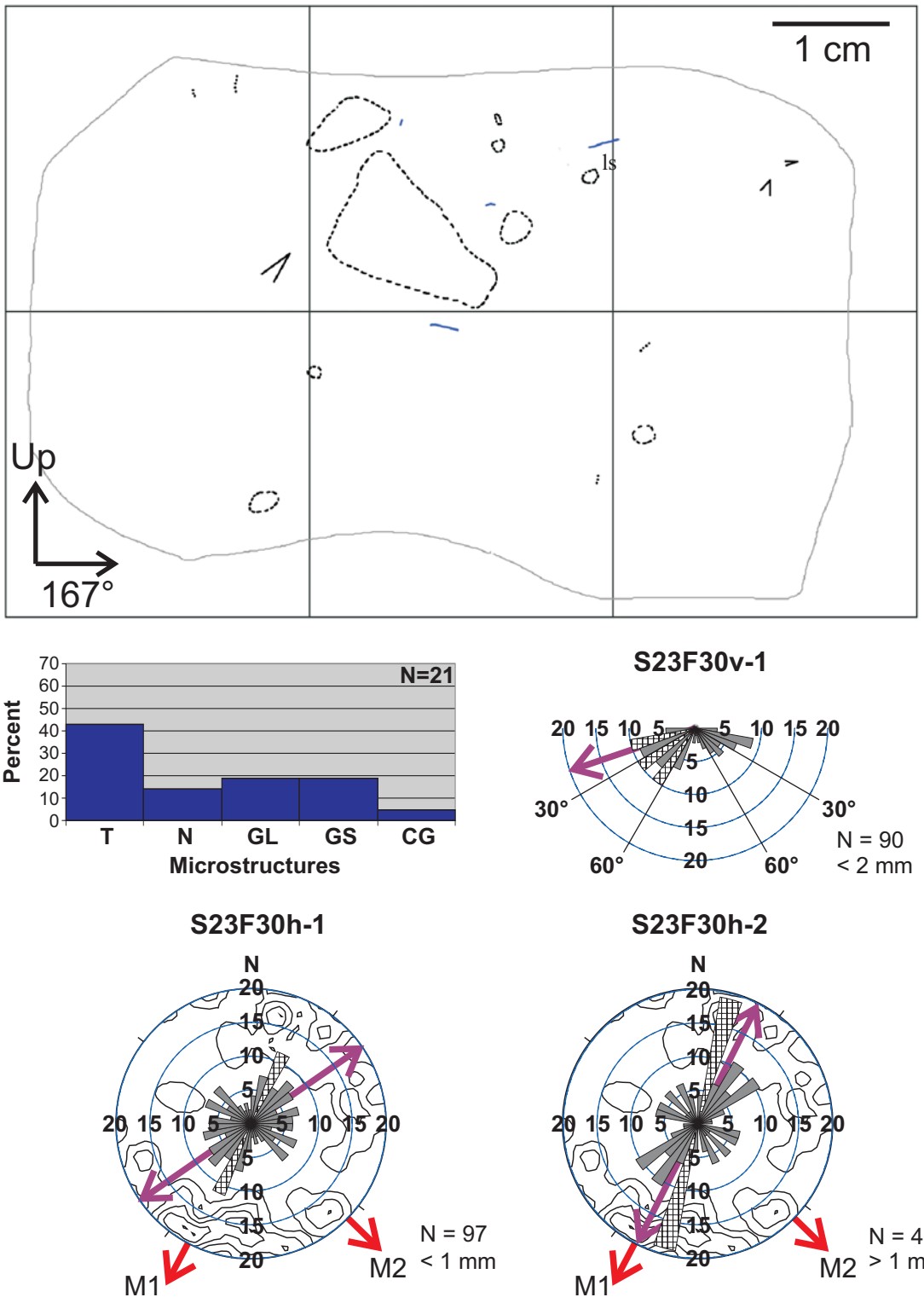

Figure 4.2-7. Microfabrics S23F30v-1, S23F30h-1 and S23F30h-2, and microstructure map and frequency histogram for thin section S23F30v. See Figures 3.3-4 and 3.3-5 for legends.

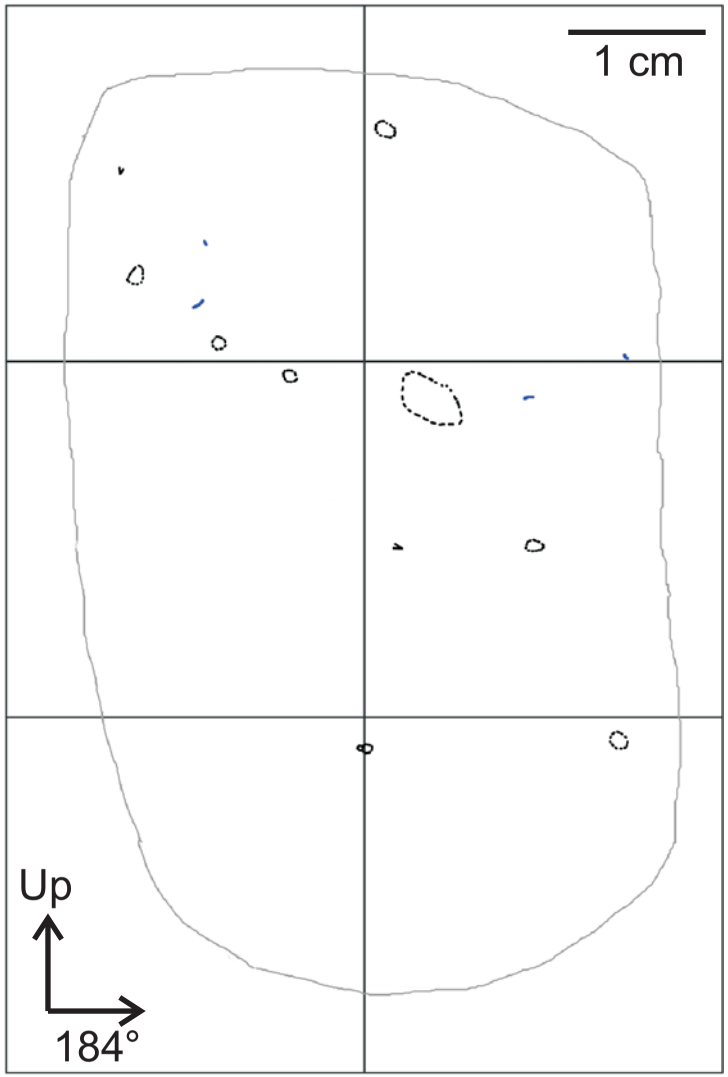

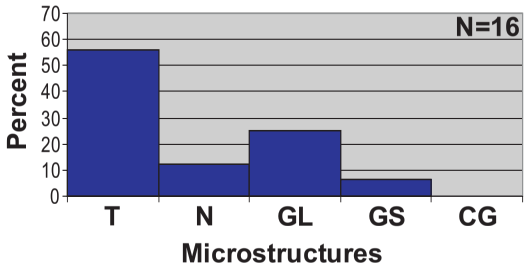

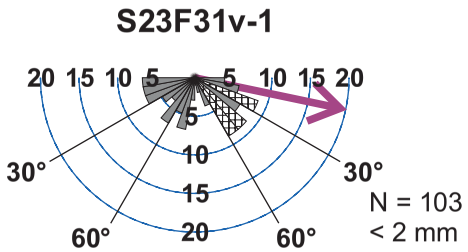

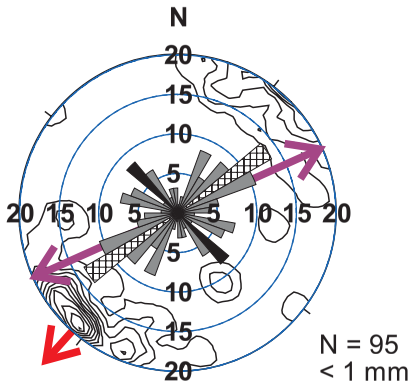

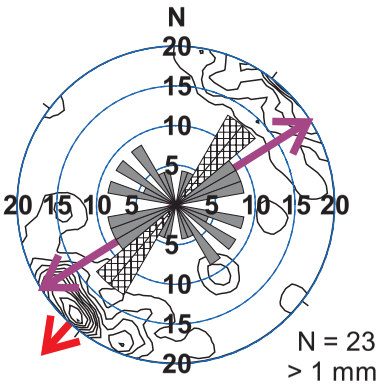

Figure 4.2-8. Microfabrics S23F31v-1, S23F31h-1 and S23F31h-2, and microstructure map and frequency histogram for thin section S23F31v. See Figures 3.3-4 and 3.3-5 for legends.

macrofabrics F30 and F31, respectively (Figs 4.2-7, 4.2-8). Sand grain orientations outside these clusters are quite spread out, but a paucity of observations occurs in the NNW-SSE direction in microfabrics S23F30h-1, S23F31h-1 and S23F31h-2.

4.2.3 Interpretation

Unit 1, site 23 is overconsolidated, has high silt content, and contains subhorizontal fissility planes, clasts with abundant glacigenic wear features, and spread bimodal and spread unimodal clast fabrics with consistently oriented principal eigenvectors. These characteristics suggest that unit 1 is a subglacial till, as suggested by Lian (1997) and Lian and Hicock (2000). The presence of facets, bullet noses and keels suggest that clasts in the diamicton were initially deposited by lodgement. The spread nature of the modes in the clast fabrics may be attributed to re-orientation of subglacial till clasts that come into contact with ploughing clasts at the ice-bed interface, or to post-depositional deformation.

Unit 1, site 23 was previously classified as lodgement till (Lian 1997; Lian and Hicock 2000). This interpretation is supported here by the consistent orientation of clast fabric primary modes and principal eigenvectors. In contrast to the data reported by Lian (1997) and Lian and Hicock (2000) (Fig. 4.2-1), however, fractured ends and bullet noses recorded in this study show no preferred direction. Either fractured end and bullet nose directions record clast re-orientation after ploughing and (or) lodgement, or some or all of them have been inherited from an earlier time in the transport history of the pebbles. Clast wear features recording ice flow direction during lodgement have been observed to be better preserved on relatively large cobbles and boulders than on smaller clasts in front of contemporary glaciers (Benn 1994; 1995). Thus, it is suspected that more definitive evidence for preserved lodgement till might have been obtained if clast wear features recorded in this study were not restricted to pebble-sized clasts.

Clast upper surface striae in unit 1 are commonly parallel to the long axes of pebbles suggesting that slip between the pebble surface and the till matrix or overriding debris rich ice occurred while the long axes of pebbles were oriented in the direction of shear. This interpretation is consistent with blade-shaped clasts dominating the transverse mode in F30, because when there is slip between particle surfaces and the surrounding matrix, blades should be slower to reach a shear parallel orientation than their more prolate counterparts (Glen *et al.* 1957; Drake 1974). Blade-shaped clasts in the transverse mode that were striated, however, had striae parallel to clast long axes,

rather than perpendicular or oblique to them, suggesting that striae formation occurred when these clast long axes were oriented parallel to the shear direction before they were re-oriented.

If pebbles were deposited during lodgement processes along a horizontal paleo-surface, then the plunge of the main mode of the fabrics suggest ice flow from the SW, and may reflect till deposition during an early phase of glaciation by ice filling the Jesmond valley from nearby NE trending tributary valleys emanating from the Edge Hills (Fig. 3.1-1). Because the till is located near the ground surface, however, this explanation would require that all sediments related to deposition during and after the last glacial maximum have since been eroded. Thus, the SW-NE trending primary mode and principal eigenvector of F30 and F31, respectively should alternatively be explained by ice that was locally flowing NE across site 23 during the last glacial maximum. The southward, (though shallow) dipping fissility planes also suggest ice flow to the N. This interpretation is consistent with northernly flowing ice along Jesmond valley during the last glacial maximum (Lian and Hicock 2000).

Fissility planes in till have been previously interpreted to be the result of shear (van der Meer *et al.* 2003; Larsen 2006) and elongate particles in the vicinity of shear planes are expected to rotate until their long axes become aligned parallel to the direction of shear (Hiemstra and Rijsdijk 2003; Thomason and Iverson 2006). In thin section S23F30v, skeletal grains whose maximum dimension approaches the distance between the subparallel planar voids are oriented in a similar direction to the planar voids while smaller grains are often oriented oblique to the planar voids (Fig. 4.2-5A). The distance between subparallel planar voids are wider in S23F31v, however many skeletal grains seem to align themselves subparallel to them (Fig. 4.2-6A). These observations would appear to support Larsen's (2006) assertion that closely spaced shear planes may lead to the alignment of larger grains in the direction of shear, while smaller particles are less affected, unless they lie within a shear zone. His concept would also explain why many sand sized particles in microfabric S23F31v-1, and most sand sized particles in microfabric S23F30v-1 do not follow the orientation of the subparallel planar voids (Figs 4.2-7, 4.2-8). Alternatively, the fissility planes may be: 1) fractures that propogated along paths of least resistence to tensile stress during unloading of the sediment after ice retreat, and are only partly influenced by the orientation of grains in the diamicton, or 2) part of a blocky or platy structure that can

develop in silty sediments or soils as a result of ice lens formation and melting during seasonally driven freeze-thaw cycles (van Vliet-Lanoë *et al.* 1984; Sveistrup *et al.* 2005).

Horizontal microfabrics S23F30h-1, S23F30h-2, S23F31h-1, and S23F31h-2 show a striking correlation between the orientation of sand-sized particles (relative to N), and the main mode of the macrofabrics (Figs 4.2-7, 4.2-8). This correlation implies that, like the pebble sized grains, sand sized grains reached a stable position with their long axis oriented in the direction of shear, and may be the result of inter-particle slip leading to March-type rotation of grains in a shearing plastic medium (Iverson *et al.* 2003).

Evidence of porewater and chemical weathering of skeletal grains exists in the form of precipitates and clay coatings. The calcite deposits lining the underside of some grains have likely been deposited by meteoric water percolating down the sediment profile from above. This may also be the source of some clay and iron/manganese oxide deposits (reddish-brown residue). At the macroscale, carbonate precipitate could be seen lining the subhorizontal fissility planes near the upper contact of the till, however, below this zone (which never exceeded 10 cm in thickness) where the micromorphological sample was extracted, the lack of carbonates made the fissility planes macroscopically undetectable. It has been proposed that fissility planes in till do not only accommodate shear strain in a subglacial environment, but also the evacuation of porewater (van der Meer *et al.* 2003). In thin section, clay deposits or precipitates are scarce along the subparallel planar voids, suggesting either that 1) they were not hydraulically active, 2) porewater pressure and temperature conditions were not conducive to the precipitation of solutes or the deposition of clay when they were hydraulically active, or 3) the calcium carbonate deposition near the upper contact was derived from meteoric waters that became depleted of dissolved carbonates by the time it percolated to lower levels in the till.

The relatively low number of identified discrete structures in thin sections S23F30v and S23F31v may be due to masking effects of the carbonates in the matrix, and the relatively high porosity observed in S23F31v. These structures suggest nevertheless that skeletal grains rotated (turbates), small particles were squeezed between large particles (necking structures), particles aligned along discrete shear planes (grain lineations), and inter-particle friction occasionally lead to the stacking of grains (grain stacks) (Figs 4.2-7, 4.2-8). Crushed or split grains are rare, and subrounded and rounded grains are common, even within the coarse sand size fraction (Figs 4.2-5D, 4.2-5E). This would suggest that particle breakage was either rare, or, as

the high silt fraction would suggest, limited to asperities on grain surfaces (particle abrasion) (Hooke and Iverson 1995).

Unit 2, site 23 has a similar texture to unit 1, but is less consolidated and has been penetrated by more roots from above. Unit 2 records pedogenesis of the till in unit 1.

4.3 Site 20

4.3.1 Macroscale sedimentology and structural geology

Site 20 is a small (~1.5 m high) exposure located in the northern part of Jesmond valley (Fig. 3.1-1). It contains fissile, massive, matrix-supported silty sand diamicton (Fig. 4.2-2). The clast concentration within the diamicton is 7-8% (Table 4.2-1). Two fabrics, F7 and F8 were taken on orthogonal exposures approximately 10 m away from each other at ~0.65 m below the ground surface (Figs 4.3-1, 4.3-2). Three fractures lined with calcium carbonate were measured at F7. These fractures have a steep dip down to the S-SW with an average strike roughly parallel to the principal eigenvectors of F7 and F8. The fissility of the matrix at both fabric locations is subhorizontal with a gentle dip down to the NW, and is accentuated by subhorizontal carbonate coated discontinuities at F7 (Fig. 4.3-1).

F7 and F8 are unimodal with S_1 values of 0.797 and 0.796 respectively (Table 4.2-1), and their principal eigenvectors are parallel to the axis of Jesmond valley (Fig. 3.1-1). In general, the orientation of striae on clast tops, and keels on clast bottoms in both fabrics follow a similar trend (Figs 4.3-1, 4.3-2). Out of all clasts measured at the site, only six had clast top striae with multiple orientations, and only one clast had striae curving around a convexity (Table 4.2-3). At F7, 37% of clasts are faceted and 12% of clasts have keels. At F8, 45% of clasts are faceted, and 13% of clasts have keels (Table 4.2-3). Lian's (1997) fabric 20 (fab-20, Fig. 4.3-1) is spread unimodal with two outliers. The principal eigenvector of fabric 20 trends NW-SE.

Both bladed and elongate pebble shapes of various levels of compactness (Sneed and Folk 1958) characterize the modes in F7 and F8, though most of the pebbles within the lowest contour class in F7 are blade shaped (Fig. B-1, Appendix B). These bladed clasts have striae parallel to clast a-axes.

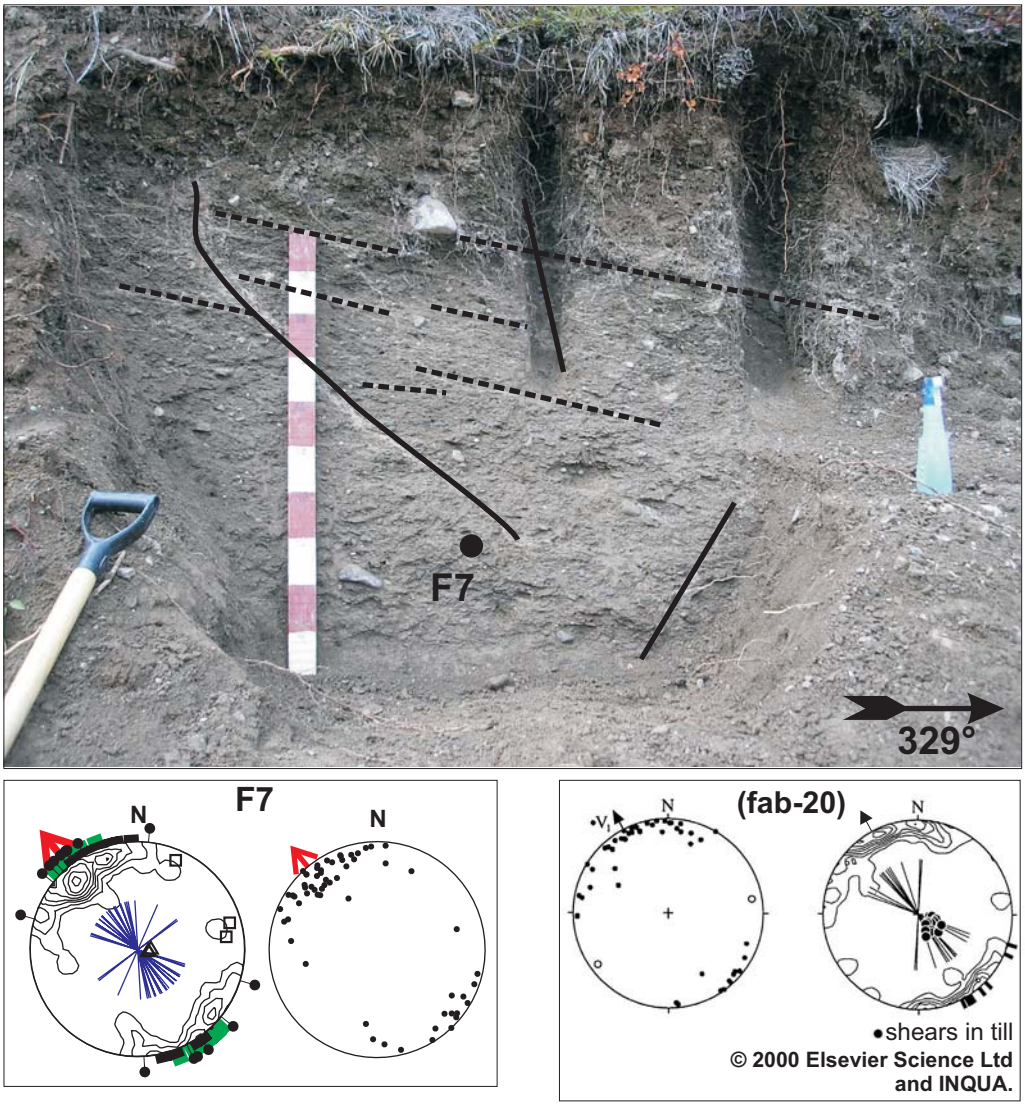

Figure 4.3-1. F7 and fractures (solid lines) and shears (dashed lines) in the diamicton at site 20. The stereogram of fabric 20 (fab-20) reported by Lian and Hicock (2000) is reprinted with permission. Fabric 20 was collected from the same exposure as F7. Clast fabric data collected in this study is shown to the left. See Figure 3.3-1 for stereogram legend. Metre stick with decimetre subdivisions for scale.

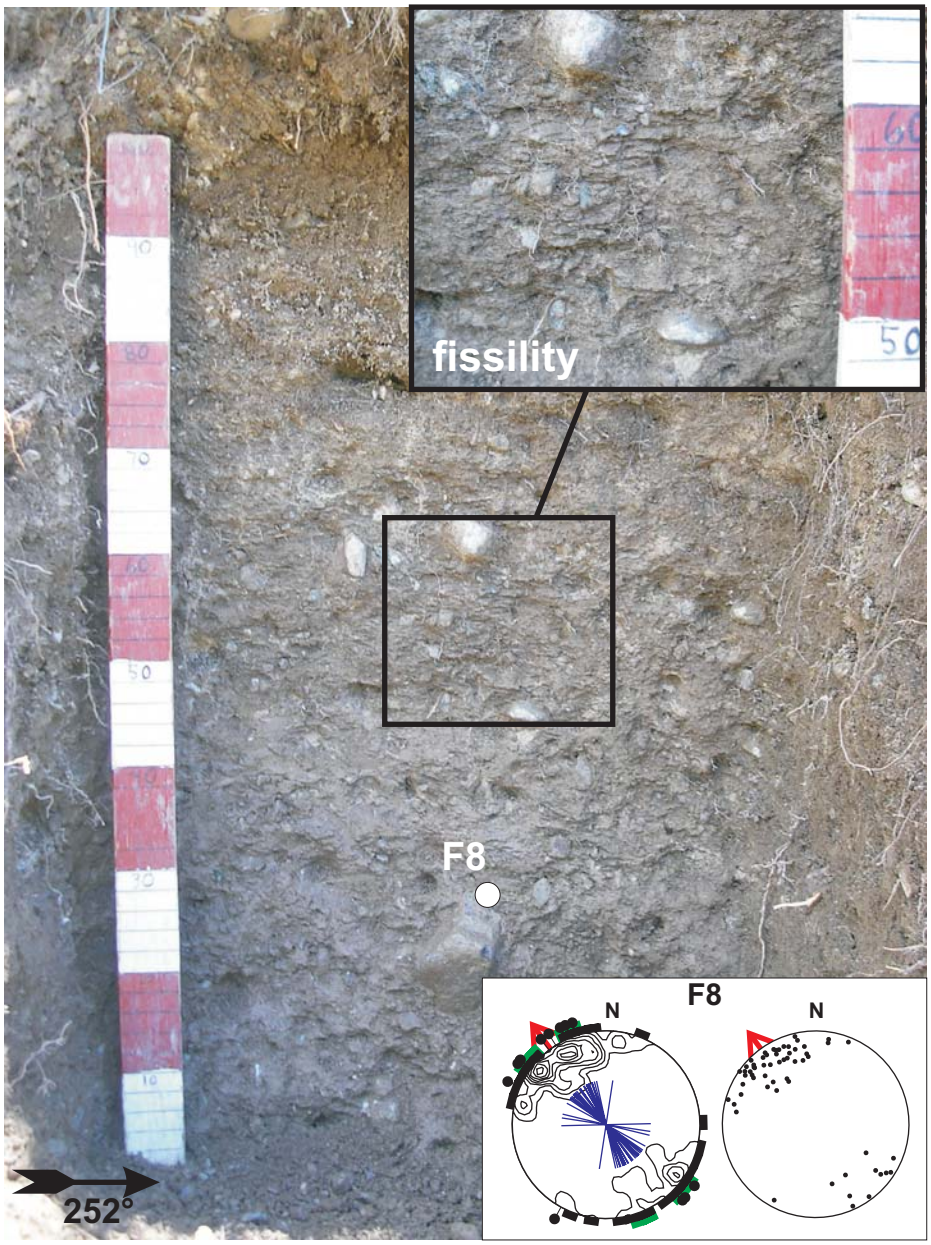

Figure 4.3-2. F8 and fissility planes in the diamicton at site 20. The orientation of fissility planes is similar to that exposed at F7. See Figure 3.3-1 for stereogram legend. Metre stick with decimetre subdivisions for scale.

4.3.2 Micromorphology

Although a diamicton sample was extracted from each fabric location at site 20, only one sample (from the site of F7) survived the thin sectioning process. This yielded one vertically oriented thin section (S20F7v) and one horizontally oriented thin section (S20F7h). In thin section, the diamicton at site 20 appears to be plasma supported and dominated by, in order of abundance, subangular to subrounded limestone skeletal grains, subangular to subrounded metasedimentary skeletal grains and subrounded volcanic skeletal grains (Fig. 4.3-3A). A series of subparallel planar voids have an apparent dip of ~40° down to 103° azimuth in thin section S20F7v (Fig. 4.3-3A). Some large (blue dashed-line arrows, Fig. 4.3-3A) and small (green solid-line arrows, Fig. 4.3-3A) skeletal grains in contact with the planar voids are oriented subparallel to them. Two of the largest skeletal grains are imbricated (Fig. 4.3-3A). Planar void walls and the matrix surrounding skeletal grains are often darker than the surrounding matrix in some areas, particularly in areas where more transmissive light can pass through (Figs 4.3-3B, 4.3-3C, 4.3-3E). The relatively light coloured areas in the matrix are artifacts of the hand grinding phase of thin section preparation, during which the water saturated grinding powder migrates to low-pressure areas between the thin section and the grinding wheel (Kramer 2006 *pers. comm.)*. Vughs and voids that previously housed grains are more common in these areas (Figs 4.3-3B, 4.3-3C 4.3-3E). Unlike sections S23F30v and S23F31v, identifiable (under magnifications of 40x or lower) deposits of calcite or iron oxide are rare in the matrix and along the walls of voids, however thin coatings of calcium carbonate are visible along the edges of some skeletal grains.

Discrete microstructures present within S20F7v include turbates (Fig. 4.3-3G), necking structures (Fig. 4.3-3F), grain stacks (Fig. 4.3-3D) and crushed/broken grains (Figs 4.3-3D, 4.3-3F). No grain lineations were observed, and over 80% of all discrete microstructures were turbates (Fig. 4.3-4).

Vertical microfabric S20F7v-1 consists of a spread out cluster of grains with plunges of up to 60-70° (Fig. 4.3-4). The majority of sand grains plunge down to the SE, and the principal eigenvector is subparallel to the planar voids seen in the vertical thin section. Horizontal microfabric S20F7h-1 shows considerable spread with a slight clustering of observations in the NE-SW direction and three relatively isolated peaks in the NW –SE direction (Fig. 4.3-4). Horizontal microfabric S20F7h-2 consists of a tight

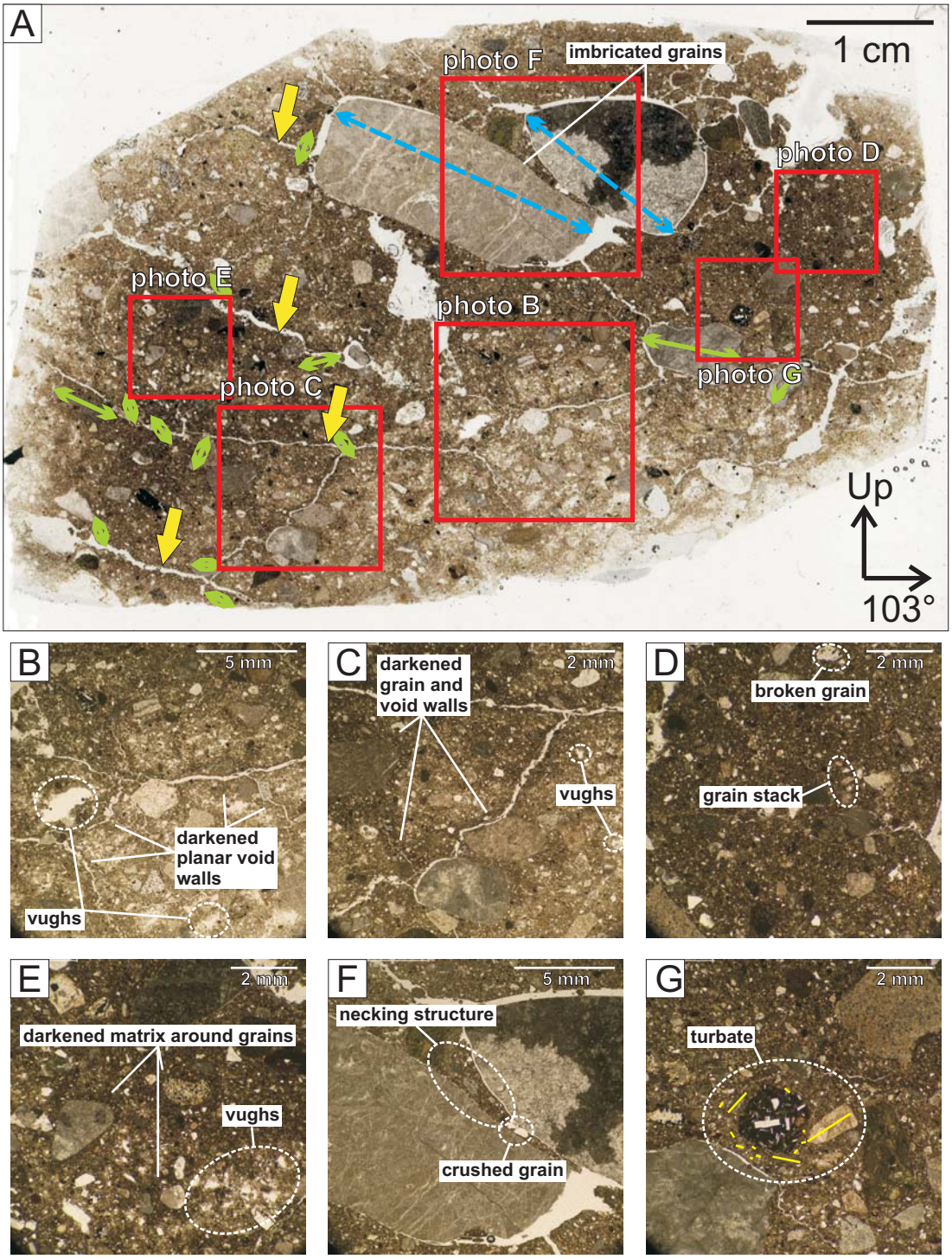

Figure 4.3-3. Thin section S20F7v. A) A 2400 dpi scan of thin section showing planar voids (yellow arrows). Large grains (blue arrows) are oriented subparallel to planar voids and smaller grains (green arrows) are oriented oblique to planar voids. The locations of microphotographs B, C, D, E, F and G are indicated by red squares. Microphotographs show planar voids and grains with darkened walls (B, C), vughes (B, C, E), a broken grain (D), a grain stack (D), a necking structure (F), a crushed grain (F) and a turbate (G).

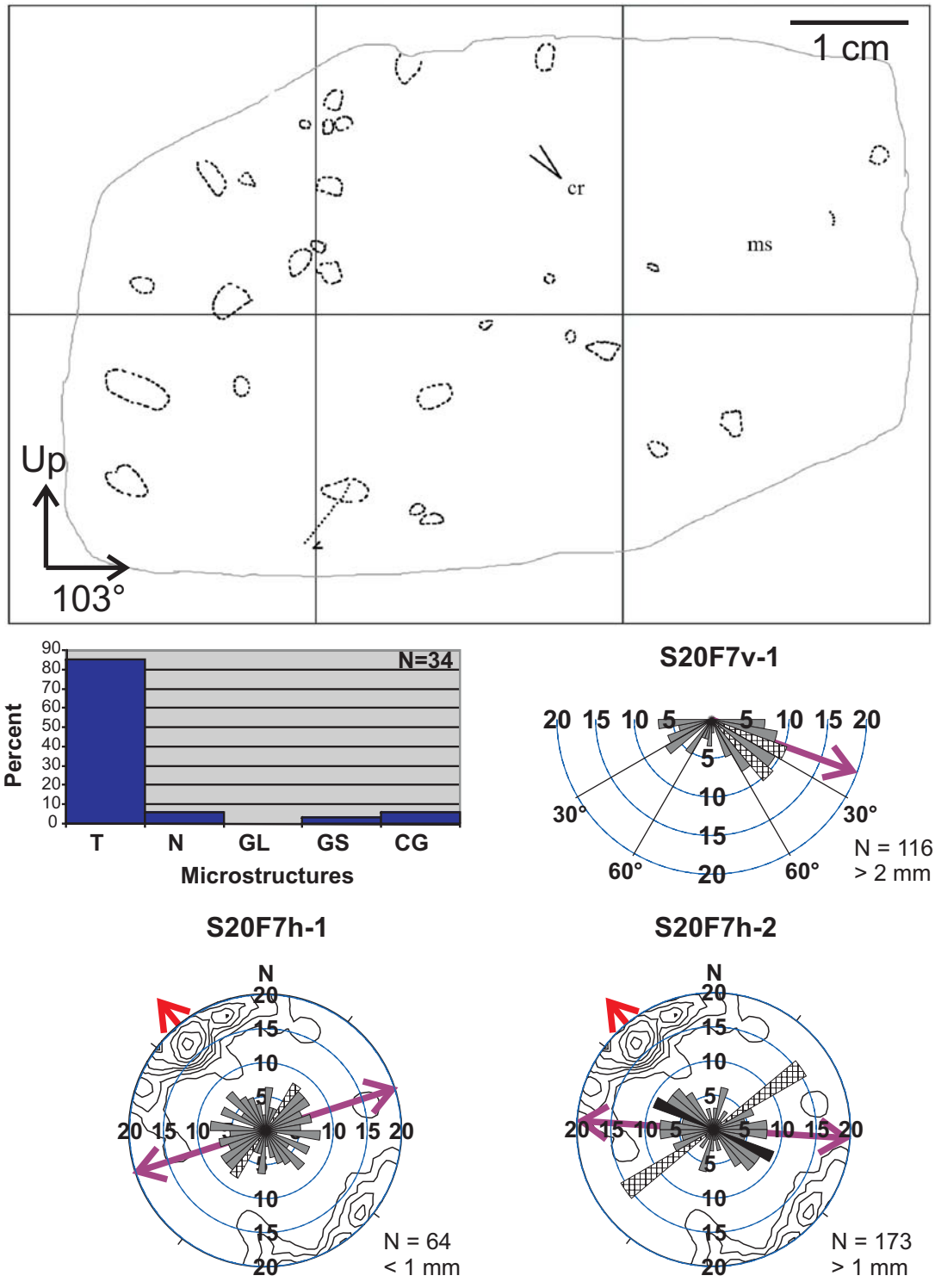

Figure 4.3-4. Microfabrics S20F7v-1, S20F7h-1 and S20F7h-2, and microstructure map and frequency histogram for thin section S20F7v. See Figures 3.3-4 and 3.3-5 for legends.

cluster oriented approximately perpendicular to the principal eigenvector of the macrofabric. A second spread out cluster has a peak oriented oblique to the principal eigenvector of macrofabric S20F7 (Fig. 4.3-4).

4.3.3 Interpretation

The diamicton at site 20 has high silt content and contains subhorizontal fissility planes, clasts with abundant glacigenic wear features, and unimodal clast fabrics with consistently oriented principal eigenvectors. These characteristics suggest that unit 1 is a subglacial till, as suggested by Lian (1997) and Lian and Hicock (2000). The presence of facets, bullet noses and keels suggest that clasts in the diamicton were initially deposited by lodgement.

The diamicton at site 20 was previously classified as lodgement till (Lian 1997; Lian and Hicock 2000). This interpretation is supported here by the unimodal shape of the clast fabrics and the consistently oriented clast fabric principal eigenvectors. In contrast to the data reported by Lian (1997) and Lian and Hicock (2000) (Fig. 4.3-1), however, bullet noses in F7 and fractured ends in both fabrics in this study show no preferred direction. Either these features record clast re-orientation during ploughing and (or) after lodgement at the ice-bed interface, or some or all of them have been inherited from an earlier time in the transport history of the pebbles. Clast wear features recording ice flow direction during lodgement have been observed to be better preserved on relatively large cobbles and boulders than on smaller clasts in front of contemporary glaciers (Benn 1994; 1995). Thus, it is suspected that more definitive evidence for preserved lodgement till might have been obtained if clast wear features recorded in this study were not restricted to pebble-sized clasts.

Clast upper surface striae were commonly parallel to the long axes of pebbles suggesting that slip between the pebble surface and the till matrix or overriding debris rich ice occurred while the long axes of pebbles were oriented in the direction of shear. Most of the pebbles within the lowest contour class in F7 are blade-shaped, a possible indication that blade shaped clasts were slower to rotate to a shear-parallel direction than more elongate pebbles. This interpretation is consistent with March-type rotation of clasts along a shear zone where slip occurs between the rotating particles and the shear zone walls (Glen *et al.* 1957; Drake 1974). Striated, bladed clasts within the lowest contour class, however, had striae parallel to clast long axes, rather than perpendicular

or oblique to them, suggesting that striae formation occurred when bladed clast long axes were oriented parallel to the shear direction before they were re-oriented.

The NW dipping fissility planes and NW plunging macrofabric principal eigenvectors are consistent with ice flow from the NW, as previously proposed by Lian (1997) and Lian and Hicock (2000) before last glacial maximum. These authors also report fissility planes, clast fabrics and clast fractured ends in what they have inferred to be lodgement till at site 19 (not examined in this study, but located a few metres NW of site 20, and several metres higher in elevation than site 20). The deposition of the site 19 diamicton was inferred to have occurred under northwestward flowing ice during the last glacial maximum, after the deposition of the diamicton at site 20 (Lian 1997; Lian and Hicock 2000).

In thin section S20F7v, fissility planes appear as planar voids. Skeletal grains that are in contact with planar voids tend to be aligned subparallel to them (Fig. 4.3-3). The microfabric measured from S20F7v shows that most sand sized grains are oriented subparallel to planar voids (Figs. 4.3-3A, 4.3-4). These observations suggest that either: 1) the planar voids are shear planes, and the alignment of shear planes and sand sized grains occurred under a similar (or the same) shear stress event, or 2) the planar voids are fractures that developed as a result of unloading of the sediment after ice retreat, and were influenced by the orientation of grains in the diamicton as they propogated along paths of least resistence to tensile stress.

The microfabrics for the horizontally oriented section, S20F7h, show many sand grains oriented transverse or oblique to the principal eigevector of the macrofabric. The transverse or obliquely oriented sand grains may be indicative of 1) the increased sensitivity of sand sized grains to reorientation as they interact with larger heavier grains during shear (Thomason and Iverson 2006), 2) sand grain rotation in a ductile/viscous matrix that flows around larger more stable particles (Benn 1995), or 3) a local area of compression.

Calcite coatings around some skeletal grains likely originated from meteoric and (or) groundwater. The darkened void walls and matrix surrounding skeletal grains (Figures 4.3-3B, 4.3-3C, 4.3-3E) appear to have been more resistant to hand grinding than the surrounding material, suggesting that these areas are more dense and cohesive. These areas could represent sites where calcium carbonates, clays, and (or) iron/magnesium oxides derived from porewater have penetrated the matrix. They could also represent differential compaction around skeletal grains (Hiemstra and Rijsdijk

2003) and dilatant hardening due to shear along fissility planes (Iverson *et al.* 1998), which was accompanied by the migration of fines to low pressure areas in shear zones and around rotating elements during shearing events (Kilfeather and van der Meer 2008).

The discrete microstructure distribution is dominated by turbates suggesting that grain rotation was common during emplacement (Fig. 4.3-3G). Though the evidence is less abundant, grain stacking and crushing, and squeeze flow between particles also occurred (Figs 4.3-3D, 4.3-3F). As with site 23, the low abundance of crushed grains, the subangular to subrounded nature of the skeletal grains, and the high silt fraction in the matrix suggests that particle breakage was limited to abrasion along grain surfaces (Hooke and Iverson 1995).

4.4 Site 44

4.4.1 Macroscale sedimentology and structural geology

Site 44 is located close to where the floor of Jesmond valley is at its highest elevation, ~12 km south of site 20 (Figs 3.1-1). The exposure at site 44 contains four units. Unit 1 is imbricated, weakly cross-bedded, matrix-supported, sandy cobble gravel with a minimum thickness of 2 m exposed. Clast fabrics were not measured in unit 1, however clast imbrication (observed in 2D) suggests flow to the WSW.

Unit 1 is conformably overlain by unit 2; a ~0.5 m thick unit of macroscopically massive, matrix-supported clast poor (6-8%, Table 4.2-1), sandy silt diamicton (Fig. 4.2-2). Two fabrics (F5 and F6, Fig. 4.4-1) were taken ~1.25 m apart from each other within unit 2. Both fabrics are girdle-shaped with principal eigenvectors plunging to the NW (F5) or N (F6) (Figs 4.4-2, 4.4-3). In F5, only 13% of clasts have striae on their upper surfaces, and all of them are oriented parallel to clast a-axes. Two clasts have upper surface striae with multiple orientations (Table 4.2-3). No keels were identified and 10% of measured clasts are faceted on at least one side (Table 4.2-3). In F6, only 7% of clasts have striae on their tops, and most of these are parallel to clast a-axes (Table 4.2-3). One keel was identified on a clast bottom, and is oriented NW-SE. Out of all clasts in the sample, 7% are faceted on at least one side (Table 4.2-3). Lian's (1997) fabric 44 (fab-44, Fig. 4.4-1) is also girdle-like with the strongest clustering toward the NW. Both bladed and elongate clasts of various levels of compactness were measured in F5 and F6, with no particular particle shape showing any preference in orientation (Fig. B-1, Appendix B).

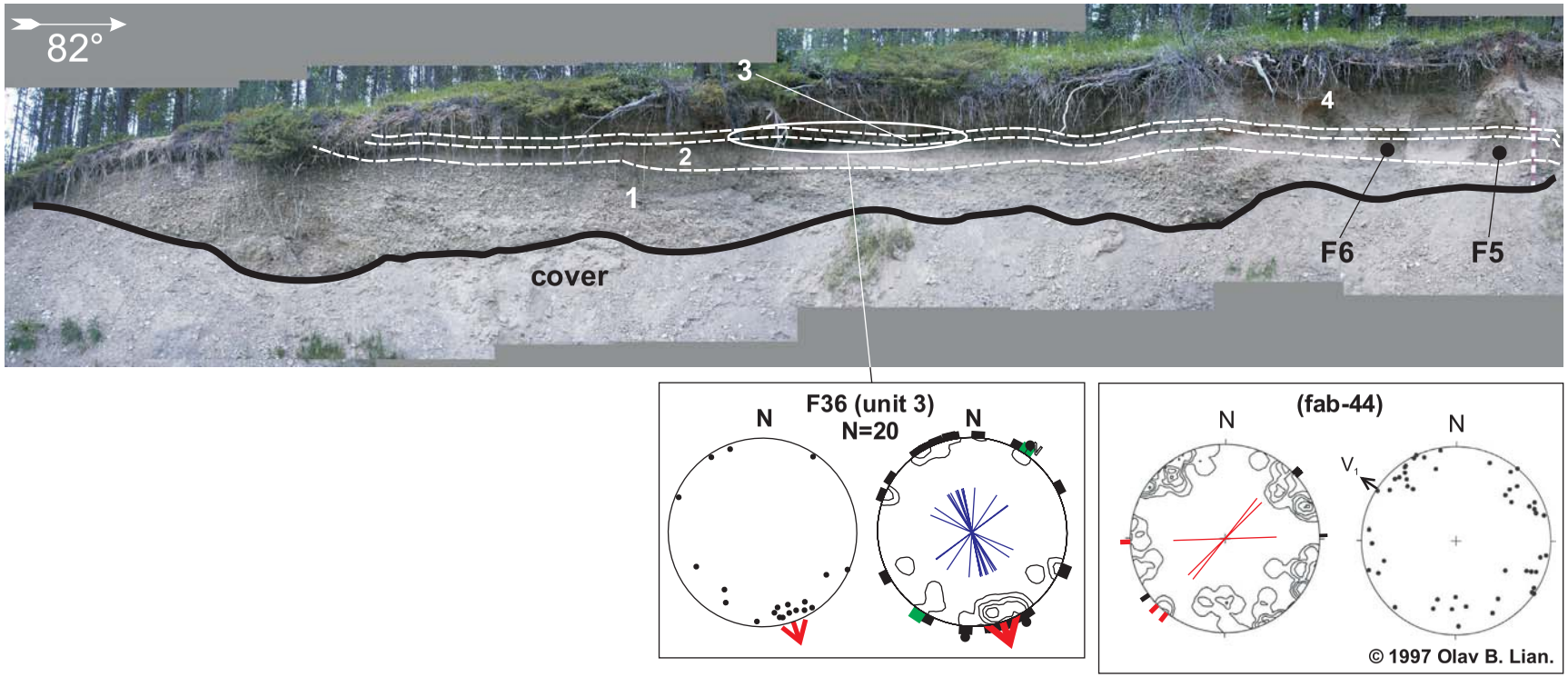

Figure 4.4-1. Site 44, units 1 (sandy gravel), 2 (diamicton), 3 (boulder-cobble pavement), and 4 (silt and clay rhythmites). The location of F5 and F6 within unit 2 is indicated with black dots. The stereogram for fabric 44 (fab-44) (measured in unit 2 - exact location unknown) is adapted from Lian (1997) with permission. Striae measurements reported by Lian (1997), coloured red on the fab-44 stereogram, were taken from the tops of cobbles and boulders in unit 3. Fractured ends reported by Lian (1997) from clasts in unit 2 are shown in black, and fractured ends reported by Lian (1997) from the cobble-boulder pavement are shown in red on the stereogram of fab-44. F36 is the boulder-cobble pavement fabric measured in this study from unit 3. See Figure 3.3-1 for stereogram legend. Metre stick with decimetre subdivisions for scale.

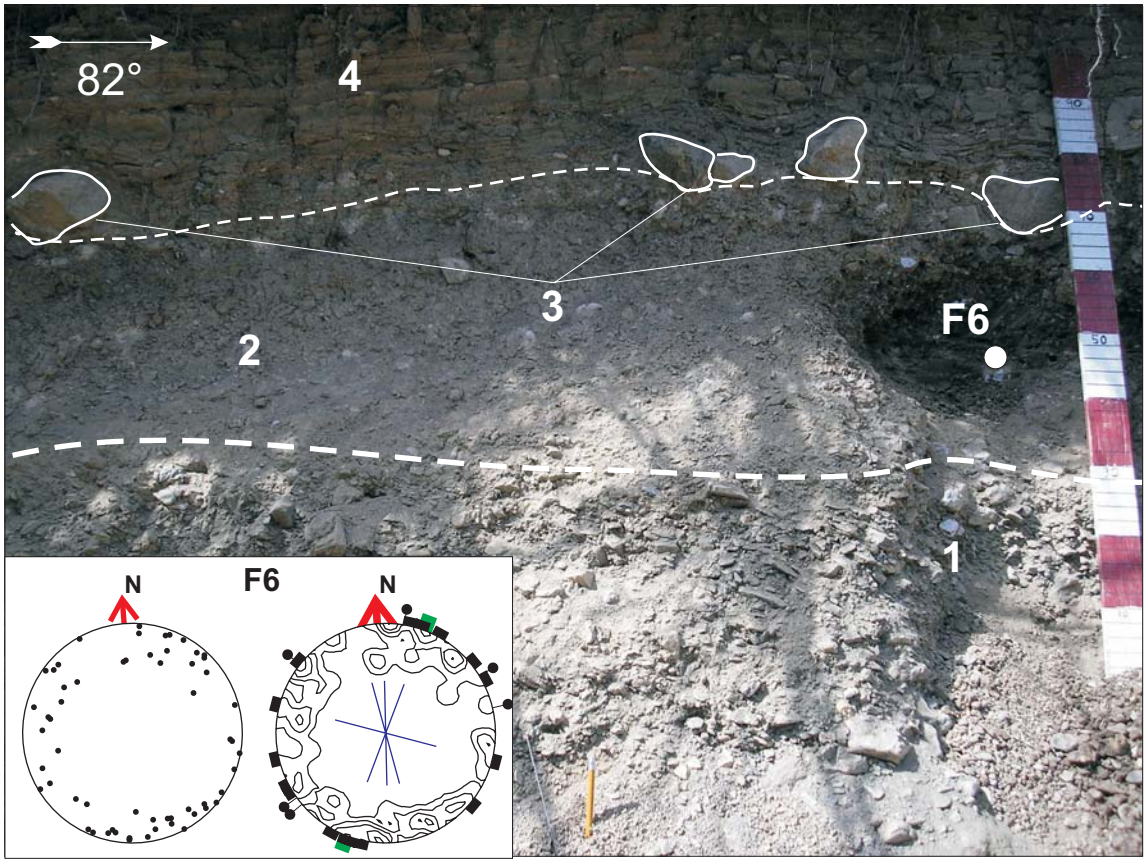

Figure 4.4-2. F6 and units 1 (sandy gravel), 2 (diamicton), 3 (boulder-cobble pavement) and 4 (silt and clay rhythmites) at site 44. See Figure 3.3-1 for stereogram legend. Metre stick with decimetre subdivisions for scale.

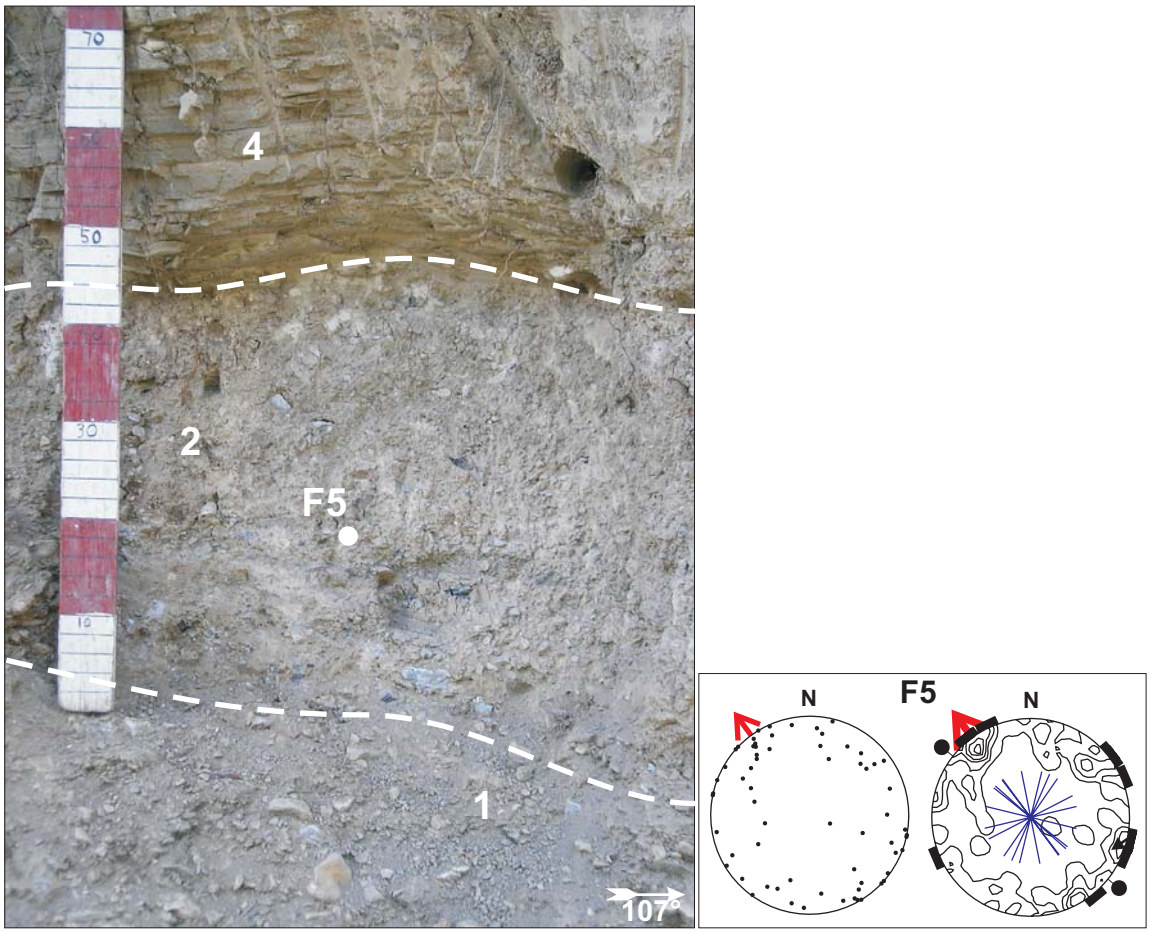

Figure 4.4-3. F5 and units 1 (sandy gravel), 2 (diamicton) and 4 (silt and clay rhythmites), site 44. See Figure 3.3-1 for stereogram legend. Metre stick with decimetre subdivisions for scale.

Unit 3 consists of a discontinuous series of cobbles and boulders situated on top of unit 2 (Fig. 4.4-1). These cobbles and boulders have glacigenic wear features and rarely penetrate the underlying diamicton more than a few centimetres. Three striae sets on cobble and (or) boulder tops were measured by Lian (1997), and are plotted in red on the stereogram for his fabric 44 (Fig. 4.4-1). These are generally oriented NE-SW. Fractured ends on the same cobbles and boulders (also in red on the stereogram of fabric 44) point to the SW. The trends, plunges and the orientation of clast wear features of 20 cobbles and boulders from unit 3 were measured and plotted in this study (F36, Fig. 4.4-1, Table 4.2-3). More clasts should be measured to determine the modality of F36 with confidence; however the number of clasts that could be measured was limited by accessibility. The long axes of most cobbles and boulders are oriented NW-SE, with clast surface striae generally following the long axes of the clasts (Fig. 4.4-1). One keel was located on a clast bottom, and is oriented NW-SE. Ten clasts (50%) have at least one facet (Table 4.2-3).

Unit 4 is up to 1 m in thickness and contains sand and silt rhythmites that drape the cobbles and boulders of unit 3. Lonestones were not observed in unit 4.

4.4.2 Micromorphology

One diamicton sample was extracted from both fabric sampling locations at site 44, however only one sample survived the thin sectioning process. This sample was extracted from the site of F5, and from it one vertically-oriented thin section (S44F5v, Fig. 4.4-4A) and one horizontally-oriented thin section (S44F5h) were cut. In thin section, the diamicton at F5 appears to be plasma supported and dominated by, in order of abundance, angular to subangular metasedimentary skeletal grains, subangular to subrounded limestone skeletal grains and subrounded volcanic skeletal grains (Fig. 4.4-4A).

The matrix of the diamicton in S44F5v is heterogeneous, particularly in the upper-central portion of the thin section (Figs 4.4-4B, 4.4-4C) where elongate interfingering bands of coarse and fine textured domains are juxtaposed. These bands have an apparent dip of ~40-45° down to 304° azimuth, which is similar to the orientation of most sand grains (see microfabric S44F5v-1, Fig. 4.4-5, Table 4.12-2). Similar interfingering textural domains were not identified in the horizontally-oriented thin section, S44F5h, which appears homogenous (Appendix H). Laminae in thin section S44F5v follow the orientations of the larger textural bands and microfabric, and at

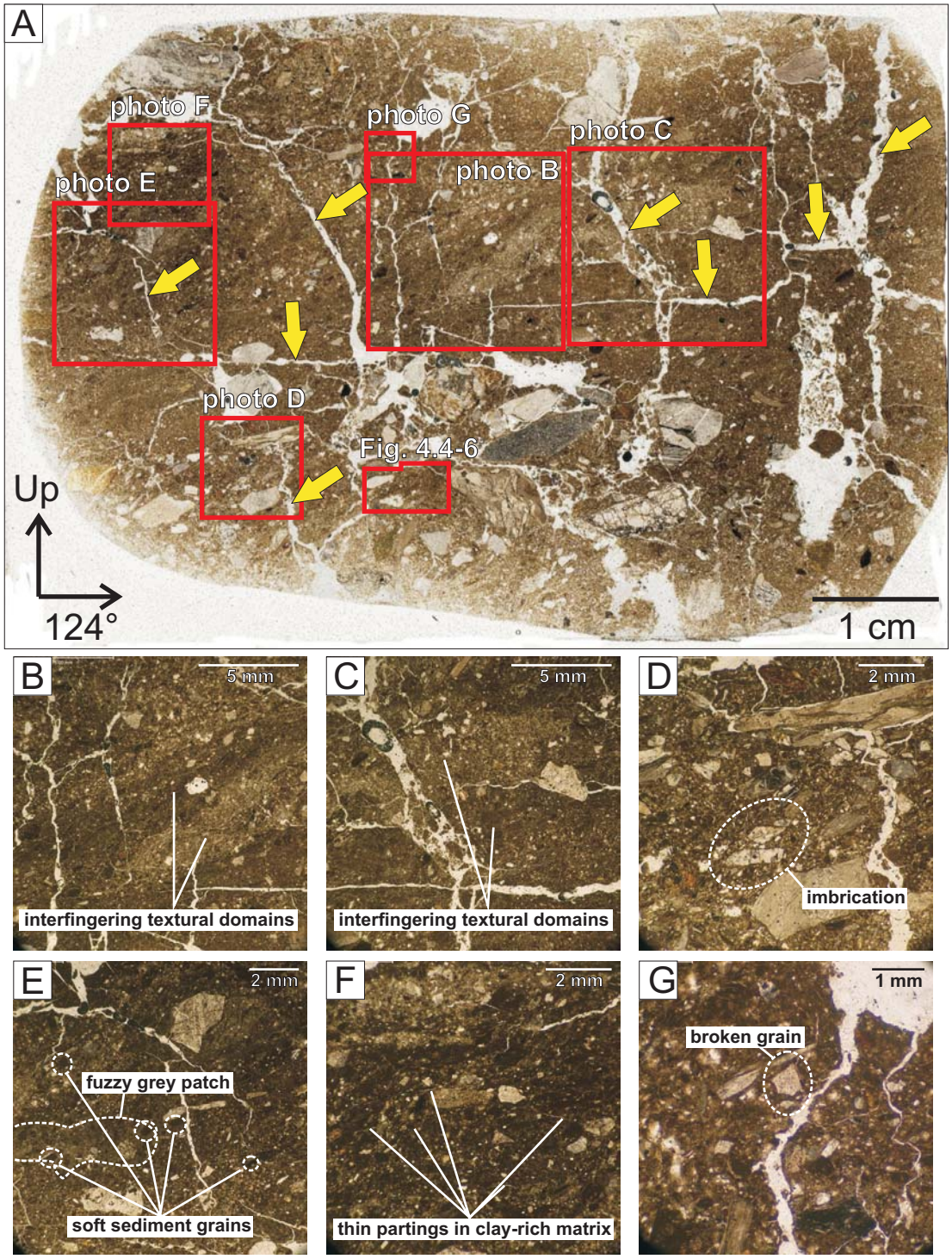

Figure 4.4-4. S44F5v thin section. A) A 2400 dpi scan of thin section S44F5v showing subvertically and subhorizontally oriented fractures (yellow arrows). The locations of microphotographs B, C, D, E, F and G are indicated by red squares. Microphotographs show interfingering coarse (light coloured) and fine (dark coloured) textured domains (B, C), a skeletal grain-rich area of the thin section containing imbrication (D), soft sediment grains (E), a fuzzy grey patch inferred to be an area of calcium carbonate deposition (E), thin partings in a clay-rich area of the matrix (F) and a broken grain (G).

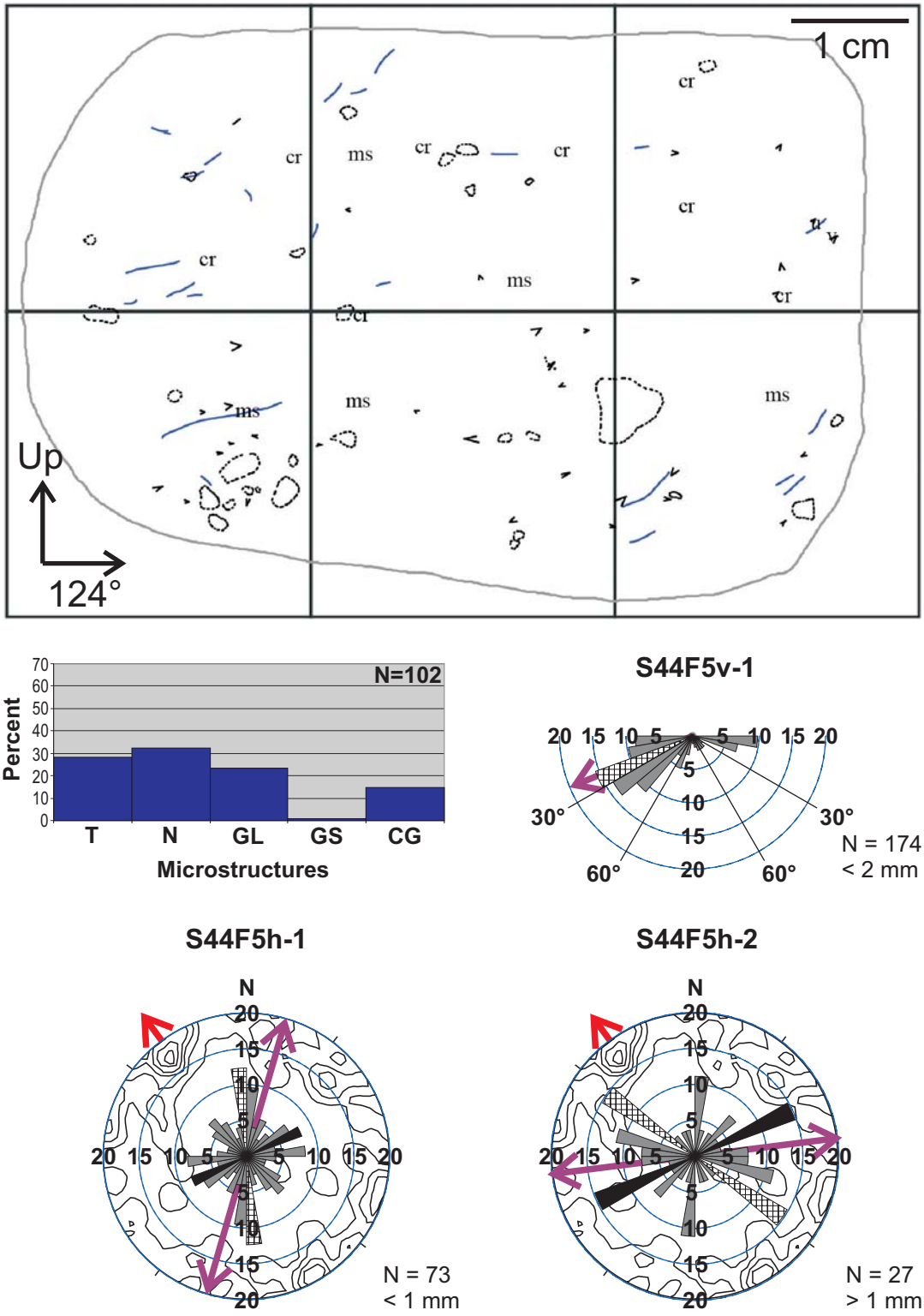

Figure 4.4-5. Microfabrics S44F5v-1, S44F5h-1 and S44F5h-2, and microstructure map and frequency histogram for thin section S44F5v. See Figures 3.3-4 and 3.3-5 for legends.

magnifications of up to 20x, thin partings subparallel to these laminations can be observed in clay-rich areas of the matrix (Fig. 4.4-4F). Most major planar voids are oriented subvertically but a few are oriented orthogonal to these (Fig. 4.4-4A). The continuity of the textural banding in the matrix suggests that no significant displacement has occurred along the planar voids (Figs 4.4-4A, 4.4-4B, 4.4-4C). The lower third of the thin section shows a significant increase in skeletal grain concentration and includes imbricate grains (Fig. 4.4-4D). Subangular to subrounded dark coloured soft sediment grains are ubiquitous throughout the matrix in S44F5v (Figs 4.4-4E, 4.4-6). These grains are opaque under cross polarized light, and thus do not exhibit plasmic fabrics. Planar void walls and grain surfaces generally appear clean, however, rare 'fuzzy' grey patches are visible in the diamicton matrix (Fig. 4.4-4E).

A large number (n=102) of discrete microstructures are visible in thin section S44F5v (Fig. 4.4-5). These include similar numbers of turbates, necking structures, grain lineations and crushed grains (Fig. 4.4-4G), and few grain stacks.

A tight cluster with a shallow plunge down to the NW dominates vertical microfabric S44F5v-1 (Fig. 4.4-5). Horizontal microfabrics S44F5h-1 and S44F5h-2 have multiple clusters and principal eigenvectors that are oriented obliquely to each other as well as to the principal eigenvector of macrofabric S44F5 (Fig. 4.4-5). The tightest cluster of microfabric S44F5h-1 has a major peak oriented NNW-SSE. The peak of the second tightest cluster is oriented NE-SW. Microfabric S44F5h-2 has two large majour peaks oriented NW-SE and WSW-ENE. Both peaks represent 15% of all grains counted. Two slightly smaller peaks, each representing 12% of all grains counted, are oriented NNE-SSW and WNW-ESE. The NW-SE trending majour peak is considered to be the peak of the tightest cluster because it is aligned relatively close to the smaller WNW-ESE trending peak that represents 12% of all grains. The NE-SW trending majour peak is considered to be the peak of the second tightest cluster because sand grain orientations in the NE-SW quadrants appear more spread.

4.4.3 Interpretation

The previously inferred late glacial history of site 44 is the following: 1) glacial ice overrides alluvial sediments deposited during nonglacial time (unit 1), 2) subglacial till is deposited (proto-unit 2), 3) during the waning stages of the Fraser glaciation, basal debris-rich ice stagnates and melts, 4) faceted, striated, and bullet-shaped clasts are released onto the till surface and meltout till accumulates around them (unit 3), 5) an

increase in porewater causes the till to flow, and its primary pebble fabric is destroyed (unit 2), 6) ice recedes and a proglacial lake is formed (unit 4) (Lian 1997).

The imbricated, weakly cross-bedded, matrix supported gravel of unit 1 were likely deposited by water, as suggested by Lian (1997). Unit 2 was previously classified as a gravity flow diamicton. The glacigenic wear features observed on the clasts in unit 2 suggest that at least some clasts were subglacially transported and (or) deposited by lodgement. The girdled distribution of the macrofabrics and inconsistent alignment of clast wear features are consistent with Lian's (1997) observations, and suggest that final deposition of unit 2 was by gravity flow.

Lachniet *et al.* (1999) compared the micromorphology of dry-type (Lawson type I and II) and wet-type (Lawson type III and IV) subaerial glacigenic sediment flow deposits formed at the terminus of Matanuska Glacier, Alaska. In thin section, dry-type flow deposits included brittle to plastic deformation structures including folds, a poorly developed microfabric, evidence of underlying sediment deformation, fluid escape and injection structures, and thick haloes (Lachniet *et al.* 1999).

Wet-type flow deposits included thin flow laminations, a strongly aligned 'laminar flow fabric', imbrication, smooth lower contacts, fluid escape and injection structures, and thin or non-existent haloes. Haloes were defined as silt coatings around skeletal grains that were derived either from grain rotation, or simply the coating of wet silt around the clast. Haloes were thought to be thicker in dry type debris flows because the relatively low water concentration in the silt increased its cohesivity (Lachniet *et al.* 1999). The unidirectional orientation of grains leading to strongly oriented microfabrics was attributed to laminar flow within water saturated sediment outside the plug of the debris flow (Hampton 1975).

Laboratory experiments have shown that debris flows can develop layers of various grain sizes as a result of zones of various competences within the flow (Hampton 1975; Lachniet *et al.* 1999). Sediment competence (defined as the diameter of the largest transported grain) is variable within debris flows because of its dependence on shear duration and water content (Hampton 1975).

The interfingering textural domains and contrasting skeletal grain concentrations observed in thin section S44F5v can be explained in terms of intermixing of sediment from multiple sources, and (or) fluctuating sediment competence associated with unsteady shear rates and fluctuating water contents that are driven by the migration of the debris flow plug boundary (Hampton 1975). The laminations, imbrication, clean

grain surfaces and strong microfabric associated with S44F5v are consistent with wet-type glacigenic flow deposits and can be attributed to laminar flow (Lachniet *et al.* 1999). The thin laminae-parallel partings as well as the larger subvertical and subhorizontal fractures are likely associated with post-depositional desiccation of the diamicton matrix and may have widened during sampling and processing in the laboratory.

The subangular to subrounded soft sediment grains observed in S44F5v appear to have been formed within the debris flow as opposed to being entrained from sediments below. The colour and texture of the soft sediment grains resemble heavily fractured or brecciated silt and clay rich areas of the matrix (Fig. 4.4-6) suggesting that local dewatering of these areas lead to their subdivision into discrete, cohesive, mobile grains, which became more rounded during transport.

Discrete microstructure distributions show that grain rotation, squeeze flow, and grain crushing processes were prevalent during deposition of the diamicton. The abundance of fractured grains may be due to internal defects in the crystalline grains, or fractures in the argillite (metasedimentary) grains. Many grain lineations were identified, but are likely a consequence of the ubiquitous alignment of particles that result from laminar flow, rather than isolated shear events along discrete shear zones.

Microfabrics measured from the horizontally-oriented thin section, S44F5h, are not as strong as that measured from the vertically-oriented thin section and the orientation of the principal eigenvector for grains less than 1 mm is almost orthogonal to the eigenvector for grains greater than 1 mm (Fig. 4.4-5). The horizontal thin section may have been cut from a drier, more cohesive area of the matrix that did not

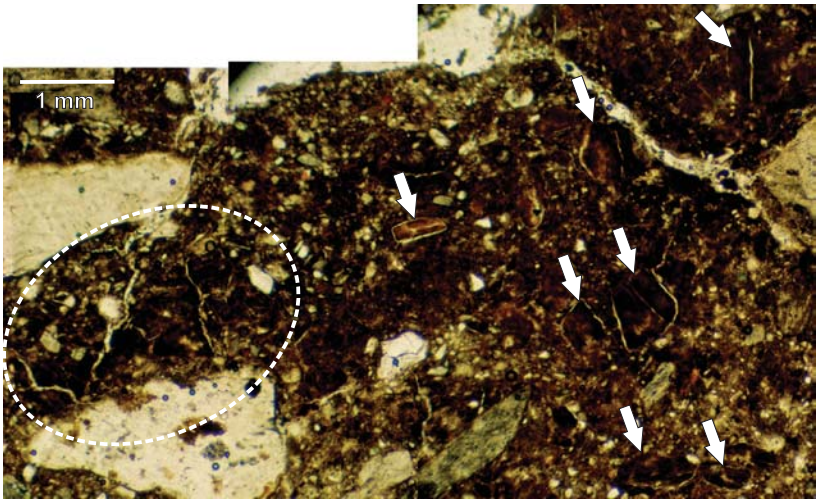

Figure 4.4-6. The formation of soft sediment grains. Silt and clay rich areas of the matrix (ellipse) fracture and divide into discrete mobile soft sediment grains (arrows) that become more rounded during transport.

experience laminar flow (Lachniet *et al.* 1999). The absence of textural domains similar to those observed in thin section S44F5v supports this interpretation.

The macroscale sedimentology of the unit 2 diamicton at site 44 suggests that it is a glacigenic debris flow. Microscale characteristics of this diamicton, when interpreted within this context, resemble those associated with Lawson's type III and type IV glacigenic sediment flow deposits (Tables 1 and 2 in Lachniet *et al.* 1999).

Unit 3 was previously interpreted as a pavement deposited subglacially through melt-out processes (Lian 1997). This interpretation was based on the position of the cobbles and boulders within the sedimentary sequence, and the orientation of their clast wear features (plotted on fab-44 stereogram, Fig. 4.4-1). The glacigenic wear features observed in unit 3 in this study are consistent with the subglacial transport and (or) deposition of cobbles and boulders. Additional fabric and clast wear feature data collected from unit 3 shows that cobbles and boulders are aligned consistently with the valley axis (Fig. 4.4-1), and upper surface striae are parallel to the long axes of cobbles and boulders (Table 4.2-3). Bullet noses and fractured ends show no preferred direction. Either these features record clast re-orientation after lodgement processes, or some or all of them have been inherited from an earlier time in the transport history of the clasts. The cobbles and boulders of unit 3 are draped by the rhythmites in unit 4, which record suspension settling of fines in a pond or a lake.

There are three possible interpretations of the sedimentary sequence at site 44. The first entails lodgement of unit 3 into unit 2, and the last two involve melt-out of either unit 3, or both units 2 and 3. Each interpretation is outlined below:

Interpretation I:

1) Alluvium is deposited by flowing water.
2) Diamicton (unit 2) containing glacigenic debris and possibly some non-glacigenic debris is deposited proglacially from gravity flows off the glacier snout. Some or all of this material may be derived from englacial debris that has experienced transport in the traction zone of a glacier before being entrained into the ice.
3) The glacier advances and lodges cobbles and boulders (unit 3) into unit 2. The absence of a lodgement till in, above or below unit 3 suggests that the overriding ice contained little fine grained debris, or that the lodgement till was eroded, transported and re-deposited down-valley by glaciofluvial processes during ice retreat.

4) Ice retreats or melts in place, leaving a pond or lake.

Interpretation II:

1) Alluvium and gravity flow diamicton are deposited as described in stages 1 and 2 of interpretation I.
2) The glacier advances over site 44, erodes the substrate or deposits no debris, then stagnates.
3) Cobbles and boulders (unit 3) melt-out from the stagnant ice. Clast wear features on boulders and cobbles are preserved from transport in the traction zone of the glacier before melt-out. The absence of a identifiable melt-out till in, above or below unit 3 suggests that a) the stagnating ice was not rich in debris, or b) that melt-out till was deposited and later eroded and transported and re-deposited down-valley by glaciofluvial processes during ice retreat.
4) Ice retreats or melts in place, leaving a pond or lake.

Interpretation III:

1) Alluvium is deposited by flowing water.
2) A glacier with debris-rich basal ice containing a range of grain sizes, overlain by debris-poor englacial ice containing dispersed cobbles and boulders but little sand, silt or clay (Mickelson *et al.* 1992) advances over site 44, erodes the substrate or deposits no debris, then stagnates.
3) Melt-out till (proto-unit 2) is deposited from the melting of the debris-rich ice. The cobbles and boulders subsequently melt out of the debris-poor ice forming unit 3 (Mickelson *et al.* 1992). The glacigenic wear features in unit 3 develop: a) as the cobbles and boulders in faster moving debris-poor ice are ploughed into the slower moving or stagnant debris-rich basal ice before melt-out (Mickelson *et al.* 1992), or b) during subglacial transport in the traction zone prior to entrainment into the ice.
4) Units 2 and 3 are remobilized by gravity causing re-orientation of clasts in unit 2 and minor remobilization of cobbles and boulders in unit 3.
5) Ice retreats or melts in place, leaving a pond or lake.

Interpretations I, II and III are all considered to be plausible explanations for the sedimentary sequence observed at site 44.

4.5 Site 6

4.5.1 Macroscale sedimentology and structural geology

Site 6 is located in a tributary valley cut in the Edge Hills and trending NE-SW between Jesmond valley and the Fraser River (Fig. 3.1-1). This site consists of massive, matrix-supported, clast poor (3-7%, Table 4.2-1) silty sand diamicton (Fig. 4.2-2) with a minimum thickness of 1.25 m. This diamicton was studied at two cleaned exposures (exposure 1 and exposure 2, Fig. 4.5-1) separated by a distance of ~20 m. At exposure 1, a subtle shear plane with an apparent dip of 20° down to 301° azimuth overlies an asymmetrical fold with a subhorizontal axis trending NE-SW (Fig. 4.5-2). The three dimensional strike and dip of the shear plane could not be measured due to difficulty in identifying a planar surface. Three fabrics were measured within 1 m of the landsurface at this site, two fabrics (F6, F7) within 1 m of one another at exposure 1, and

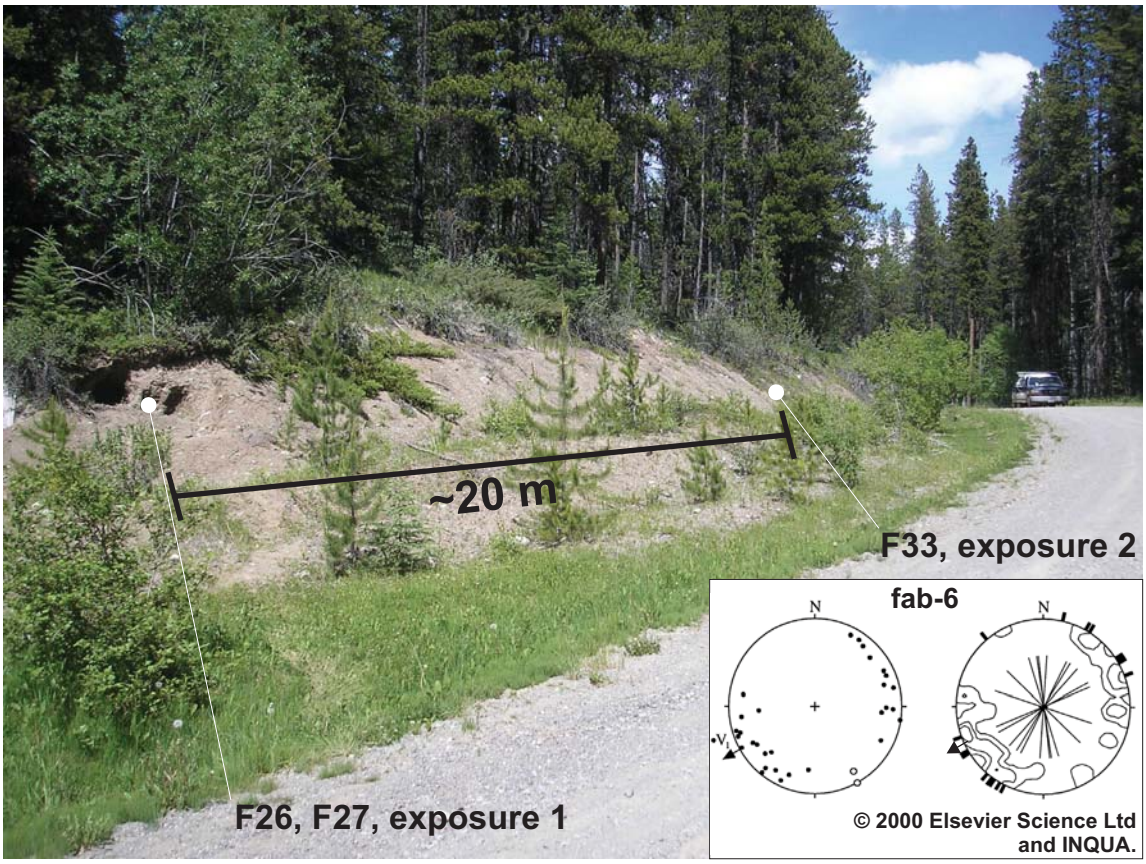

Figure 4.5-1. F26 and F27 (exposure 1) and F33 (exposure 2), site 6 in a valley tributary to Jesmond valley (Fig. 3.1-1). The stereogram for fabric 6 (fab-6) reported by Lian and Hicock (2000) is reprinted with permission and shown in the bottom right. The exact location of this fabric is unknown. See Figure 3.3-1 for stereogram legend.

a third (F33) at exposure 2 (Fig. 4.5-1). F26 was measured just above the shear plane in exposure 1, and F27, just below it.

F26 is unimodal with three outliers and a principal eigenvector pointing SW (Fig. 4.5-2, Table 4.2-1). Most clast upper surface striae are parallel to clast a-axes. One measured clast has upper surface striae with multiple orientations, and one clast was observed to have striae curving around convexities and concavities. Keels on clast bottoms are subparallel to the principal eigenvector (Table 4.2-3). Bullet noses and fractured ends show no preferred direction (Table 4.2-3). Out of all clasts measured, 45% are faceted and 7% have keels (Table 4.2-3).

F27 is spread bimodal with a primary mode trending SW and a secondary transverse mode (Fig. 4.5-2, Table 4.2-2). Most clast upper surface striae are parallel to clast a-axes (Table 4.2-3). No keels were identified. Fractured ends show no preferred direction and most bullet noses point to the SW. Out of all clasts in the sample, 32% are faceted (Table 4.2-3)

F33 is also spread bimodal with a primary mode trending SW and a secondary transverse mode (Fig. 4.5-3, Table 4.2-2). Again, most clast upper surface striae are parallel to clast a-axes, and keels on clast bottoms are subparallel to the primary mode (Table 4.2-3). Bullet noses and fractured ends show no preferred direction (Table 4.2-3). Out of all clasts in the sample, 32% are faceted and 7% have keels (Table 4.2-3). Lian's (1997) fabric 6 (fab-6, Fig. 4.5-1) is spread unimodal with two outliers and a principal eigenvector that points to the SW. Fractured ends in fabric 6 show no preferred direction.

In general, bladed and elongate clasts of various levels of compactness comprise all modes within F26, F27 and F33. The three outliers in F26, however, are characterized only by bladed clasts (Fig. B-1, Appendix B). Two of these bladed clasts do not have upper surface striae, and one has upper surface striae oriented ~60° relative to the clast a-axis. The axis of the fold measured in exposure 1 is roughly parallel to the principal eigenvectors of all fabrics at site 6 (Figs 4.5-2, 4.5-3).

4.5.2 Micromorphology

One sample was extracted from each of the fabric locations at site 6 for thin section preparation. In total, three horizontal (S6F26h, S6F27h and S6F33h) and three vertical (S6F26v, S6F27v and S6F33v) thin sections were cut from these samples. In general, the diamicton in the three vertical thin sections (S6F26v, S6F27v and S6F33v)

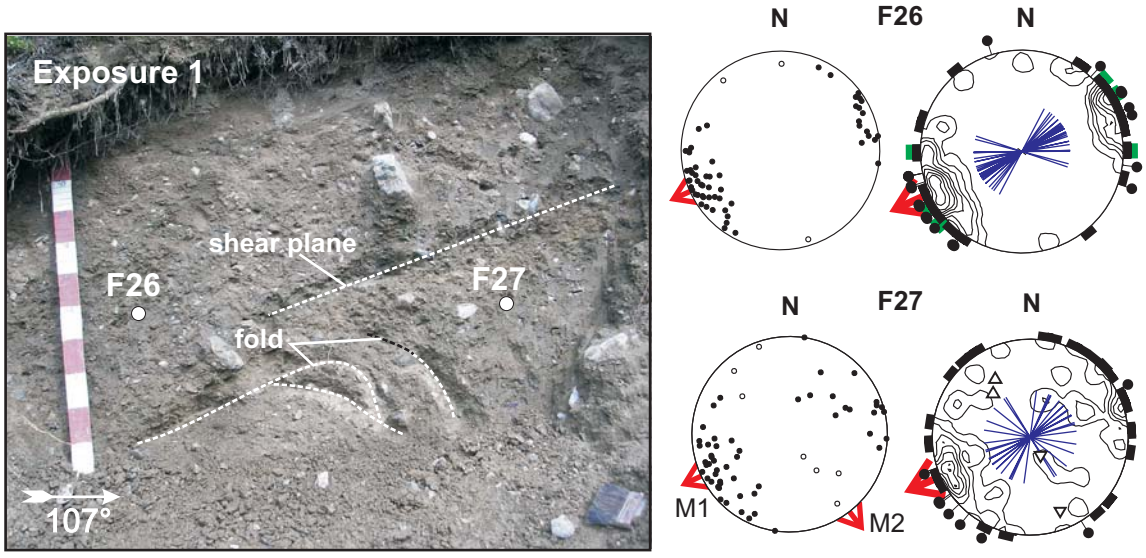

Figure 4.5-2. F26 and F27 in unit 1, exposure 1, site 6. A shear plane and a fold are annotated on the photograph. The southeast dipping and northwest dipping limbs of the fold are represented by upright and inverted triangles, respectively on the contour stereogram of F27. The strike and dip of the shear plane could not be measured. Metre stick with decimetre subdivisions for scale. See Figure 3.3-1 for stereogram legend.

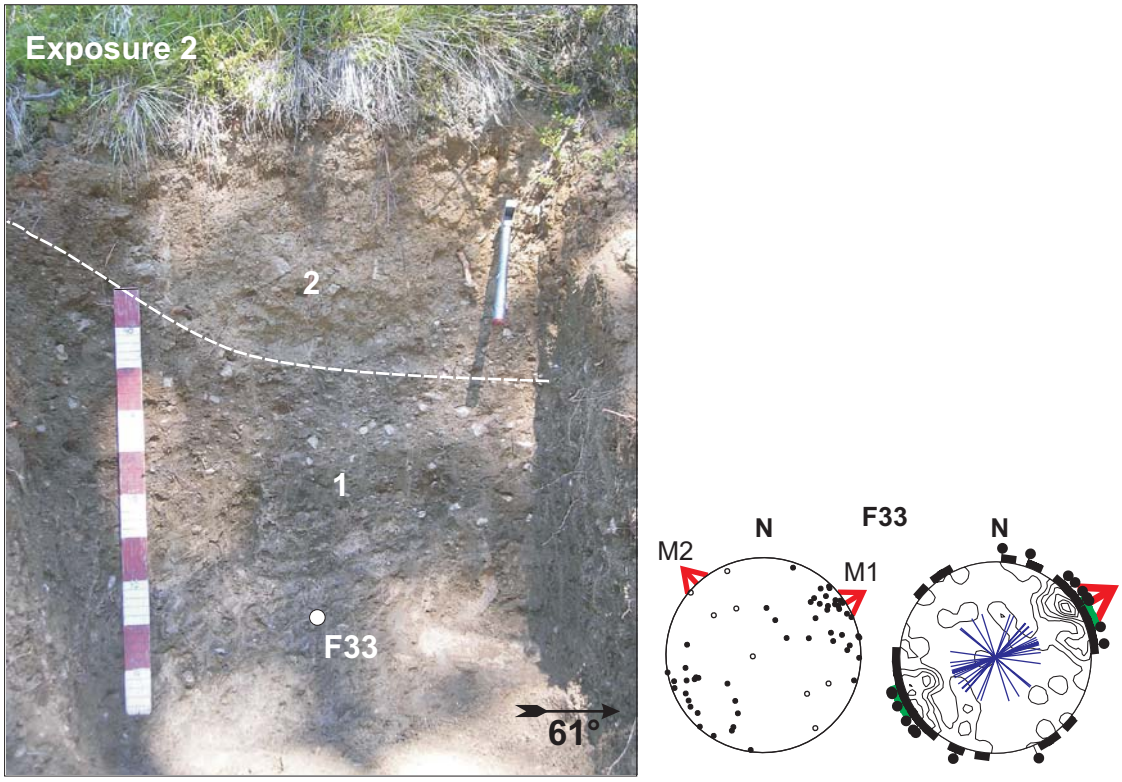

Figure 4.5-3. F33, exposure 2, site 6. Metre stick with decimetre subdivisions for scale. See Figure 3.3-1 for stereogram legend.

are plasma supported, and dominated by angular to subrounded metasedimentary skeletal grains (argillite grains often appear as elongate angular shards), with smaller amounts of subangular to rounded limestone grains and subrounded volcanic grains (Figs 4.5-4A, 4.5-5A, 4.5-6A).

Two of the three vertical thin sections, S6F26v and S6F33v, contain subparallel planar voids (Figs 4.5-4A and 4.5-6A), but all three thin sections contain vughs of various sizes (Figs 4.5-4F, 4.5-5B, 4.5-6E). The planar voids in S6F26v have an apparent dip of ~8° down toward 208° azimuth, and those in S6F33v have an apparent dip of ~30° down toward 202° azimuth. A consistent relationship between the orientation of skeletal grains and the orientation of planar voids is not apparent. Some areas have commonly aligned (subparallel) grains (e.g., Figs 4.5-4C, 4.5-5E). Evidence of calcite or iron oxide deposition in thin section S6F26v is scant (Fig. 4.5-4B). Darkened matrix surrounds some grains (pressure shadows?) and fractures curve around this dark matrix (Fig. 4.5-4E). Calcite coats some skeletal grains in thin section S6F27v (Fig. 4.5-5F), and a dark grey opaque patch in the matrix (Fig. 4.5-5D) may be the site of secondary mineral or clay accumulation due to the heavy weathering of a grain. Thin section S6F33v shows heavy calcite deposition along voids (Fig. 4.5-6D), around cavities of absent grains (Fig. 4.5-6B), and penetrating deep into the matrix (Fig. 4.5-6C).

Fourty-two discrete microstructures were counted in thin section S6F26v (Fig. 4.5-7). These include abundant turbates (including one without a core stone, Figure 4.5-4G), necking structures, and grain lineations (Fig. 4.5-4D), and few grain stacks (Fig. 4.5-4F) and crushed grains. Fifty-seven discrete microstructures were identified in thin section S6F27v (Fig. 4.5-8). These include abundant turbate and necking structures (Fig. 4.5-5C), and fewer grain lineations (Fig. 4.5-5G), grain stacks (Fig. 4.5-5G) and crushed grains. Only 15 microstructures were identified in section S6F33v (Fig. 4.5-9). These include turbates (Fig. 4.5-6F), grain lineations, necking structures (Fig. 4.5-6E), and a few crushed grains.

Sand-sized grains in vertical microfabric S6F26v-1 with apparent plunges of 0-60° are well represented in a spread out cluster (Fig. 4.5-7). This cluster has a peak in the 30-40° range. The principal eigenvectors of horizontal microfabrics S6F26h-1 and S6F26h-2 suggest that a higher proportion of smaller grains are oriented closer to the principal eigenvector of the macrofabric than the larger grains (Fig. 4.5-7, Table 4.2-5). S6F26h-1 contains multiple clusters with the tightest cluster oriented parallel to the microfabric and macrofabric principal eigenvectors. S6F26h-2 contains two tight

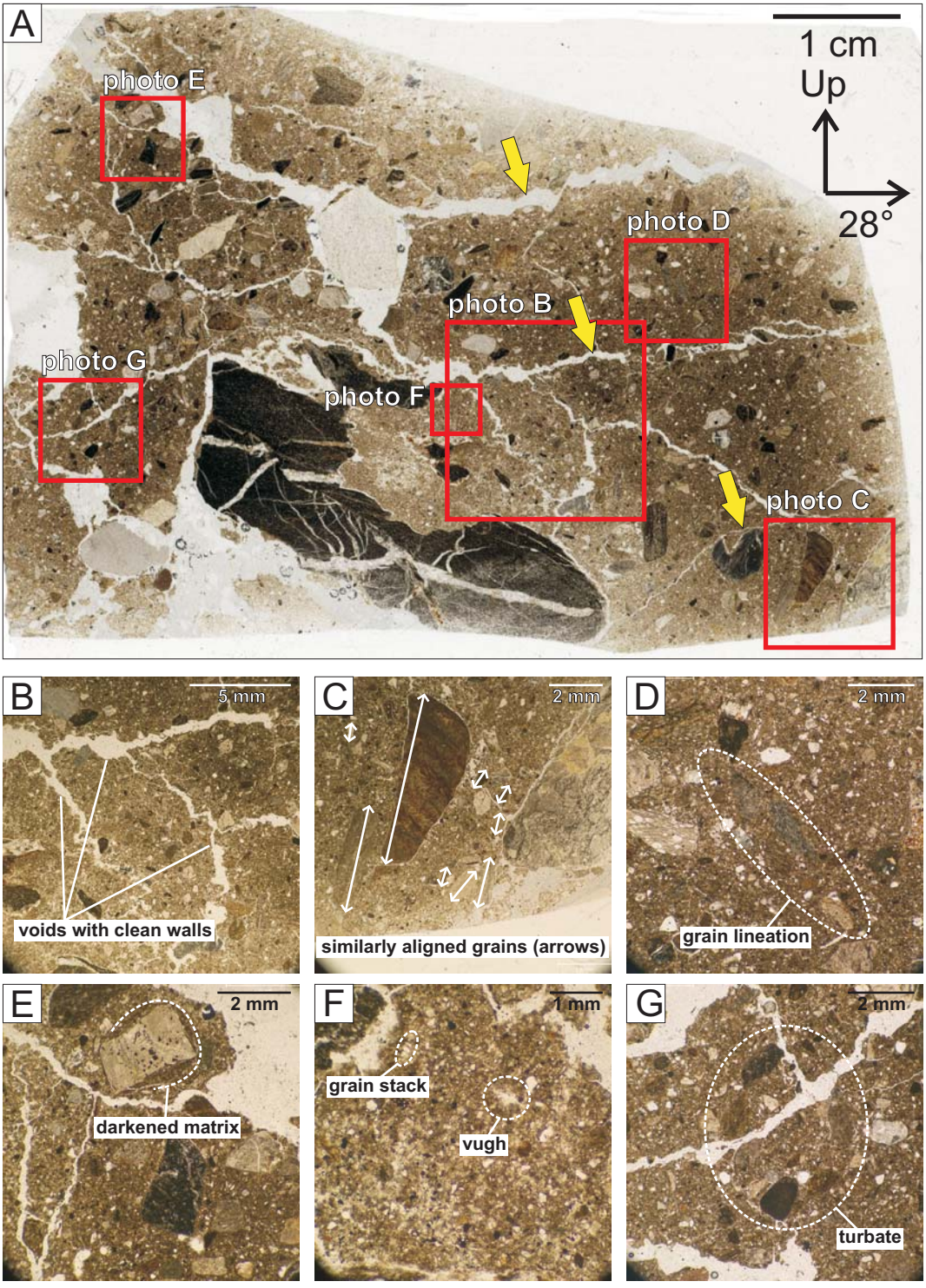

Figure 4.5-4. Thin section S6F26v. A) 2400 dpi scan of thin section showing subparallel planar voids (yellow arrows). The locations of microphotographs B, C, D, E, F and G are indicated by red squares. Microphotographs show planar voids with clean walls (B), similarly aligned grains (C), a grain lineation (D), dark matrix/residue surrounding a grain (E), a grain stack (F), a vugh (F) and a turbate (G).

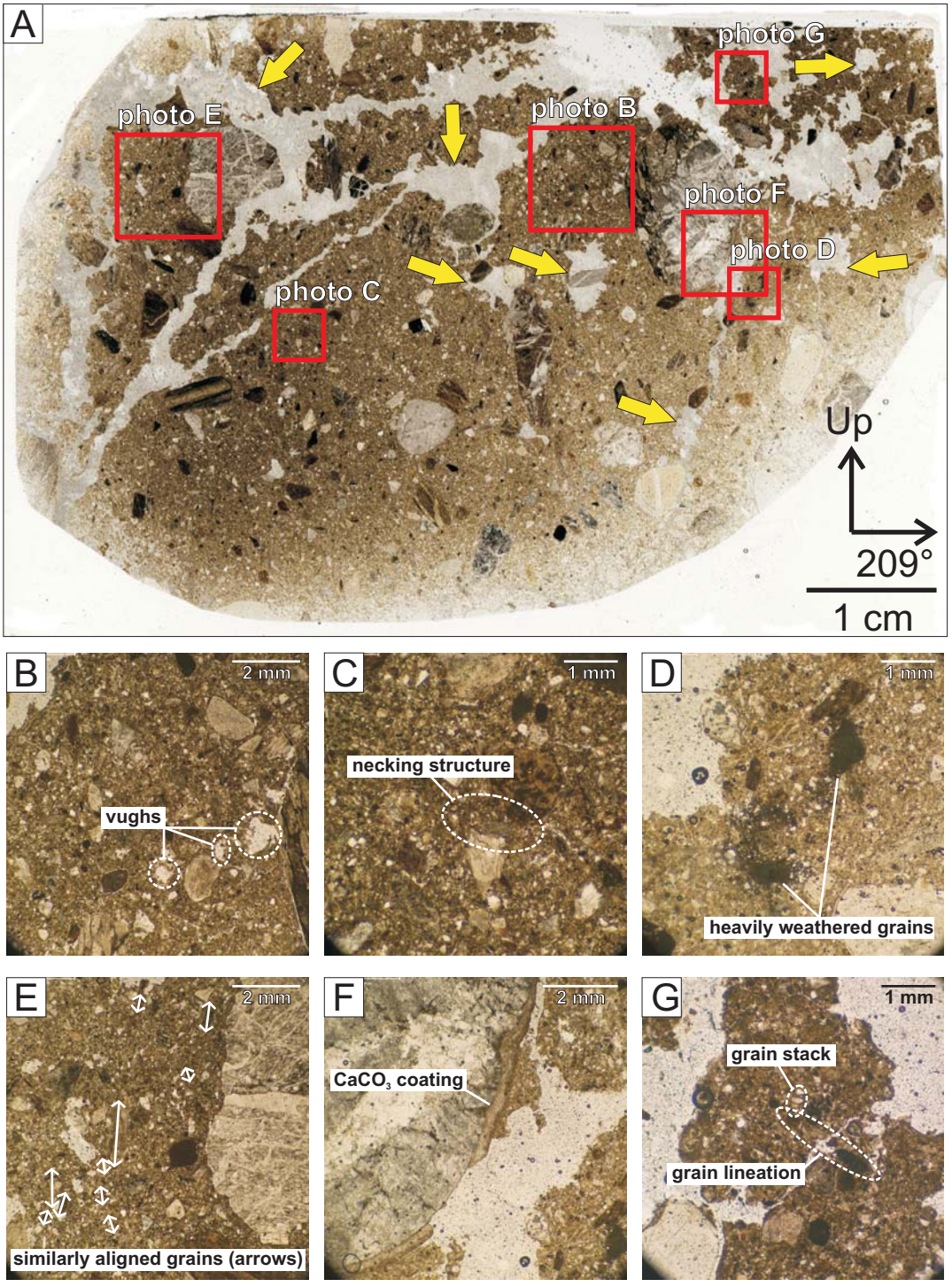

Figure 4.5-5. Thin section S6F27v. A) 2400 dpi scan of thin section showing large vughs and planar voids (yellow arrows). The locations of microphotographs B, C, D, E, F and G are indicated by red squares. Microphotographs show vughs (B), a necking structure (C), heavily weathered grains (D), similarly aligned grains (E), calcium carbonate precipitate (F), a grain stack (G) and a turbate (G).

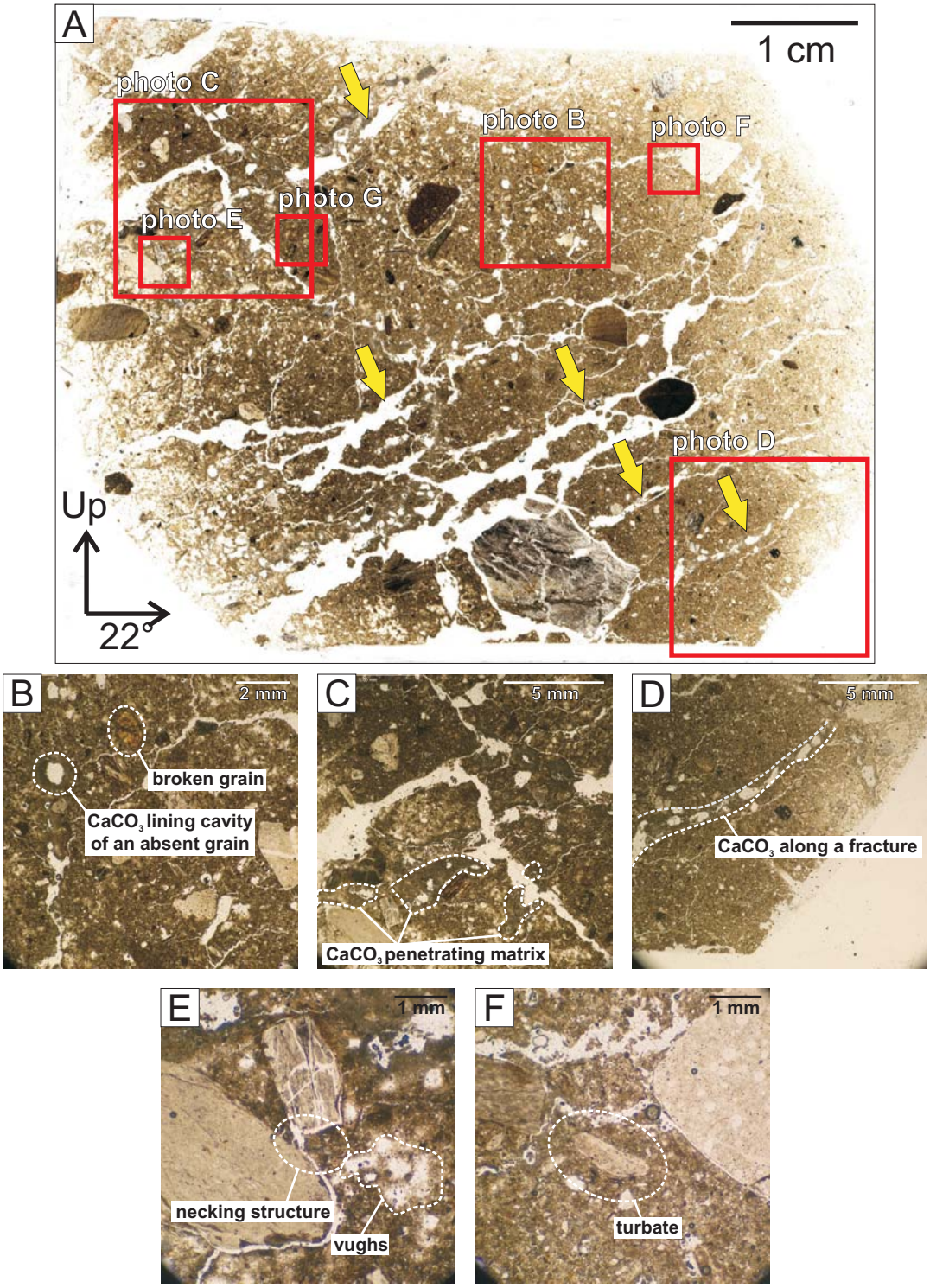

Figure 4.5-6. Thin section S6F33v. A) A 2400 dpi scan of the thin section showing subparallel planar voids (yellow arrows). The locations of microphotographs B, C, D, E, and F are indicated by red squares. Microphotographs show a broken grain (B), calcium carbonate precipitate (B, C, D), a necking structure (E), vughs (E), and a turbate (F).

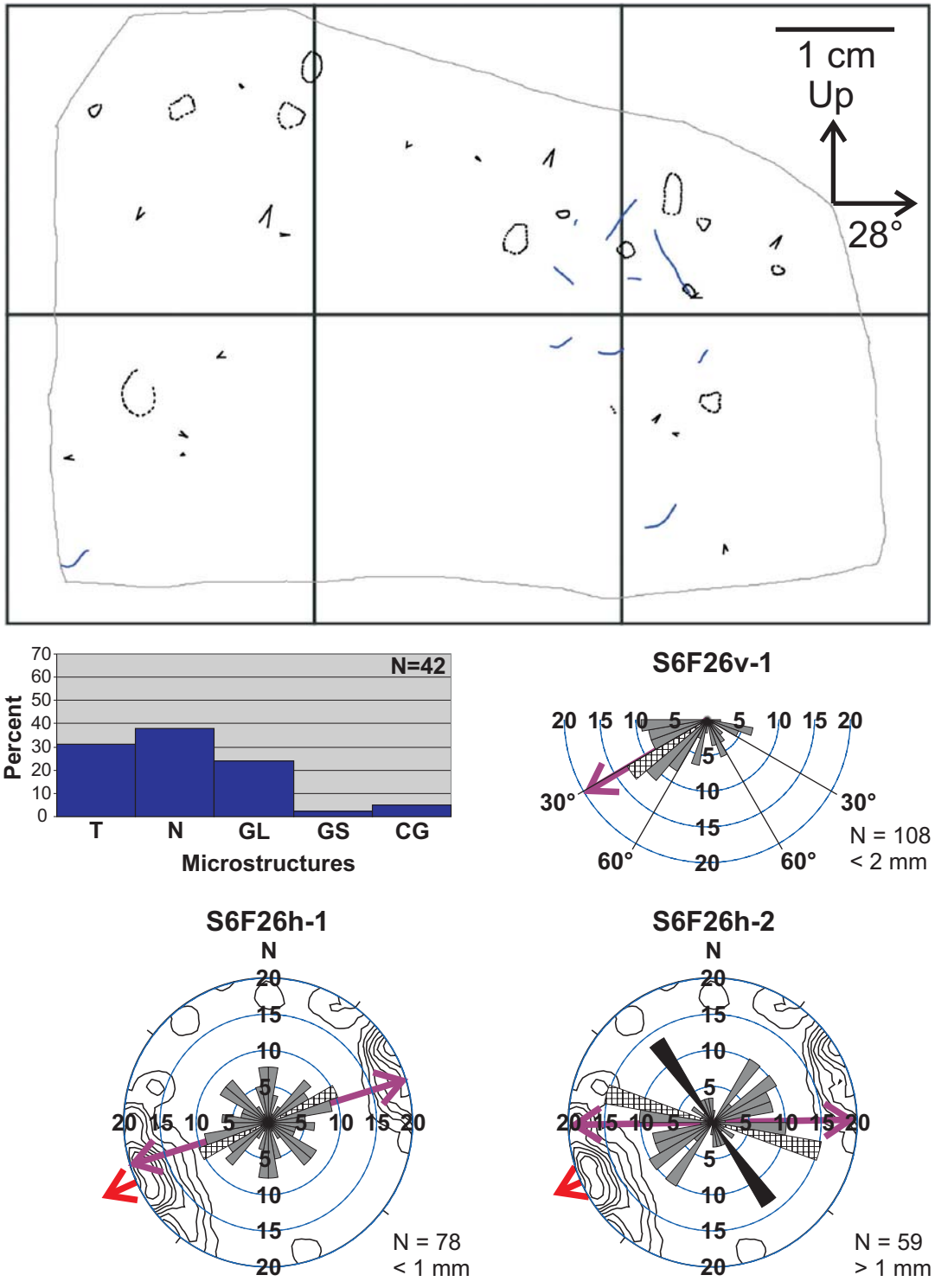

Figure 4.5-7. Microfabrics S6F26v-1, S6F26h-1 and S6F26h-2, and microstructure map and frequency histogram for thin section S6F26v. See Figures 3.3-4 and 3.3-5 for legends.

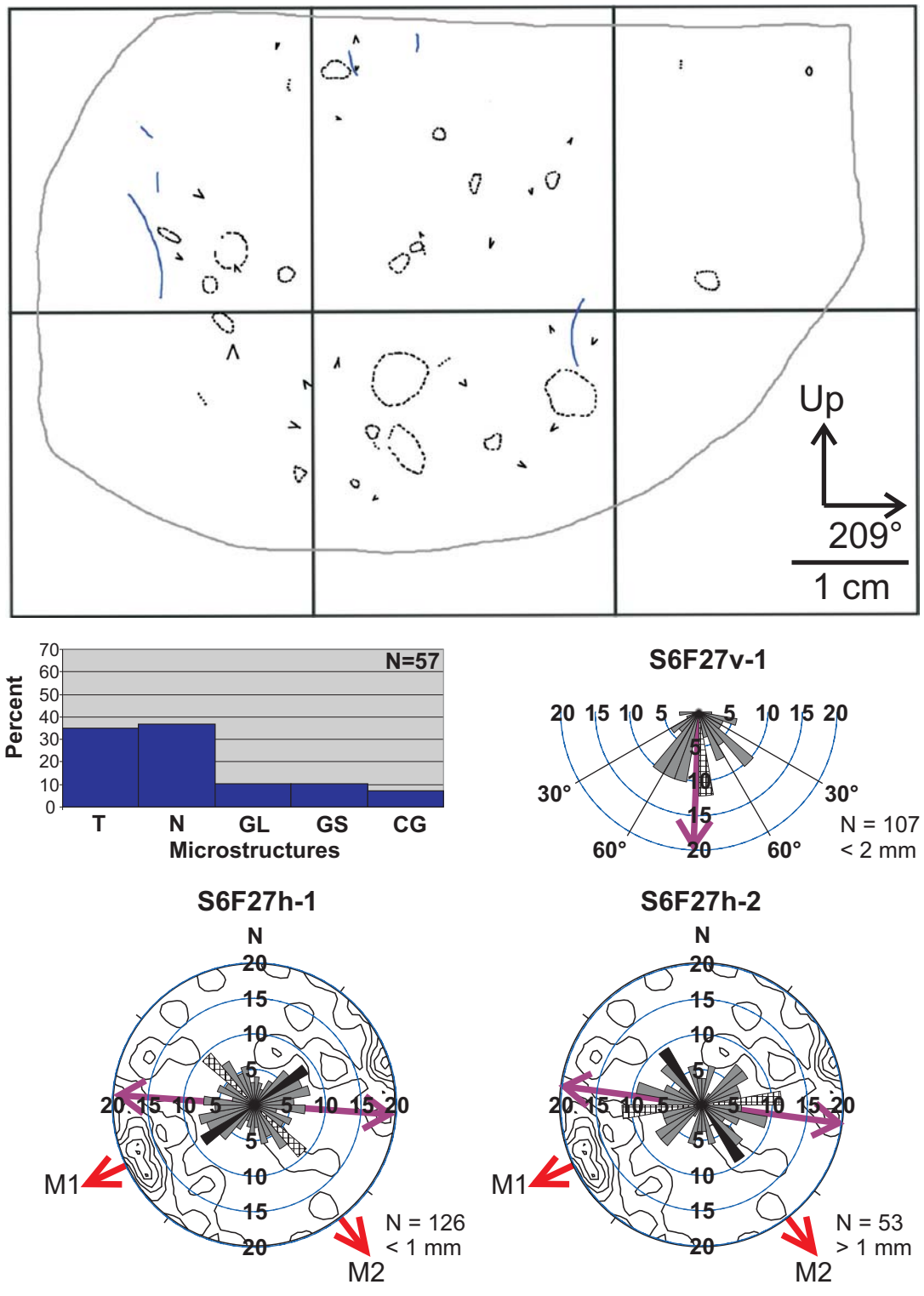

Figure 4.5-8. Microfabrics S6F27v-1, S6F27h-1 and S6F27h-2, and microstructure map and frequency histogram for thin section S6F27v. See Figures 3.3-4 and 3.3-5 for legends.

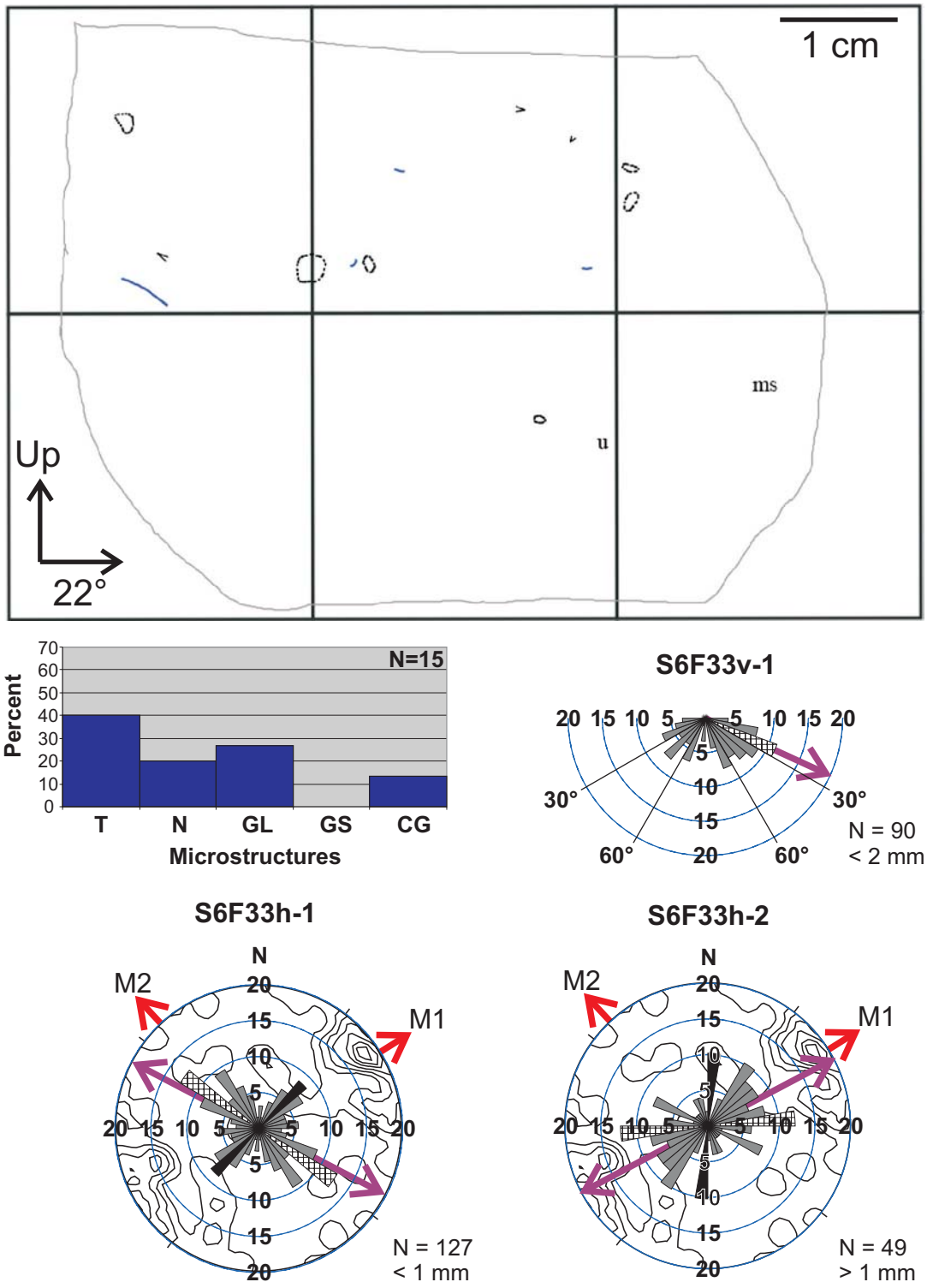

Figure 4.5-9. Microfabrics S6F33v-1, S6F33h-1 and S6F33h-2, and microstructure map and frequency histogram for thin section S6F33v. See Figures 3.3-4 and 3.3-5 for legends.

clusters, one oriented oblique to the primary mode of the macrofabric, and one oriented almost perpendicular to it. Both S6F26h-1 and S6F26h-2 have principal eigenvectors oriented within 30° of the macrofabric eigenvector (Fig. 4.5-7, Table 4.2-5).

Vertical microfabric S6F27v-1 shows that most grains are oriented subvertically. Grains comprising the tightest cluster have plunges of 50-90° (Fig. 4.5-8). Horizontal microfabrics S6F27h-1 and S6F27h-2 are spread with principal eigenvectors that differ from that of the macrofabric by ~30° (Fig. 4.5-8, Table 4.2-5). S6F27h-1 contains two clusters, one, subparallel to the principal eigenvector of the macrofabric, and the second, nearly transverse to it. The 10° class with the most measurements in S6F27h-2 is oriented subparallel to the principal eigenvector of the macrofabric. The peak of the second tightest cluster is oriented NW-SE (Fig. 4.5-8).

Vertical microfabric S6F33v-1 has a principal eigenvector almost orthogonal to the orientation of major planar voids (Figs 4.5-6A, 4.5-9). Grains with plunges between 10-70° form a spread out cluster with a peak containing grains that plunge 20-30° (Table 4.12-2). Horizontal microfabric S6F33h-1 is spread out, with a principal eigenvector obliquely oriented to the eigenvector of the macrofabric (Fig. 4.5-9). The cluster containing the most measurements is oriented subparallel to the secondary mode of F33. The second tightest cluster is oriented subparallel to the primary mode of F33. S6F33h-2 contains a single spread out distribution and a principal eigenvector that differs from that of the macrofabric by only 3° (Fig. 4.5-9, Table 4.2-5). The 10° class with the highest number of observations is considered to be the peak of the tightest cluster and is oriented within 30° of the principal eigenvector of the macrofabric. The peak of the second tightest cluster trends N-S (Fig. 4.5-9).

4.5.3 Interpretation

The diamicton at site 6 was previously interpreted as a deformed lodgement till (Lian and Hicock 2000). This diamicton has high silt content, contains clasts with abundant glacigenic wear features, and unimodal and spread bimodal clast fabrics with consistently oriented primary/only modes. These characteristics suggest that unit 1 is a subglacial till. The presence of facets, bullet noses and keels suggest that clasts in the diamicton were initially deposited by lodgement as suggested by Lian (1997) and Lian and Hicock (2000). The spread modes in F27 and F33, and the deformation structures (a fold and a shear plane) in exposure 1 suggest that the till experienced post-depositional deformation as suggested by Lian (1997) and Lian and Hicock (2000).

Bullet noses and fractured ends show no preferred direction. Either these features record clast re-orientation during ploughing or after lodgement at the ice-bed interface, or some or all of them have been inherited from an earlier time in the transport history of the pebbles.

The vast majority of the youngest clast upper surface striae identified at site 6 are oriented parallel to clast long axes (Table 4.2-3). This suggests that clast upper surface striae were formed during shear when clast long axes were aligned parallel to the shear direction. The bladed clasts that lie outside the main mode of F26 may reflect March-type rotation of clasts along a shear zone, where slip between the pebbles and the surrounding material causes wider, flatter clasts to take longer to point in the direction of shear than more prolate clasts (Glen *et al.* 1957; Drake 1974). This process may explain the lack of a-axis parallel striae on these clasts. The plunge direction of the principal eigenvectors of F26 and F27 are opposite to that at F33 suggesting that local paleo-slopes might be too variable to estimate ice-flow direction from clast attitude, alone.

Post-depositional compression and shear is evident from the fold and shear plane observed at exposure 1, and may be responsible for the difference in fabric strengths between F26 (located above the shear plane), and F27 (located below the shear plane near the fold) (Table 4.2-1). The strike and dip of the shear plane could not be measured in three dimensions; however the apparent alignment of the plane with the north-dipping limb of the fold suggests that the shearing event occurred either at the same time, or after the compression event. In two dimensions, the shear plane appears to be parallel to the local surface slope and may record a gravitational slump or glide down toward 287°.

Though fissility planes were not identified at the macroscale, the subparallel planar voids visible in thin sections S6F26v and S6F33v confirm fissility planes at the microscale. Skeletal grains in contact with these voids are not consistently aligned parallel to them, suggesting that they are not shear zones. Vertical microfabrics also suggest that the orientation of sand sized grains was not controlled or influenced by the development of the planar voids. Therefore fissility planes in the diamicton at site 6 may be attributed to post-depositional unloading of the sediment after ice retreat, or ice lens formation during freezing of the sediment in winter (van Vliet-Lanoë *et al.* 1984; Sveistrup *et al.* 2005). Horizontal microfabrics are surprisingly consistent with their macrofabric counterparts, and suggest that the processes responsible for the orientation

of the pebbles (i.e., March-type rotation of pebbles along shear zones or at the ice-bed interface) are also responsible for the orientation of the sand sized particles.

Evidence of porewater (glacial, meteoric and (or) groundwater) is evident from the calcite deposits, and likely facilitated the weathering of susceptible grains (e.g., Figure 4.5-5D). Though some calcite deposition occurred within planar voids, it was by no means confined to these areas, and most planar void walls appear relatively clean. This observation would suggest that the fissility planes were not hydraulically active (perhaps only widening during the sampling and thin section preparation process), or porewater pressure and temperature conditions were not conducive to the precipitation of solutes when they were hydraulically active.

The quantitative data suggests that, in general, grain rotation, squeeze flow, and discrete shear during deposition and deformation of the diamicton were more common processes than grain crushing and stacking. Although many argillite grains observed in thin section appeared as angular shards, subrounded and rounded grains were common among grains of limestone or volcanic lithologies. This suggests that different lithologies may have experienced different transport distances (the volcanic grains, for instance, were likely derived from the Fraser Plateau on the other side of the Marble Range, Fig. 3.1-1). The different grain lithologies also have distinct internal structures, strengths and hardnesses (cleavage planes were observed to be common in argillite rocks, for example), making some more susceptible to fracture than others. Thus, despite the frequency of angular argillite grains, qualitative and quantitative micro-scale observations suggest that inter-particle friction was limited during till deposition and subsequent deformation, and porewater facilitated more ductile type deformation and discrete shear events, such as those observed at the macroscale.

4.6 Site 60

4.6.1 Macroscale sedimentology and structural geology

Site 60 is located on the NE side of Jesmond valley, ~0.5 km south of a small NE-SW trending tributary valley draining the Marble Range (Fig. 3.1-1). Two exposures were studied (exposures 1 and 2, Figs 4.6-1, 4.6-2). Exposure 1 (referred to as site 4 in Lian 1997, and as site 60 in Lian and Hicock 2000), is in a road cut on the NE side of Jesmond Road. Exposure 2 is ~200 m down a logging road that runs behind and above exposure 1. Due to inaccessibility, geological measurements and diamicton samples were not collected from exposure 1.

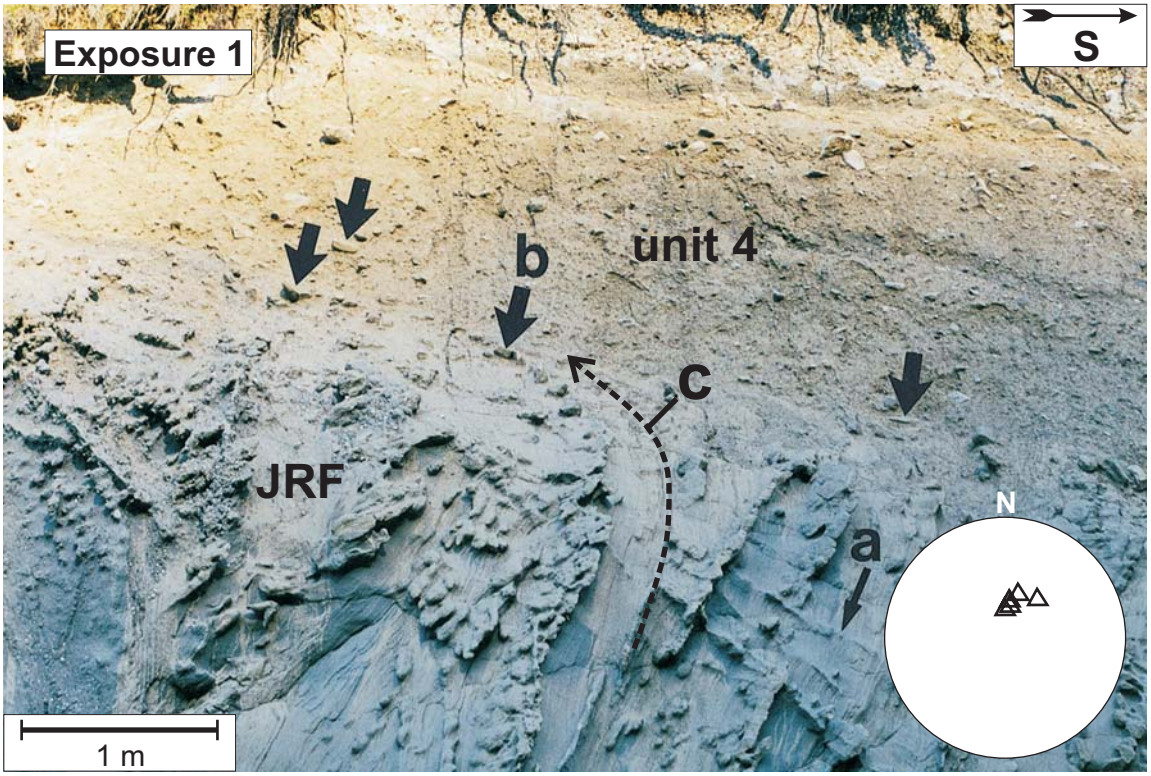

Figure 4.6-1. Site 60, exposure 1 (site 4 in Lian (1997)) showing unit 4. The diamicton in this exposure is considered to be equivalent to unit 4 in exposure 2. 'a' points to shears previously measured to be dipping to the SW, 'b' points to imbricated sandstone blocks from the Jesmond valley formation (JRF) that have been entrained into the overlying diamicton, and 'c' points to folds in the JRF. SW dipping shears are plotted as poles to planes in the stereogram. (Photograph and stereogram data source: Lian and Hicock 2000, by permission. © 2000 Elsevier Science Ltd. and INQUA).

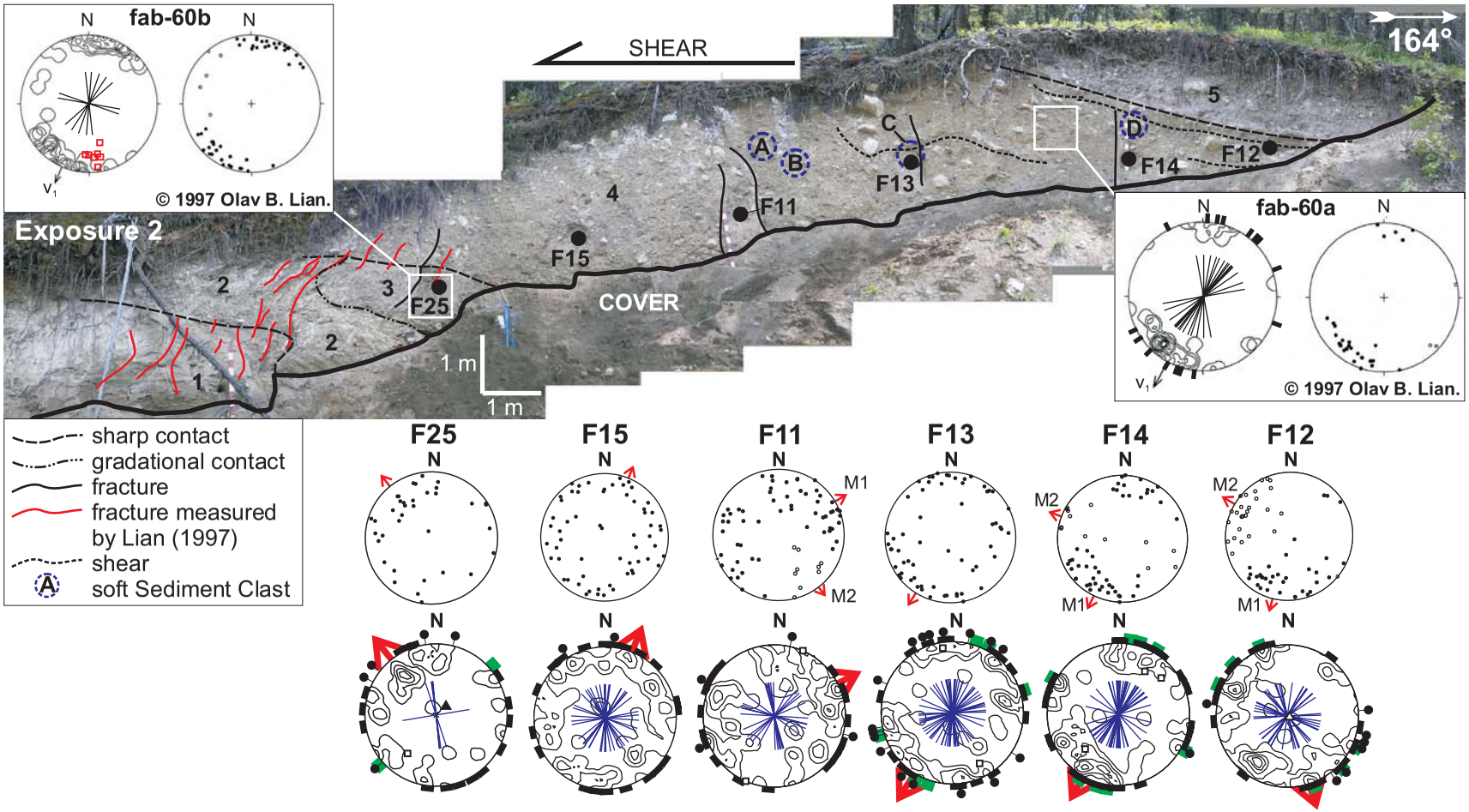

Figure 4.6-2. Site 60, exposure 2 showing units 1 (horizontally bedded and rippled sand), 2 (interbedded pebbly sand and gravel), 3 (massive, clast-poor diamicton), 4 (massive, clast-rich diamicton) and 5 (sandy gravel). Shears and fractures are plotted on the contour stereogram of the fabric they are closest to on the exposure. Only those that are visible from the base of the exposure are annotated in the photograph. The contact between units 3 and 4 was measured and plotted as a shear plane on the stereogram of F25 (black triangle). The positions of indurated sediment clasts A, B, C and D (shown in Fig. 4.6-2) are indicated with a blue dashed circle. The approximate position of Lian's (1997) fab-60a and fab-60b (stereograms reprinted with permission) is indicated by white boxes. The red squares on the stereogram of fabric 60b represent a group of fractures (red lines) measured by Lian (1997, p. 204). See Figure 3.3-1 for stereogram legend.

At exposure 1, diamicton directly overlies the Jesmond Road formation (JRF) (Lian 1997) (Fig. 4.6-1). This diamicton is similar in colour and clast concentration (visual estimate) to unit 4, exposure 2 (described below) and is considered here and by Lian (1997) and Lian and Hicock (2000) to be part of the same unit. At exposure 1, shear planes in the Jesmond Road formation were measured by Lian (1997) and dip SW (Fig. 4.6-1). Blocks of sandstone, excavated from the JRF, and have been entrained into the diamicton. The folded strata at the base of the diamicton and the imbrication of the sandstone blocks within the diamicton indicate a northward shear direction (Fig. 4.6-1).

Exposure 2 contains 5 units (Fig. 4.6-2). Unit 1 is a package of horizontally bedded and cross-laminated medium to coarse sand with a minimum thickness of 1 m. Unit 1 is truncated by interbedded pebbly sand and pebble-gravel (unit 2), which grade both vertically and laterally into the diamicton that constitutes unit 3. Unit 3 is a massive, matrix-supported silty sand diamicton (Fig. 4.2-2), with a clast concentration of 10% (Table 4.2-1).

Unit 4 is a consolidated, massive, matrix-supported, silty sand diamicton (Fig. 4.2-2) with a minimum thickness of 2 m and a sharp lower contact. The clast concentration in unit 4 ranges from 14-26% (Table 4.2-1). Four indurated sediment clasts were found in this unit, two located between F11 and F13 (A & B), one within the sampling area of F13 (C), and one ~0.5 m above F14 (D) (Figs 4.6-2, 4.6-3). These clasts, though indurated, break apart when they are dropped onto the ground, are tapped with a geologic hammer, or are exposed to small shear stresses, (e.g., the clast edges will crumble and (or) fracture if rubbled vigorously by hand).

Sediment clasts A and C are composed of indurated, pale yellow (Munsell colour 2.5Y 7/2) pebbly silt and have an apparent b-axis length of ~3 cm (Fig. 4.6-3). Blocks of indurated, pebbly silt of a similar colour (Munsell colour 2.5Y 7/2) has been identified in colluvium at the base of exposure 1. Clast A is subrounded and contains ~30% subangular to subrounded pebbles. Clast C is well rounded and contains ~10% subangular to subrounded pebbles. Clast B is angular, has an apparent b-axis length of ~2 cm and is composed of grey, indurated laminated silt and sand. The Munsell colour of clast B could not be measured due to inaccessibility. Sediment clast D is the largest sediment clast observed in unit 4 (~20 cm apparent b-axis length), and is rounded, light gray (Munsell colour 10YR 7/2) and consists of indurated massive, partially oxidized, pebbly, medium sand. A highly oxidized steeply dipping pebble layer is visible on the

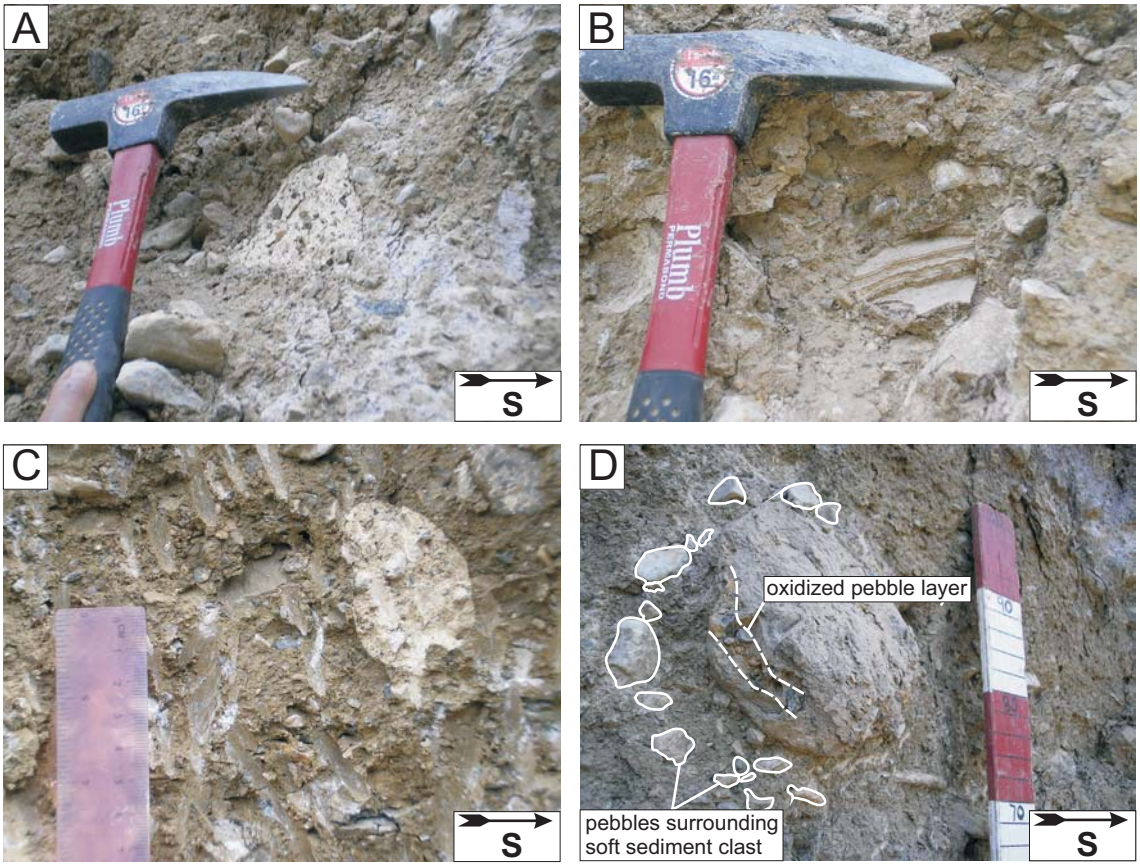

Figure 4.6-3. Indurated sediment clasts found in unit 4, site 60. Photographs A-D correspond to clasts A-D labelled in Figure 4.6-2. Sediment clasts A and C are composed of a light yellow massive pebbly silt. Sediment clast B is composed of laminated silt and sand. Sediment clast D consists of pebble-sized clasts suspended in massive, partially oxidized sand. The head of the geologic hammer is 6 cm wide. The right margin of the ruler in photograph C is subdivided into centimetre subdivisions. The metre stick in photograph D is subdivided into red and white decimetre subdivisions.

underside of the clast, and a concentration of pebbles (~1-2 cm apparent b-axis lengths) within the surrounding diamicton curves around the edge of the clast on its north facing side (Fig. 4.6-3). The Munsell colour and hardness of sediment clast D is identical to that of fine, medium and coarse sand beds observed in the JRF in exposure 1. The contacts between all sediment clasts and the surrounding diamicton are sharply defined; there is no evidence of deformation or mixing with the surrounding diamicton.

Unit 4 underlies a weakly bedded coarse sandy cobble-boulder gravel unit (unit 5) with a moderately sharp lower contact (apparent dip ~13° down to the S, Fig. 4.6-2). This study focussed on the character of units 3 and 4 and the geological structures within and below them.

Ten fractures and shears were measured throughout units 3 and 4, exposure 2. Due to the homogeneity of the diamicton, the presence or amount of displacement along planar discontinuities could not be determined. Therefore, because tension fractures are typically steeper than shear planes (Lian 1997; Lian and Hicock 2000), steeply dipping planes are classified as fractures, whereas planes with shallow dips are considered to be shear planes (Fig. 4.6-1). This rather arbitrary classification may not be the reality, however, and should be treated with caution. Shear planes in exposure 2 contain ~2 cm thick zones of massive medium sand.

Fractures and shears in close proximity to clast fabric measurement sites are shown in the contour stereograms in Figure 4.6-2. Only major fractures and shears (i.e., those that are long enough to be visible from the logging road) were annotated in Figure 4.6-2. Some fractures and shears that are annotated in the photograph of Figure 4.6-2 could not be measured due to inaccessibility or difficulties in identifying a planar surface. Those fractures annotated in red were measured by Lian (1997) and are plotted on the stereogram of fabric 60b. Because a sand layer is present at the contact between units 3 and 4, the contact is interpreted as a shear plane and is plotted as such on the stereogram of F25 (black filled triangle). Fracture orientations for the entire exposure have strikes trending ~ESE-WNW to SE-NW. The shear plane near F12, and the contact between units 3 and 4 near F25, both have shallow dips down to the SW (Fig. 4.6-2). Two shear planes in the upper half of unit 4 could not be measured but have apparent dips to the SE.

In exposure 2, one clast fabric (F25) was measured in unit 3, and five clast fabrics (F11, F12, F13, F14 and F15) were measured in unit 4 to capture vertical and (or) lateral changes in fabric modality, strength, and in the orientation of glacigenic clast

wear features (Fig. 4.6-2). F25 was measured ~0.30 m below the upper contact of unit 3, near the vicinity of Lian's (1997) fabric 60b (Fig. 4.6-2). It contains a multimodal to girdle-like distribution with a NW plunging principal eigenvector (Fig. 4.6-2, Table 4.2-1). Few clasts have striae, but most follow the orientation of clast a-axes (Table 4.2-3). One keel was identified on the bottom of a SW plunging clast (Table 4.2-3). Fractured ends show no preferred direction, and most bullet noses point toward the NW. Out of all clasts in the sample, 42% have facets (Table 4.2-3). Lian (1997) describes fabric 60b as being unimodal with five outliers and a principal eigenvector that points to the SW. Clast lee ends in fabric 60b show no preferred direction.

F15 is girdled with a NE plunging principal eigenvector (Fig. 4.6-2, Table 4.2-1). Striae on clast tops follow the orientation of clast a-axes, and 5% of clasts have upper surface striae with multiple orientations. Out of all clasts in the sample, ~7% have striae that curve around convexities and (or) concavities (Table 4.2-3). One keel was identified, but it was located on the top of the clast (Table 4.2-3). Fractured ends and bullet noses show no preferred direction. Faceted clasts comprise 27% of the sample (Table 4.2-3).

F11 exhibits a spread bimodal distribution with a primary mode trending NE-SW and a secondary mode trending NW-SE (Fig. 4.6-2, Table 4.2-2). Striae on clast tops show variable orientations with respect to N, but most follow the orientation of clast a-axes. Out of all clasts in the sample, 3% have upper surface striae with multiple orientations (Table 4.2-3). No keels were identified (Table 4.2-3). Fractured ends and bullet noses show no strongly preferred direction; they are very spread out in the eastern and western hemispheres of the stereogram (Fig. 4.6-2). Only 12% of clasts have facets (Table 4.2-3).

F13 consists of a single very spread out mode trending NE-SW (Fig. 4.6-2, Table 4.2-1). The orientations of striae and keels on clast bottoms are variable, but generally follow the orientation of the spread mode. All striae are aligned with clast a-axes, 5% of clasts have upper surface striae with multiple orientations, and 5% of clasts have striae curving around convexities and (or) concavities (Table 4.2-3). Fractured ends and bullet noses show no preferred direction. Faceted clasts comprise 35% of the sample and clasts with keels comprise 10% of the sample (Table 4.2-3).

F14 was measured in close proximity to Lian's (1997) fabric 60a (fab-60a, Fig. 4.6-2). F14 is spread bimodal with a primary mode trending NE-SW and a secondary transverse mode (Fig. 4.6-2, Table 4.2-2). Most striae sets on clast tops follow the

orientation of clast a-axes, and 5% of clasts have upper surface striae with multiple orientations (Table 4.2-3). Keels on clast bottoms follow the orientation of the primary mode. Fractured ends and bullet noses show no preferred direction. Out of all clasts in the sample, 38% are faceted and 7% have keels (Table 4.2-3). Lian (1997) describes fabric 60a as unimodal with three outliers. Clast fractured ends in fabric 60a show no preferred direction.

F12 was measured ~20 cm below the lower contact of unit 5 (Fig. 4.6-2). The majority of clasts plot in the WSW half of the stereogram, with three clasts plotting close to the NE margin. A break in the contours in the southeastern section of the stereogram might justify subdividing the plot into two spread-out orthogonal modes (Fig. 4.6-2). Two modes delineated in this way are statistically significant at the 95% confidence level (Table 4.2-2). Most striae on clast tops are aligned with clast a-axes (Table 4.2-3), but show no preferred orientation (Fig. 4.6-2). Out of all clasts in the sample, 10% have striae on their upper surfaces with multiple orientations (Table 4.2-3). Clasts with keels on their bottoms have a-axes trending NW-SE. Fractured ends show no preferred direction, but bullet noses generally point to the SE. Faceted clasts comprise 23% of the sample, and clasts with keels comprise 7% of the sample (Table 4.2-3). For all clast fabrics, particular clast shapes do not conform to predefined modes, or prefer any specific orientation (Fig. B-1, Appendix B).

Unit 5 is 1-2 m of weakly bedded, poorly sorted pebble-cobble gravel and sand that contains the occasional boulder. It has a sharp lower contact and overlies unit 4 in both exposure 1 and 2.

4.6.2 Cobble and boulder striae measurements

Striae sets (114) preserved on the tops of 30 cobbles and boulders (mostly limestone) were measured within the upper half of unit 4; few cobbles and boulders were accessible in the lower part of the unit (Fig. 4.6-4). Because the orientations of the youngest striae sets were desired, only the faintest striae sets, (i.e., those which presumably would have been eroded during subsequent shearing events) were measured on each clast.

Two groups of stones (groups 1 and 2) are plotted separately to detect any trends in striae orientation related to shear planes. Group 1 is located below the lowest subhorizontal shear plane, and group 2 is located above it (Fig. 4.6-4). The striae from each group of stones are plotted on two circular diagrams (raw data (a), and circular

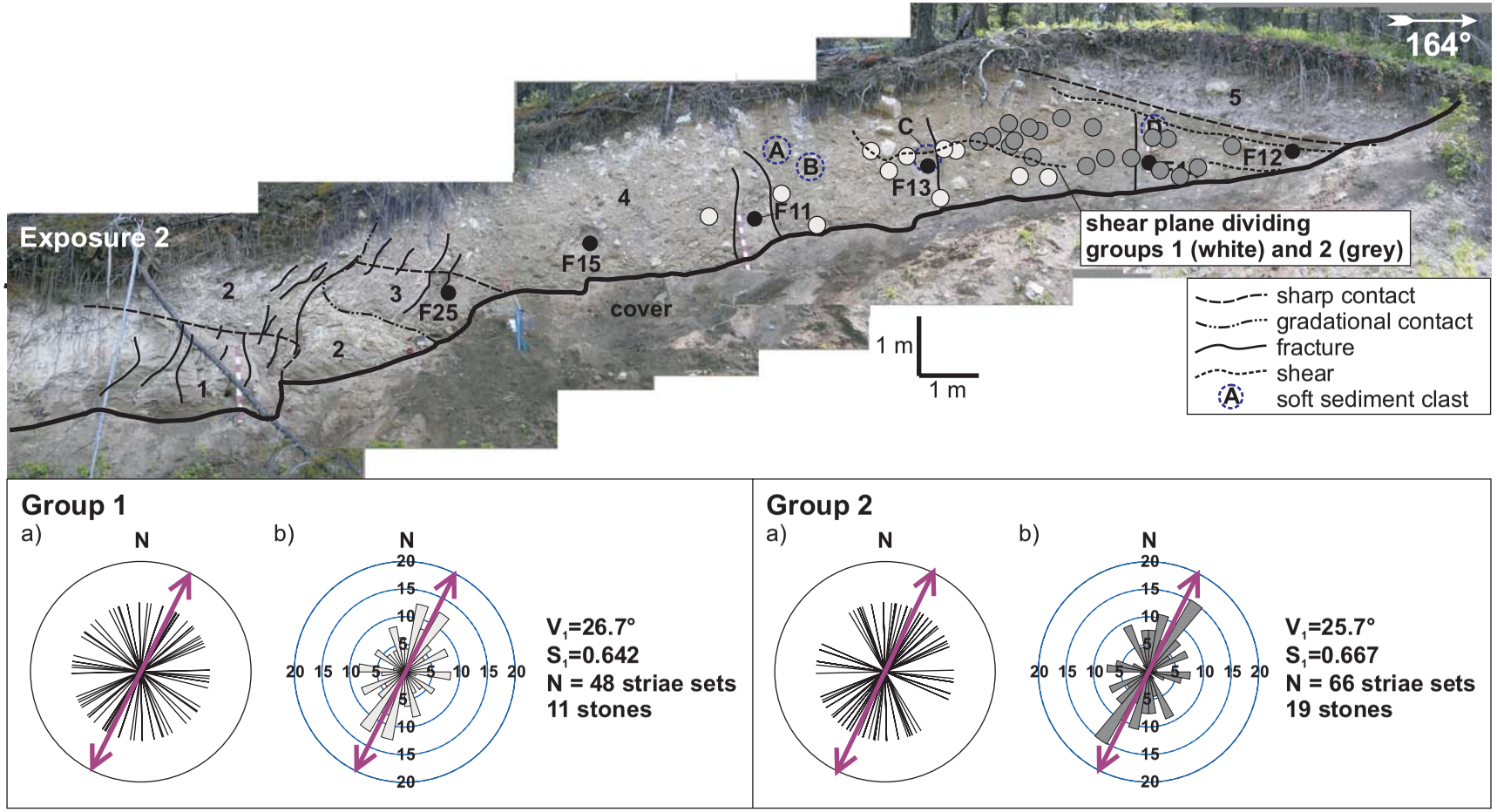

Figure 4.6-4. Striae measurements from two groups of boulder and cobble-sized clasts in unit 4, site 60 (exposure 2) . Striae sets are plotted both as raw data (one line per striae set) (a), and as a circular frequency distribution with a 10° class interval (b). Purple bidirectional arrows represent principal eigenvectors (V_1). Concentric circles on the rose diagrams are numbered as percentages of the total number of striae sets measured (N). Rose diagrams are shaded to match the circles on the photograph, which indicate individual stone locations in the face. Stones located below (group 1) and above (group 2) the shear plane above F13 (annotated) are plotted separately and show no differences in boulder-cobble striae orientation.

frequency histogram (rose diagram) with 10° classes (b), Fig. 4.6-4). Eigenstatistics for 2-dimensional data are presented for each group (Fig. 4.6-4). In both groups 1 and 2, the tightest clusters are oriented NNE-SSW and are subparallel to the principal eigenvector (Fig. 4.6-4).

4.6.3 Micromorphology

Four samples were collected within unit 4 for thin section preparation. These were collected at F15, F11, F13 and F14. One vertical and one horizontal thin section were cut from each sample and these are named S60F15h, S60F15v, S60F11h, S60F11v, S60F13h, S60F13v, S60F14h and S60F14v. In all thin sections, the diamicton is dominated by subangular to subrounded limestone and metasedimentary skeletal grains, and fewer smaller subrounded to rounded volcanic grains (Figs 4.6-5A, 4.6-6A, 4.6-7A, 4.6-8A). In general the diamicton appears plasma supported, except for a sand inclusion on the left side of section S60F13v (Fig. 4.6-7B). Some areas within the thin sections contain similarly aligned (subparallel) elongate grains (Fig. 4.6-6B).

Major fractures and voids show no systematic pattern or preferred orientation within any of the thin sections, and sections S60F14v and S60F15v have larger, more frequent fractures and voids than S60F11v and S60F13v (Figs 4.6-5A, 4.6-6A, 4.6-7A, 4.6-8A). A series of minor fractures in the lower right part of section S60F15v have a steep apparent dip toward 165° azimuth (Fig. 4.6-5D). All thin sections have vughs that follow fractures, or occur in isolation within the matrix, and smaller vughs (< 1 mm wide) are particularly abundant in areas where uneven hand grinding has reduced the thin section thickness (e.g., Figs 4.6-5B, 4.6-8E). Precipitates are not abundant, but do occur in sections S60F13v and S60F14v in the form of grey patches (calcium carbonate?) within the matrix (Fig. 4.6-7C) and around skeletal grains (Fig. 4.6-7D). Calcium carbonate deposition appears to have occurred within the matrix surrounding the sand inclusion in section S60F13v (Fig. 4.6-7C). Parts of the matrix in section S60F15v have a reddish-brown patchy appearance (Fig. 4.6-5C).

Sections S60F14v and S60F15v have 31 and 49 microstructures, respectively, which consist of abundant turbates (Figs 4.6-8F; 4.6-8G), necking structures (Fig. 4.6-5E) and grain lineations (Fig. 4.6-8D), and fewer grain stacks (Figs 4.6-5F, 4.6-8C) and crushed grains (Figs 4.6-5G, 4.6-8B, 4.6-9, 4.6-12). Sections S60F11v and S60F13v have a higher number of visible discrete microstructures (73 and 79 respectively), and are dominated by turbates (Figs 4.6-6E, 4.6-7E, 4.6-10, 4.6-11). The relative distribution

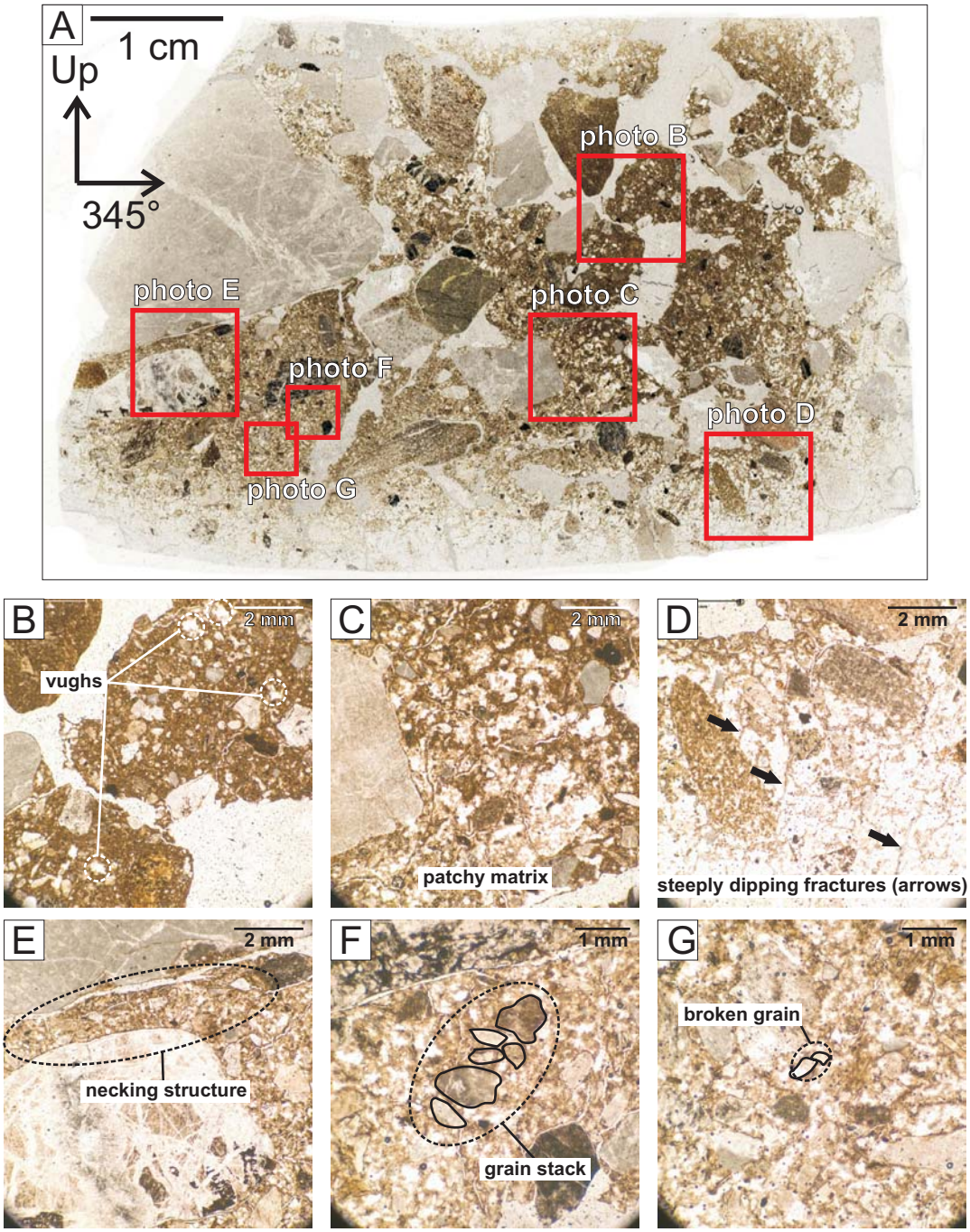

Figure 4.6-5. Thin section S60F15v. A) A 2400 dpi scan of the thin section. The locations of microphotographs B, C, D, E, F and G are indicated by red squares. Microphotographs show vughs (B), an opaque residue creating a patchy matrix (C), steeply dipping fractures (D), a necking structure (E), a grain stack (F), and a broken grain (G).

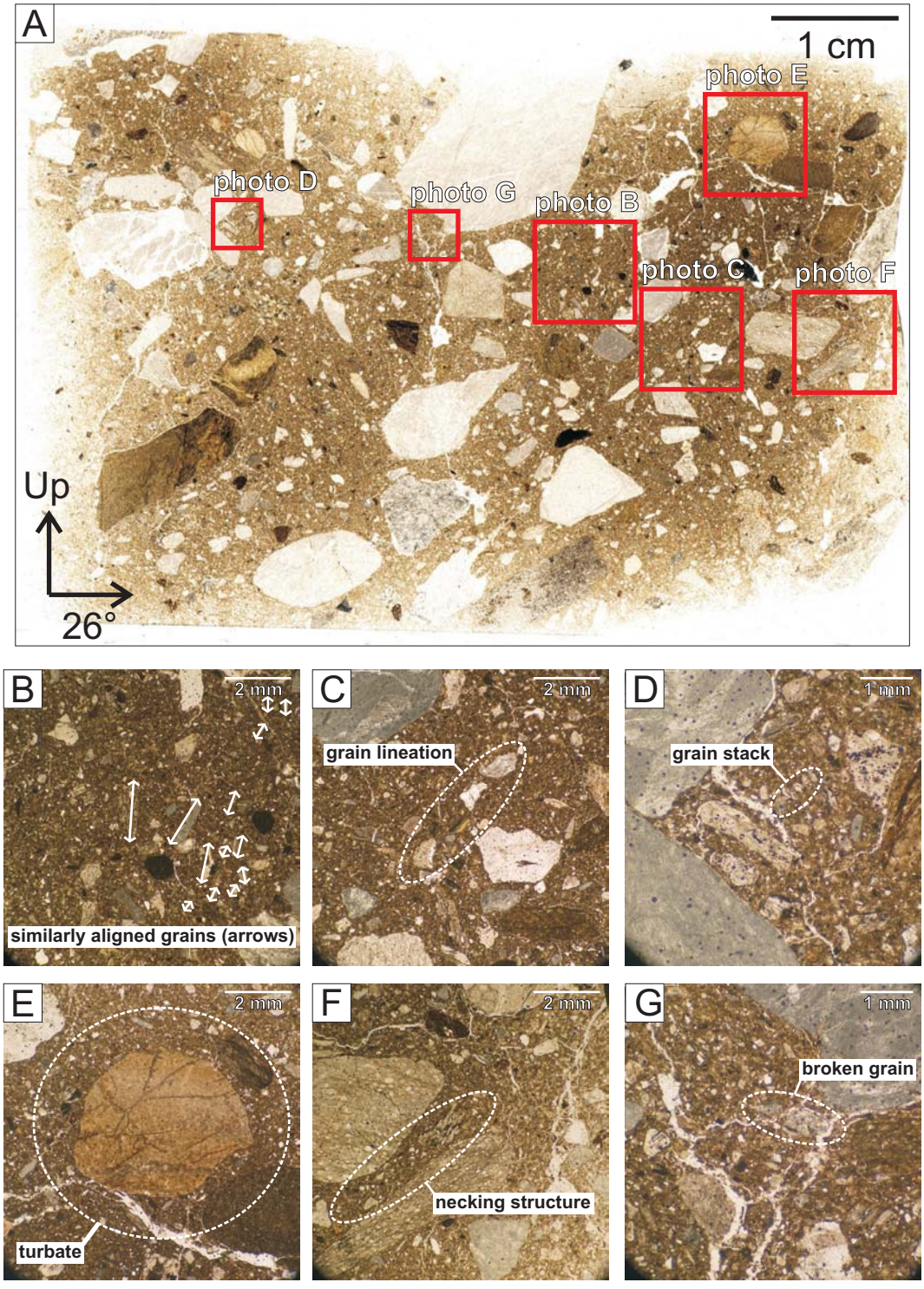

Figure 4.6-6. Thin section S60F11v. A) A 2400 dpi scan of the thin section. The locations of microphotographs B, C, D, E, F and G are indicated by red squares. Microphotographs show similarly aligned grains (B), a grain lineation (C), a grain stack (D), a turbate (E) a necking structure (F) and a broken grain (G).

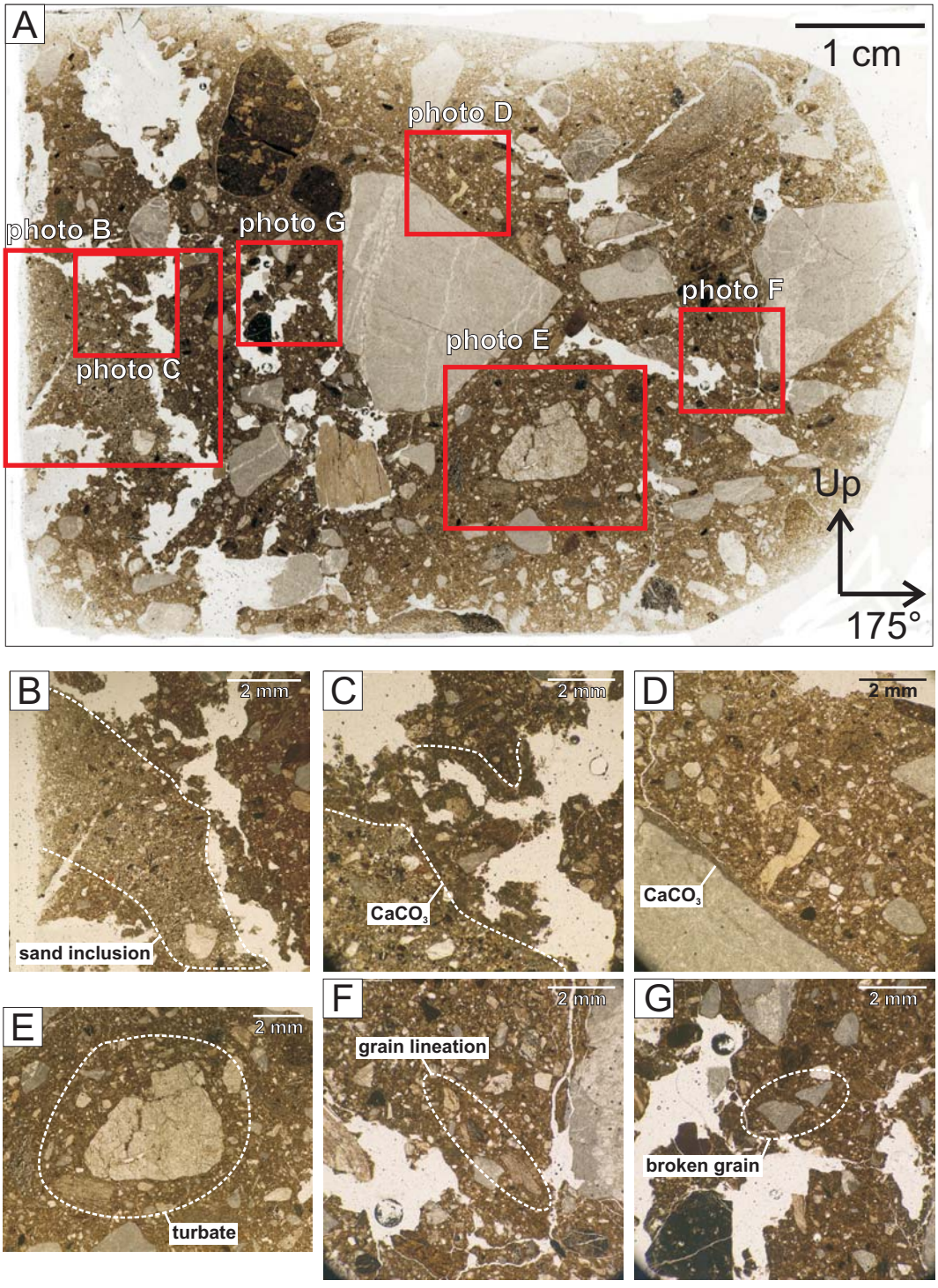

Figure 4.6-7. Thin section S60F13v. A) A 2400 dpi scan of the thin section. The locations of microphotographs B, C, D, E, F and G are indicated by red squares. Microphotographs show a sand inclusion (B), calcium carbonate precipitate in the matrix (C), calcium carbonate coating a grain (D), a turbate (E) a grain lineation (F) and a broken grain (G).

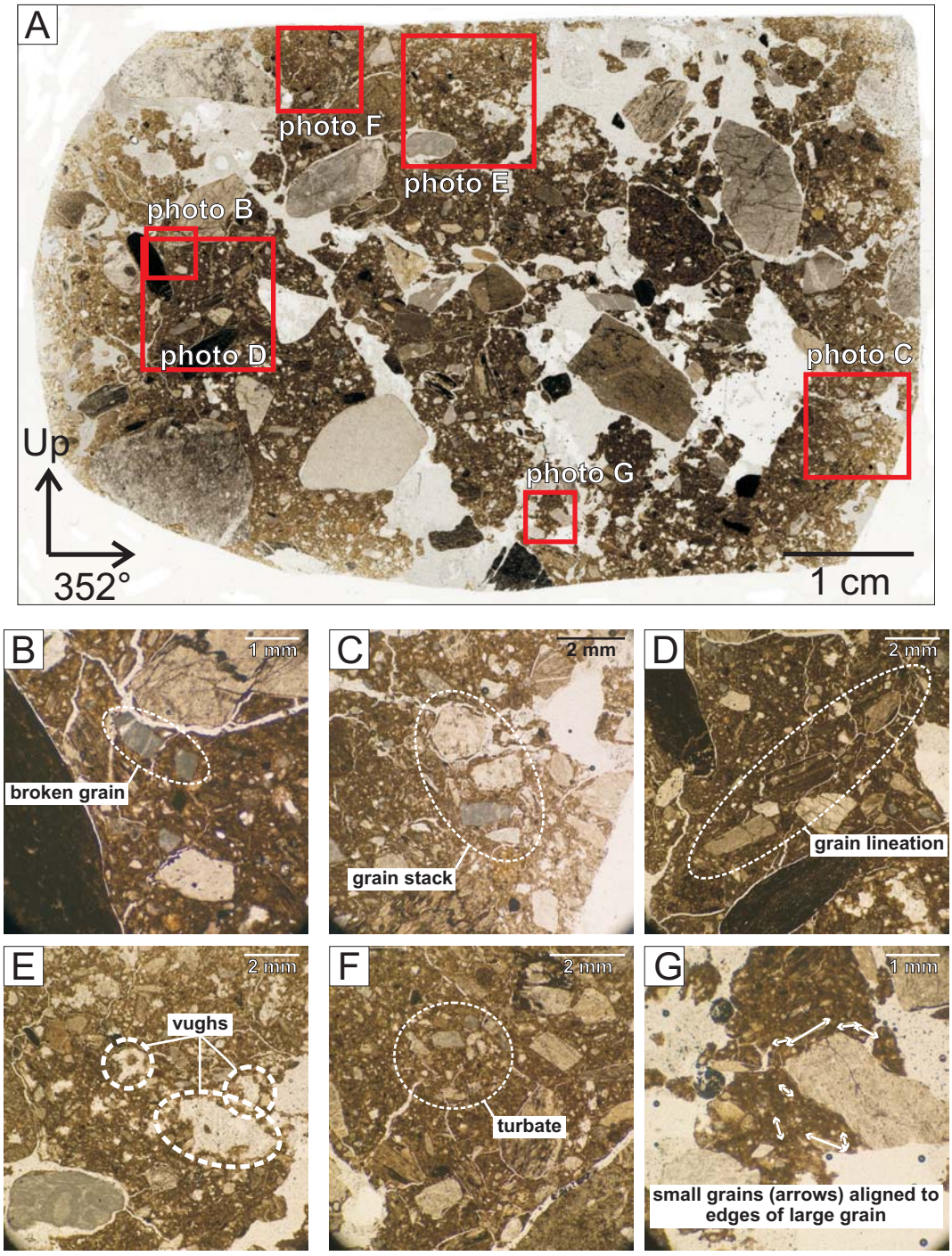

Figure 4.6-8. Thin section S60F14v. A) A 2400 dpi scan of the thin section. The locations of microphotographs B, C, D, E, F and G are indicated by red squares. Microphotographs show a broken grain (B), a grain stack (C), a grain lineation (D), vughs (E), a turbate (F) and small grains that are aligned to the edges of a large grain (G).

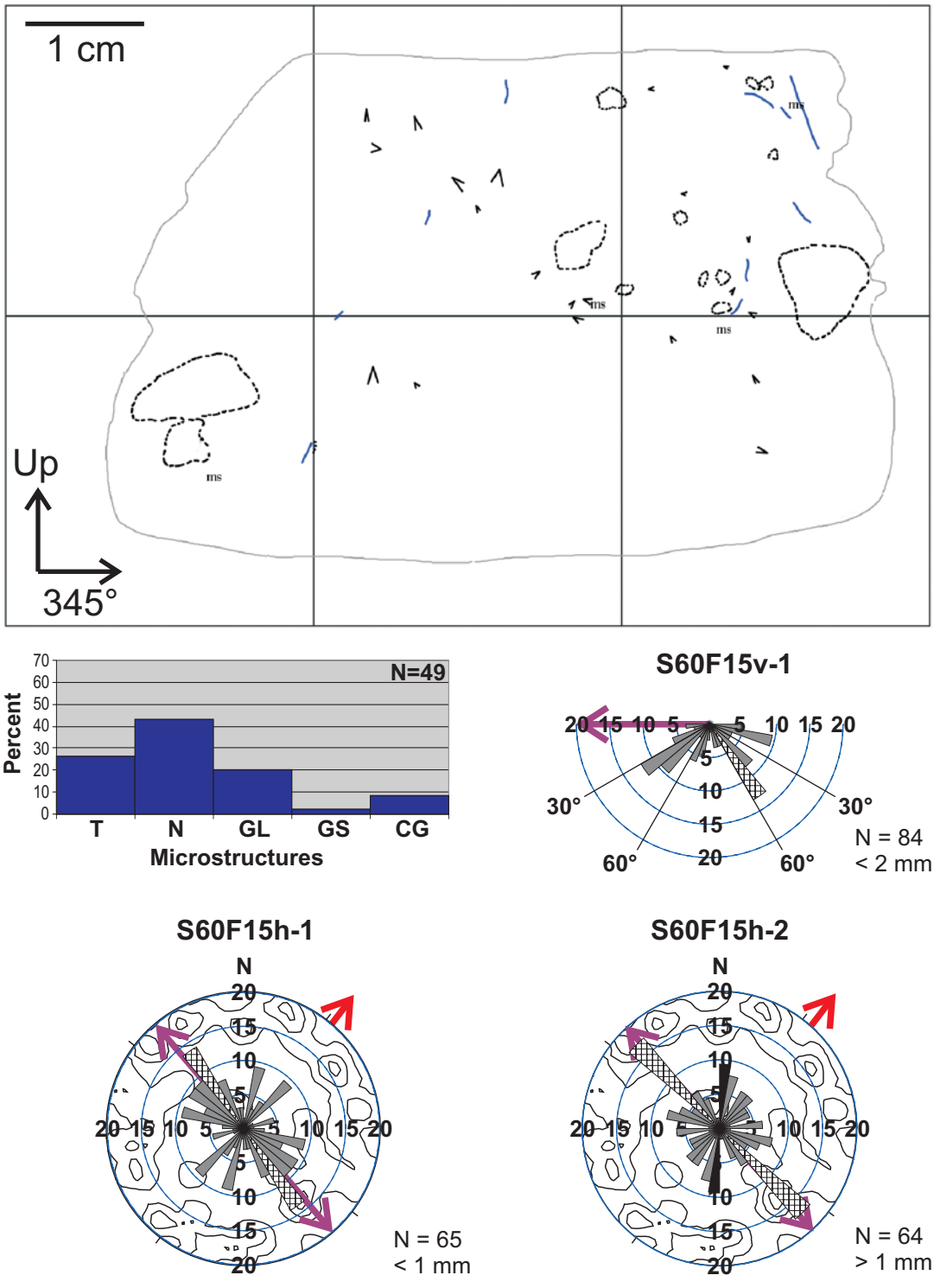

Figure 4.6-9. Microfabrics S60F15v-1, S60F15h-1 and S60F15h-2, and microstructure map and frequency histogram for thin section S60F15v. See Figures 3.3-4 and 3.3-5 for legends.

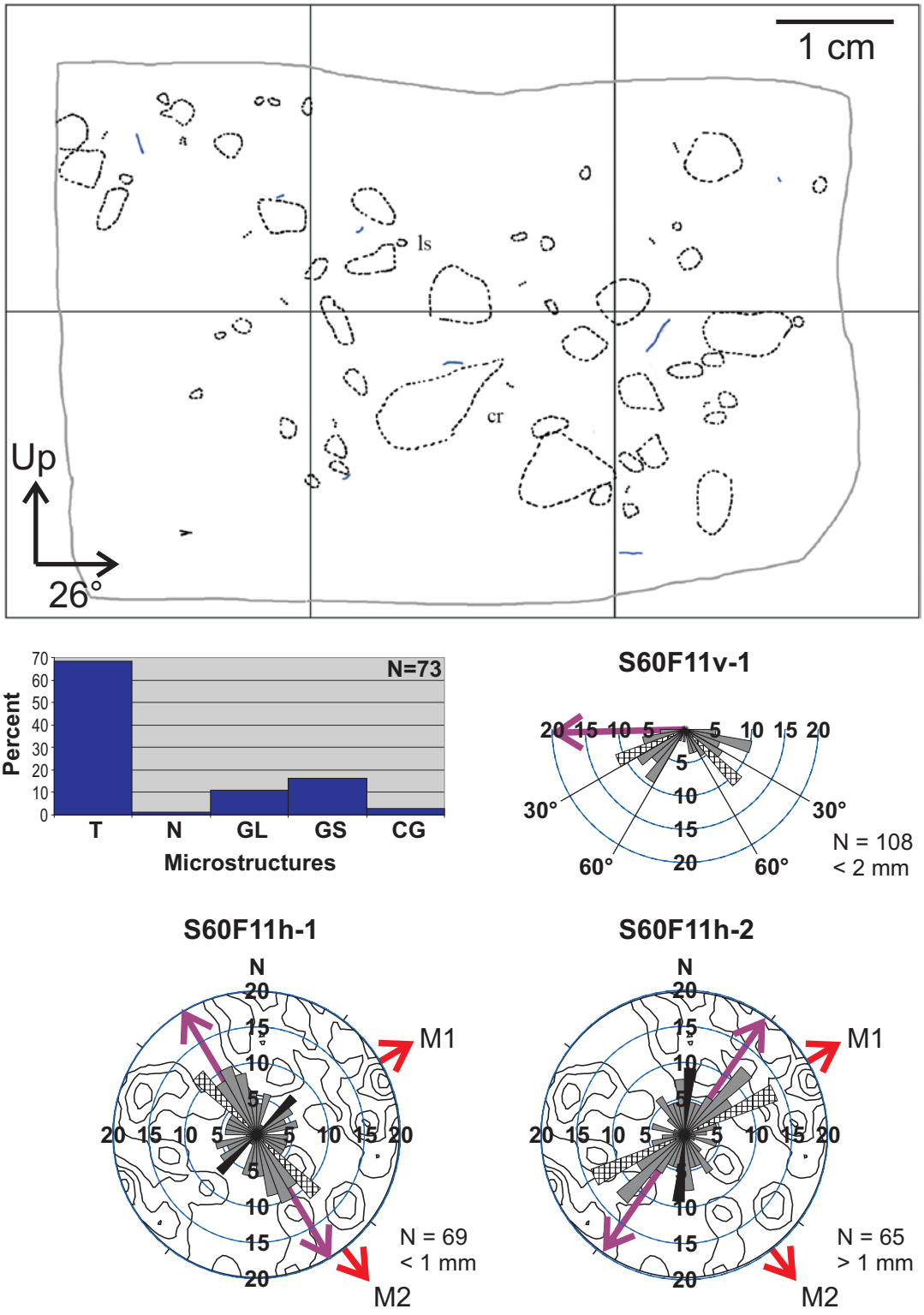

Figure 4.6-10. Microfabrics S60F11v-1, S60F11h-1 and S60F11h-2, and microstructure map and frequency histogram for thin section S60F11v. See Figures 3.3-4 and 3.3-5 for legends.

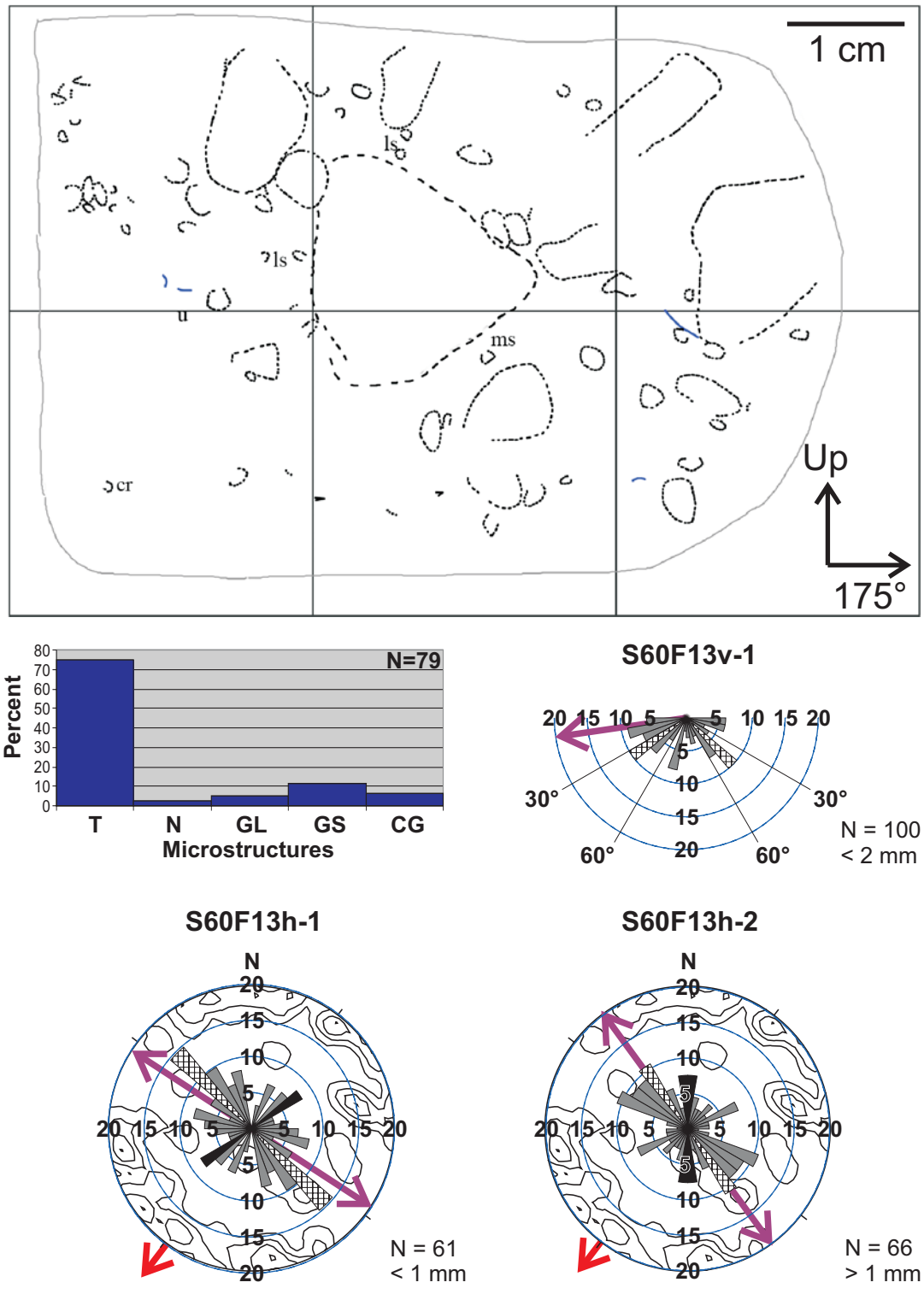

Figure 4.6-11. Microfabrics S60F13v-1, S60F13h-1 and S60F13h-2, and microstructure map and frequency histogram for thin section S60F13v. See Figures 3.3-4 and 3.3-5 for legends.

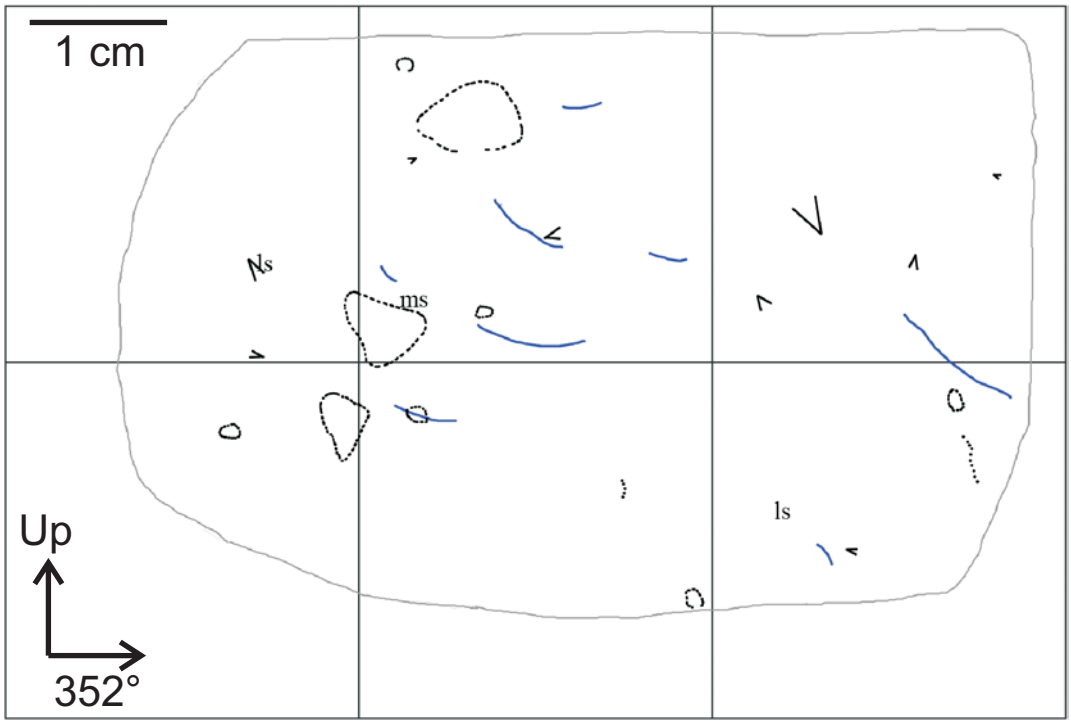

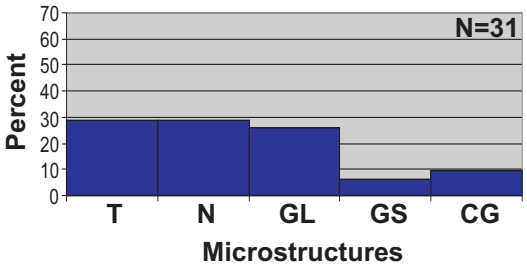

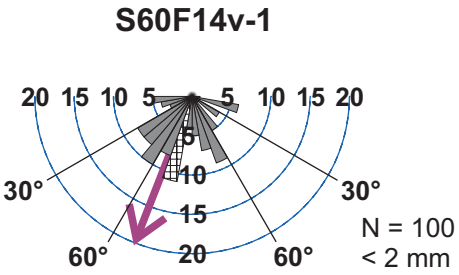

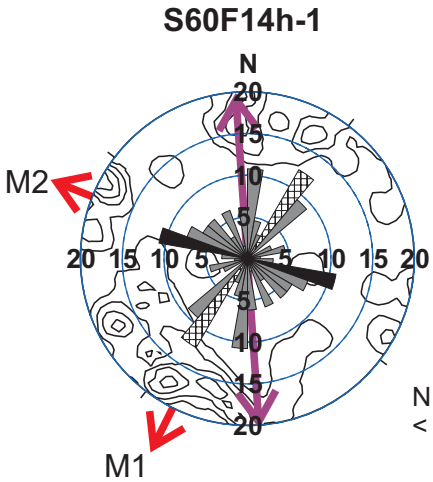

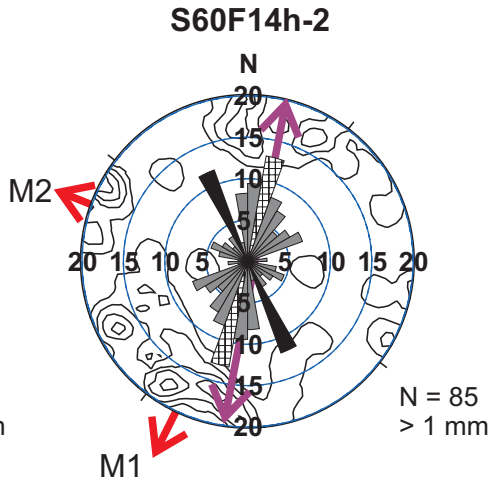

Figure 4.6-12. Microfabrics S60F14v-1, S60F14h-1 and S60F14h-2, and microstructure map and frequency histogram for thin section S60F14v. See Figures 3.3-4 and 3.3-5 for legends.

of microstructures is similar for both thin sections, in that the remaining microstructures constitute less than 35% of the total, and are dominated by grain stacks (Fig. 4.6-6D). Necking structures (Fig. 4.6-6F) are the rarest type of discrete microstructure.

Horizontal microfabrics measured from thin sections S60F13h and S60F15h have tight clusters trending NE-SW, orthogonal to the spread modes of macrofabrics F13 and F15, respectively (Figs 4.6-9, 4.6-11). Most sand grains in vertical microfabric S60F13v-1 have apparent plunges ranging from 0-80° (Fig. 4.6-11). Most sand grains in vertical microfabric S60F15v-1 have apparent plunges ranging from 10-60° (Fig. 4.6-9). Horizontal microfabrics from thin section S60F11h show that grains less than 1 mm in apparent length are more likely to trend subparallel to the secondary mode of macrofabric F11 (NW-SE), and grains greater than 1 mm in apparent length are more likely to trend subparallel to the primary mode of macrofabric F11 (NE-SW) (Fig. 4.6-10). Grains with apparent plunges ranging from 10-60° are best represented in vertical microfabric S60F11v-1.

In horizontal microfabric S60F14h-1, grains less than 1 mm in apparent length form two clusters, one subparallel to the primary mode of F14, and the other subparallel to the secondary mode of F14 (Fig. 4.6-12). Horizontal microfabric S60F14h-2 contains a tight cluster oriented NNE-SSW, subparallel to the secondary mode of F14. Grains with steep (up to 80°) apparent plunges are well represented in vertical microfabric S60F14v-1 (Fig. 4.6-12). Three (S60F15v-1, S60F11v-1, S60F14v-1) out of four vertical microfabrics measured from site 60 have principal eigenvectors that plunge down to the S (Figs 4.6-9, 4.6-10, 4.6-12).

4.6.4 Interpretation

The diamicton in units 3 and 4 at site 60 was previously classified as a deformation till (Lian 1997; Lian and Hicock 2000). Lian's (1997) interpretation of diamicton genesis at site 60 was based on its stratigraphic position, clast glacigenic wear features, two clast fabrics (fab-60a and fab-60b), and the orientation of shears and fractures in the diamicton and underlying sediments. His rendition of events is as follows: 1) advance of Fraser ice in Jesmond valley, erosion of older sediments and the deposition of glacial outwash (units 1 and 2). 2) The ice front arrives and the proglacial sediments (units 1 and 2) freeze and become fractured, and the JRF forms up-ice dipping shears with very little displacement. Alternatively, some or all of the fractures in units 1, 2 3 and 4 may have occurred during stage 5 (below). 3) Warm-based ice arrives

and lodgement till is deposited (unit 3 and 4). 4) As the till layer thickens and porewater increases, the till becomes saturated and deforms by viscous flow. Lodged clasts are remobilized, but still maintain their primary a-axis orientation.

As till flows over the substrate, sandstone blocks (from the JRF) are detached and entrained and some near the lower contact of unit 4, exposure 1, become imbricated within the diamicton (units 3 and 4). 5) The upper 1-2 m of till drains and brittle deformation ensues yielding large-scale shear planes. This shear, however, was not pervasive enough to destroy soft sandstone clasts near the base of the unit. It is possible that the upper part of the till drained and stiffened while the lower part remained viscous. Pebble fabric strength in the upper part of unit 4 may have increased during this stage (Lian 1997).

In this study, the diamicton at site 60 was subdivided into two units (units 3 and 4) on the basis of clast upper surface striae frequency, clast concentration, the orientation of the main mode and principal eigenvector of the clast fabric, and the location of a discontinuity (i.e. the sand-filled lower contact of unit 4). Only 22% of clasts measured from unit 3 had upper surface striae, while on average, 56% of clasts measured from each fabric in unit 4 had upper surface striae (Table 4.2-3). The clast concentration within unit 3 is also lower than the clast concentration of unit 4 (Table 4.2-1), and unit 3 has a gradational contact with the underlying sand and gravel of unit 2, whereas a sharp contact exists between units 3 and 4 (Fig. 4.6-2). The contact between units 3 and 4 is sand-filled, and therefore is thought to have acted as a shear zone after part or all of unit 4 was deposited above unit 3.

The glacigenic wear features on clasts in unit 3 suggest that they were subglacially transported, and (or) they originated from subglacial till. The laterally-restricted extent of unit 3, its gradational lower contact with unit 2, its multimodal to girdle-like macrofabric, the lack of preferred orientation or direction of glacigenic wear features, and the relatively small percentage of clasts exhibiting striae support emplacement of unit 3 by a glacigenic debris flow. This debris flow may have originated from the ablating glacier snout during ice advance.

The high silt content of unit 4, the frequent occurrence of glacigenic wear features on clasts and the fact that the vast majority of clasts with upper surface striae have striae parallel to their long axes, suggests that unit 4 is a subglacial till with deposition initiated by lodgement supporting the interpretation of Lian (1997). The orientations of clasts, and their glacigenic wear features are quite spread, suggesting

that subsequent remobilization occurred. The indurated sediment clasts serve as evidence for erosion of preglacial sediments. Indurated sediment clasts A and C resemble the colour and texture of other blocks of indurated pebbly silt found at the base of exposure 1, however it was unclear whether the source of the pebbly silt was derived from the JRF, or from a previously eroded indurated unit that used to overly the JRF. The source of sediment clast B is unknown. It is finer grained, and more indurated than the sediments in units 1, 2 and 3, and thus may be derived from preglacial sediments older than these units, or from the JRF. Sediment clast D was likely sourced from the JRF because it is similar in hardness, colour and texture to sand beds observed in the JRF. The preservation of sediment clasts has been attributed to their rotation within a ductile deforming bed sustaining high pore water pressure (Hicock and Dreimanis 1992; Lian 1997; Lian and Hicock 2000). The pebbles surrounding clast D (located near the upper contact of unit 4) suggest clast rotation within ductily deforming diamicton. The poorly aligned clasts in F15, F11 and F12, thus, may be associated with increases in subglacial porewater pressure and consequent clast rotation during ductile deformation of a deforming bed.

The sharp contacts between sediment clasts A, B, C and D and the surrounding diamicton (Fig. 4.6-3) are puzzling, however, given that these clasts will crumble or fracture when vigorously rubbed by hand. Piotrowski *et al.* (2001) suggest that tills containing such clasts should be interpreted as melt-out material transported englacially prior to deposition, because a pervasively deforming layer would lead to diffusive contacts between the clasts and the surrounding material (Piotrowski and Tulaczyk 1999; Hooyer and Iverson 2000a). Some authors are sceptical that enough is known about the behaviour of deforming materials with different stiffness and drainage properties to make this assumption (Boulton *et al.* 2001), and Piotrowski *et al.*'s (2001) interpretation requires an explanation for the preservation of sediment clasts within deforming englacial ice.

Other alternative explanations for the sharp sediment clast boundaries may involve the development of a mobile deforming bed that excavates and entrains material from a frozen substrate (Menzies 1990). The size of the sediment clasts in unit 4 in both exposures 1 and 2, however, suggest that if they were frozen prior to entrainment, they would have thawed relatively quickly once entrained into a water-saturated diamicton. Thus the preservation of the sediment clasts in unit 4 and their sharp contacts may be attributed to one or more of the following factors: 1) their hardness or induration, 2) the

minimization of shear stress and strain at the sediment clast boundary during subglacial transport as a result of clast rotation within a ductily deforming bed (Hicock and Dreimanis 1992), and 3) during periods of low porewater content, plastic or brittle deformation is non-pervasive as suggested by Lian (1997), but confined to localized shear planes in the diamicton, or to thin shear zones below the ice-bed interface preventing brittle deformation or smearing of the sediment clasts.

The orientation of most clast fabric principal eigenvectors and modes, the youngest striae on cobbles and boulders, both measured shear planes, and most steeply dipping fractures within unit 4 all point to a shearing force from the SW (Fig. 4.6-2). These measurements are consistent with the shear plane measurements made by Lian (1997) within the JRF at exposure 1, and may suggest ice flow from the SW (Figs 4.6-1, 4.6-2). This ice flow direction is not consistent with the general trend of Jesmond valley (Fig. 3.1-1), yet it is consistent with local valley wall orientation. (Large scale aerial photographs and topographic maps show that the eastern valley side trends NE-SW at site 60).

The erosion and entrainment of the JRF sandstone into the diamicton of unit 4 in exposure 1 indicates that northward flowing ice must have become dominant. The southward sloping valley bottom at site 60 suggests that glacial meltwater would have accumulated proglacially and (or) subglacially beneath the northward flowing ice. Increasing porewater pressures would have reduced inter-particle effective stresses and potentially facilitated the re-orientation of till clasts and the erosion of earlier units (units 1, 2 and the JRF) by a mobile deforming bed (unit 4).

The maximum thickness of subglacial deformation at any one time cannot be estimated from the evidence attained thus far, however. The clast fabrics in unit 4, exposure 2, suggest that at any one time, deformation occurred within a layer that was less than the thickness of the diamicton unit. Because the clast fabrics were sampled along a diagonal with height from the base of unit 4, as opposed to along a vertical transect, horizontal variations in strain magnitudes, strain orientations and diamicton rheology likely affected fabric shapes. Nonetheless, clast fabrics do not record a systematic increase in strain with height from the lower contact that might be consistent with either a viscously deforming mobile bed (where clasts exhibit Jeffery-style rotation and rotate transverse to shear at high strains), a plastically deforming mobile bed (where clasts rotate via the March model and become aligned parallel to flow at high strains), or

a deforming bed with both a ductile deforming A and a brittle-ductile deforming B horizon containing weak and strong fabrics, respectively (Benn 1995).

Modern conceptual models of the subglacial bed include a patchwork of deforming and stable spots, the spatial extent of which changes through time, resulting in subglacial sediments that may record only the most recent deformation event, or several deformation events superimposed on one another (Hicock and Dreimanis 1992; Piotrowski *et al.* 2004; Evans *et al.* 2006). Therefore it is possible, and perhaps very likely, that the thickness of the deforming layer was at times reduced to thicknesses approximating the diameter of single pebbles, cobbles or boulders, leading to lodgement and melt-out processes under a glacier that is effectively sliding over its bed. F14, for example, contains the most organized fabric distribution and may record such an event where particles were lodged under ice sliding toward the NE. Striae sets, measured on the tops of cobbles and boulders in the upper part of unit 4, also tend to trend NE-SW, and may record faceting and abrasion of larger boulders at the ice-bed interface, while smaller pebbles flow around them in a ductily deforming matrix (Benn 1995).

Shear planes in the upper part of unit 4 (exposure 2, Fig. 4.6-2) likely record dewatering and non-pervasive brittle deformation of the diamicton under the weight of northward flowing ice. The group of fractures superimposed on units 1, 2, 3 and 4 in the lower part of exposure 2 (Fig. 4.6-2) may also be associated with brittle fracture of the substrate under northward flowing ice as suggested by Lian (1997), or post-depositional fracturing as a result of unloading.

Evidence for grain rotation, squeeze flow, discrete shear, grain stacking and grain crushing exists throughout unit 4. A higher number of discrete microstructures were identified in thin sections with fewer fractures and voids, and these sections also contained the highest number of turbates. In this study, a skeletal grain is considered to be part of a turbate structure if most of the elongate grains surrounding it appear to be subparallel to its edges on a minimum of three sides (see Appendix F for discrete microstructure identification criteria). Thus, multiple major fractures and voids, including many along the edges of skeletal grains likely inhibit the identification of turbates in favour of more necking structures, and would explain the relative distribution of discrete microstructures in sections S60F14v and S60F15v. The high number of fractures and voids in these thin sections may be the result of poor impregnation of the sample in the lab. The red-brown residue and calcite linings around skeletal grains and in the matrix

are not deformed and are likely derived from glacial, meteoric or groundwater sources after the deposition of the diamicton.

In unit 4, some horizontal microfabrics have clusters that are consistent with the orientations of one or more of the macrofabric modes (S60F11h-1, S60F11h-2, S60F14h-1, and S60F14h-2, Figs 4.6-10, 4.6-12), while others have clusters that are orthogonal to macrofabric modes (S60F13h-1, S60F13h-2, S60F15h-1 and S60F15h-2, Figs 4.6-9, 4.6-11). Inconsistencies between macrofabric modes and microfabric clusters may be due to high subglacial porewater pressure conditions that are thought to weaken clast macrofabrics, and (or) the re-orientation of sand sized grains around larger clasts as evidenced by turbate and necking structures (Benn 1995; Thomason and Iverson 2006). Vertical microfabrics show that steeply plunging sand grains are common and can be attributed to grain rotation due to grain collisions or elevated porewater pressures during subglacial deformation of the unit 4 diamicton.

The unit 4 diamicton at site 60 was previously classified as a deformation till (Lian 1997; Lian and Hicock 2000). Spread unimodal, spread bimodal and girdled clast fabrics, re-oriented clast wear features, entrained sediment clasts, and the ring of pebbles surrounding sediment clast D suggest that, at times, the diamicton in unit 4 behaved as a ductile deforming bed capable of eroding its substrate. Therefore, Lian (1997) and Lian and Hicock's (2000) classification of unit 4, site 60 will be accepted in this thesis, however it is recognized that the subglacial processes responsible for the deposition of the entire thickness of unit 4 was probably complex. Clast fabrics, and striae orientations on cobbles and boulders suggest that the thickness of the deforming layer varied over time and space, and that some of the diamicton in unit 4 may have been deposited by lodgement and (or) melt-out processes.

The weakly bedded, coarse sandy cobble-boulder gravel of unit 5 may record rapid sedimentation rates from high energy water flows during ice retreat or during post-glacial alluvial fan deposition.

4.7 Site 48

4.7.1 Macroscale sedimentology and structural geology

Site 48 is located near the southern end of Jesmond valley (Fig 3.1-1). This exposure consists of ~4 m of exposed massive, matrix-supported, silty sand diamicton (Fig. 4.2-2) (unit 1, Fig. 4.7-1). The diamicton is overlain by up to 2 m of weakly bedded

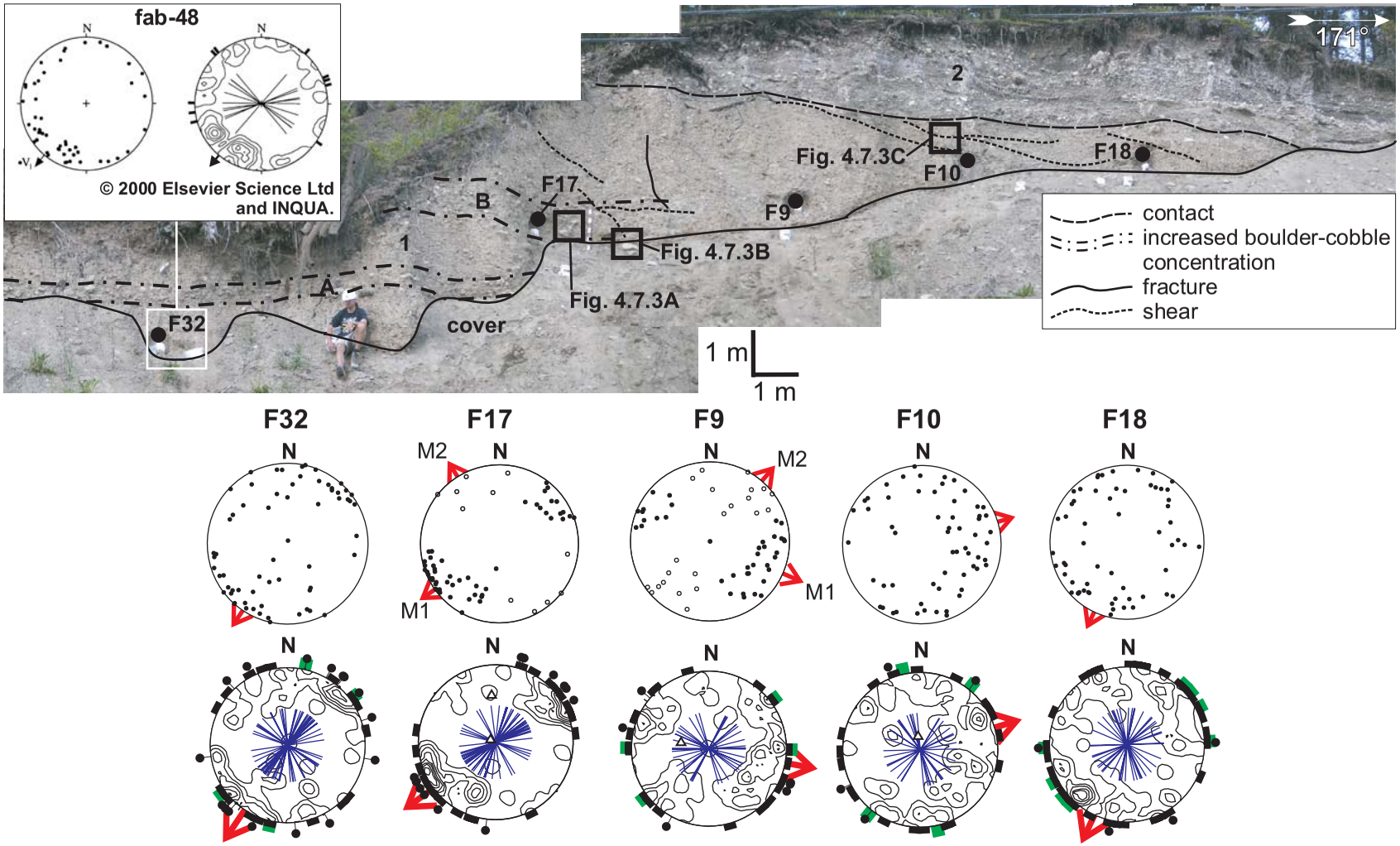

Figure 4.7-1. Site 48, units 1 (diamicton) and 2 (sandy gravel). Zones A and B mark zones of increased boulder-cobble concentration within unit 1. Fractures and shears are annotated on the photograph. Due to accessibility issues, only four shear planes were measured in the field. These are plotted as poles to planes on the contoured stereogram of the fabric they are closest to. The stererogram of fabric 48 (fab-48) is adapted from Lian and Hicock (2000) with permission. See Figure 3.3-1 for stereogram legend.

and massive sand and sandy cobble-boulder gravel (unit 2, Fig. 4.7-1). The lower contact of unit 2 is moderately sharp with an apparent dip of ~6° to the south.

The diamicton at this site contains two subhorizontal zones (zones A and B) 0.5-0.75 m thick, where clast concentration and the number of cobbles and boulders are high relative to those in the rest of the diamicton (Fig. 4.7-1). The clast concentration measured at F17 in zone B, for example, is 25%, while the clast concentration at F9 above zone B is 8% (Fig. 4.7.1, Table 4.2-1). Clast concentrations measured at F32, F10 and F18 are 21%, 19% and 18% respectively (Table 4.2-1).

Sand filled shears in unit 1 (Fig. 4.7-2C), have steep apparent dips near F17, and shallower apparent dips near the unit's upper contact (Fig. 4.7-1). Four of these shear planes were measured and plotted on the stereogram of the fabric site they are closest to (Fig. 4.7-1). In general, the shear planes have dip angles up to 50°, with dip directions to the S and SE. A set of three striated cobbles near F17 form a stack that plunges to the NW (Figs 4.7-1, 4.7-2).

Five clast fabrics (F9, F10, F17, F18 and F32) were measured in unit 1 to gauge vertical and lateral changes in macrofabric strength, modality, and orientation and preservation of clast glacigenic wear features (Fig. 4.7-1). The fabric sampling sites are the locations of five samples extracted for micromorphological analysis (Section 4.7.2).

F32, located just below zone A was measured in the vicinity of Lian (1997) and Lian & Hicock's (2000) fabric 48 (fab-48, Fig. 4.7-1). F32 has one spread mode oriented NE-SW (Fig. 4.7-1, Table 4.2-1). Most striae on clast tops are oriented parallel to clast a-axes, and one clast has upper surface striae with multiple orientations (Table 4.2-1). Keels on clast bottoms generally follow the orientation of the mode. Fractured ends and bullet noses show no preferred direction (Fig. 4.7-1). Out of all clasts in the sample, 55% are faceted and 7% have keels (Table 4.2-3). Lian's (1997) fabric 48 is girdle-like, with a principal eigenvector pointing to the SW. Fractured ends in fabric 48 show no preferred direction.

F17, located within zone B is bimodal with a primary mode oriented NE-SW and a secondary (n=10) transverse mode (Fig. 4.7-1, Table 4.2-2). Striae on clast tops generally follow the orientation of clast a-axes (Table 4.2-3) and cluster with the main mode (Fig. 4.7-1). Out of all clasts in the sample, 10% have upper surface striae with multiple orientations, and ~7% have striae curving around convexities and (or) concavities (Table 4.2-3). No keels were identified. Fractured ends and bullet noses

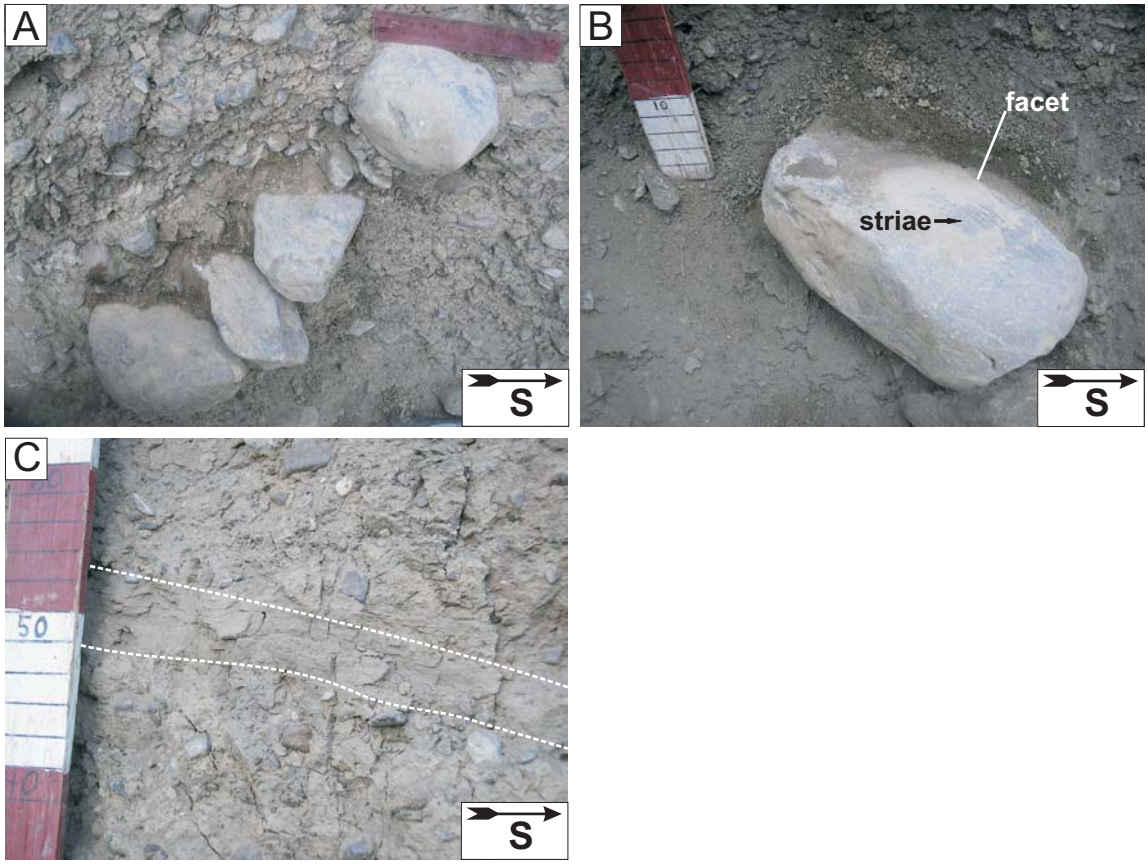

Figure 4.7-2. Sedimentological and structural features within the diamicton (unit 1) at site 48. A) Stacked cobbles and boulders. The ruler is 15 cm long. B) A faceted and striated boulder located at F17. C) A sand filled shear plane measured above F10. The metre stick in B & C has red and white decimetre subdivisions. Photograph locations are indicated in Figure 4.7-1.

show no preferred direction (Fig. 4.7-1). Faceted clasts comprise 18% of the sample (Table 4.2-3).

F9 is located just above zone B ~5 m south of F17. This fabric is classified as spread bimodal (Fig. 4.7-1). It has a primary mode that is oriented NW-SE and a transverse mode oriented NE-SW (Fig. 4.7-1, Table 4.2-2). Clast upper surface striae orientations are spread out with deficits in the NNE-SSW orientation (Fig. 4.7-1), and the vast majority follow the orientation of clast a-axes (Table 4.2-3). One clast has upper surface striae with multiple orientations (Table 4.2-3). Keels on clast bottoms are oriented subparallel to both modes. Fractured ends and bullet noses show no preferred direction (Fig. 4.7-1). Out of all clasts in the sample, 15% are faceted, and 7% have keels (Table 4.2-3).

F10, located ~3 m south of F9 has a girdled distribution with a principal eigenvector pointing ENE (Fig. 4.7-1, Table 4.2-1). Most striae follow clast a-axes, ~3% of clasts have upper surface striae with multiple orientations, and one clast has striae curving around convexities and (or) concavities (Table 4.2-3). Keels on clast bottoms show no preferred orientation (Fig. 4.7-1). Out of all clasts in the sample, 18% are faceted and 5% have keels (Table 4.2-3).

F18 is closest to the top of unit 1 and is multimodal to girdle-shaped (Fig. 4.7-1, Table 4.2-1). Striae on clast tops are variably oriented (Fig. 4.7-1) and most follow clast a-axes (Table 4.2-3). Out of all clasts in the sample, 5% have upper surface striae with multiple orientations (Table 4.2-3). Most keels on clast bottoms are found on clasts oriented NE-SW. Fractured ends and bullet noses show no preferred direction (Fig. 4.7.1). Faceted clasts comprise 43% of the sample, and clasts with keels comprise 7% of the sample (Table 4.2-3). Clast shapes do not conform to predefined modes, or prefer any specific orientation (Fig. B-1, Appendix B).

4.7.2 Micromorphology

One sample was extracted from each fabric location at site 48 for thin section preparation. Both vertical and horizontal thin sections were cut from samples collected at F9 (S48F9h and S48F9v), F10 (S48F10h and S48F10v), F17 (S48F17h and S48F17v) and F32 (S48F32h and S48F32v). Due to the small sample size, only one vertical thin section was cut from the sample collected at F18 (S48F18v). In thin section, the diamicton exposed at site 48 appears to be plasma supported, with a mixture of

subangular to subrounded limestone and metasedimentary grains, and subrounded to rounded volcanic grains (Figs 4.7-3A, 4.7-4A, 4.7-5A, 4.7-6A, 4.7-7A).

Three thin sections, S48F9v, S48F17v and S48F32v, have distinct fracture patterns. In section S48F9v, a single, long and relatively straight fracture has an apparent dip of ~30° toward 243°, and is intercepted by two subparallel fractures dipping ~25° toward 63° azimuth (Fig. 4.7-5A). In section S48F17v, two major and some minor subparallel fractures have an apparent dip of 75° toward 17° azimuth (Fig. 4.7-4A). In section S48F32v, a series of narrower and shorter, subparallel fractures within the right half of the thin section have a consistent apparent dip of ~80° toward 357° azimuth (Fig. 4.7-3A). Skeletal grain orientations do not seem to be influenced by fracture patterns in any of the vertical thin sections, except for S48F9v (see below).

Vughs (Fig. 4.7-5B) and voids that previously housed grains (Fig. 4.7-3B) are common. All vertical thin sections have a dark reddish-brown opaque residue that exists in dark patches (Figs 4.7-3D, 4.7-4C, 4.7-5C, 4.6-5D, 4.7-6C), lines fractures and voids (Figs 4.7-3F, 4.7-5D, 4.7-6G, 4.7-7C), and creates a mottled appearance in some areas of the matrix (Figs 4.7-3C, 4.7-5F, 4.7-6B). The contact between dark/mottled areas of the matrix and areas with little or no red-brown residue is sharp in places (e.g., Fig. 4.7-4E), and encircles grains or turbates (Figs 4.7-3E, 4.7-4D). Evidence for calcium carbonate deposition is rare.

Sections S48F9v, S48F10v, S48F18v, and S48F32v have similar discrete microstructure distributions (Figs 4.7-8, 4.7-10, 4.7-11, 4.7-12). Turbates (e.g., Figs 4.7-3G, 4.7-4B, 4.7-4D, 4.7-5G, 4.7-7F) are relatively abundant and represent 50% to 65% of all microstructures, while necking structures (Fig. 4.7-5F), grain lineations (Figs 4.7-3B, 4.7-5E, 4.7-6D, 4.7-7E), grain stacks (Figs 4.7-4B, 4.7-4G, 4.7-6E), and crushed grains (Figs 4.7-4F, 4.7-6F, 4.7-7G) individually contribute no more than 20% of the total. S48F17v is an exception to this rule, and has similar amounts of turbates, necking structures and grain stacks (~30% each), and a relative paucity of grain lineations and crushed grains.

Horizontal microfabrics S48F32h-1 and S48F32h-2 have relatively tight NE-SW trending clusters that are subparallel to the spread mode of macrofabric F32 (Fig. 4.7-8). Sand grains with 0-80° apparent plunges down to the N are well represented in vertical microfabric S48F32v-1 (Fig. 4.7-8). Horizontal microfabric S48F17h-1 (Fig. 4.7-9) shows two tight clusters of grains (<1 mm in apparent length) following the primary mode of macrofabric F17, and a more spread out cluster following the secondary mode of

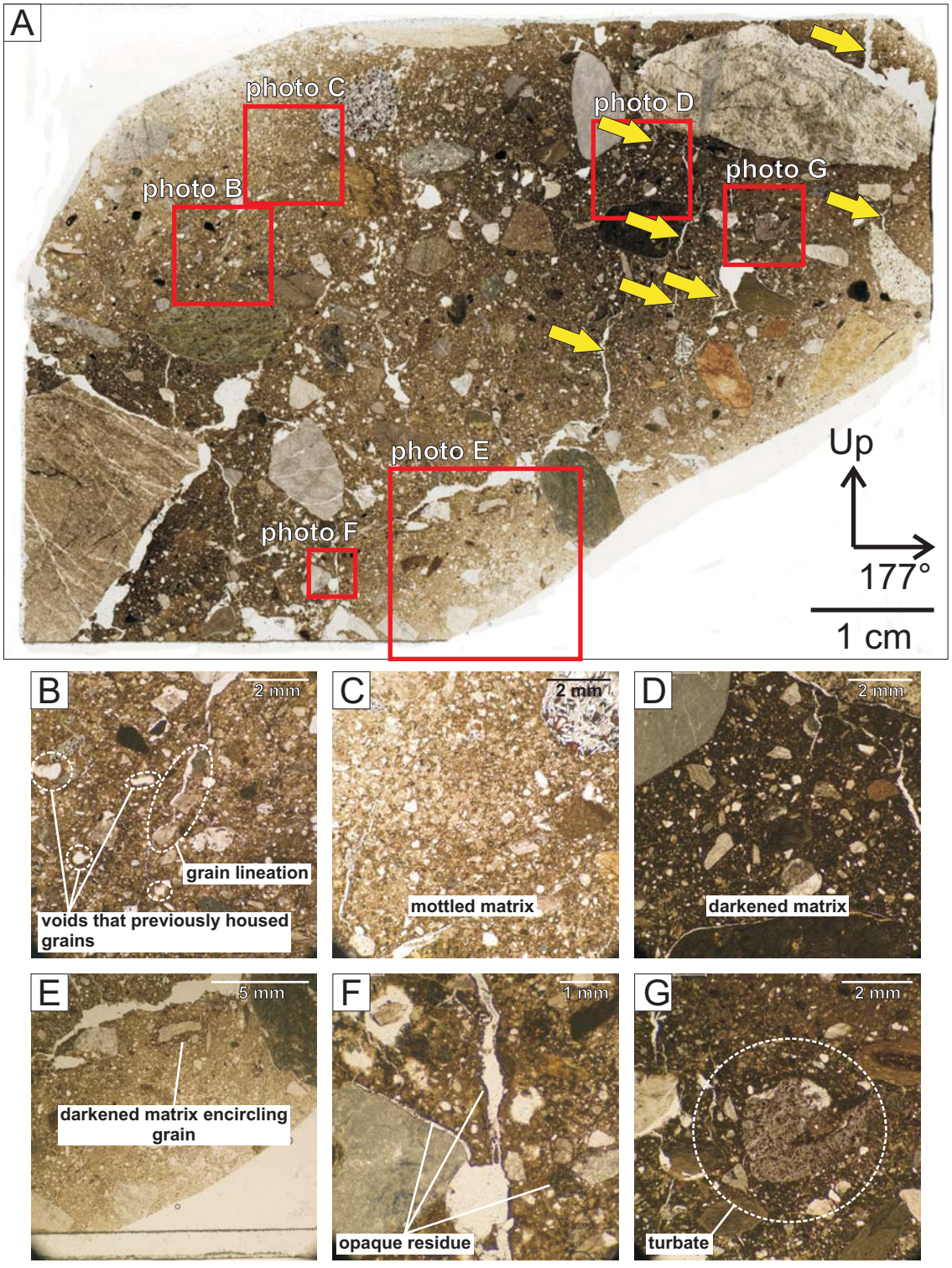

Figure 4.7-3. Thin section S48F32v. A) A 2400 dpi scan of the thin section showing steeply dipping narrow planar voids (yellow arrows). The locations of microphotographs B, C, D, E, F and G are indicated by red squares. Microphotographs show voids that previously housed grains (B), a grain lineation (B), mottled matrix (C), a close-up of darkened matrix (D), darkened matrix encircling a grain (E), opaque residue in the matrix and lining the walls of voids (F) and a turbate (G).

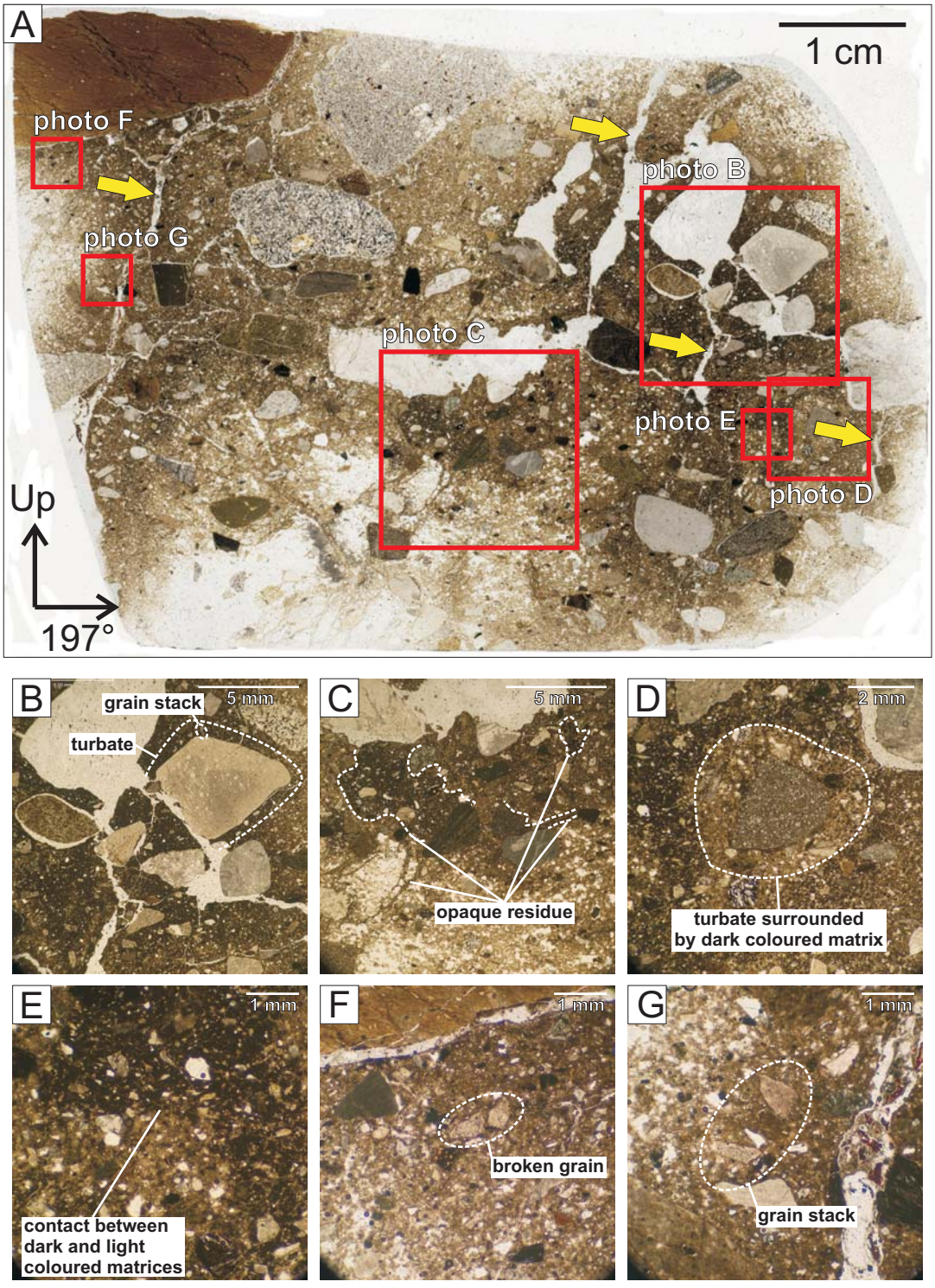

Figure 4.7-4. Thin section S48F17v. A) A 2400 dpi scan of the thin section showing steeply dipping planar voids (yellow arrows). The locations of microphotographs B, C, D, E, F and G are indicated by red squares. Microphotographs show turbates (B, D), grain stacks (B, G), opaque residue creating dark coloured patches in the matrix (C, D, E) and a broken grain (F).

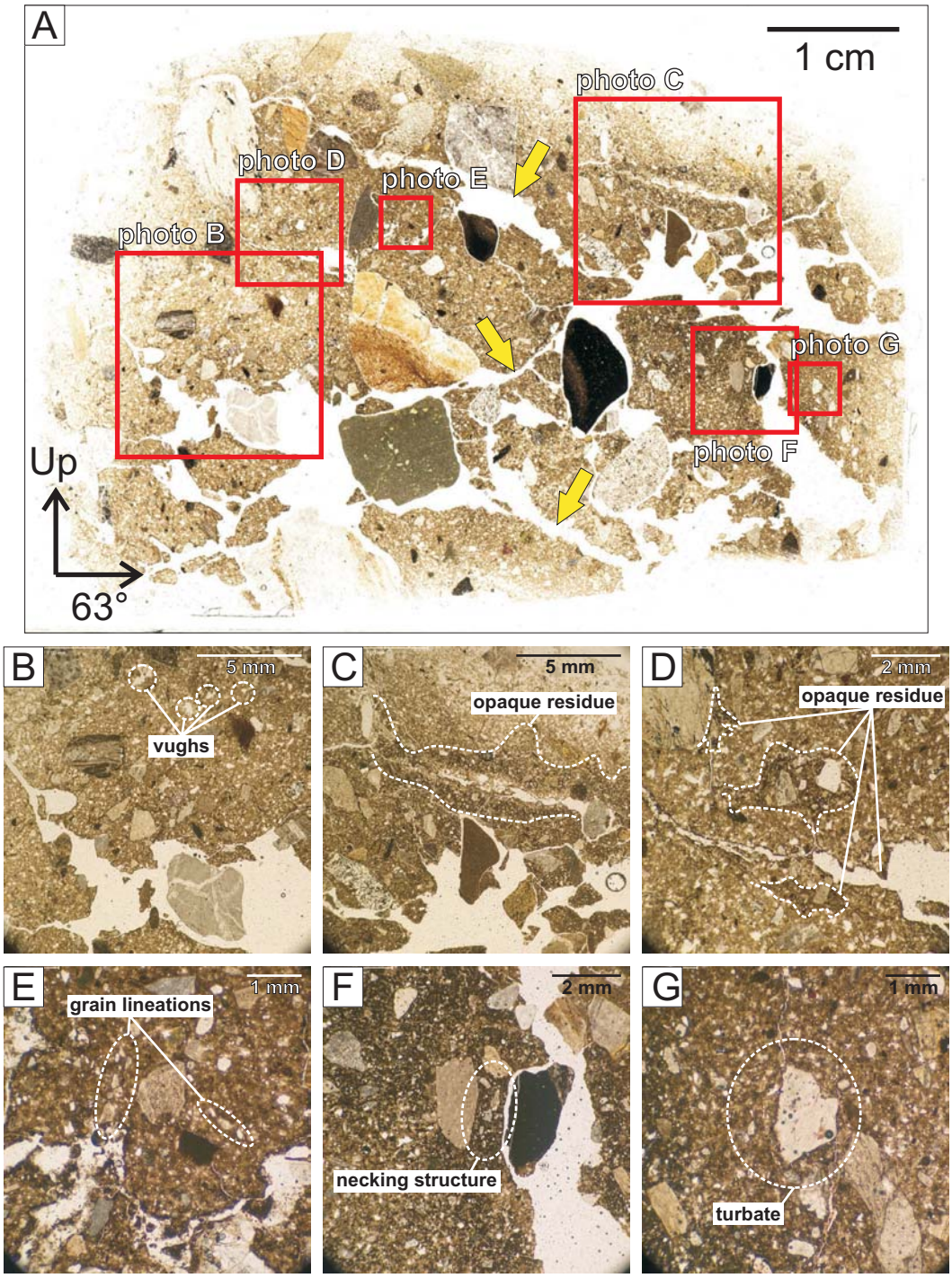

Figure 4.7-5. Thin section S48F9v. A) A 2400 dpi scan of the thin section showing NE and SW dipping planar voids (yellow arrows). The locations of microphotographs B, C, D, E, F and G are indicated by red squares. Microphotographs show vughs (B), an opaque residue (C, D), grain lineations (E), a necking structure (F) and a turbate (G).

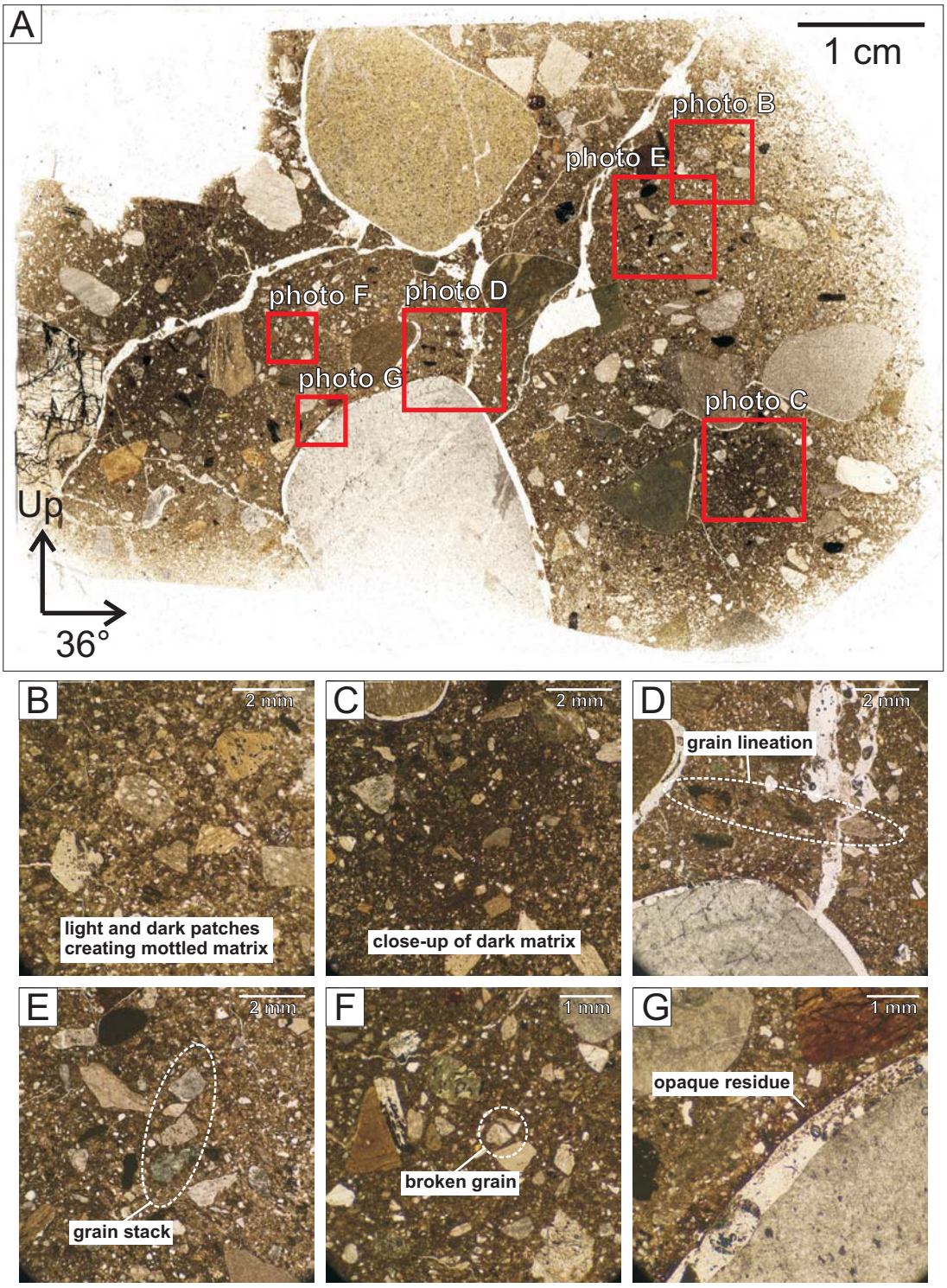

Figure 4.7-6. Thin section S48F10v. A) A 2400 dpi scan of the thin section. The location of microphotographs B, C, D, E, F and G are indicated by red squares. Microphotographs show mottled areas of the matrix (B), a close-up of a dark patch (C), a grain lineation (D), a grain stack (E), a broken grain (F), and an opaque residue (G).

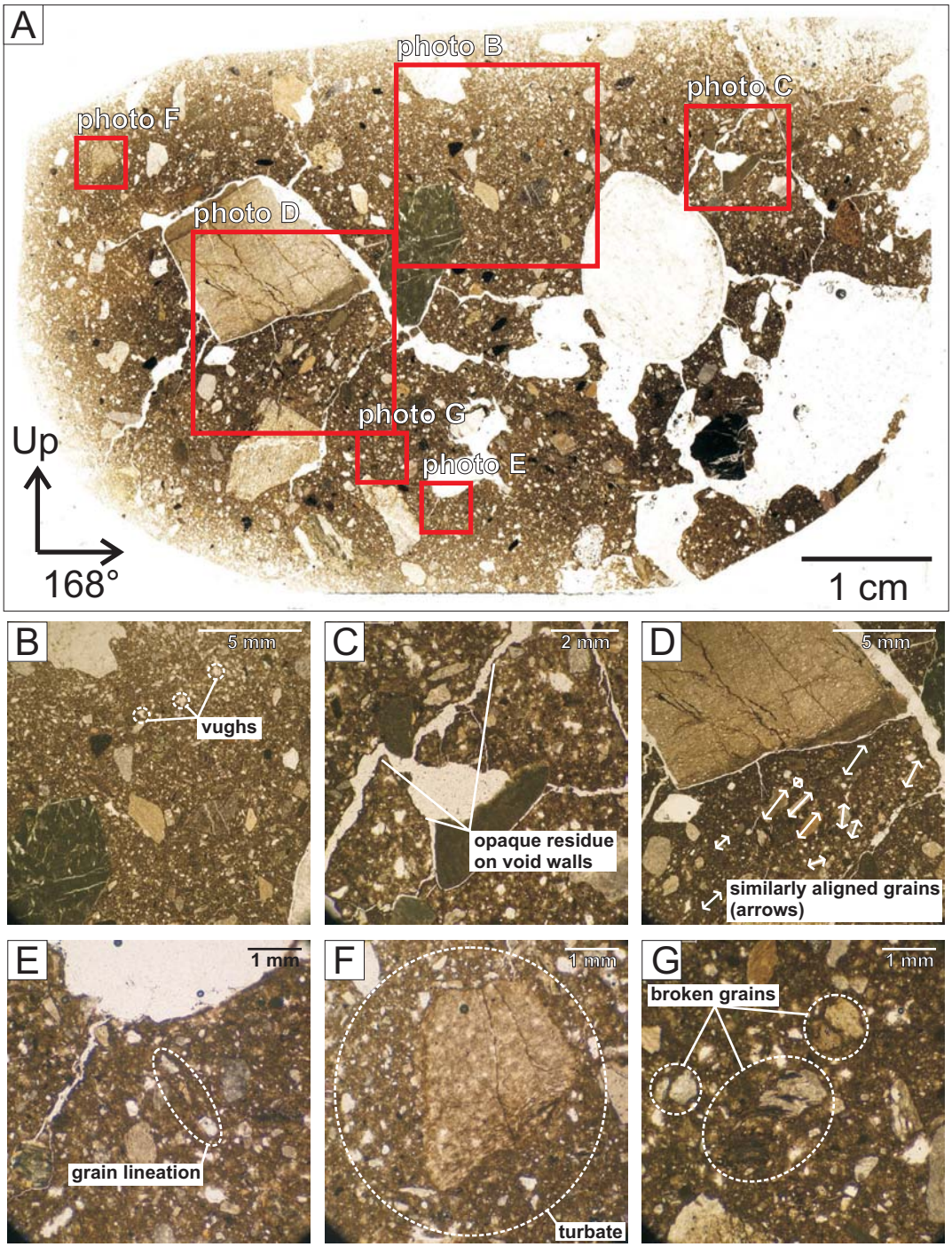

Figure 4.7-7. Thin section S48F18v. A) A 2400 dpi scan of the thin section. The locations of microphotographs B, C, D, E, F and G are indicated by red squares. Microphotographs show vughs (B), an opaque residue (C), similarly aligned grains (D), a grain lineation (E) a turbate (F) and broken grains (G).

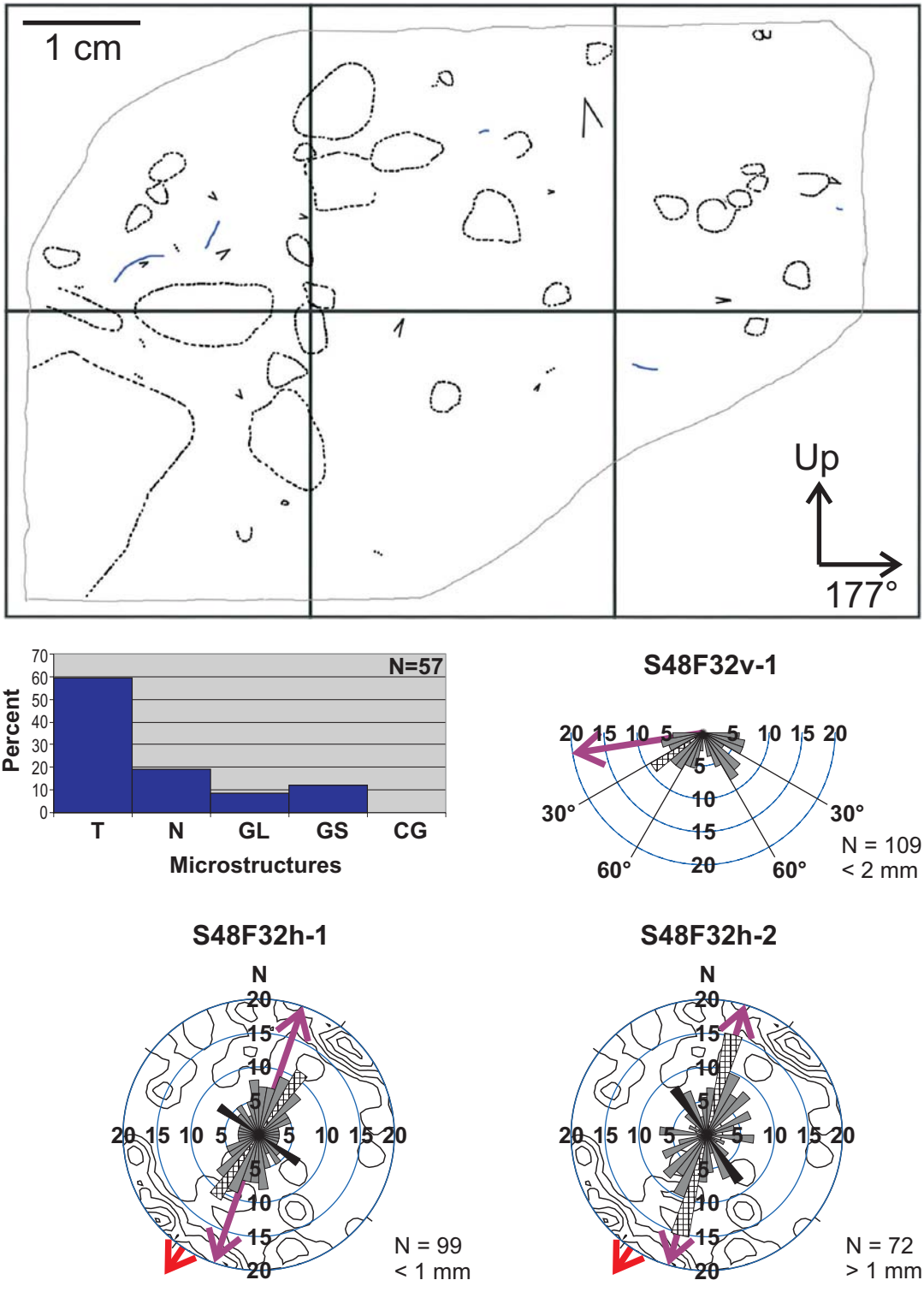

Figure 4.7-8. Microfabrics S48F32v-1, S48F32h-1 and S48F32h-2, and microstructure map and frequency histogram for thin section S48F32v. See Figures 3.3-4 and 3.3-5 for legends.

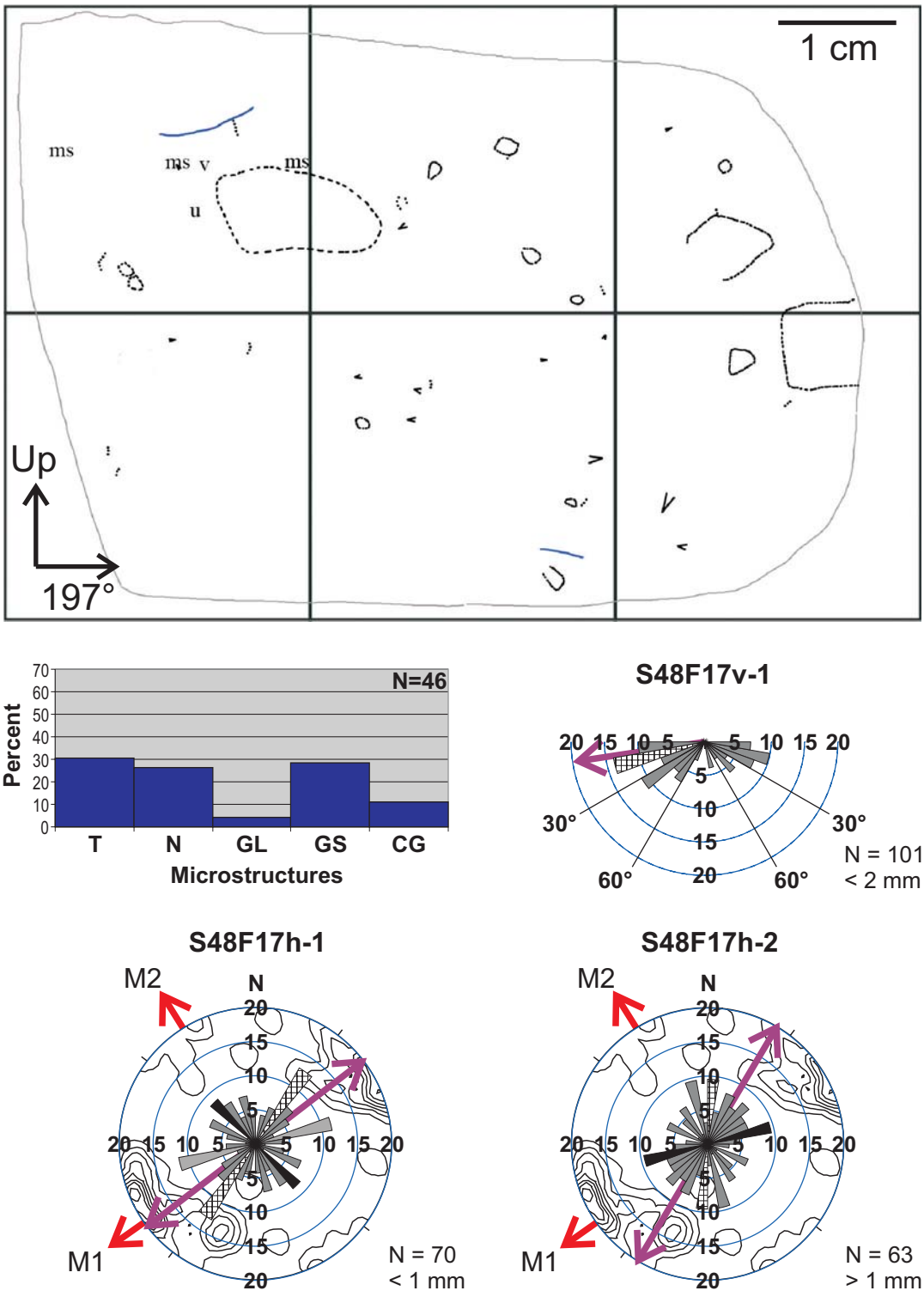

Figure 4.7-9. Microfabrics S48F17v-1, S48F17h-1 and S48F17h-2, and microstructure map and frequency histogram for thin section S48F17v. See Figures 3.3-4 and 3.3-5 for legends.

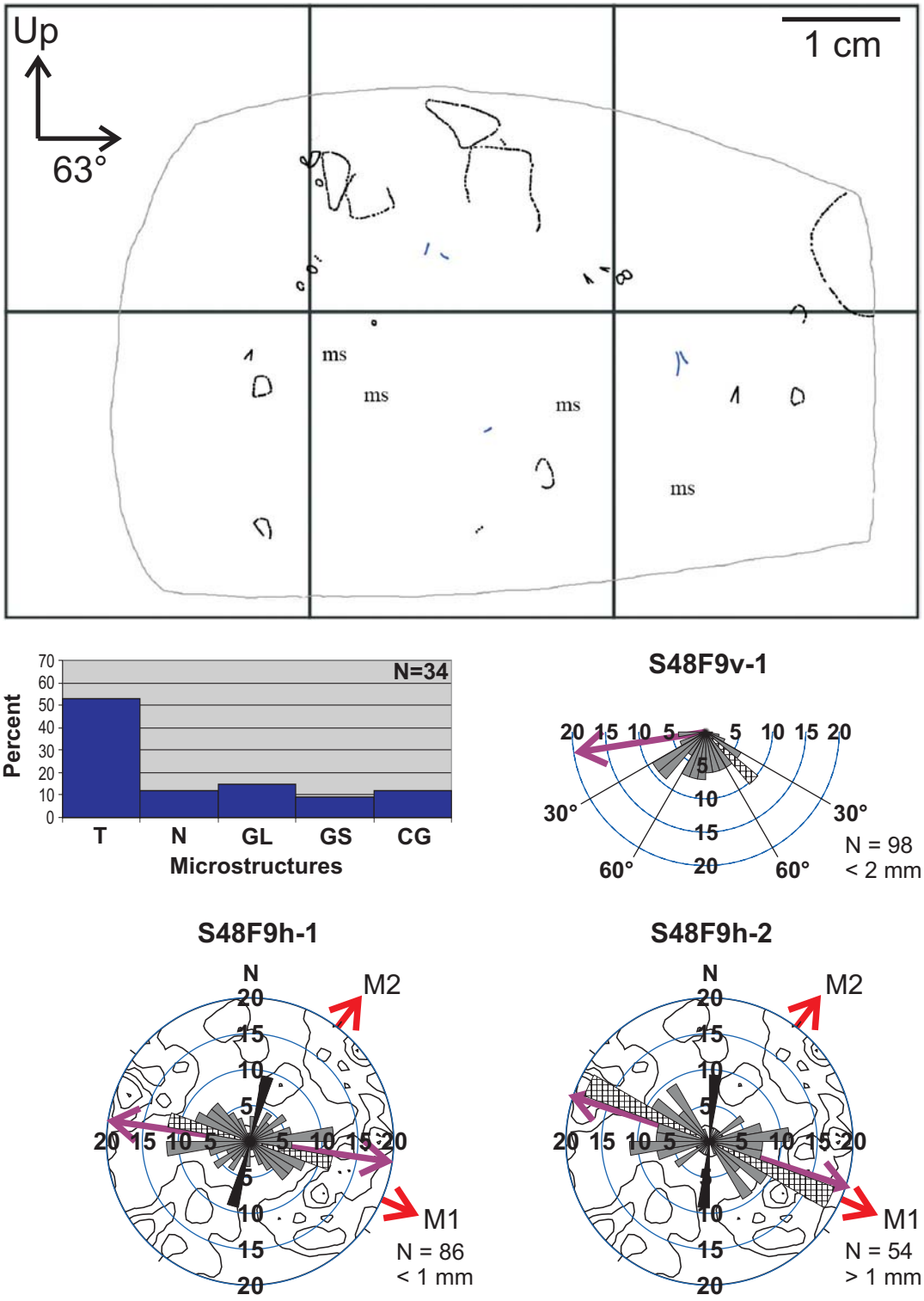

Figure 4.7-10. Microfabrics S48F9v-1, S48F9h-1 and S48F9h-2, and microstructure map and frequency histogram for thin section S48F9v. See Figures 3.3-4 and 3.3-5 for legends.

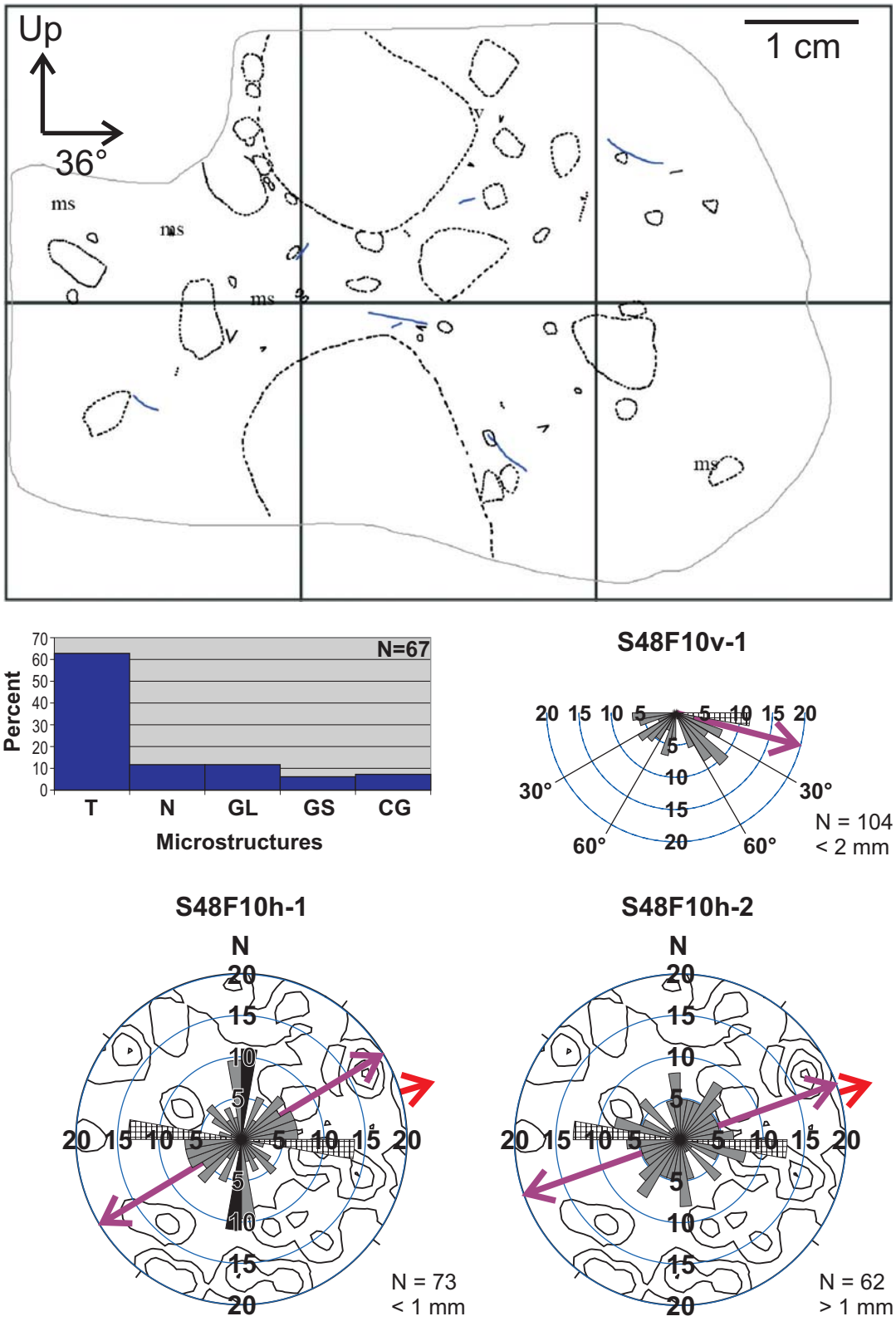

Figure 4.7-11. Microfabrics S48F10v-1, S48F10h-1 and S48F10h-2, and microstructure map and frequency histogram for thin section S48F10v. See Figures 3.3-4 and 3.3-5 for legends.

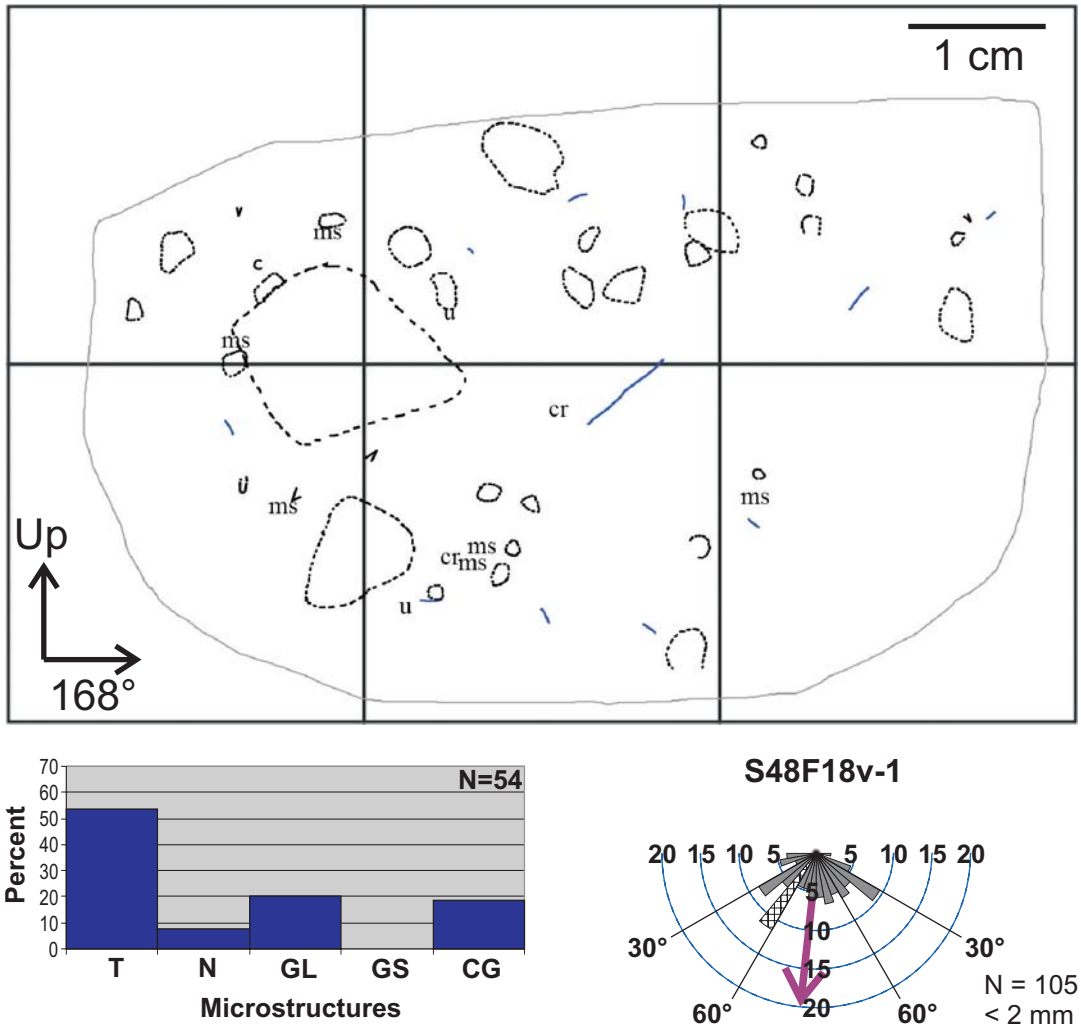

Figure 4.7-12. Microfabric S48F18v-1, microstructure map and frequency histogram for thin section S48F18v. See Figures 3.3-4 and 3.3-5 for legends.

macrofabric F17. Microfabric S48F17h-2 has two spread out clusters, one oriented ~N-S, and the other ENE-WSW (Fig. 4.7-9). Subhorizontal grains are common in vertical microfabric S48F17v-1, and most grains have apparent plunges of less than 60° (Fig. 4.7-9).

Both horizontal microfabrics S48F9h-1 and S48F9h-2 have a prominent cluster oriented subparallel to the primary mode of macrofabric F9, and a smaller isolated cluster oriented NNE-SSW (Fig. 4.7-10). Grains with steep to near-vertical apparent plunges are common in vertical microfabric S48F9v-1, and few grains have apparent plunges less than 30° (Fig. 4.7-10). Two clusters with apparent plunges of 40-50° down to the NE, and 30-50° down to the SW are oriented similarly to the two fracture sets in thin section S48F9v (Figs 4.7-5A, 4.7-10).

Horizontal microfabrics S48F10h-1 and S48F10h-2 have tight clusters oriented WNW-ESE. S48F10h-1 has a second cluster oriented ~N-S, and grains lying outside of the tightest cluster in S48F10h-2 have variable orientations (Fig. 4.7-11). Both subhorizontal and steeply plunging grains are common in vertical microfabric S48F10v-1 with the majority of grains plunging to the N (Fig. 4.7-11). The vertical microfabric measured from thin section S48F18v shows that most sand grains have 30-90° apparent plunges (Fig. 4.7-12).

4.7.3 Interpretation

Unit 1 at site 48 was previously classified as a deformed lodgement till (Lian 1997; Lian and Hicock 2000). The high silt content and frequent occurance of striae, facets and bullet noses on clasts suggests that unit 1 is a subglacial till that was initially deposited by lodgement. Considerably spread modes in some clast fabrics (Fig. 4.7-1) serve as evidence for post-lodgement re-orientation of clasts. There is no evidence of entrainment of sub-diamicton materials into a mobile deforming bed (no soft sediment clasts were observed and the lower contact of unit 1 was covered), therefore data from this study support Lian (1997) and Lian and Hicock's (2000) interpretation of unit 1 as a deformed lodgement till. Bullet noses and fractured ends show no preferred direction (Table 4.2-3). These either record clast re-orientation during ploughing or after lodgement at the ice-bed interface, or some or all bullet noses and fractured ends have been inherited from an earlier time in the transport history of the pebbles.

All clast fabrics, including Lian's (1997) fabric 48, have either a principal eigenvector or a mode that trends NE-SW, suggesting that local ice flow direction was

influenced by the orientation of neighbouring Cutoff Valley (Fig. 3.1-1). Both the secondary mode of F17 and the primary mode of F9 trend NW-SE, and may record the deflection of Cutoff Valley ice as it flowed NW into Jesmond valley. This NW-SE signal is substantiated by the southward stacking of cobbles near F17 (suggestive of northward flowing ice) (Fig. 4.7.2), and the SE dipping shear planes measured near F17, F9, and F10 (Fig. 4.7.1).

Both F10 and F18 show girdle-like distributions, and may record either: 1) the smearing of fabrics as a result of changes in ice flow direction from SW (parallel to Cutoff Valley) to NW (parallel to Jesmond valley), 2) the rotation of clasts during an increase in subglacial porewater pressure and subsequent till deformation, 3) remobilization of the till by gravity in a proglacial setting during a brief retreat of the ice margin, or 4) remobilization of the till through gravity in one or more subglacial cavities. A series of shear planes with both measured and apparent dips down to the SE near F10 and F18 suggest that remobilization of the till was subglacial, rather than proglacial, and was followed by dewatering and brittle fracture under northwestward flowing ice. No evidence for subglacial cavities was observed in the form of discontinuous sand or gravel lenses. Therefore the girdled shape of F10 and F18 may record post-depositional subglacial deformation of unit 1 as a result of elevated till porewater pressures and (or) fabric smearing during local shifts in ice flow direction. If high porewater pressures contributed to clast rotation at this site, they may have been the result of topographic damming of meltwater flow within the substrate as ice flowed uphill toward the NW (Fig. 3.3-1). This interpretation is consistent with observations and interpretations made at site 60 (Section 4.6), ~6 km NW of site 48 in Jesmond valley.

In general, fracture patterns observed in thin sections from site 48 do not seem to be influenced by skeletal grain orientations, though they, like other voids and vughs, likely served as conduits for glacial, meteoric and (or) groundwater as evidenced by the reddish-brown residue commonly observed along their walls. Curved contacts between light and dark coloured areas of the matrix, sometimes observed to encircle turbate structures, are evidence of the intermixing of diamictons of different compositions and different susceptibilities to weathering (Khatwa and Tulaczyk 2001). The largest colour contrasts, and the sharpest contacts are found in section S48F17v, and suggests that sediment intermixing may not have been as thorough at F17, as it was at other fabric locations (Khatwa and Tulaczyk 2001). The abundance of the reddish-brown residue within thin sections at site 48 relative to other sites along Jesmond valley could reflect a

slightly different sediment source. Site 48 is closer to weathered volcanic rocks (Eocene dacite and basalt bedrock) located in the upper reaches of the Cutoff Valley (Roddick *et al.* 1976) than sites 60, 6, and 44. Thus, the reddish-brown residue in the diamicton at site 48 may contain clay and (or) iron oxides derived from hydrolosis and oxidation of volcanic minerals.

Skeletal grain rotation dominates microscale deformation mechanisms at all fabric localities, save for F17, where squeeze flow and grain stacking seem to be equally as important. The increased number of grain stacks at F17 could be related to the relatively high coarse sand fraction in this sample (Fig. 4.2-2, Table E-1, Appendix E).

The clusters in the horizontal microfabrics measured from thin sections S48F32h, S48F17h, S48F9h and S48F10h show some tendency for sand grains to orient themselves subparallel to macrofabric modes (Figs 4.7-8, 4.7-9, 4.7-10, 4.7-11). This seems to indicate that processes responsible for the orientation of pebbles at site 48 (lodgement and deformation) contributed to the final orientation of sand sized grains. It may not be a coincidence that the strongest vertical microfabric was measured from a sample from the location of the strongest and most organized macrofabric, (F17, Fig. 4.7-9). Sand-sized grains are subhorizontally oriented in thin section S48F17v, and may have been emplaced during subhorizontal shear during deposition. Vertical and subvertical sand grains are more common in all other vertical thin sections, reflecting either smaller strain magnitudes (Thomason and Iverson 2006), higher porewater pressures, or an increase in frequency of grain collisions during deposition and (or) subsequent deformation.

The weakly bedded and massive sand and sandy cobble-boulder gravel of unit 2 may record rapid sedimentation rates from high energy water flows during ice retreat or during post-glacial alluvial fan deposition.

4.8 Site 27

4.8.1 Macroscale sedimentology and structural geology

Site 27 consists of two exposures (exposure 1 and exposure 2) in a roadcut along Pavilion-Clinton road on the south side of Cutoff Valley (Fig. 3.1-1). Exposure 1 faces WNW and is on the N side of a gully that runs NW down the steep slope of the valley side (Fig. 4.8-1). Exposure 2 faces NW and is on the S side of the same gully ~10 m SW of exposure 1 (4.8-1). Both exposures show the same three units (units 1-3, Fig. 4.8-1).

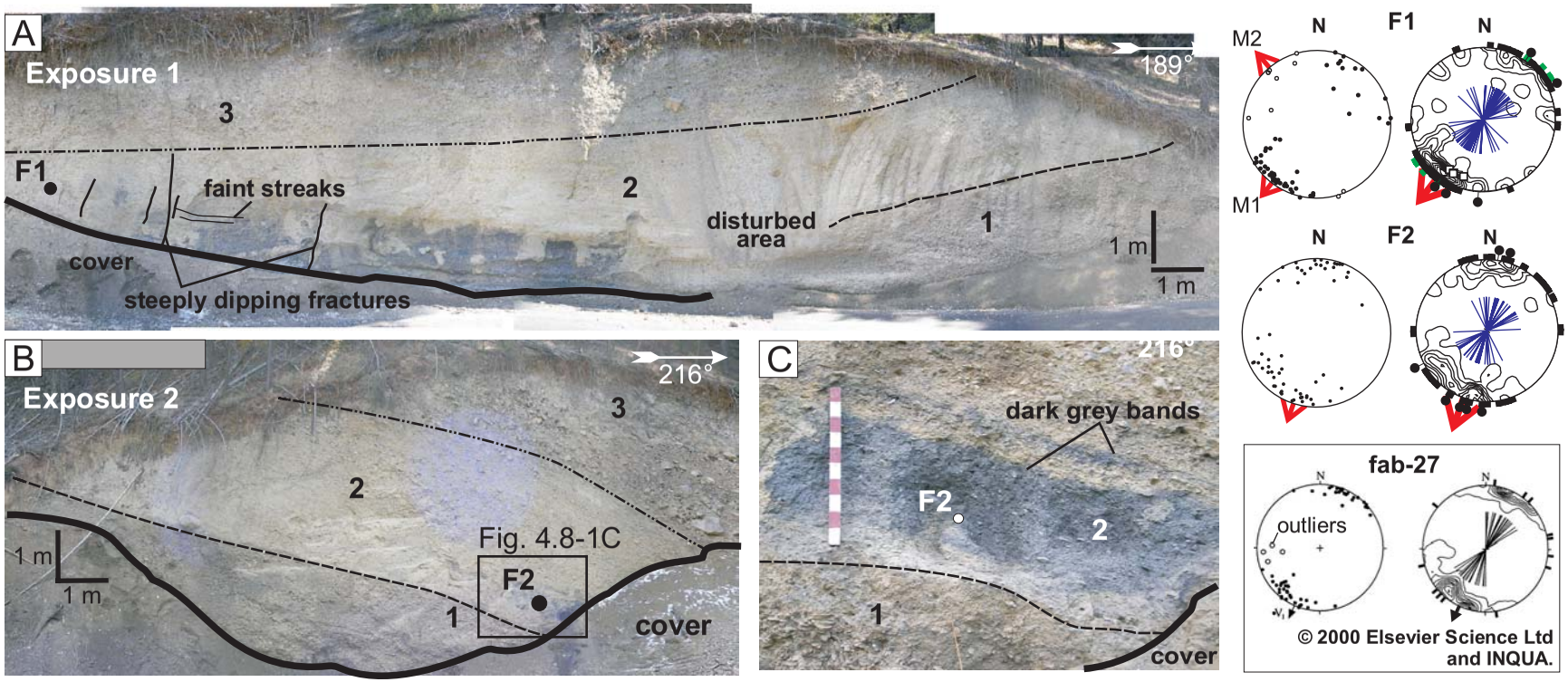

Figure 4.8-1. Site 27, exposures 1 (A) and 2 (B), showing units 1 (interbedded pebble-boulder gravel and diamicton), 2 (sandy silt clast-poor diamicton) and 3 (sandy silt clast-rich diamicton). The stereogram of fabric 27 (fab-27) is adapted from Lian and Hicock (2000) with permission. Fabric 27 was collected near the centre of unit 2 in exposure 1 (the exact location is unknown). The location of F1 and F2 (this study) are shown in 'A' and 'B' respectively. Blue banding (C) can be seen near the lower contact of unit 2, exposure 2. Metre stick with red and white decimetre subdivisions for scale. See Figure 3.3-1 for stereogram legend.

Unit 1 (Fig. 4.8-1) is at least 3 m thick and is composed of 10-30 cm thick discontinuous beds of clast-supported pebble- through boulder gravel with a sandy matrix that is interbedded with matrix-supported, clast-rich, silty sand diamicton. The diamicton beds are thickest (~1 m thick) near the bottom of the exposure, and become thinner (down to ~10 cm thick) toward the upper contact. Contacts between gravel and diamicton beds in unit 1 are gradational, and have an apparent dip of ~14° down to the SSW in exposure 1, and ~30° down to the SW in exposure 2 (Fig. 4.8-1). These beds are truncated at the sharp lower contact of unit 2. This contact forms a broad convexity with an apparent dip of 13° down to the NNE in exposure 1, and 16° down to the SW in exposure 2. Cobbles and boulders in the gravel and diamicton beds of unit 1 are subangular to angular, and are largely composed of argillite, which is abundant in the local bedrock (Fig. 3.1-2). Few stones exhibit glacigenic wear features.

Unit 1 is overlain by up to 3.25 m of massive, matrix-supported highly consolidated silty sand diamicton (Fig. 4.2-2) (unit 2) with abundant striated (Table 4.2-3) argillite stones (Fig. 4.8-1). Measured clast concentrations within unit 2 are on the order of 8-13% (Table 4.2-1). Unit 2 grades into a 3 m thick unit of mainly matrix-supported, stony sandy silt diamicton (unit 3). Unit 3 contains discontinuous beds of pebble- to boulder-sized clast-supported diamicton that are thickest (up to 1 m thick) in exposure 2. These beds are generally parallel to the lower contact of unit 3, which is gradational, and has an apparent dip of ~5° down to the NNE in exposure 1, and ~20° down to the SW in exposure 2 (Fig. 4.8.1). Clasts in unit 3 are subangular to angular and of local (argillite) lithology.

The unit 2 diamicton colour ranges from dark grey (Munsell colour 7.5YR 4/0) near the lower contact, to light grey (Munsell colour 2.5Y 7/2) near the upper contact. Dark grey bands are visible near the lower contact of unit 2 (exposure 2), and are essentially the same colour as the argillite clasts encased in the diamicton (Fig. 4.8-1C). These bands have an apparent dip down to the SW, parallel to the lower contact of unit 2, exposure 2. Near the middle and upper portions of unit 2 (exposure 1, Fig. 4.8-1), the distinct banding grades into a subtler streaking (apparent dip of 9° down to the SSW). Within 1 m of the upper contact of unit 2, the streaked diamicton grades vertically to a light grey diamicton that appears homogenous from a distance. Close inspection of the light grey diamicton matrix, however, shows a heterogenous mixture of light grey and dark grey patches (Fig. 4.8-2A). Near the upper contact of unit 2, evidence of clast imbrication is visible (Fig. 4.8-2).

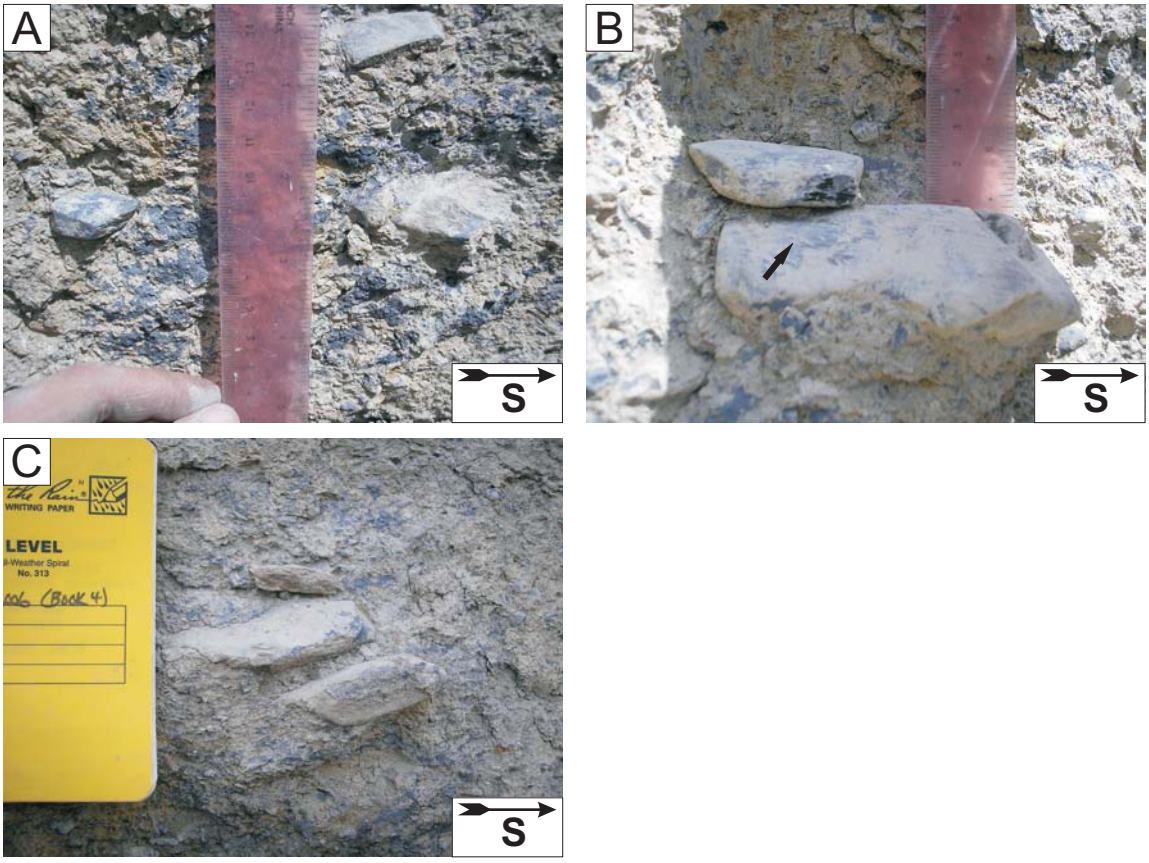

Figure 4.8-2. Sedimentological features near the upper contact of unit 2 at exposure 1, site 27. A) Heterogenous diamicton matrix showing dark grey and light grey patches. B & C) Imbricated and striated (arrow) pebbles. Left margin of ruler shows numbered centimetre intervals for scale. Field book is 18 cm tall.

Two fabrics (F1 and F2) were taken from unit 2 at site 27. F2 was measured near the lower contact, and F1 near the upper contact (Fig. 4.8-1). F1 is spread bimodal, with a NE-SW trending primary mode and a transverse secondary mode (Table 4.2-2). Keels on clast bottoms and striae on clast tops generally follow clast a-axis orientations, and ~8% of clasts have upper surface striae with multiple orientations (Fig. 4.8-1, Table 4.2-3). Fractured ends and bullet noses show no preferred direction. Out of all clasts in the sample, 32% are faceted and 7% have keels (Table 4.2-3). Four steeply dipping (~74°) fractures were measured near F1 in exposure 1 (Fig. 4.8-1). These fractures dip down to the NE.

F2 is spread unimodal with a principal eigenvector pointing to the SSW (Fig. 4.8-1, Table 4.2-1). Striae on clast tops are generally oriented parallel to clast a-axes, and 5% of clasts have upper surface striae with multiple orientations (Fig. 4.2-3). Fractured ends and bullet noses show no preferred orientation. Out of all clasts in the sample, 48% are faceted and only one keel was identified (Table 4.2-3). Lian's (1997) fabric 27 (fab-27) was measured near the centre of unit 2 in exposure 1. Fabric 27 contains a spread unimodal distribution with a principal eigenvector pointing to the SW, and fractured (lee) ends falling in the NE and SW quadrants.

Clasts that deviate the most from the orientation of the principal eigenvector in F1 and F2 are commonly blade-shaped (Fig. B-1, Appendix B). Striae orientations (relative to clast a-axes) on these bladed clasts do not differ significantly from those of the rest of the sample.

4.8.2 Micromorphology

One sample was collected from each fabric location at site 27 for thin section preparation and analysis. Due to laboratory error, the thin section cut from the sample collected at F1 (here named S27F1n) was not properly oriented so microfabrics were not measured. Thin sections S27F1n and S27F2v show that the diamicton at site 27 is plasma supported, with subangular to subrounded skeletal grains dominated by local grey argillaceous bedrock lithologies, and fewer smaller limestone and volcanic grains (Figs 4.8-3A, 4.8-4A). In thin section S27F2v, elongate grains are commonly aligned with one another (Figs 4.8-4D, 4.8-4E).

The diamicton in section S27F1n is a mixture of two diamictons of different colours, one dark grey (Figs 4.8-3A, 4.8-3E) and one brown (Fig. 4.8-3A). The dark grey diamicton in S27F1n forms jagged, semi-continuous patches with diffuse to sharp edges

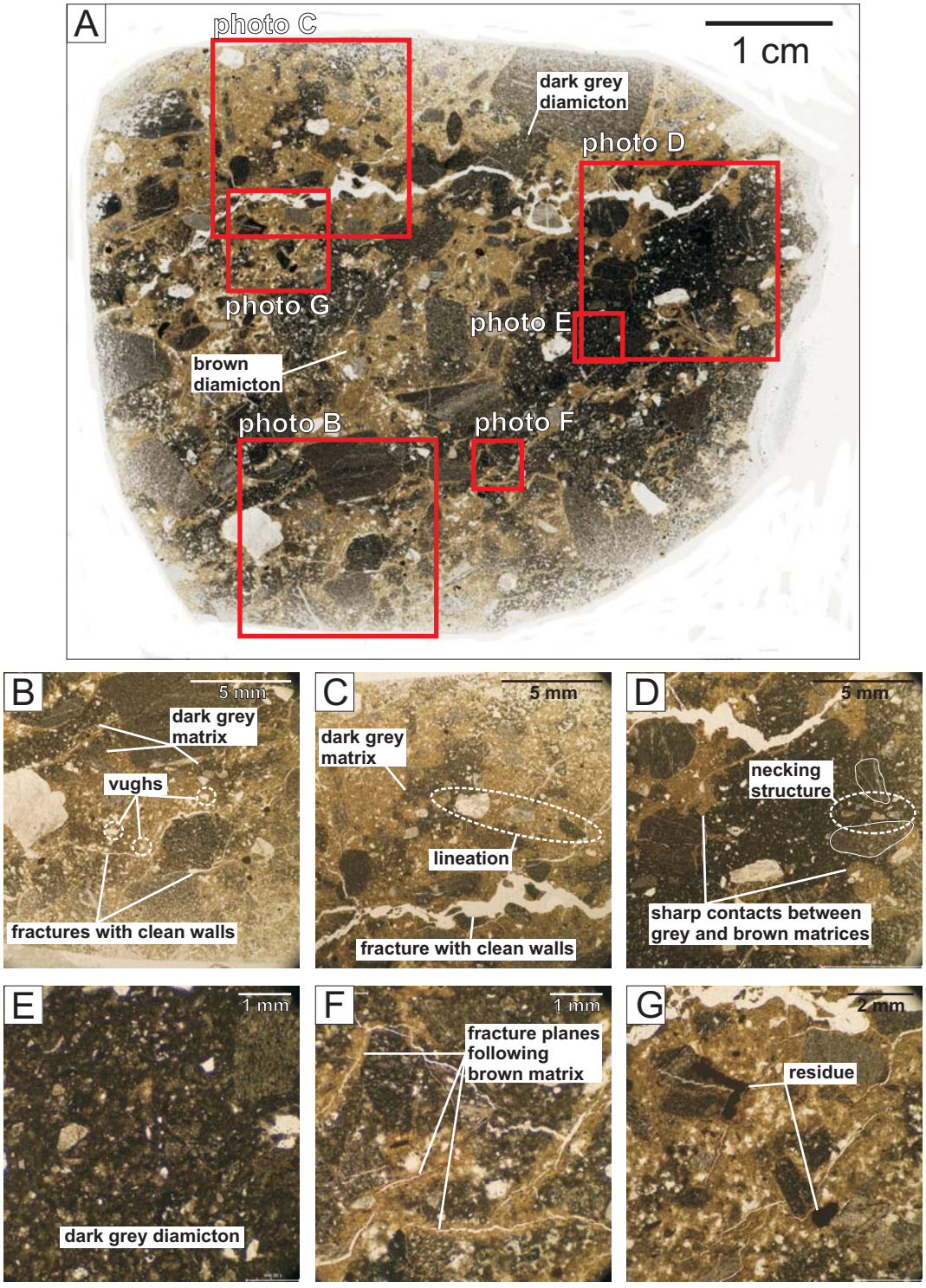

Figure 4.8-3. Thin section S27F1n. A) A 2400 dpi scan of the thin section showing dark grey and brown matrices. The locations of microphotographs B, C, D, E, F and G are indicated by red squares. Microphotographs show vughs (B), patches of dark grey matrix with diffuse and sharp edges (B, C, D), fractures with clean walls (B, C), a grain lineation (C), a necking structure (D), a close-up of the grey diamicton (E), fractures following paths restricted to the brown diamicton (F), and a dark opaque residue (G).

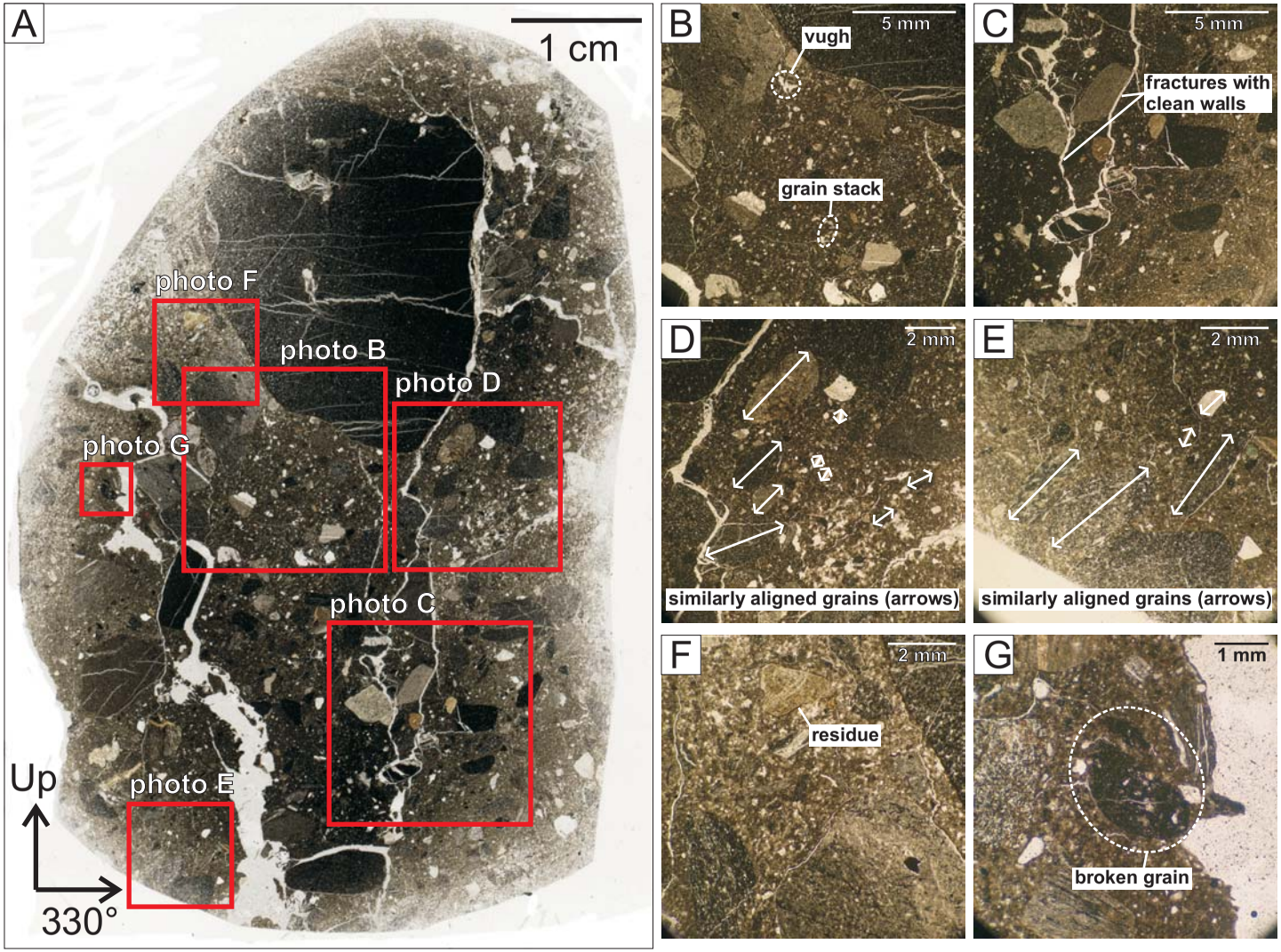

Figure 4.8-4. Thin section S27F2v. A) A 2400 dpi scan of the thin section. The locations of microphotographs B, C, D, E, F and G are indicated by red squares. Microphotographs show vughs (B), a grain stack (B), fractures with clean walls (C), similarly aligned skeletal grains (D, E), an opaque residue around a skeletal grain (D) and a broken grain (G).

(Figs 4.8-3B, 4.8-3C, 4.8-3D) that appear dispersed throughout the brown coloured diamicton (Fig. 4.8-3A). The diamicton in thin section S27F2v is predominantly dark grey (Figs 4.8-4A, 4.8-4B). In both thin sections S27F1n and S27F2v, major fractures follow no systematic pattern and are not lined heavily with precipitates (Figs 4.8-3B, 4.8-3C, 4.8-4C). Many fractures in thin section S27F1n appear to follow paths restricted to the brown diamicton (Fig. 4.8-3F). Some skeletal grains contain patches or linings of a dark, opaque residue (Fig. 4.8-3G, 4.8-4F). Vughs are common (Figs 4.8-3B, 4.8-4B), particularly in areas where the thin section has been hand ground relatively thin. Both sections S27F1n and S27F2v are represented by relatively abundant turbates, necking structures (Fig. 4.8-3D), grain lineations (Fig. 4.8-3C), and crushed grains (Fig. 4.8-4G), with few or no grain stacks (Figs 4.8-5, 4.8-6).

Horizontal microfabric S27F2h-1 contains two tight orthogonal clusters (one oriented ~N-S; the other oriented ~E-W, Fig. 4.8-6). Microfabric S27F2h-2 contains one tight cluster oriented NE-SW and two more spread out clusters oriented ~N-S and WNW-ESE (Fig. 4.8-6). The majority of grains in vertical microfabric S27F2v-1 have plunges ranging from 0° to 70°, and fall within a large spread out cluster plunging toward 330° azimuth (Fig. 4.8-6).

4.8.3 Interpretation

Unit 1, site 27 was previously interpreted as an alluvial fan deposit (Lian 1997). Macroscale observations of unit 1 include sloping beds of gravel and diamicton, and subangular to angular clasts with few glacigenic wear features. These observations are consistent with an alluvial fan that has been built by both colluvial and alluvial depositional processes.

Unit 2, site 27 was previously interpreted as lodgement till (Lian 1997). The sharp erosional lower contact of unit 2, its high silt content, the frequent occurrence of glacigenic wear features on clasts, and the fact that the vast majority of clasts with upper surface striae have striae parallel to their long axes (Table 4.2-3) suggest that unit 2 is a subglacial till that was initially deposited by lodgement. Bullet noses and fractured ends show no preferred direction (Table 4.2-3). These either record clast re-orientation during ploughing or after lodgement at the ice-bed interface, or some or all bullet noses and fractured ends have been inherited from an earlier time in the transport history of the pebbles. Thus, like sites 23 and 20, more definitive evidence for undeformed lodgement

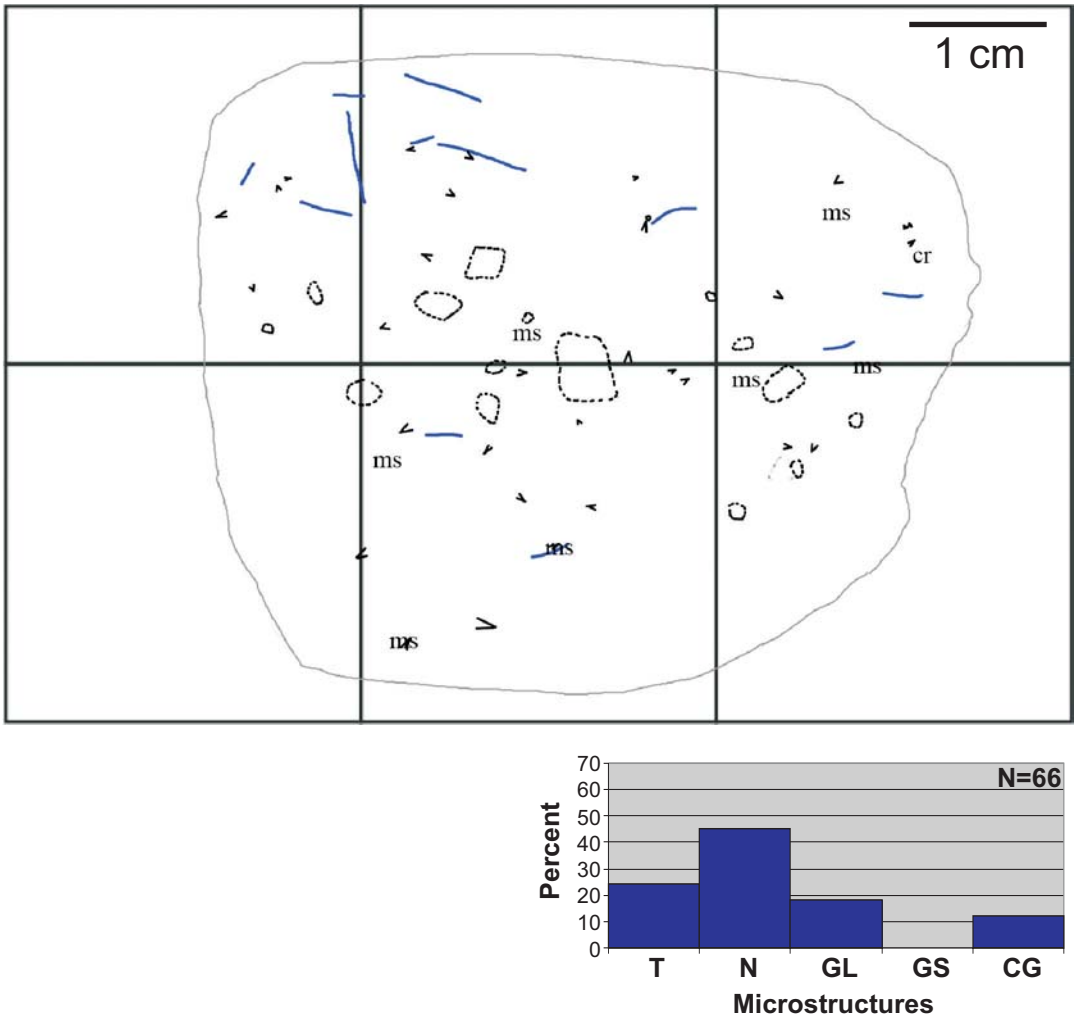

Figure 4.8-5. Microstructure map and frequency histogram for thin section S27F1n. See Figure 3.3-5 for legend. Because this thin section was not oriented, microfabrics were not measured.

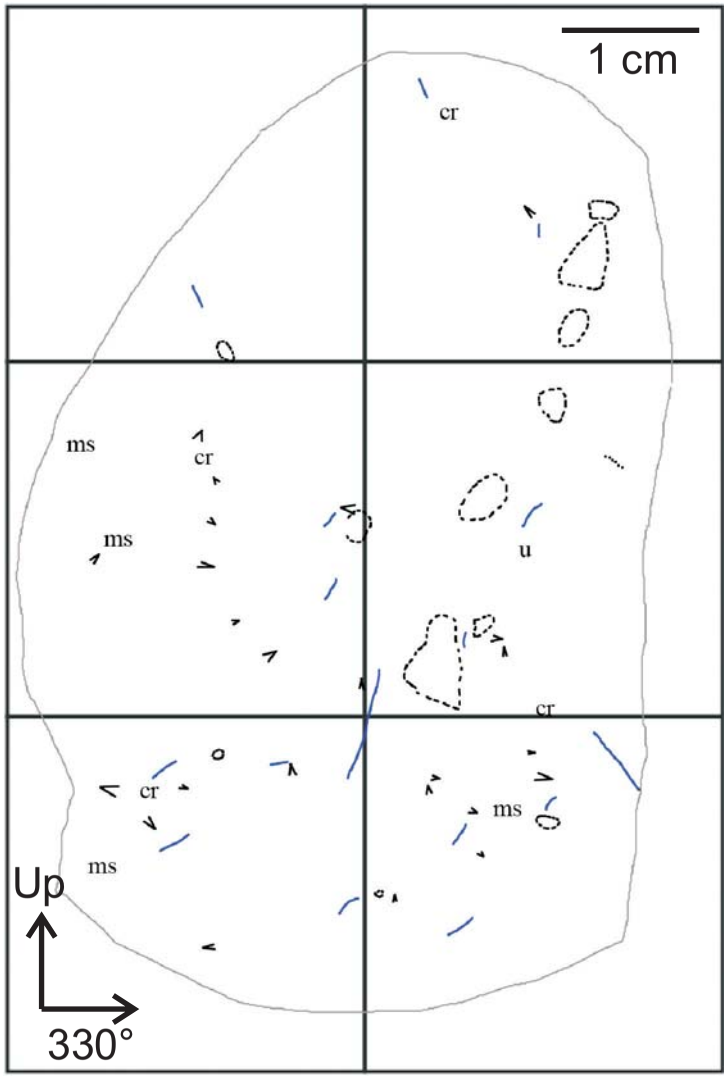

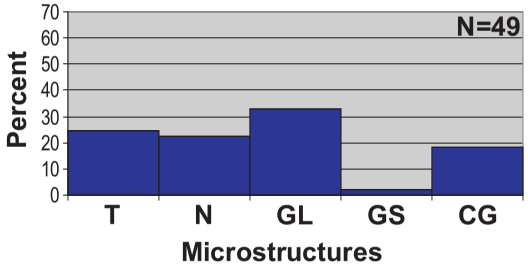

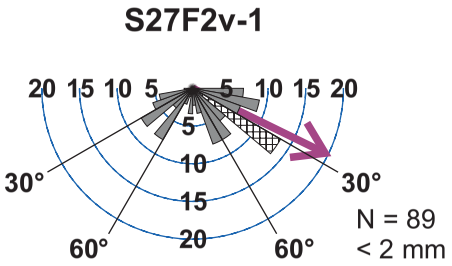

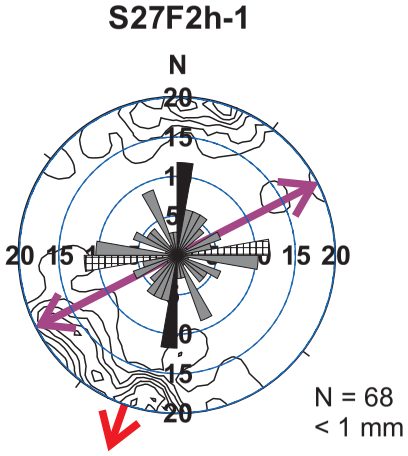

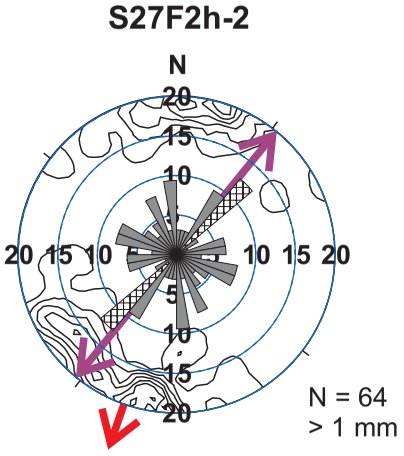

Figure 4.8-6. Microfabrics S27F2v-1, S27F2h-1 and S27F2h-2, and microstructure map and frequency histogram for thin section S27F2v. See Figures 3.3-4 and 3.3-5 for legends.

till might have been obtained at this site if clast wear feature data were not restricted to pebble-sized clasts (Benn 1994; 1995).

The orientation of the main mode of F1 and the principal eigenvector of F3 are consistent with the principal eigenvector of fabric 27 reported by Lian (1997) and Lian & Hicock (2000) (Fig. 4.8-1), and imply a shearing force parallel to Cutoff Valley during the deposition of unit 2. The inclined lower contact of unit 2 is an indication that the paleo-slope was not horizontal at the time of deposition, so clast plunge directions are an unreliable means of estimating ice flow direction. Previous studies in the region have inferred the general ice flow direction to be toward the south during the last glacial maximum (Clague *et al.* 1989). If ice was locally constrained by topography during the last glacial maximum as suggested by previous authors (Tipper 1971; Lian and Hicock 2000), then it is likely it would have flowed SW along Cutoff Valley toward Fraser Valley (Fig. 3.1-1).

The colour variations (observed both at the macroscale and micro-scale) within the diamicton of unit 2 suggest that sediment was derived from at least two different sources and has experienced some intermixing. The brown coloured diamicton observed in thin section is likely equivalent to the light grey patches observed at the macroscale within the unit 2 diamicton near its upper contact (Fig. 4.8-2A). The dark grey diamicton observed in thin section likely corresponds to the macroscopically observed dark grey patches (Fig. 4.8-2A). As with units 1 and 3, the clasts in unit 2 are dominated by local bedrock lithologies. Though the lower contact of unit 2 is erosional, it is impossible to determine how much of the diamicton material was sourced directly from unit 1 and how much has been sourced from bedrock or sediment further NE up the valley. Imbricated clasts and striae observed on the surfaces of clasts are a testament to slip between particles during lodgement processes at the ice-bed interface and (or) plastic shear deformation of the diamicton. The colour changes in the till could either be linked to shifts in sediment type supplied by the glacier, shifts in sediment type supplied by a plastically deforming bed, or a combination of both. If a plastically deforming layer was present, it could have been as thin as a few centimetres below the glacier sole, but no thicker than 3.25 m (the thickness of the diamicton unit). The intermixing between the light and dark coloured diamictons could have occurred during plowing at the ice-bed interface and (or) during subglacial shear deformation of a lithologically heterogeneous glacier substrate (Hooyer and Iverson 2000a). At the microscale, the sometimes sharp and angular contacts between the brown and grey matrices, and the tendency for

fractures to follow paths within the brown matrix suggests that the dark grey matrix was slightly more cohesive than the brown matrix, causing the grey matrix to break apart in angular fragments during diamicton deposition and mixing.

Grain rotation, squeeze flow, discrete shear, and grain crushing were common micro-scale deformation processes. The N-S trending cluster in microfabric S27F2h-1, and the NE-SW trending cluster in microfabric S27F2h-2 may record the alignment of sand-sized grains subparallel to the main shear direction implied by the orientation of the principal eigenvector of macrofabric F2 (NNE-SSW) (Fig. 4.8-6). The E-W trending cluster in S27F2h-1 and the spread out WNW-ESE cluster in S27F2h-2 (Fig. 4.8-6) may reflect a tendency for sand sized grains to rotate during shear under elevated subglacial porewater pressures (Benn 1995), or to collide with grains of similar or larger sizes (Thomason and Iverson 2006). Grain collisions and rotations would also explain the wide range of sand grain apparent plunges measured from vertical microfabric S27F2v-1.

Lian (1997) does not describe unit 3 in detail, but suggests it could be winnowed subglacial till, or ablation till. The unit 3 diamicton contains angular clasts of local lithology and indistinct layering approximately parallel to its lower contact. Its position at the top of the sequence and under a steeply sloping ground surface suggests that at least part of this unit consists of post-glacial colluvial and (or) alluvial deposits.

4.9 Sites 25 & 26

4.9.1 Macroscale sedimentology and structural geology

Sites 25 and 26 are located in a road cut on Pavilion plateau at an elevation of ~1500 m asl (Fig. 3.1-1). Exposed at site 26 is about 1 m of partially deformed argillite bedrock, sharply overlain by two diamictons (units 1 and 2) (Figs 4.9-1, 4.9-2). Only unit 2 diamicton is exposed at site 25 (Fig. 4.9-3), which is located ~5 m NW of the left side of the exposure shown in Figure 4.9-1. Diamicton samples for micromorphological analyses and clast fabric data (F28 and F29, Figs 4.9-1, 4.9-3) were collected from unit 2 at both sites 25 and 26.

Seven breaks in the argillite bedrock were measured and reported as a series of fractures and shears by Lian (1997). These fractures and shears were measured from an ~30 m length of exposed bedrock starting from the site of F28 to ~10 m SE of F29, and are plotted on the stereograms of Lian's (1997) fabric 25 (fab-25) and F29 (Figs 4.9-1, 4.9-3). The fractures have steep (~50°) dips down toward the N. The shear planes

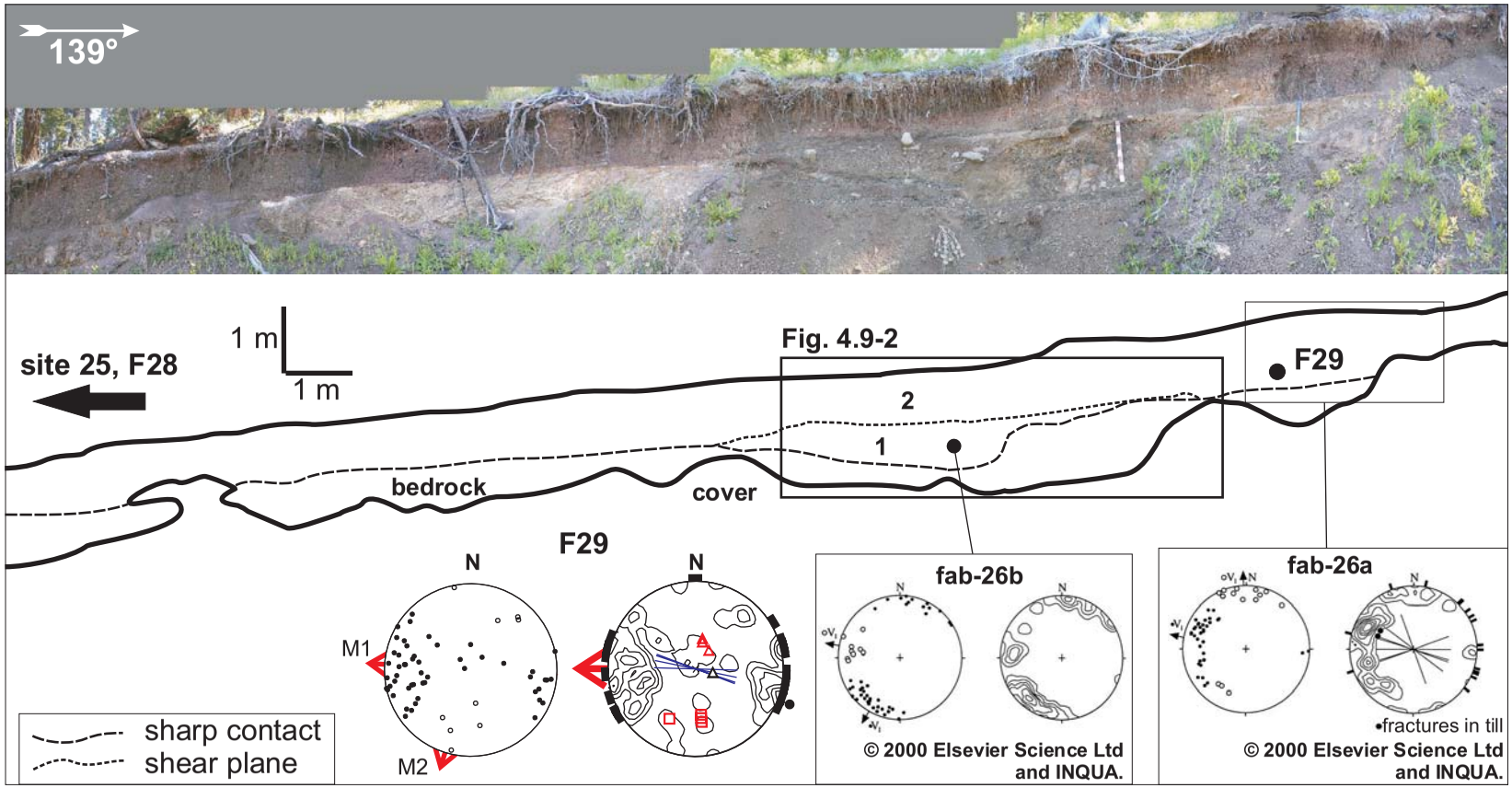

Figure 4.9-1. Site 26 showing two diamicton units (1 and 2), and the location of F29. Unit 1 is restricted to the bedrock depression and overlies the bedrock (Fig. 4.9-2). Unit 2 overlies unit 1 in the depression, and bedrock on either side of the depression. F28, site 25 (Fig. 4.9-3) is located ~20 m NW of F29 within the unit 2 diamicton (black arrow). The shear plane separating diamicton units 1 and 2 (Fig. 4.9-2) is plotted as a pole to plane on the contour stereogram of F29 (black triangle). The red squares and triangles on the contour stereogram of F29 record fractures (squares) and shear planes (triangles) measured by Lian (1997) in the underlying bedrock. These fractures and shears have since been covered by colluvium. The stereograms of Lian and Hicock's (2000) fabrics (fab-26a and fab-26b) are reprinted with permission and the approximate location of these fabrics are shown. See Figure 3.3-1 for stereogram legend.

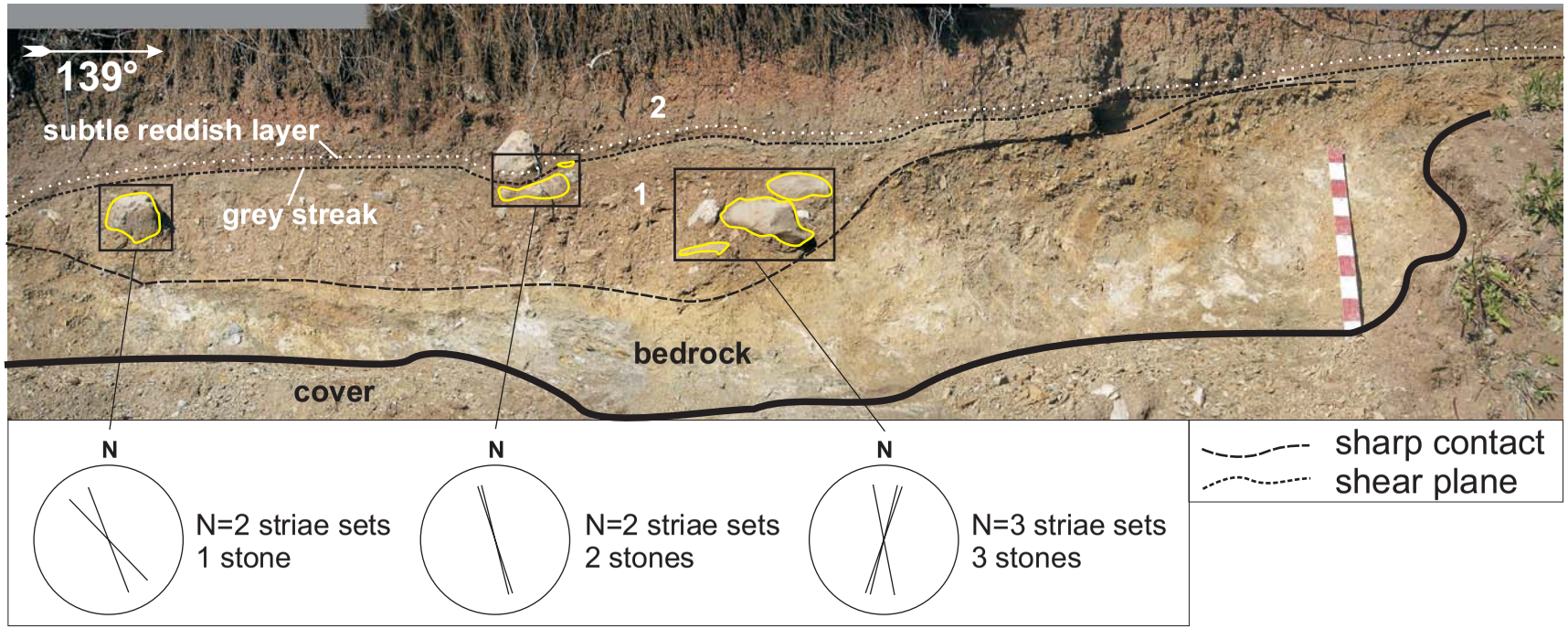

Figure 4.9-2. Close-up of the bedrock depression at site 26, showing argillite bedrock, and diamicton units 1 and 2. The orientations of striae sets were measured on the tops of seven cobble to boulder-sized stones (delineated in yellow) in unit 1 and are plotted as lines on stereograms (see Fig. 3.3-1 for stereogram legend). A subtle reddish layer is visible at the base of unit 2 (white dotted line), and a grey streak follows the shear zone between units 1 and 2. Metre stick with decimetre subdivisions for scale.

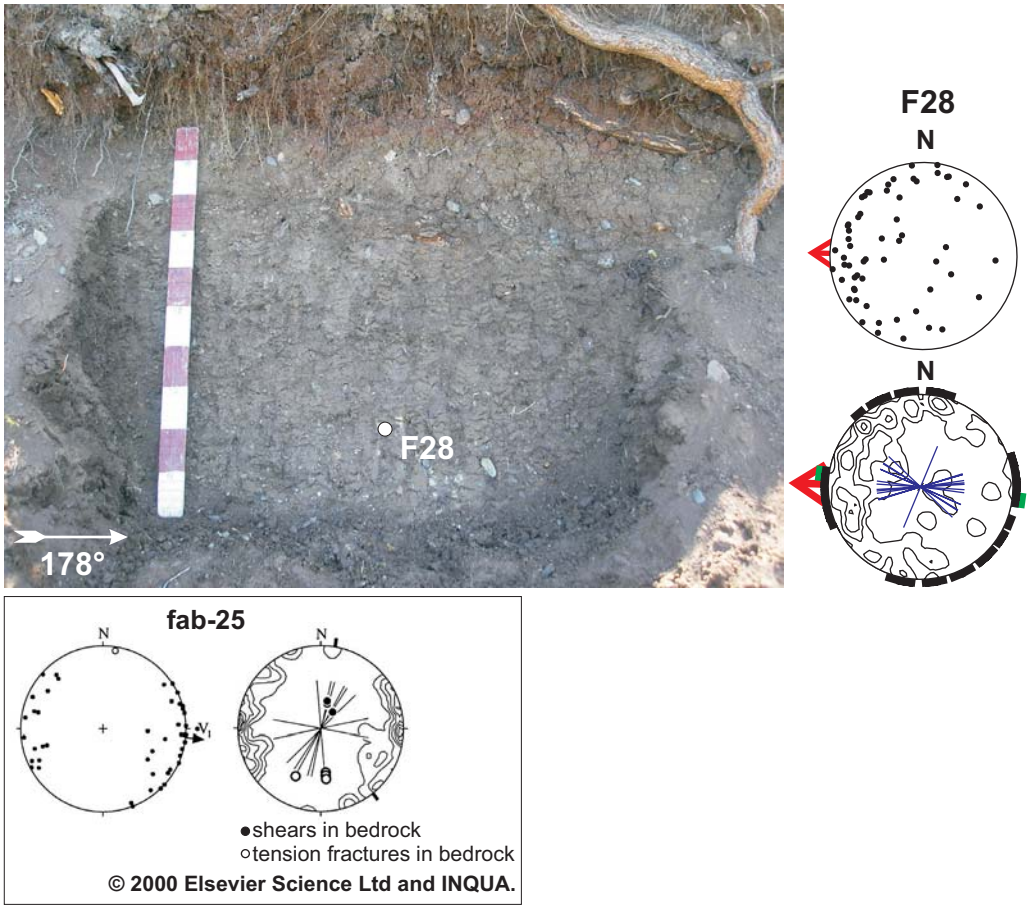

Figure 4.9-3. F28, site 25. The stereogram of fabric 25 (fab-25) is adapted from Lian and Hicock (2000) with permission. Fabric 25 was measured from the same exposure as F28. The shear plane and tension fracture measurements recorded in the fabric 25 stereogram were obtained from the bedrock that underlies unit 2 between the locations of F28 and the bedrock depression shown in Figure 4.9-2. These shear planes and tension fractures are now covered. See Figure 3.3-1 for stereogram legend. Metre stick with decimetre subdivisions for scale.

consist of pulverized bedrock and have shallower (~25°) dips down to the SW (Lian 1997). These fractures and shears in the bedrock have since been covered by colluvium and thus, were not observed in this study.

Unit 1, site 26 is 0.75 m thick, has a sharp lower contact, and is confined to a bedrock depression just NW of F29 (Figs 4.9-1, 4.9-2). Its clast concentration is visually estimated to be ~15%, and it has a higher frequency of cobbles and boulders than unit 2. The orientation of the youngest (faintest) striae sets preserved on the tops of 6 cobbles and boulders were measured in unit 1 (Fig. 4.9-2). These generally trend N-S. An undulating shear plane marked by a grey streak separates units 1 and 2 (Fig. 4.9-2). The general orientation of the shear plane was measured and is plotted as a pole to plane (black triangle) on the stereogram of F29. It has a gentle dip down to the E. Lian's (1997) fabric 26b (fab-26b, Fig. 4.9-1) was measured in unit 1, and shows a bimodal distribution containing a NE-SW trending primary mode, and a WNW plunging secondary mode.

Unit 2 is ~2 m thick and contains massive, matrix-supported, clast poor (3-5%, Table 4.2-1), sandy silt diamicton (Fig. 4.2-2). The diamicton is heavily fractured with a prismatic structure, and falls apart easily when touched. Reddish, elliptical shaped zones, several metres in diameter were observed in unit 2, site 25 by Lian (1997). These zones were not observed in unit 2 in this study and may have since eroded away from the exposure face. A subtle reddish layer, also reported by Lian (1997), is visible near the base of unit 2 at site 26 (Fig. 4.9-2). F29 was measured in unit 2 at site 26, adjacent to the bedrock depression at ~0.65 m below the surface. F28 was measured at a similar depth in unit 2 at site 25, ~20 m north of F29 (Figs 4.9-1, 4.9-3).

F29 is spread bimodal with a primary mode oriented E-W and a secondary (n=9) transverse mode (Fig. 4.9-1, Table 4.2-2). The majority of striae on clast tops are parallel to clast a-axes and no keels were identified (Table 4.2-3). Fractured ends show no preferred direction, and one bullet nose points to the E (Fig. 4.9-1). Faceted clasts comprise 7% of the sample (Table 4.2-3). F29 was measured in the vicinity of Lian's (1997) fabric 26a (fab-26a, Fig. 4.9-1), which contains a primary mode plunging to the WNW, a secondary N-S trending mode, and a high number of fractured (lee) ends pointing E.

F28 shows a single very spread out mode with a principal eigenvector similar to that of F29 (Fig. 4.9-3, Table 4.2-1). Clast surface striae generally follow clast a-axes (Table 4.2-3) and one keel on a clast bottom is oriented subparallel to the principal

eigenvector (Fig. 4.9-3). One clast has striae curving around convexities and concavities (Table 4.2-3). Out of all clasts in the sample, 38% are faceted and 3% have keels (Table 4.2-3). F28 was measured in the vicinity of Lian's (1997) fabric 25 (fab-25, Fig. 4.9-3), which is spread unimodal with a single fractured (lee) end pointing to the SE. In F28 and F29, particular clast shapes do not conform to predefined modes, or prefer any specific orientation (Fig. B-1, Appendix B).

4.9.2 Micromorphology

Two samples were collected for thin section analysis, one from the site of F28 and the other from the site of F29. A horizontal and vertical thin section was cut from each sample for qualitative and quantitative analysis. These are labelled S25F28v, S25F28h, S26F29v and S26F29h. In thin section, the diamicton at sites 25 and 26 is heavily fractured, plasma supported and dominated by subangular to subrounded metasedimentary (argillite) skeletal grains (Figs 4.9-4A, 4.9-5A).

The orientations of major and minor fractures in thin section S26F29v show no systematic pattern (Figs 4.9-5A, 4.9-5D). Major fractures in thin section S25F28v are somewhat more systematic (Fig. 4.9-4A). Four of these have moderate apparent dips (65-40°) down toward 54° azimuth, and two have more shallow apparent dips (15-25°) down toward 234° azimuth. Some skeletal grains in both thin sections are aligned subparallel to major fractures (Figs 4.9-4A, 4.9-5A). Some dark grey patches are visible within the matrix of thin section S25F28v, and the largest of these is heavily fractured (Figs 4.9-4B, 4.9-4D).

Visible discrete microstructures were rare in both vertical thin sections (Figs 4.9-6, 4.9-7). A necking structure (Fig. 4.9-4E), grain lineation (Fig. 4.9-4F) and a crushed grain (Fig. 4.9-4G) were identified in section S25F28v, and three grain lineations (Fig. 4.9-5B) and five crushed grains (Fig. 4.9-5F) were identified in section S26F29v. No turbates were identified, however small grains in close proximity to relatively larger grains often had apparent long axes aligned subparallel to the edges of the larger grain (Fig. 4.9-5C).

Vertical microfabrics S25F28v-1 and S26F29v-1 show that sand grain plunges are variable, and both vertically and horizontally oriented grains are common (Figs 4.9-6, 4.9-7). Microfabric S26F29v-1 has a much steeper plunging principal eigenvector than S25F28v-1. Horizontal microfabrics S25F28h-1, S26F29h-1 and S26F29h-2 have principal eigenvectors and tight clusters that are oriented roughly perpendicular to the

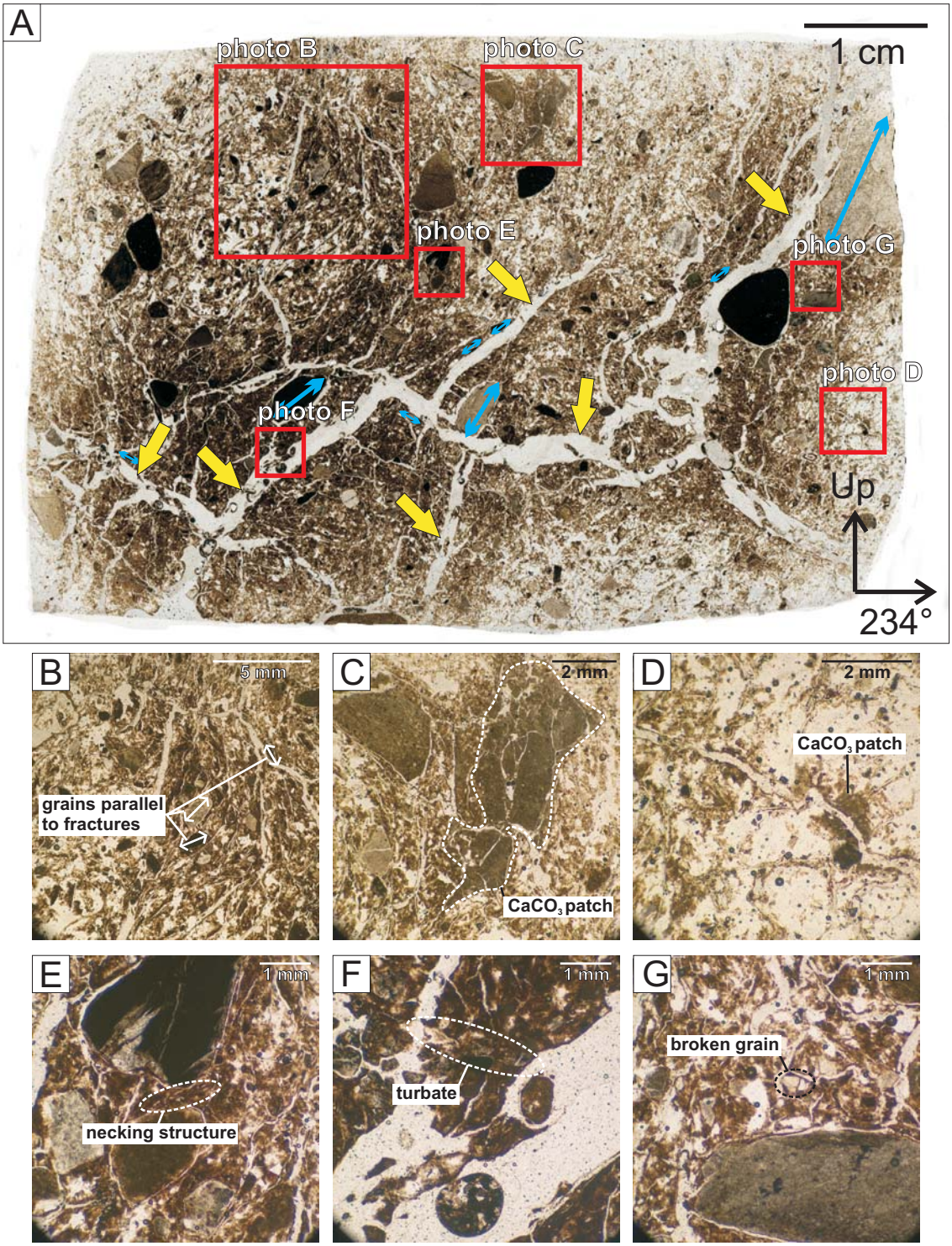

Figure 4.9-4. Thin section S25F28v. A) A 2400 dpi scan of the thin section showing planar voids (yellow, wide arrows) and skeletal grains (blue, narrow arrows) aligned parallel to them. The locations of microphotographs B, C, D, E, F and G are indicated by red squares. Microphotographs show sand grains oriented parallel to fractures (B), calcium carbonate patches (C, D), a necking structure (E), a grain lineation (F), and a broken grain (G).

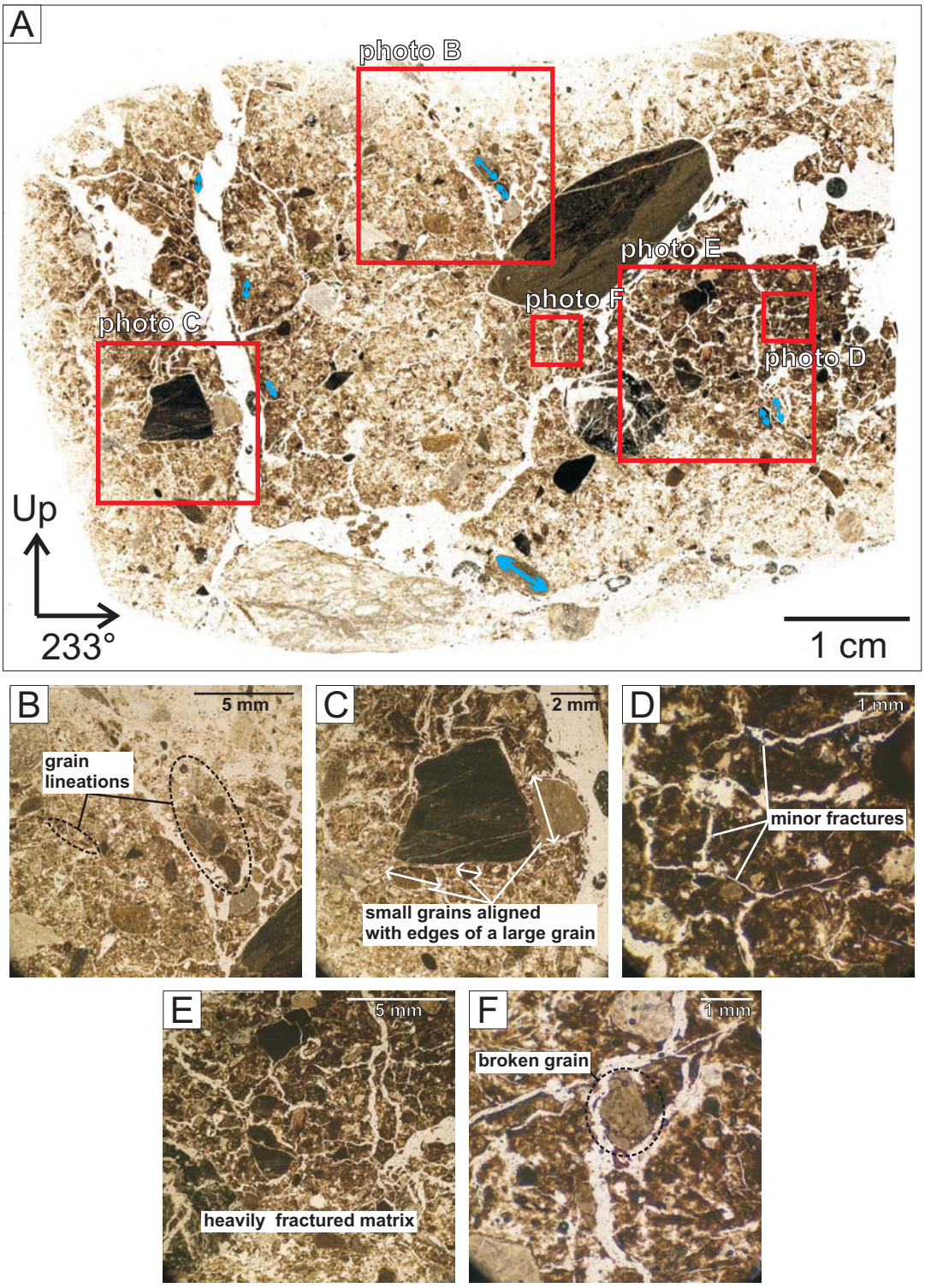

Figure 4.9-5. Thin section S25F29v. A) A 2400 dpi scan of the thin section showing skeletal grains (blue arrows) aligned with planar voids. The locations of microphotographs B, C, D, E, and F are indicated by red squares. Microphotographs show grain lineations (B), small grains aligned with the edges of a large grain (C), minor fractures with variable orientations (D), a heavily fractured matrix (E), and a broken grain (F).

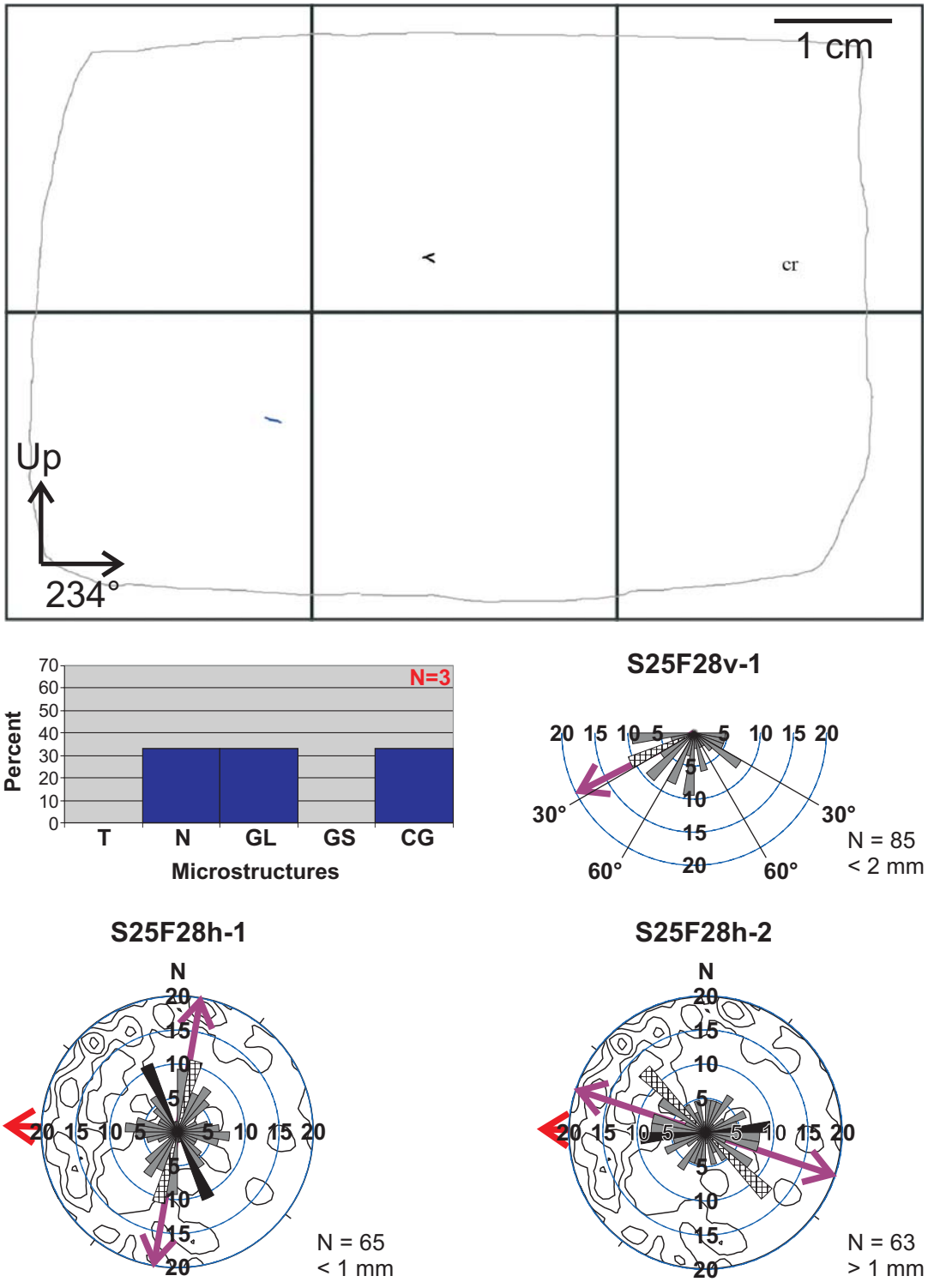

Figure 4.9-6. Microfabrics S25F28v-1, S25F28h-1 and S25F28h-2, and microstructure map and frequency histogram for thin section S25F28v. See Figures 3.3-4 and 3.3-5 for legends.

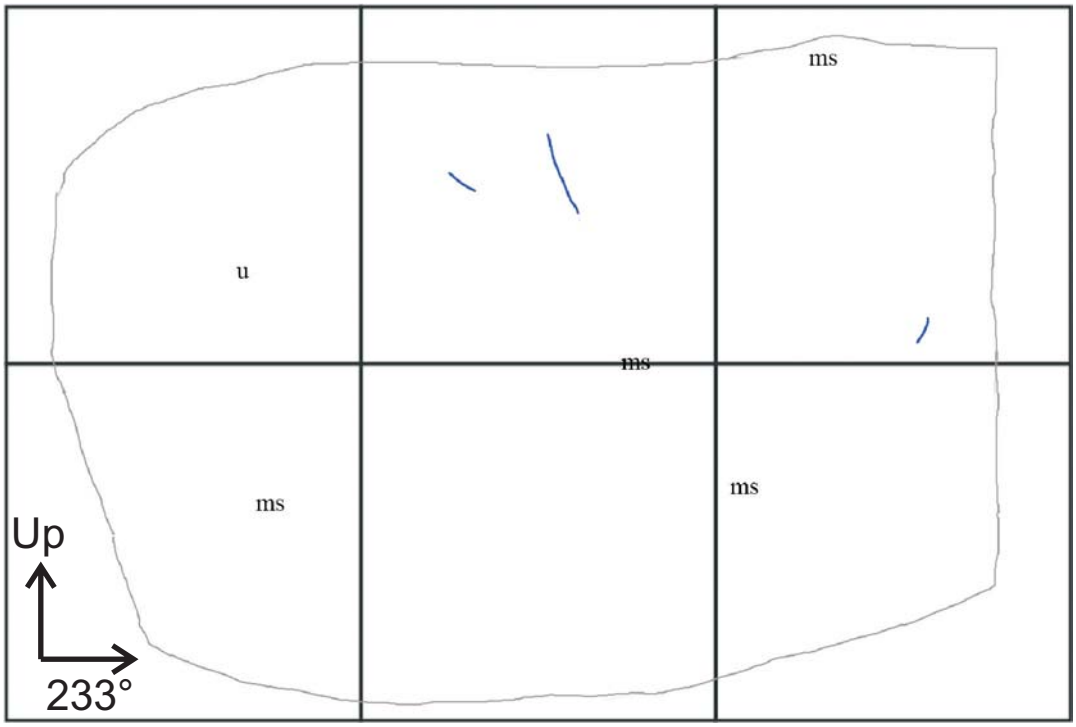

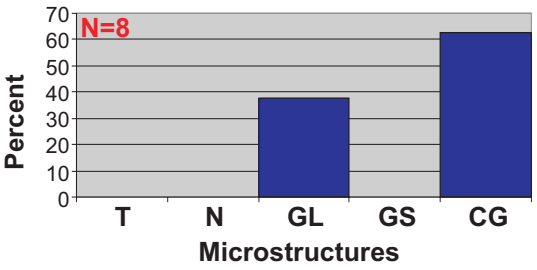

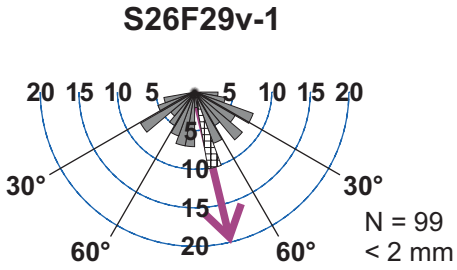

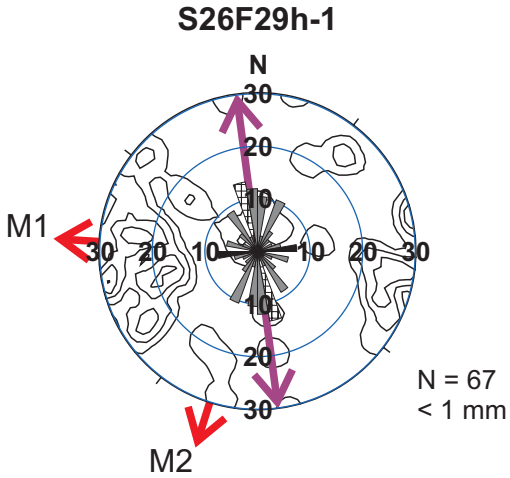

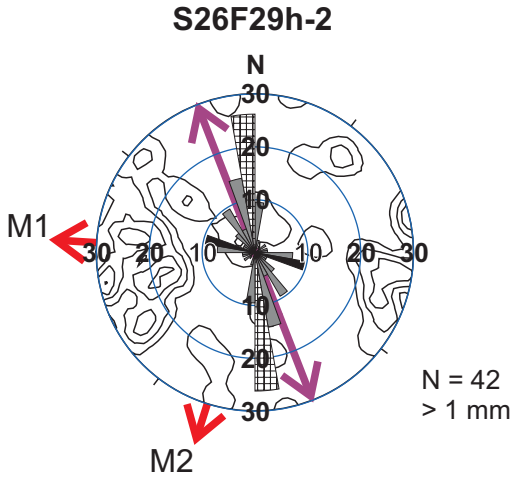

Figure 4.9-7. Microfabrics S26F29v-1, S26F29h-1 and S26F29h-2, and microstructure map and frequency histogram for thin section S26F29v. See Figures 3.3-4 and 3.3-5 for legends.

primary mode or principal eigenvector of macrofabrics F28 and F29, respectively (Figs 4.9-6, 4.9-7). Horizontal microfabric S25F28h-2 shows maximum clustering in a direction parallel and oblique to that of the principal eigenvector of macrofabric F28 (Fig. 4.9-6).

4.9.3 Interpretation

Lian's (1997) interpretation of diamicton genesis of units 1 and 2 at sites 25 and 26 was based on the structural geology of the diamicton and bedrock, glacigenic wear features on clasts, and three clast fabrics; one located in unit 2 near F28 (his fabric 25), one located in unit 2 near F29 (his fabric 26a), and one located in unit 1, north of F29 (his fabric 26b) (Figs 4.9-1, 4.9-3). Lian (1997) and Lian and Hicock (2000) have classified both units 1 and 2 as deformed lodgement till. Their proposed rendition of events is as follows: 1) ice advanced generally northward over the Pavilion plateau and eroded older sediments, 2) a cold-based ice front reached and passed over sites 25 and 26. During this time bedrock was fractured, 3) warm-based ice arrived and till was deposited mainly by lodgement (unit 1 and possibly part of unit 2), 4) as the till thickened and porewater increased, ductile and (or) ductile-brittle deformation ensued (unit 2). Clasts of pre-glacial sediments (reddish diamicton) were eroded up-glacier of sites 25 and 26, entrained, and smeared within the deforming till creating the reddish elliptical zones previously observed at site 25 (Lian 1997) and the thin reddish layer at site 26 (unit 2, Fig. 4.9-2).

The high silt content, glacigenic clast wear features and sharp lower contacts of units 1 and 2 (Figs 4.9-1, 4.9-2, 4.9-3) suggest that they are subglacial tills that were initially deposited by lodgement. Bullet noses and fractured ends recorded in this study show no preferred direction (Table 4.2-3) and clast fabric modes are spread. The bullet noses and fractured ends may be inherited features, and (or) clasts have been re-oriented during ploughing or after lodgement at the ice-bed interface. Significant entrainment of sub-till material into either units 1 or 2 was not observed. Therefore units 1 and 2 are also classified here as deformed lodgement tills.

If the fracture and shear planes measured in the bedrock by Lian (1997) at site 26 are associated with glaciotectonic deformation, they would indicate brittle deformation of the substrate as a result of stresses imposed by overlying (possibly cold-based) ice, and a northward ice flow direction (Lian 1997). If subglacial till was being deposited at this time, it would have had to have been sufficiently rigid to allow subglacial shear

stress to penetrate and deform the underlying bedrock (Boulton 1996). The NNE-SSW primary mode in Lian's (1997) fabric 26b, as well as the ~N-S trending striae on the upper surfaces of cobbles and boulders in unit 1 (Fig. 4.9-2) suggests that the unit 1 diamicton may have been deposted during northward flowing ice during or shortly after the formation of the glaciotectonic features.

The ~E-W trending principal eigenvectors and (or) primary modes of clast fabrics F28, F29 and Lian's (1997) fab-26a (unit 2) suggest that ice flow direction shifted from a northward direction to either an eastward or a westward direction during the deposition of unit 2 (Figs 4.9-1, 4.9-3). An eastward ice flow direction up-slope toward Pavilion Mountain is considered less likely than a westward ice flow direction where ice would flow downhill, therefore a westward shift in ice flow direction is inferred here. The shear zone marked by a grey streak, separating units 1 and 2 suggests that basal ice and (or) mobile till slid over the bedrock depression while the diamicton in the depression (unit 1) remained immobile. In the shear zone, pulverized bedrock was smeared over the diamicton-filled depression forming the grey streak (Fig. 4.9-2).

The heavily fractured matrix observed in thin sections S25F28v and S26F29v includes many subvertical major and minor fractures that contribute to the prismatic structure of the unit 2 diamicton observed at the macroscale (Figs 4.9-4A, 4.9-5A). This structure develops as moist soil dries out, with subvertical fractures forming when shrinkage forces are largely resolved in a lateral direction (Chadwick and Graham 2000). Fracture orientations likely followed the sides of roots and particles as the drying matrix pulled away from these and other more cohesive entities in the matrix. The dark grey precipitates observed in thin section S25F28v (Fig. 4.9-4C, 4.9-4D) are likely calcium carbonate deposits and could be derived from glacial meltwater, meteoric waters, or groundwater.

Few discrete microstructures could be counted within thin sections S25F28v and S26F29v as a result of the high fracture density (Figs 4.9-6, 4.9-7). Nevertheless, they provide evidence of squeeze flow, discrete shear and grain crushing. The subvertical grains measured in the vertical microfabrics (Figs 4.9-6, 4.9-7) may have been re-oriented by the roots penetrating the diamicton from above (both F28 and F29 were measured within 1 m below the ground surface). Given the small size of the particles measured in thin section, it is also conceivable that the lateral shrinkage due to desiccation of this relatively clay-rich diamicton matrix (Table E-1, Appendix E) influenced grain orientation, contributing to the high number of subvertical grains.

The tightest clusters observed in horizontal microfabrics S25F28h-1, S26F29h-1 and S26F29h-2 are transverse to the primary modes and (or) principal eigenvectors of F28 and F29, unit 2 (Figs 4.9-6, 4.9-7). Grain collisions during till deposition and deformation may have contributed to the re-alignment of grains in the horizontal thin sections, however this is hard to justify, given the low clast and skeletal grain and clast concentration of the diamicton (Figs 4.9-4A, 4.9-5A, Table 4.2-1). Alternatively, transversely oriented clusters may record, 1) microscale ductile deformation leading to Jeffrey-style rotation of sand-sized grains into "least-energy" positions during periods of elevated subglacial porewater pressure in unit 2 under westward flowing ice (Jeffery 1922; Hicock *et al.* 1996), or 2) local compression of the till under westward flowing ice where sand grains became oriented transverse to the shear direction.

4.10 Site 57

4.10.1 Macroscale sedimentology and structural geology

Site 57 is located on the Fraser Plateau near Big Bar Lake at ~1100 m asl (Figs 3.1-1, 4.10-1). A road cut exposes ~3 m of over-consolidated, massive, matrix-supported, clast-poor (6-10%, Table 4.2-1), silty sand diamicton (Fig. 4.2-2) (unit 1). Clast concentrations measured in unit 1 may be underestimates, because most of the clasts are similar in colour to the surrounding diamicton matrix (Fig. 4.10-2, Appendix C). Unit 1 is conformably overlain by ~0.5-0.70 m of less cohesive, sandy diamicton with a similar colour, clast concentration and clast lithologies (Figs 4.10-2, 4.10-3). Two clast fabrics, (F19 and F20), were measured within 5 m of each other in unit 1. F19 was measured ~1.25 m below the ground surface and F20 was measured ~0.80 m below the ground surface, the latter just above the site of Lian's (1997) fabric 57 (Fig. 4.10-1). Steeply dipping fractures, were measured at both fabric sites (Figs 4.10-2, 4.10-3).

F19 has a spread bimodal fabric with a principal eigenvector plunging toward the SSE (Fig. 4.10-2, Table 4.2-2). Striae on clast tops generally follow the orientation of clast a-axes, and only one clast had upper surface striae with multiple orientations (Table 4.2-3). Keels on clast bottoms show no preferred orientation, and bullet noses and fractured ends show no preferred direction (Fig. 4.10-2). Out of all clasts in the sample, 42% are faceted and 8% have keels (Table 4.2-3).

F20 has a spread unimodal fabric with two outliers and a principal eigenvector plunging toward the S (Fig. 4.10-3, Table 4.2-1). Clast upper surface striae tend to follow clast a-axes (Table 4.2-3). No keels were identified. Two out of three bullet

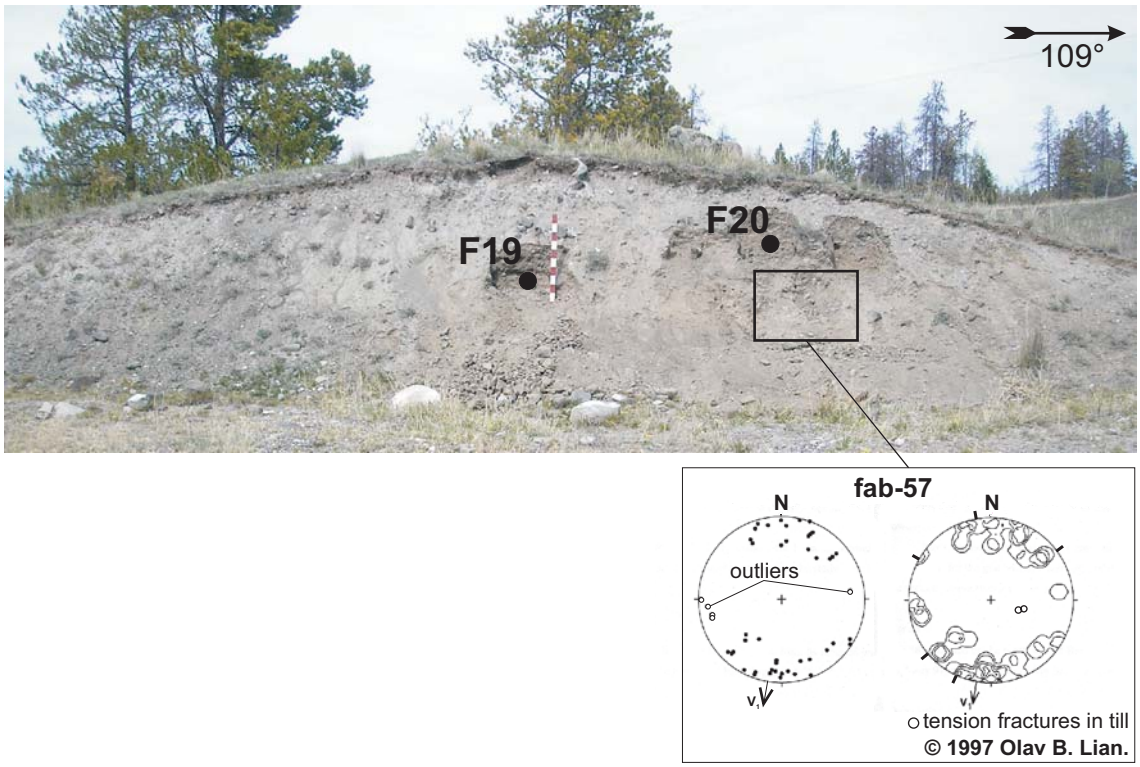

Figure 4.10-1. F19 and F20, site 57. The stereogram of fabric 57 (fab-57) is adapted from Lian (1997). Metre stick with decimetre subdivisions for scale. See Figure 3.3-1 for stereogram legend.

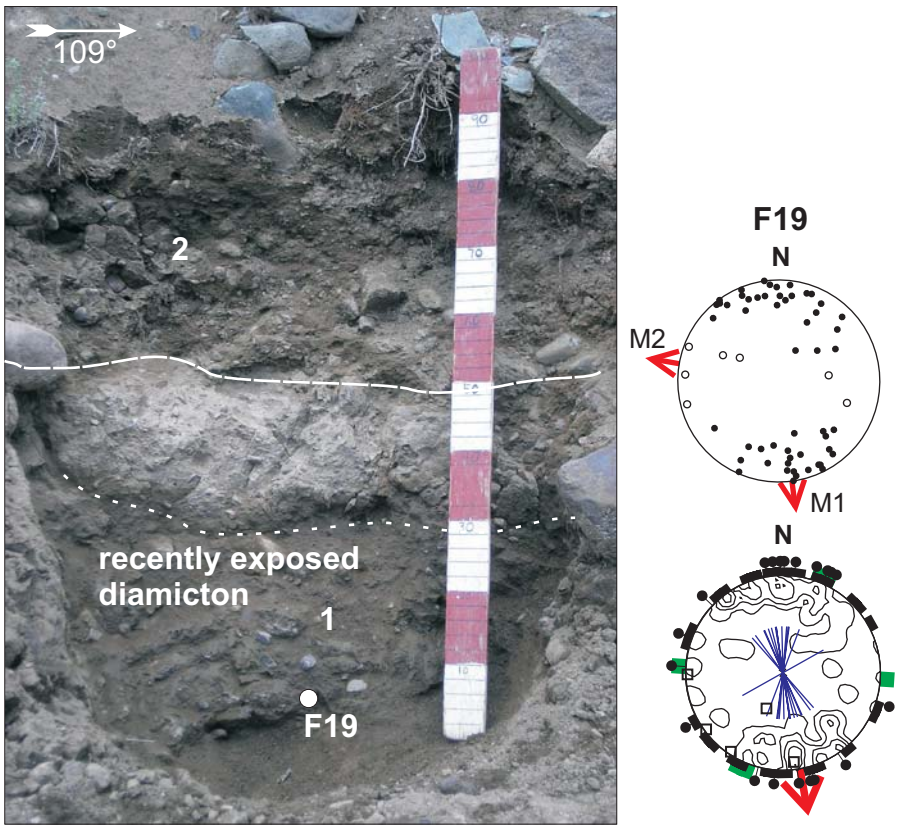

Figure 4.10-2. Sedimentology of site 57 around F19. Unit 1 is over-consolidated clast poor glacigenic diamicton, the darkest part of which has been recently exposed at the time this photograph was taken. Unit 2 is stoney colluvium. Fractures in unit 1 (not visible in the photograph) are plotted as poles to planes on the contour stereogram. See Figure 3.3-1 for stereogram legend. Metre stick with decimetre subdivisions for scale.

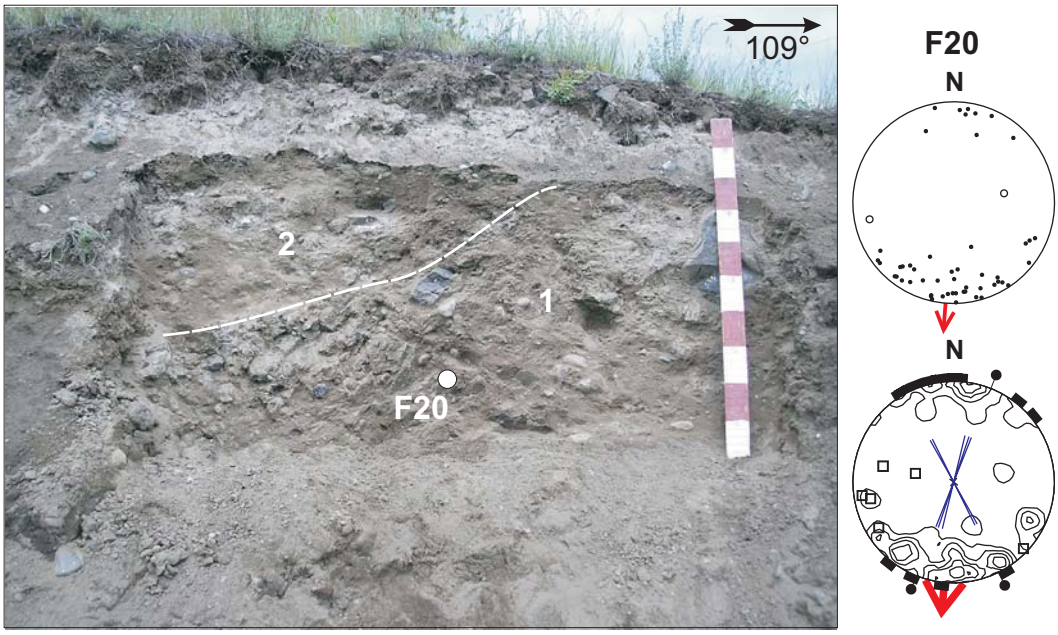

Figure 4.10-3. Sedimentology of site 57 around F20. Unit 1 is over-consolidated clast poor glacigenic diamicton. Unit 2 is stoney colluvium. Fractures in unit 1 (not visible in photograph) are plotted as poles to planes on the contour stereogram. See Figure 3.3-1 for stereogram legend. Metre stick with decimetre subdivisions for scale.

noses point to the S, and fractured ends show no preferred direction (Fig. 4.10-3. Only 6% of clasts were faceted (Table 4.2-3). F20 was measured just above the approximate location of Lian's (1997) fabric 57 (fab-57, Fig. 4.10-1). Fabric 57 is spread unimodal with 5 outliers, a principal eigenvector that plunges to the SSW, and fractured (lee) ends that show no preferred direction. In F19 and F20, particular clast shapes do not conform to predefined modes, or prefer any specific orientation (Fig. B-1, Appendix B).

4.10.2 Micromorphology

Two samples were collected from unit 1 for thin section analysis at site 57, one from the site of F19 and the other from the site of F20. A horizontal (S57F19h) and a vertical (S57F19v) thin section were cut from the sample collected at F19. The fractures in the diamicton at F20, however, made it difficult to obtain a sufficiently large cohesive sample, so only one vertical thin section (S57F20v) was cut from it. In thin section the diamicton at site 57 appears plasma supported, and has abundant subrounded to rounded volcanic grains and a few subrounded to rounded limestone grains (Figs 4.10-4A, 4.10-5A).

Continuous elongate fractures (e.g., Fig. 4.10-4C) are rare in thin sections S57F19v and S57F20v, but vughs lined with a brown opaque residue are common. These are particularly visible in areas where uneven hand grinding has reduced the thin section thickness (Figs 4.10-4B, 4.10-4D). Brown residue also lines the edges of many volcanic grains (Fig. 4.10-4A). A subhorizontal, curvilinear light-coloured band, characterized by a slightly coarser texture than the surrounding matrix, is visible above a large volcanic skeletal grain in section S57F20v (Fig. 4.10-5A, 4.10-5B).

Twenty-five discrete microstructures were identified in section S57F19v, and 42 were identified in section S57F20 (Figs 4.10-6, 4.10-7). Crushed grains (Figs 4.10-5C, 4.10-5G) appear to be the most common discrete microstructure in both thin sections, with turbates (Figs 4.10-5D, 4.10-5F) and necking structures (Figs 4.10-5C, 4.10-5E) together generally representing less than 50% of structures. Grain lineations were only identified in thin section S57F19v (Fig. 4.10-4E), and grain stacks were only identified in thin section S57F20v (Fig. 4.10-5F).

Vertical microfabrics S57F19v-1 and S57F20v-1 show that sand grain plunges typically range from 0° to 70-80° (Figs 4.10-6, 4.10-7). Sand grains plunging down to the NW and SE are well represented in vertical microfabric S57F19v-1, whereas, the majority of sand grains in vertical microfabric S57F20v-1 plunge down to the NW (Figs

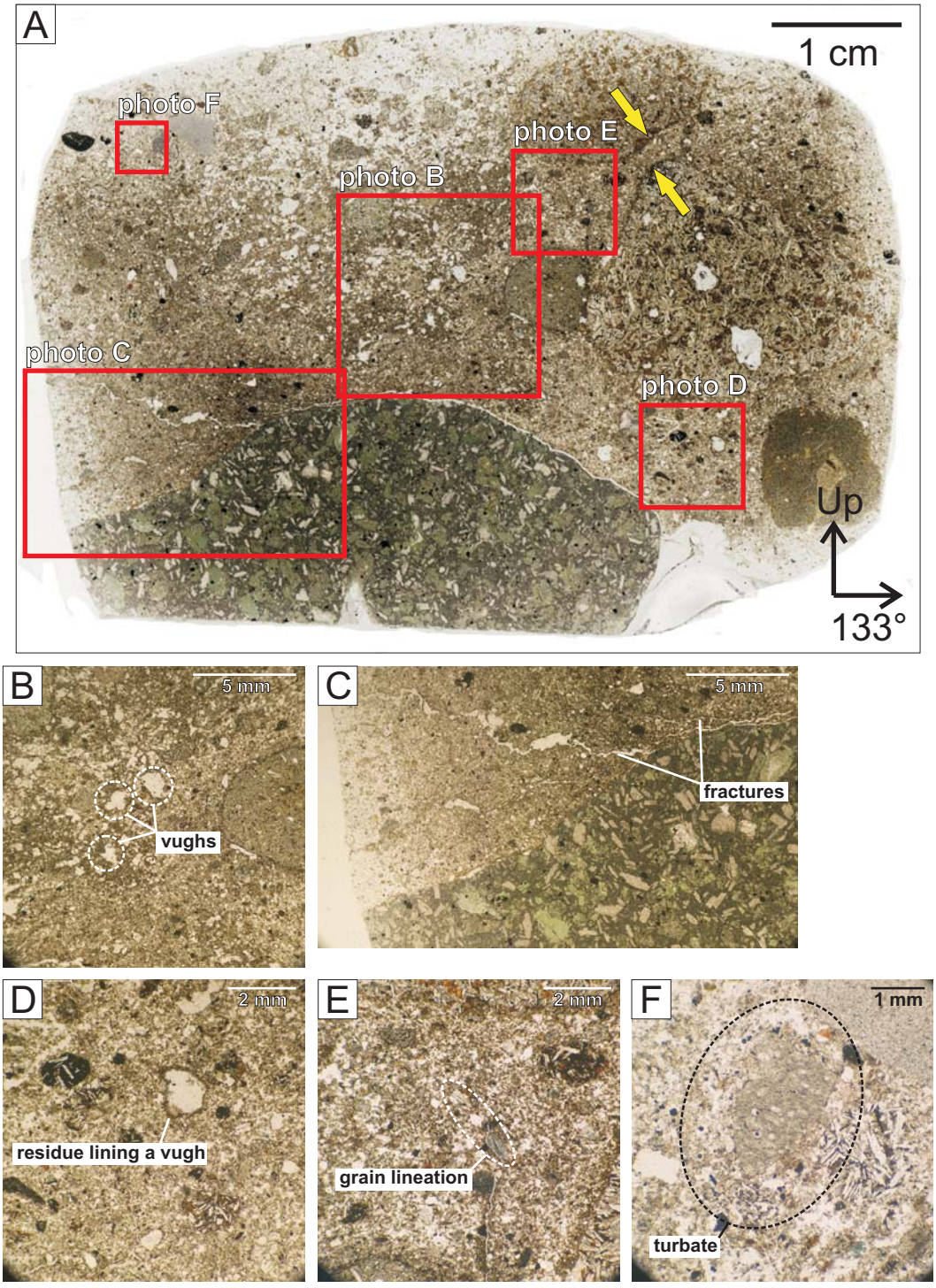

Figure 4.10-4. Thin section S57F19v. A) A 2400 dpi scan of the thin section. Yellow arrows point to a brown residue on the edges of 2 large skeletal grains. The locations of microphotographs B, C, D, E and F are indicated by red squares. Microphotographs show vughs (B), fractures (C), dark residue lining a vugh (D), a grain lineation (E) and a turbate (F).

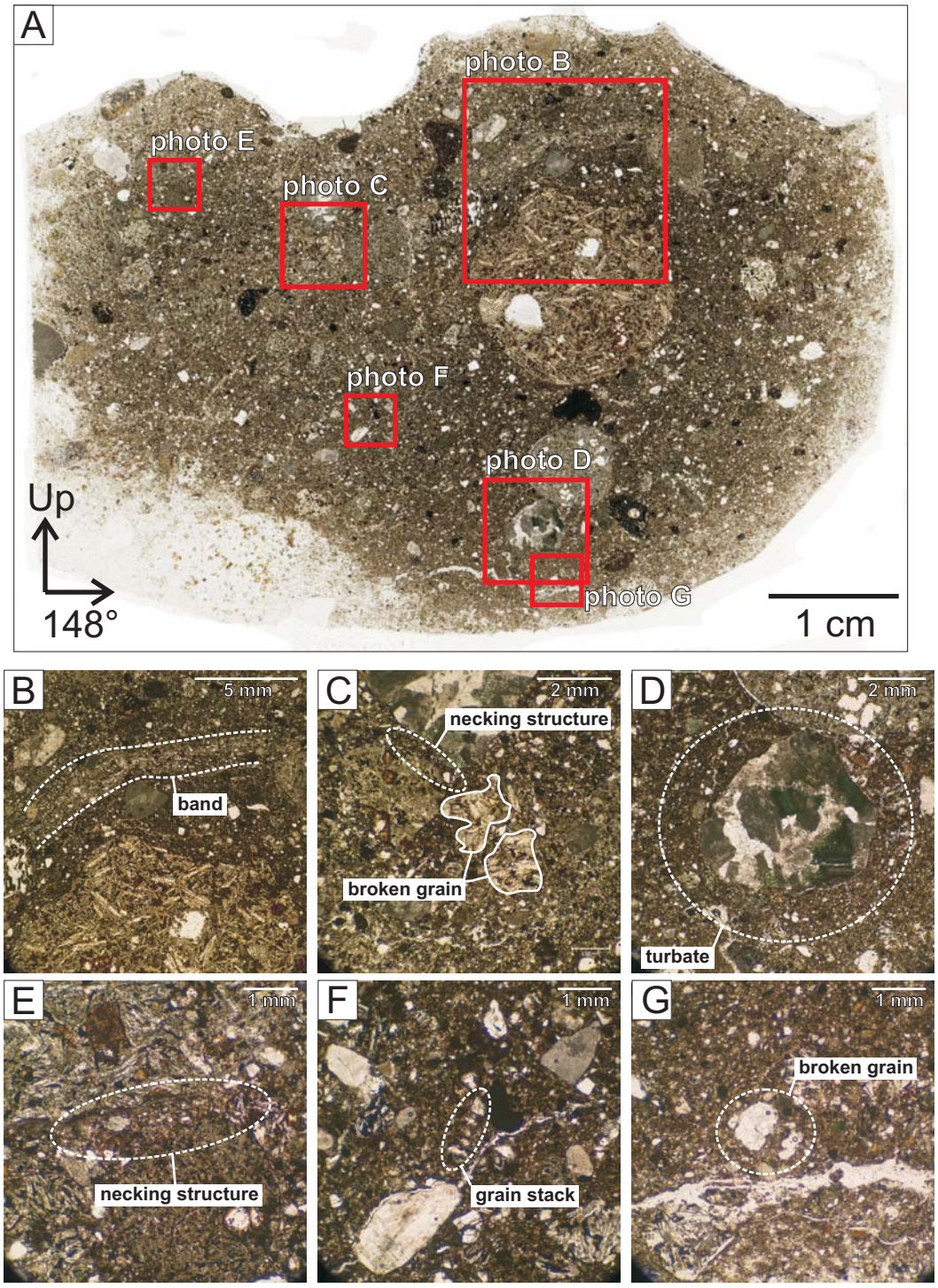

Figure 4.10-5. Thin section S57F20v. A) A 2400 dpi scan of the thin section. The locations of microphotographs B, C, D, E, F and G are indicated by red squares. Microphotographs show a coarse textured domain forming a band (B), necking structures (C, E), broken grains (C, G), a grain stack (F) and a turbate (D).

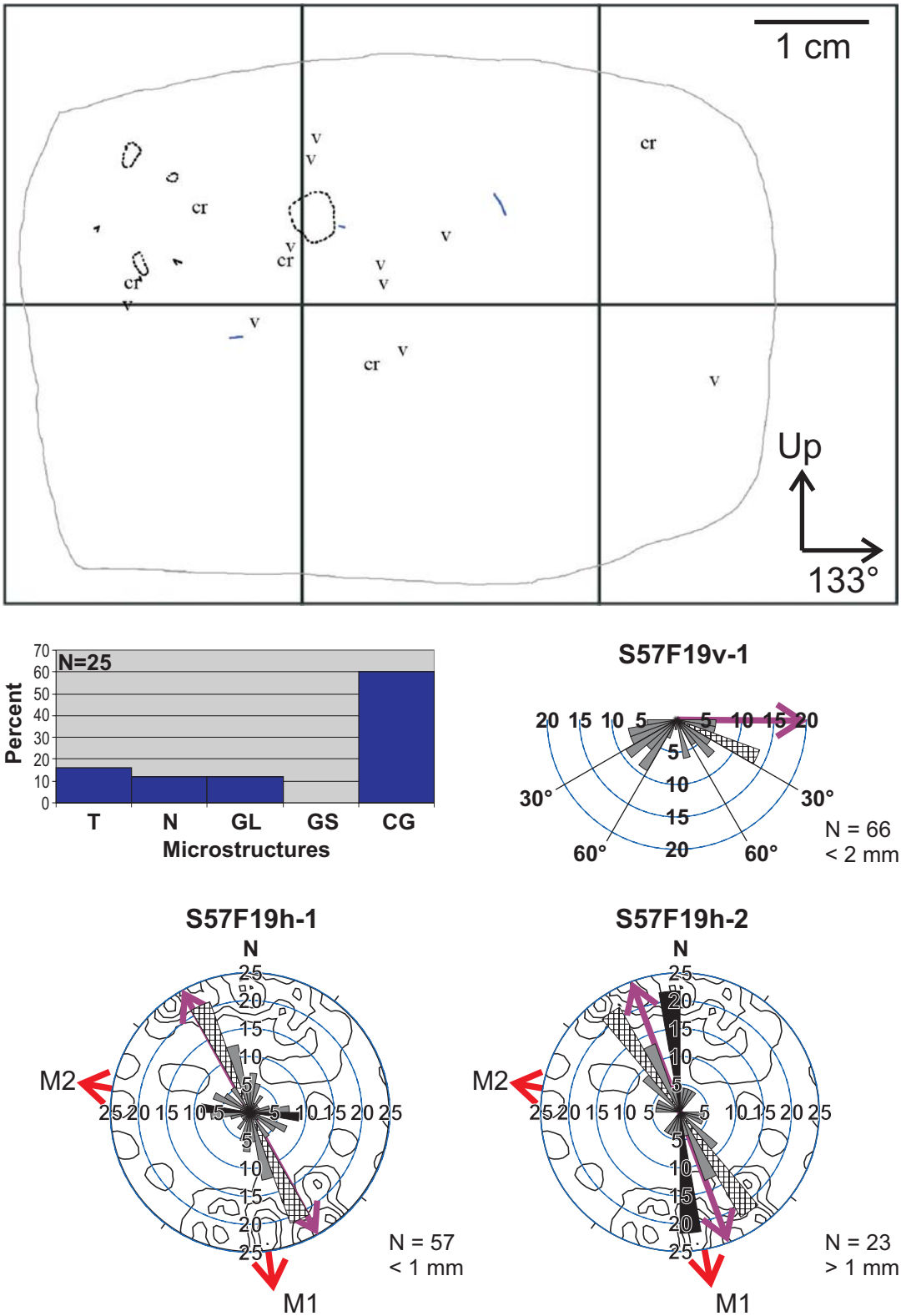

Figure 4.10-6. Microfabrics S57F19v-1, S57F19h-1 and S57F19h-2, and microstructure map and frequency histogram for thin section S57F19v. See Figures 3.3-4 and 3.3-5 for legends.

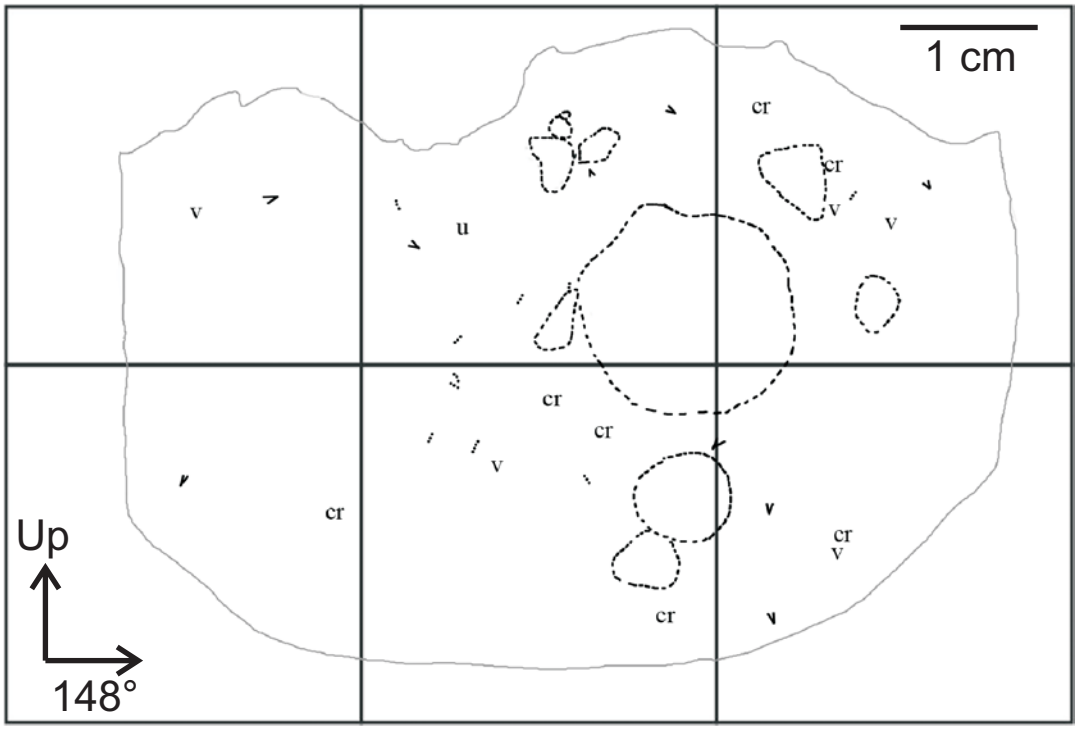

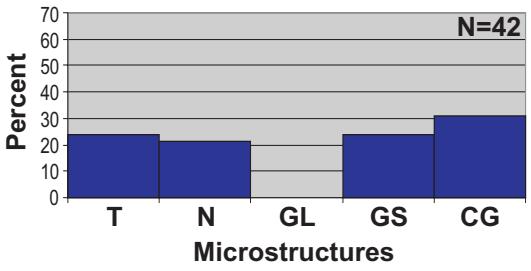

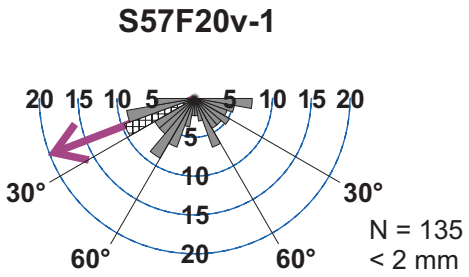

Figure 4.10-7. Microfabric S57F20v-1, and microstructure map and frequency histogram for thin section S57F20v. See Figures 3.3-4 and 3.3-5 for legends.

4.10-6, 4.10-7). Horizontal microfabrics S57F19h-1 and S57F19h-2 are strongly oriented, with principal eigenvectors and tight clusters subparallel to the primary mode of macrofabric F19 (Figs 4.10-6).

4.10.3 Interpretation

Lian (1997) and Lian and Hicock (2000) have classified unit 1, site 57 as deformed lodgement till. The unit 1 diamicton is over-consolidated, contains glacigenic clast wear features and clast upper surface striae that are parallel with clast long axes. These characteristics suggest that unit 1 is a subglacial till that was initially deposited by lodgement. Bullet noses and fractured ends show no preferred direction (Table 4.2-3). Either these features record clast re-orientation during ploughing or after lodgement at the ice-bed interface, or some or all of them have been inherited from an earlier time in the transport history of the pebbles. The spread modes in the clast fabrics (Figs 4.10-2, 4.10-3) suggest a certain degree of clast re-orientation that may also have occurred during ploughing or after lodgement. There is no direct evidence (the lower contact was not visible), of entrainment of sub-diamicton materials into a mobile deforming bed, however. Therefore, sedimentological data collected during this study support Lian (1997) and Lian and Hicock's (2000) interpretation of unit 1 as a deformed lodgement till. The steeply dipping fractures measured within the diamicton at both fabric sites are likely the result of unloading during ice retreat and (or) road excavation.

In thin section, skeletal grains in unit 1 are largely composed of local bedrock, (flow basalts of the Fraser Plateau, Roddick *et al.* 1976) (Figs 4.10-4A, 4.10-5A). Limestone grains may have originated in the Marble Range. The roundness of the skeletal grains may be indicative of fluvial transport prior to glaciation. The brown residue observed in thin section is a testament to the susceptibility of volcanic grains to chemical weathering, which likely contributed to their rounding in a glacial environment where subglacial and proglacial meltwater is present. Though few fractures were visible, the vughs observed in thin section likely served as conduits for glacial meltwater, meteoric waters and (or) groundwater. The curved light-coloured band above the skeletal grain in thin section S57F20v (Fig. 4.10-5A, 4.10-5B) is suggestive of grain rotation in a somewhat texturally heterogeneous ductile matrix.

Discrete microstructures observed in sections S57F19v and S57F20v are indicative of grain crushing and to a slightly lesser extent, grain rotation, squeeze flow, discrete shear, and grain stacking. The unusual relative abundance of brittle type

microstructures (Figs 4.10-6, 4.10-7) may be due to one or all of the following reasons: 1) ductile type microstructures are more difficult to identify in tills with such high sand content (72%, Table E-1 Appendix E). Similar correlations have been noted by Hart *et al.* (2004). 2) The brittle type microstructures are the result of deformation under low porewater pressures, which increased the friction between adjacent sand grains leading to a higher frequency of grain crushing, or 3) grain stacking and crushing was facilitated by the low silt and clay content (Fig. 4.2-2, Table E-1, Appendix E). Silt and clay serves to reduce friction between colliding grains causing them to slide past each other, rather than to break (Iverson *et al.* 1997; Hiemstra and Rijsdijk 2003).

Most sand sized grains have apparent plunges less than 60°, consistent with the plunge range of both macrofabrics (0-62° for F19, and 0-51° for F20, Figs 4.10-6, 4.10-7). The strong correlation between the horizontal microfabric orientations and the principal eigenvector of the macrofabric suggest that sand sized grains were oriented by the same lodgement or subglacial shearing processes responsible for the orientation of the pebble sized clasts.

The precise origin of unit 2 (unconsolidated stony, silty sand diamicton, Figs 4.10-2, 4.10-3) is uncertain and was not analysed in detail in this study or by Lian (1997). Because the diamicton colour, clast concentration and clast lithologies are similar to those of unit 1, it is likely that unit 2 consists of unit 1 diamicton that has been remobilized and re-deposited during excavation of the roadcut and adjacent ditch, and by colluvial processes.

4.11 Site 22

4.11.1 Stratigraphic context of site 22

Site 22 is located in a cliff on the west side of Fraser Valley and across from Big Bar Creek (Fig. 3.1-1). The lithostratigraphy of Fraser Valley along a stretch that starts ~2.5 km N of the mouth of Big Bar Creek and ends at the mouth of Cavanagh Creek (Fig. 3.1-1), has been described in detail by Lian and Hicock (2001), and is briefly summarized here. Based on sedimentological data collected from site 22 and nine other sites along this stretch (sites 14, 18, 33, 35, 40, 51, 53, 54, and 63 in figs 1-4 of Lian and Hicock 2001), these authors have divided the valley fill into seven lithostratigraphic units (units I-VII, Fig. 4.11-1). These include (glacio)fluvial or deltaic sediments overlying bedrock (unit I), re-worked glacigenic sediment (and possibly some non-glacigenic) that was deposited either subaqueously or subaerially by gravity (unit II), glaciofluvial gravel

and sand deposited by meltwater (unit III), glaciolacustrine sediment with nine optically stimulated luminescence (OSL) dates ranging from 52 ± 5 ka to 183 ± 18 ka (unit IV), subglacial till with some clasts showing evidence of lodgement (unit V), debris flow and alluvial sediments deposited soon after deglaciation (unit VI), and post-glacial fluvial gravel and sand deposited by the ancestral Fraser River (Fig. 4.11-1).

Units I-V are interpreted to be a glacial advance sequence recording 1) valley aggradation in response to glaciation (units I-III), followed by 2) the impoundment of the valley by sediment and (or) ice and the formation of large proglacial lakes (unit IV), and finally 3) the overriding of the valley fill by glaciers (unit V) (Lian and Hicock 2001). Limiting OSL ages from unit IV suggest that units I-V were deposited during the last Fraser Glaciation (MIS stage 2) (Lian and Hicock 2001). There is a small probability, however, that part or all of this sequence formed during the penultimate Okanagan Centre Glaciation (MIS stage 4) (Lian and Hicock 2001).

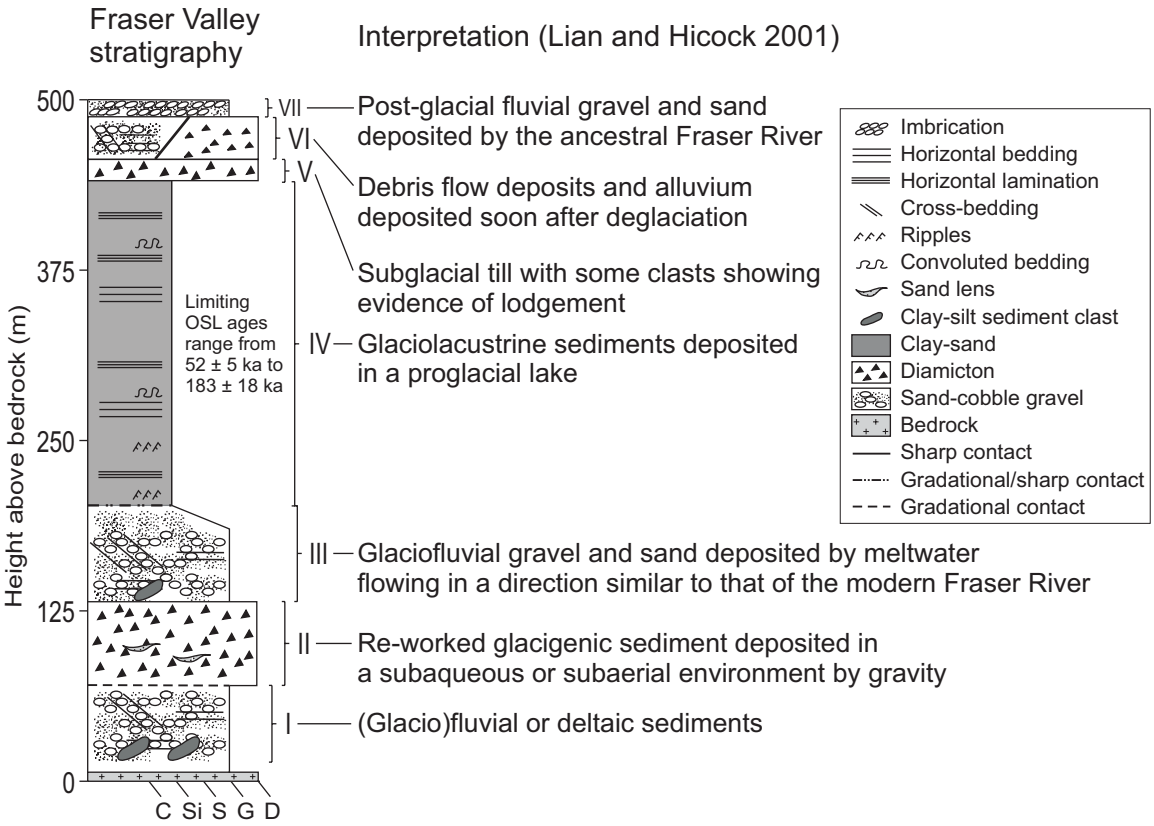

Figure 4.11-1. Composite stratigraphic log summarizing the Fraser River valley stratigraphy and associated interpretation near Clinton, B.C. (after Lian and Hicock 2001). Unit thicknesses shown in the log are general approximations; unit thicknesses vary widely from site to site. OSL stands for optically stimulated luminescence. C=clay, Si=silt, S=sand, G=gravel and D=diamicton.

The general stratigraphic interpretations of Lian and Hicock (2001) are accepted in this thesis. Additional macroscale and microscale sedimentological data were collected from Lian and Hicock's (2001) unit II to verify its genesis and to make macroscale and microscale sedimentological comparisons. This data is discussed in detail below.

4.11.2 Macroscale sedimentology and structural geology

Lian and Hicock's (2001) units II and III are exposed at site 22 (Fig. 4.11-2). Unit II is ~12 m of highly consolidated, macroscopically massive, matrix-supported sandy silt diamicton (Fig. 4.2-2). Five moderately steep to steeply dipping fractures were measured in unit II and are plotted as poles to planes on the contour stereogram of the fabric sampling site they are closest to (Fig. 4.11-2). All fractures dip down toward the Fraser River (Fig. 3.1-1).

Two clast fabrics (F34 and F35) were taken from unit II (Fig. 4.11-2), at ~1.5 m above the floor of the gully. F34 is spread unimodal with five outliers and a principal eigenvector plunging toward the WNW (Fig. 4.11-2, Table 4.2-1). All clasts measured had striae parallel to their a-axes and no keels were identified (Table 4.2-3). Fractured ends and bullet noses show no preferred direction (Fig. 4.11-2). Faceted clasts comprise 3% of the sample (Table 4.2-3). F35 is girdle-like with a principal eigenvector plunging toward the NE, approximately parallel to the local slope direction (Figs 4.11-2). Striae on clast tops are oriented parallel to clast a-axes (Table 4.2-3), and keels on clast bottoms are oriented subparallel to the clast fabric principal eigenvector (Fig. 4.11-2). Out of all clasts in the sample, 27% are faceted and 7% have keels (Table 4.2-3). In F34 and F35, clast shapes do not conform to predefined modes, or prefer any specific orientation (Fig. B-1, Appendix B). Lian's (1997) fabric 22 (fab-22, Fig. 4.11-2) is girdle-like with a principal eigenvector pointing NW (Fig. 4.11-2).

4.11.3 Micromorphology

Due to time constraints, only one sample was collected from unit II, site 22 for thin section analysis, and it was extracted from the site of F34 (Fig. 4.11-3). One horizontal (S22F34h) and one vertical (S22F34v) thin section were cut from this sample. In thin section, the unit II diamicton appears plasma supported, and dominated by subangular to subrounded metasedimentary, volcanic and limestone skeletal grains (Fig. 4.11-3A).

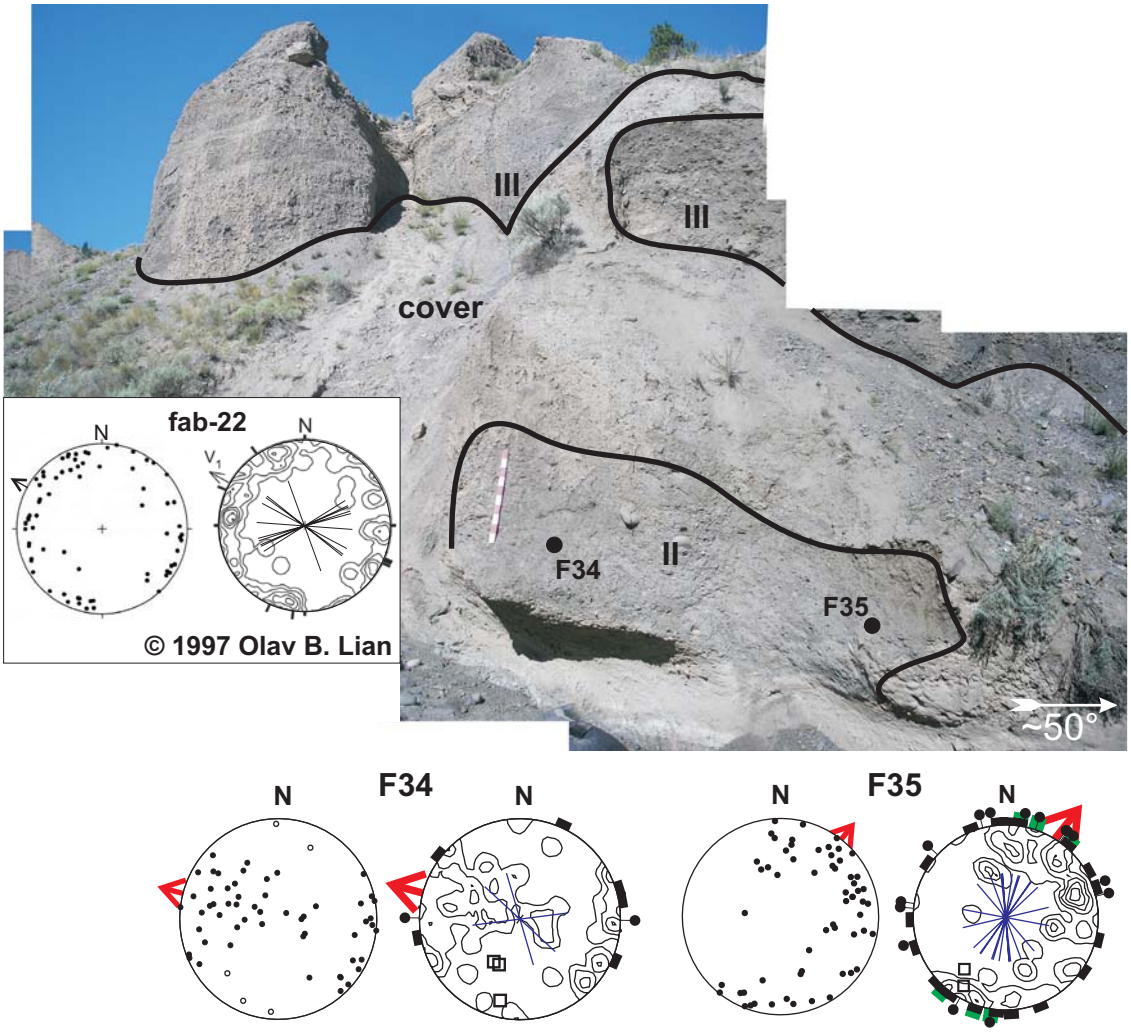

Figure 4.11-2. Site 22 showing units II (sandy silt diamicton) and III (clast- and matrix-supported pebble gravel and sand) of Lian and Hicock (2001) and the locations of F34 and F35. Fractures in unit II (not visible in photograph) dip toward Fraser River and are plotted as poles to planes on the contour stereogram of the closest fabric. The stereogram of fabric 22 (fab-22) is adapted from Lian (1997) with permission, and was collected from unit II at the same exposure (the exact location is uncertain). Metre stick with decimetre subdivisions for scale. See Figure 3.3-1 for stereogram legend.

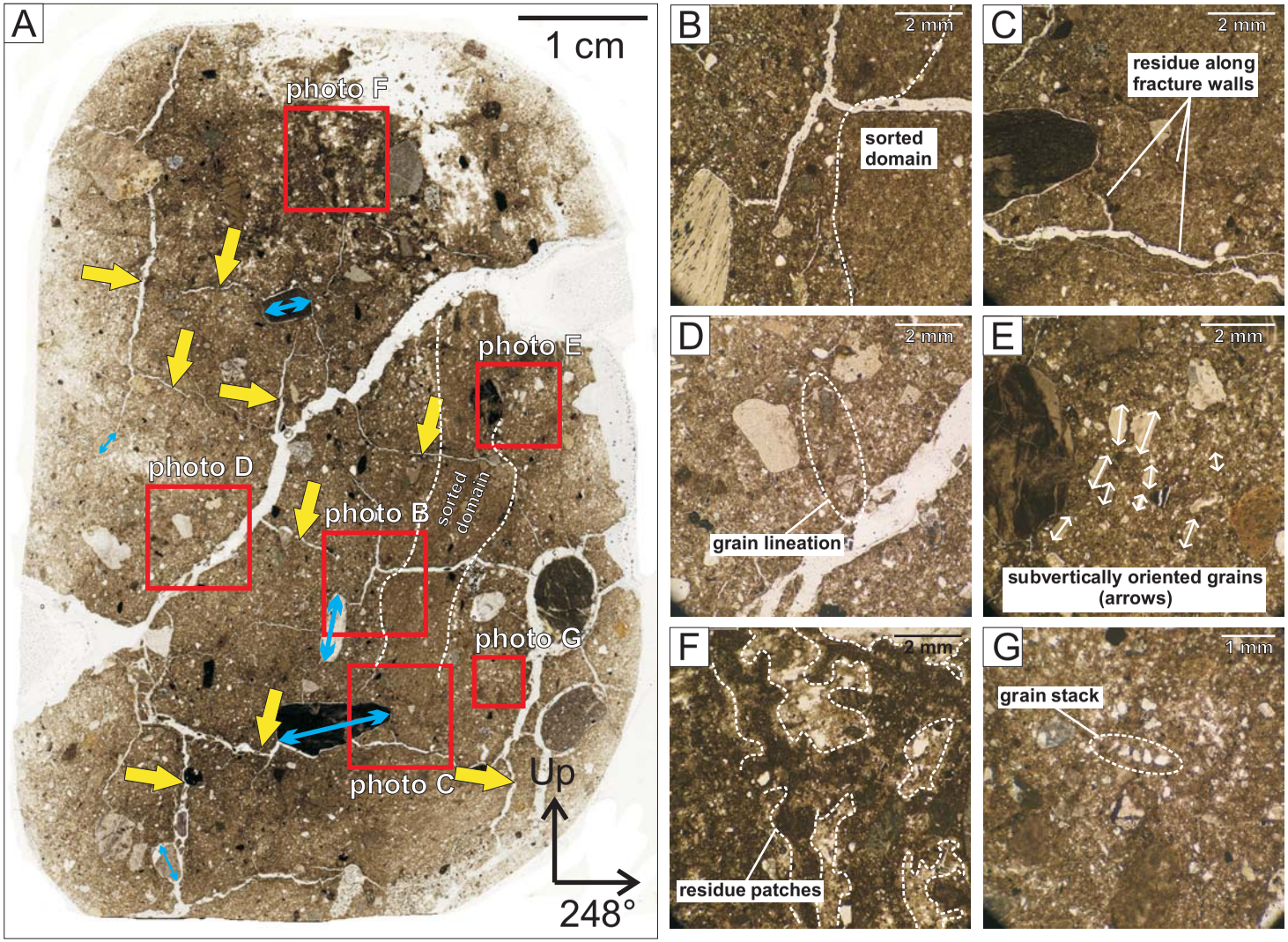

Figure 4.11-3. Thin section S22F34v. A) A 2400 dpi scan of the thin section showing orthogonal fractures (yellow, wide arrows) and a fine grained sorted domain. Some grains are oriented subparallel to the fractures (blue, narrow arrows). The locations of microphotographs B, C, D, E, F and G are indicated by red squares. Microphotographs show the sorted domain (B), residue along fracture walls (C), a grain lineation (D), subvertically oriented grains (E), residue patches (F) and a grain stack (G).

Section S22F34v is characterized by a series of subhorizontal and subvertical fractures that are almost orthogonal to each other (Fig. 4.11-3A). The subhorizontal fractures have a gentle apparent dip toward 248° and the subvertical fractures have a steep apparent dip toward 68°. One major fracture, with an apparent dip of ~45° toward 68° azimuth, crosscuts the narrower subvertical and subhorizontal fractures. A few grains are aligned subparallel to the latter fractures (Fig. 4.11-3A), but most sand-sized grains appear to be subvertically oriented (Figs 4.11-3E, 4.11-4). A dark reddish-brown residue lines many fracture walls (Fig. 4.11-3C), and appears as semi-continuous elongate patches within the matrix in the upper central part of the thin section (Fig. 4.11-3F). The diamicton matrix is texturally heterogeneous. It contains a finer grained, better sorted domain ~0.5 cm in width that runs approximately parallel to the subvertical fractures down from the right edge of the thin section (Fig. 4.11-3A). The contact between this domain and the surrounding diamicton is gradational to sharp and is shown in Figure 4.11-3B.

Fifty-five discrete microstructures were identified from thin section S22F34v, and these are dominated by turbates (Fig. 4.11-4). Crushed grains were not identified. Necking structures comprise ~25% of all discrete microstructures. Grain lineations (Fig. 4.11-4D) and grain stacks (Fig. 4.11-4G) together contribute less than 15%. Discrete microstructures are more visible within unsorted parts of the matrix (i.e., outside of the fine textured domain).

As is visually apparent from the thin section scan, subvertical sand grains are common in vertical microfabric S22F34v-1, and few grains are oriented subhorizontally (Fig. 4.11-4). Horizontal microfabrics S22F34h-1 and S22F34h-2 have similar distributions with maximum clustering in the NW-SE direction. Their tightest clusters and principal eigenvectors are oriented subparallel to the principal eigenvector of macrofabric F34 (Figs 4.11-3, 4.11-4).

4.11.4 Interpretation

The presence of glacigenic clast wear features and the orientation of most clast upper surface striae (parallel to clast long axes) in unit II, site 22 suggest that this unit contains material that was initially transported subglacially or deposited as a subglacial till. Lian (1997) and Lian and Hicock (2001) classified unit II, site 22 as a gravity flow till based on the following evidence: 1) the stratigraphic position of unit II within an inferred glacial advance sequence (Lian and Hicock 2001) (Fig. 4.11-1), 2) the presence of

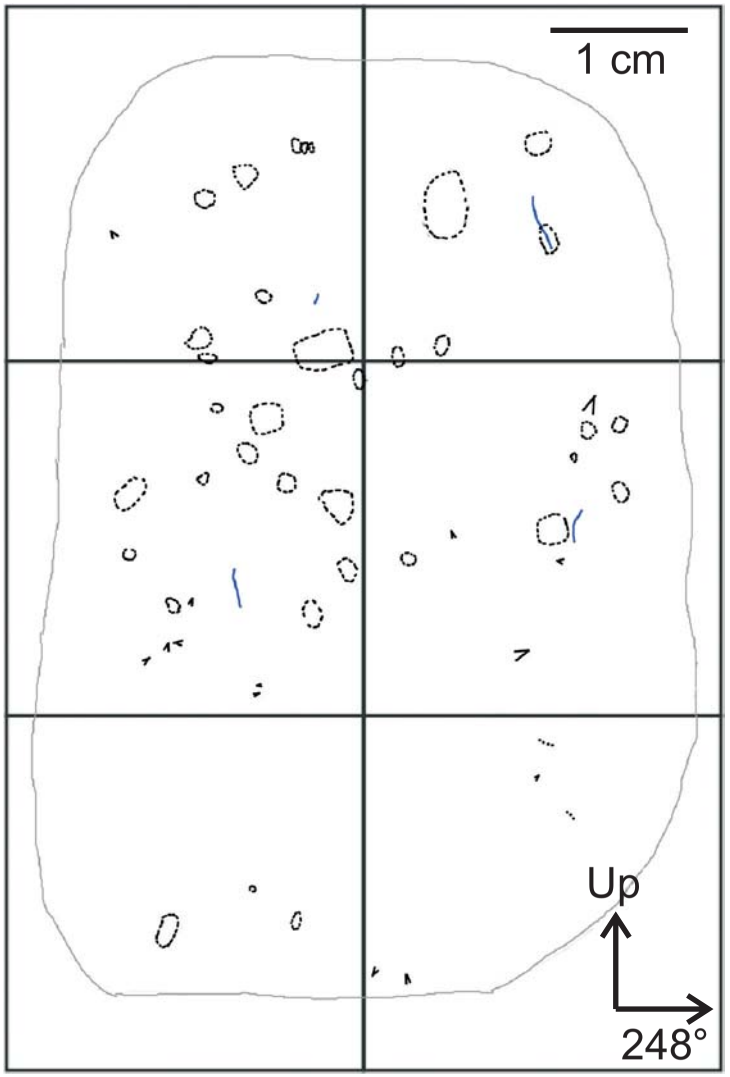

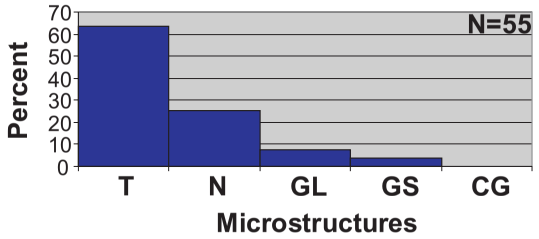

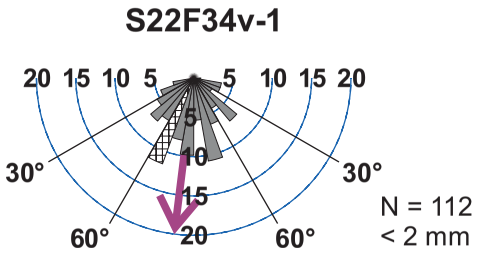

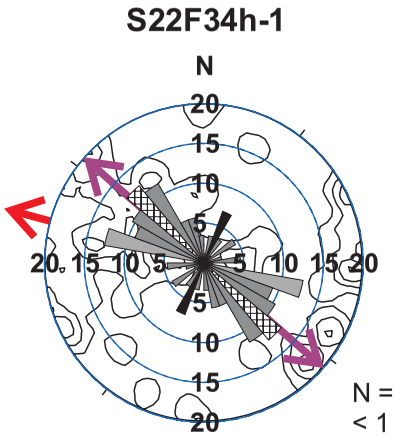

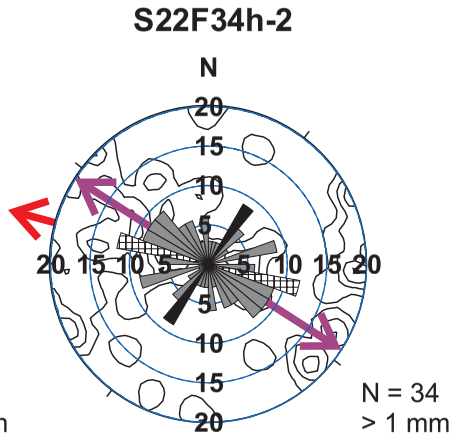

Figure 4.11-4. Microfabrics S22F34v-1, S22F34h-1 and S22F34h-2, and microstructure map and frequency histogram for thin section S22F34v. See Figures 3.3-4 and 3.3-5 for legends.

macroscopic lenses and beds of sand (not observed in this study), 3) clast fabrics that exhibit girdle-like distributions, and 4) inconsistencies between clast orientations and the orientations of clast upper surface striae, clast fractured end directions, and the dips of matrix fractures. Data collected in this study include spread unimodal and girdle-shaped clast fabrics, spread glacigenic clast wear features with no preferred directions, and diamicton matrix fracture dips that are consistent with the direction of local valley side slopes (Fig. 4.11-2). Therefore data collected in this study support Lian (1997) and Lian and Hicock's (2001) interpretation of unit II as a gravity flow diamicton.

Clast surface striae measured in unit II in this study were aligned parallel to clast long axes (Table 4.2-3), suggesting that they formed while clasts were aligned in the direction of subglacial shear during subglacial lodgement processes and (or) plastic deformation of the sediment. The spread out nature of the mode in F34, the girdle-like shape of F35 (Fig. 4.11-2), and the spread orientations and directions of clast wear features suggest that clasts were re-oriented before or during final emplacement of unit II. Because it is unknown whether unit II is remobilized glacigenic debris that was deposited in close proximity to a glacier, or is simply a debris flow deposit emplaced long after ice retreat, it will be referred to here as a gravity flow diamicton, as opposed to a gravity flow till (Dreimanis and Lundqvist 1984).

Despite their proximity to one another, the two fabrics measured in unit II are quite different in strength, modality and orientation. The strength and orientation of F34 is consistent that of Lian's (1997) fab-22 (Fig. 4.11-2). F35, however, has a principal eigenvector oriented perpendicular to that of F34 and Lian's (1997) fab-22 (Fig. 4.11-2). F35 and the fractures near it were measured at a shallow depth below the sloping upper surface, which is covered in slopewash and colluvium (Fig. 4.11-2). Thus, modern slope processes may have influenced the orientation of clasts and fractures at F35. None-the-less, adjacent clast fabrics with variable strengths and orientations are considered typical of debris flows (Benn and Evans 1998), and such fabrics characterize other glacigenic debris flow diamictons within the Fraser Valley (Eyles and Kocsis 1988). Thus, F34 and F35 may record rolling and sliding of clasts down a paleo-slope, or local compressive and extensional forces in a debris flow. The fracture planes measured at F34 and F35 dip down toward the Fraser River. Some or all of these likely record slumping of the dried out diamicton mass in response to incision of the Fraser River.

The fractures observed in thin section S22F34v may have formed from post-depositional desiccation of the diamicton matrix, or during sampling in the field and

processing in the laboratory. The alignment of the subvertical, subparallel fractures with the fine textured domain contacts and the subvertical sand grains of microfabric S22F34v-1 (Figs 4.11-3, 4.11-4) suggests that diamicton heterogeneities and fabric influenced fracture orientations while the diamicton experienced tensile stress. The reddish-brown residue observed in fractures and within the matrix could be precipitates from percolating water or resin. The textural heterogeneity in the matrix can be explained in terms of intermixing of sediment from multiple sources, and (or) fluctuating sediment competence associated with unsteady shear rates and fluctuating water contents within flowing and (or) shearing sediment in a glacigenic debris flow (Hampton 1975). The strong correlation between the orientation of sand sized grains and textural domain boundaries may be indicative of laminar flow within a relatively water saturated part of the diamicton (Lachniet *et al.* 1999).

The similarity between horizontal micro- and macro-fabrics suggests that processes that oriented pebbles at F34 are also responsible for the orientation of sand sized particles. These processes may involve sliding or rolling of particles down a paleo-surface within relatively dry, plastically deforming sediment, or laminar flow of water saturated sediment (Lachniet *et al.* 1999).

Discrete microstructures suggest that ductile deformation including the rotation of skeletal grains was more common than discrete shear events, grain stacking, or crushing. Discrete microstructures are lacking within the finer textured, sorted domain in thin section S22F34v (Fig. 4.11-3) likely because such structures are better preserved (or are more visible) in relatively unsorted sediments (Hart *et al.* 2004).

4.12 Summary and discussion

Table 4.2-1 compares diamicton classifications made in this study with those of Lian (1997), Lian and Hicock (2000) and Lian and Hicock (2001). Most macroscale sedimentological and structural data collected in this study support existing interpretations of diamicton genesis. At some sites, additional data collected during this study allows refinement of existing interpretations of ice flow direction (e.g., site 48, Section 4.7) or depositional history (e.g., site 44, Section 4.4). At sites containing what has been previously inferred as lodgement till (e.g., sites 20, 23, and 27, Sections 4.3, 4.2 and 4.8, respectively) the data collected in this study is unable to conclusively verify previous interpretations of diamicton genesis (see Section 4.12.1 below). The implications (and possible limitations) of the results of this study are discussed below.

4.12.1 Macroscopic evidence for lodgement till

a) Glacigenic clast wear features and clast size

The strength and orientation of clast macrofabrics measured from previously inferred lodgement tills (sites 20, 23, and 27) are consistent with those reported by Lian (1997) and Lian and Hicock (2000) (Sections 4.2, 4.3, 4.8). In addition, the abundance of glacigenic clast wear features, and striae on clast tops that are parallel to clast long axes (Table 4.2-3) support previous assertions that most diamictons in the study area were initially deposited by lodgement processes (Lian 1997; Lian and Hicock 2000). However, additional macroscopic evidence for preserved 'undeformed' lodgement till in the form of pebble wear features is more enigmatic. Clast bullet noses and fractured ends rarely show a preferred direction as might be expected from a lodgement till, even at sites previously classified as such (e.g., site 20, 23 and 27, Table 4.2-3). Clast facets are common in all glacigenic diamictons studied, and keels are rare on pebble-sized clasts in general (Table 4.2-3) making statistical comparisons between sites less meaningful.

The tendency for clast wear features recording lodgement processes to be better preserved on larger cobbles and boulders has been demonstrated in front of contemporary glaciers (Benn 1994; 1995). This has been attributed to the preferential lodgement of larger clasts, while the diamicton matrix and smaller stones (pebbles) continue to flow around them and (or) be re-oriented by them during ploughing. For this reason, it is suspected that more definitive evidence for undeformed lodgement till might have been obtained if measurements were not restricted to pebble sized clasts. Unfortunately Lian (1997) did not record the sizes of individual clasts from which he obtained glacigenic wear feature data (Lian 2007, pers. comm.), so a direct comparison between studies cannot be made. Therefore it is concluded here, based on available data from this and previous studies (Lian 1997; Lian and Hicock 2000), and on the interpretations made in Sections 4.2, 4.3 and 4.8, that the diamictons at sites 20, 23 and 27 could either be lodgement or deformed lodgement tills (abbreviated as L/DL, Table 4.2-1). Future work that compared the frequencies, positions and orientations of glacigenic wear features on clasts of different sizes may facilitate a more precise classification of these diamictons.

b) Facet and keel positions and problems of inheritance

Further analysis of facet and keel positions (top, bottom or sides) on clasts was pursued to see if this data would distinguish between previously inferred lodgement tills (here interpreted as lodgement or deformed lodgement tills (L/DL)) and other diamicton types (Fig. 4.12-1). The clast fabric data obtained from the cobble-boulder pavement of unit 3, site 44 (Section 4.4) is also included for comparison.

If a glacier slides over its bed, clasts at the ice-bed interface can become faceted on their upper surfaces (tops) by overriding ice after they have been lodged into the substrate. Faceting can also occur on clast bottoms if the clast is dragged over bedrock. Facets found on clast sides and some facets found on clast bottoms likely record clast re-orientation. Clast re-orientation can occur: 1) during ploughing processes due to clast collisions at the ice-bed interface, 2) within a deforming substrate as it is sheared by the overriding glacier, 3) within the ice if the clast undergoes subsequent englacial transport, or 4) during deposition by gravity in a subglacial, subaerial or subaqueous environment. Therefore intra-site, inter-site and inter-diamicton type comparisons were made with respect to the proportion of faceted clasts that fall into the following categories: 1) facets are on clast tops only *(suggests lodgement of clasts into a soft substrate)*, 2) facets are on clast tops and (or) bottoms only *(suggests ploughing or lodging of clasts into a bedrock substrate located at or up-ice of the sampling area)*, 3) facets are on clast tops and (or) bottoms and on one or more sides *(suggests that clasts have been rotated, but ploughing/lodgement is most recent process and bedrock is located at or up-ice of the sampling area)*, 4) facets are on clast bottoms and (or) on one or more sides *(suggests that clasts have rotated after ploughing/lodgement and assumes no bedrock at or up-ice of the sampling area)*, and 5) facets are on clast sides only *(suggests that clasts have rotated during or after ploughing/lodgement)* (Fig. 4.12-1a).

Ploughing of clasts into a soft substrate at the ice-bed interface may lead to the development of keels on clast bottoms (Lian 1997; Lian and Hicock 2000), so the number of clasts with keels and keel positions were recorded in the field and are presented in Figure 4.12-1b. The number of clasts with keels in each fabric sample is very low (never more than 8), thus keel statistics are reported in absolute numbers. Intra-site, inter-site and inter-diamicton type comparisons were made with respect to the number of clasts with keels that fall into the following categories: 1) keels are on clast bottoms only *(suggests ploughing or lodgement into a soft substrate)*, 2) keels are on clast bottoms and on one or more sides *(suggests that clasts have rotated, but*

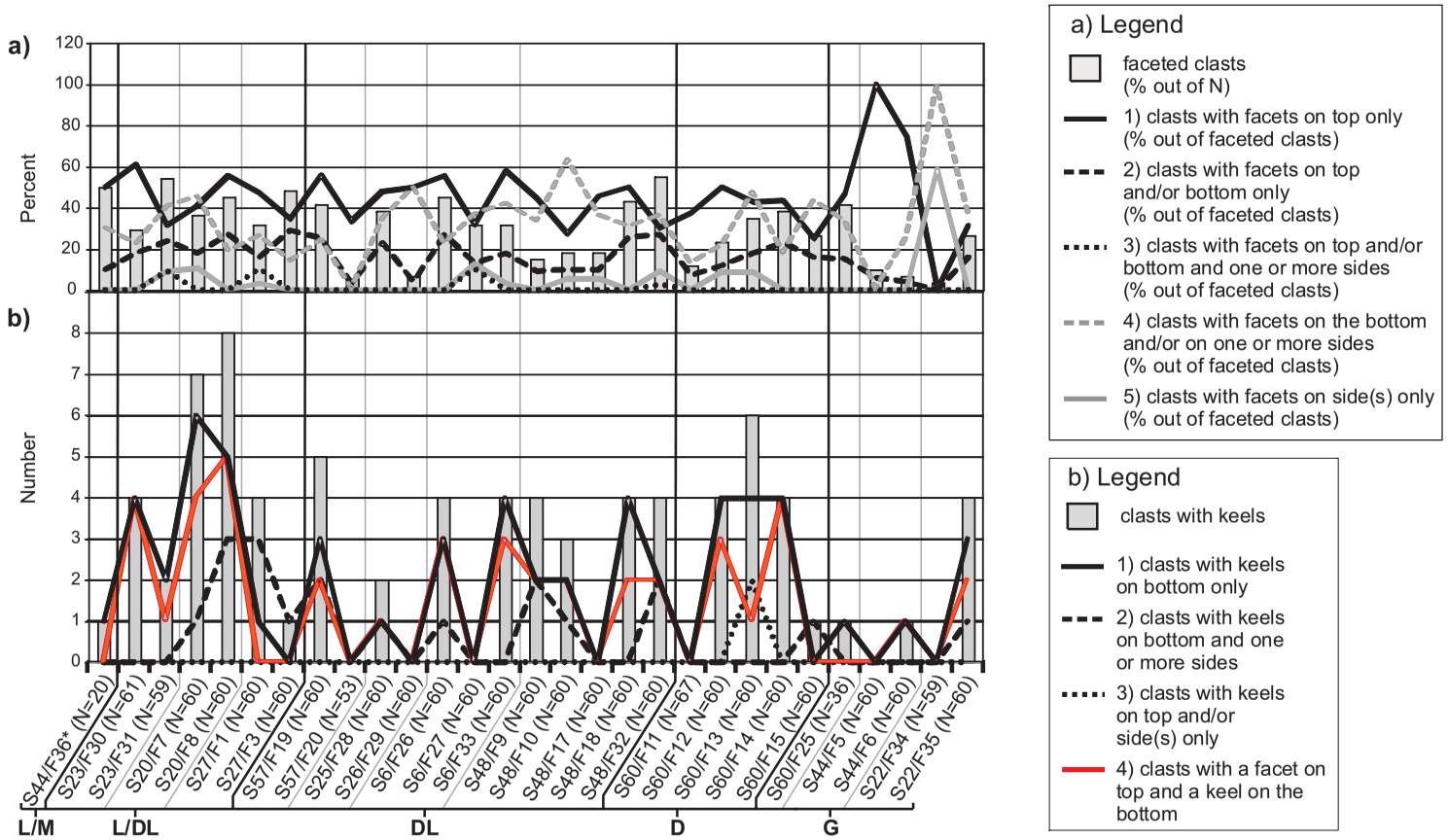

Figure 4.12-1. The positions of facets and keels on clasts in all fabric samples. N = the total number of clasts in a fabric sample. Fabric samples (recorded as site #/fabric # on the x-axis) are sorted according to inferred diamicton genesis (this study), where L = mainly lodgement, DL = deformed lodgement, D = deformation, G = gravity flow and M = melt-out. Facet data (a) is reported in percent. Keel data (b) is reported in absolute numbers. The absolute numbers of clasts that have both a facet on their top and a keel on their bottom is shown in 'b' as an orange line. All fabric samples are obtained from diamictons, except for F36, site 44, (S44/F36*) which was measured from a cobble-boulder pavement (see Section 4.4).

ploughing or lodgement is most recent process), and 3) keels are on clast tops and (or) on one or more sides *(suggests that clasts have rotated after ploughing or lodgement)* (Fig. 4.12-1b). The number of clasts that have both a facet on the top and a keel on the bottom *(suggesting ploughing and lodgement into a soft substrate)* are also recorded as a fourth category in Figure 4.12-1b.

All sites, except sites 22 and 44, have diamictons with at least one fabric sample that contains 38% or more clasts that are faceted (Fig. 4.12-1a). The lower abundance of faceted clasts within the gravity flow diamictons at sites 22 and 44 may be due to intermixing of glacigenic and non-glacigenic debris during mass wasting events. The proportion of faceted clasts (out of N) varies within individual diamicton units by as much as 36% (e.g., site 57, Fig. 4.12-1a). Intra-site variability in the abundance of faceted clasts may record changes in depositional style within individual diamicton units and (or) inter-operator variation due to subjectivity during the sampling process.

The proportion of faceted clasts with facets on their tops (category 1, Fig. 4.12-1a) varies between ~20-62% in all diamictons, except that at site 44. One fabric sampled from the site 44 gravity flow diamicton contains few faceted clasts, but all of them have facets on their tops (Fig. 4.12-1a). The proportion of clasts with facets on their tops in lodgement/deformed lodgement tills is not significantly higher than that of other diamicton types.

The proportion of faceted clasts that fall into category 2 is similar for all diamicton types (Fig. 4.12-1a). Lodgement/deformed lodgement (L/DL) tills and deformed lodgement (DL) tills have small proportions of clasts that fall into facet category 3, which may record clast rotation followed by ploughing and lodgement. Deformation till and gravity flow diamictons have no clasts that fall into facet category 3 (Fig. 4.12-1a).

The fabric sample containing the largest proportions of faceted clasts falling into facet categories 4 and 5 is F34, site 22 (Fig. 4.12-1a). These statistics may record the re-orientation of glacigenic clasts during gravity flow processes; however, the number of faceted clasts in F34 is very low and may not be representative of all faceted clasts in the diamicton. All other faceted clasts that fall in categories 4 and 5 show no preference for a particular diamicton type or depositional process (Fig. 4.12-1a).

Most fabric samples have 1-4 clasts with keels (Fig. 4.12-1b). Two lodgement/deformed lodgement till fabric samples, one deformed lodgement till fabric sample, and one deformation till fabric sample have more than 4 clasts with keels (Fig. 4.12-1b). Site 20, containing a lodgement/deformed lodgement till, has the two fabric

samples with the highest number of clasts with keels (8) (Fig. 4.12-1b). The frequency of clasts with keels at these sites supports the lodgement till interpretation, although the values are small.

Keel categories 1, 2 and 4 in Figure 4.12-1b together suggest clast rotation followed by ploughing and lodgement into a soft substrate. As may be expected, clast frequencies in these categories are highest in lodgement/deformed lodgement till types, however, clasts that fall into these categories are also present in all other diamicton types (Fig. 4.12-1b). Only one fabric sample (S60/F13), from a deformation till, has clasts that fall into category 3, which is interpreted to record clast rotation after ploughing (Fig. 4.12-1b).

The facet and keel statistics in Figure 4.12-1 show that all diamicton types in the study area contain glacigenic wear features associated with clast transport and (or) deposition at the ice-bed interface, supporting Lian (1997) and Lian and Hicock's (2000) inference that most diamictons in the study area contain material that was originally deposited by lodgement. Because many glacigenic wear features are inherited, and do not necessarily represent the most recent depositional process, the pebble facet and keel statistics in Figure 4.12-1 do not clearly differentiate between lodgement/deformed lodgement tills and other diamicton types, although they weakly support some interpretations.

4.12.2 Macro-micro comparisons

a) Microstructure types and matrix heterogeneity

All glacigenic diamictons in this study contain turbates, necking structures, grain lineations, grain stacks and crushed grains (Table 4.12-1). Qualitative microscale observations suggest that gravity flow diamictons are more likely to exhibit sorting (in the form of texturally distinct bands) and a laminar flow fabric than other diamictons deposited directly by glacial ice (sites 44 and 22, Figs 4.4-4A, 4.11-2A). Similar observations have been made by Menzies and Zaniewski (2003) and Lachniet (2001) when comparing the micromorphology of debris flow diamictons and primary tills. This sorting is inferred to record the intermixing of sediment from different sources in saturated flowing sediment, and (or) fluctuating flow competence associated with unsteady shear rates and fluctuating water contents in a debris flow (Lachniet *et al.* 1999). Macroscopic and microscopic heterogeneities observed in the matrix of other

diamicton types (i.e., sites 48 and 27, Figs 4.7-4D, 4.8-3A) appear to be the result of the intermixing of diamictons from different sources in glaciotectonically deforming sediment.

Table 4.12-1. Microstructure association data displayed in a 23 x 5 matrix. Sites are sorted according to inferred diamicton genesis (G).

Vertical thin section	G[1]	Turbates (%)	Necking structures (%)	Grain lineations (%)	Grain stacks (%)	Crushed/broken grains (%)
S23F30v	L/DL	45	15	20	20	0
S23F31v	L/DL	56	13	25	6	0
S20F7v	L/DL	85	6	0	3	6
S27F1n	L/DL	24	45	18	0	12
S27F3v	L/DL	24	22	33	2	18
S57F19v	DL	16	12	12	0	60
S57F20v	DL	24	21	0	24	31
S25F28v	DL	0	33	33	0	33
S26F29v	DL	0	0	38	0	63
S6F26v	DL	31	38	24	2	5
S6F27v	DL	35	37	11	11	7
S6F33v	DL	40	20	27	0	13
S48F9v	DL	53	12	15	9	12
S48F10v	DL	63	12	12	6	7
S48F17v	DL	30	26	4	28	11
S48F18v	DL	54	7	20	0	19
S48F32v	DL	60	19	9	12	0
S60F11v	D	68	1	11	16	3
S60F13v	D	75	3	5	11	6
S60F14v	D	29	29	26	6	10
S60F15v	D	27	43	20	2	8
S44F5v	G	28	32	24	1	15
S22F34v	G	64	25	7	4	0

[1]Genesis according to Neudorf (this study), where L/DL=lodgement or deformed lodgement, DL=deformed lodgement, D=deformation, and G=gravity flow.

b) Microfabrics

Table 4.12-2 shows the vertical microfabric statistics and explores the relationships between vertical microfabric peak orientations and the orientations of fractures observed in vertical thin sections. Vertical microfabric eigenvectors and peaks indicate that all till types can have fabrics dominated by gently plunging sand grains (i.e., peaks and (or) eigenvectors with plunges of 30° or less). Peaks and eigenvectors with steep (70-90°) plunges seem to be restricted to deformed lodgement, deformation and gravity flow diamictons (see microfabrics S26F29v-1, S6F27v-1 and S60F14v-1, Table 4.12-2). This may reflect the increased likelihood of 'end-over-end' grain rotation (i.e., rotation around grain b- or c-axes) within tills that have experienced post-depositional deformation or gravity flow. It may also record particle rotation as a result of a higher frequency of clast collisions in diamictons with relatively high clast concentrations (site 60, Table 4.2-1). Three out of seven thin sections with parallel or subparallel planar

Table 4.12-2. Vertical microfabric statistics and relationships with planar voids in vertical thin sections. Thin sections are sorted according to inferred diamicton genesis (G).

Vertical Microfabric	G[1]	Clast Concen.[2] (%)	V_1 plunge[3] (°)	V_1 direction[3] (°)	S_1[3]	Plunge range of peak(s)[4] (°)	Plunge direction of peak(s)[4] (°)	Vertical thin section planar voids[5]	Relationship between planar voids and microfabric peak orientations[6]
S23F30v-1	L/DL	18	18.7	347	0.640	10-60	347	P (13° to 167°)	N
S23F31v-1	L/DL	9	11.8	184	0.570	20-60	184	P (40° to 184°)	P
S20F7v-1	L/DL	8	10.0	103	0.661	20-50	103	P (20° to 103°)	P
S27F2v-1	L/DL	13	26.0	330	0.604	30-40	330	N	N
S57F19v-1	DL	10	0.5	133	0.637	20-30	133	N	N
S57F20v-1	DL	6	21.1	328	0.594	20-30	328	N	N
S25F28v-1	DL	3	27.0	54	0.572	20-30	54	N	N
S26F29v-1	DL	5	76.5	233	0.569	70-80	233	N	N
S6F26v-1	DL	7	30.8	208	0.664	30-40	208	P (8° to 208°)	N
S6F27v-1	DL	6	87.7	29	0.633	80-90	209	N	N
S6F33v-1	DL	3	24.7	22	0.593	20-30	22	P (33° to 192°)	N
S48F9v-1	DL	8	86.3	243	0.595	40-50	63	C (27° to 63° and 29° to 243°)	N
S48F10v-1	DL	19	14.5	36	0.588	0-10	36	N	N
S48F17v-1	DL	25	8.6	17	0.713	10-20	17	P (70° to 17°)	N
S48F18v-1	DL	18	83.8	348	0.564	50-60	348	N	N
S48F32v-1	DL	21	8.9	357	0.552	30-40	357	P (80° to 357°)	N
S60F11v-1	D	24	1.4	206	0.621	20-50	26, 206	N	N
S60F13v-1	D	25	8.3	355	0.577	30-50	175, 355	N	N
S60F14v-1	D	17	68.7	172	0.629	70-80	172	N	N
S60F15v-1	D	26	0.0	165	0.535	50-60	345	N	N
S44F5v-1	G	8	22.6	304	0.762	20-30	304	C (0° and 90°)	N
S22F34v-1	G	15	83.0	68	0.661	60-70	68	C (20° to 248° and 80° to 68°)	P

[1]Genesis of the diamicton according to Neudorf (this study), where L/DL=lodgement or deformed lodgement, DL=deformed lodgement, D=deformation, and G=gravity flow.
[2]Clast concentration measured from the diamicton in the field (see Section 3.3.1 for methodology).
[3]V_1 is the vertical microfabric principal eigenvector, S_1 is the vertical microfabric principal eigenvalue.
[4]A peak is the 10° class with the highest number of observations overall.
[5]P= planar voids are (sub)parallel to each other, C=planar voids form two cross-cutting sets, N=planar voids show no systematic orientation. The orientation of planar voids are recorded as (**apparent dip down** to **apparent dip direction**).
[6]P=the apparent dip direction of one or more planar void sets and the vertical microfabric peak(s) is the same, and the apparent dip of that/those planar void set(s) falls within the plunge range of the vertical microfabric peak(s). N= the apparent dip direction(s) of the planar void set(s) observed in thin section and the vertical microfabric peak(s) is *not* the same, and (or) the apparent dip(s) of planar void set(s) *does not* falls within the plunge range of the vertical microfabric peak(s).

voids had vertical microfabric principal eigenvectors and (or) peaks that were (sub)parallel to planar void orientations (Table 4.12-2).

Relationships between horizontal microfabrics and macrofabrics are explored in Table 4.12-3 for all diamictons classified in this study. Table 4.12-3 shows the acute (<90°) angles (β) between horizontal microfabric principal eigenvector trends and macrofabric principal eigenvector trends, as well as the acute (<90°) angle value ranges (θ) between microfabric cluster peaks (Section 3.4.4) and the principal eigenvector of the nearest macrofabric mode. Letters A and B (Table 4.12-3) record what is visually interpreted to be the peaks of the tightest (A-type) and second tightest (B-type) horizontal microfabric clusters, respectively (Section 3.4.4, Chapter 4). M1 and M2 record the principal eigenvector trend of the macrofabric primary (or only) mode and secondary mode, respectively. Acute angle ranges between microfabric cluster peaks and macrofabric mode principal eigenvector trends are divided into the following five classes: $\theta \leq 10°$, $10° < \theta \leq 20°$, $20° < \theta \leq 30°$, $30° < \theta \leq 70°$, and $70° < \theta \leq 90°$ (Table 4.12-3). These are named 'parallel', 'subparallel', 'oblique', 'oblique', and '~orthogonal', respectively. The A- and B-type cluster peaks in horizontal microfabrics measured from all till types are slotted into their appropriate class (Table 4.12-3).

The relationships between macrofabric modes and horizontal microfabric cluster peaks (quantified as θ) are described for each diamicton type. The influence these relationships have on β (the acute angle between horizontal microfabric principal eigenvector trends and macrofabric principal eigenvector trends) is also explored. Comparisons between different diamicton types with regard to these data are then made and interpreted.

Four out of six A-type cluster peaks in lodgement/deformed lodgement (L/DL) till horizontal microfabrics are parallel or subparallel to M1. B-type cluster peaks are oriented oblique (20-30°), or ~orthogonal to M1. β values less than or equal to 31.5° are associated with A-type cluster peaks that are parallel or subparallel to M1. β values greater than or equal to 47.2° are associated with A-type cluster peaks that are ~orthogonal to M1.

Microfabric cluster peaks in deformed lodgement tills can be oriented parallel, subparallel, oblique, or ~orthogonal to macrofabric mode principal eigenvectors. A and B-type cluster peaks that are oblique or ~orthogonal to M1, are more frequent in deformed lodgement tills with unimodal or spread unimodal clast fabrics, than in all other macrofabrics. Because bimodal and spread bimodal macrofabrics have modes that are

Table 4.12-3. Macrofabric and horizontal microfabric statistics. Sites are sorted first according to inferred diamicton genesis (G), then according to macrofabric modality (M).

Microfabric name[1]	G[2]	M[3]	Mac. V_1[4](°)	Mic. V_1[5](°)	Mic. S_1[5]	β[6] (°)	θ[7] ≤ 10° (parallel)		10° < θ[7] ≤ 20° (subparallel)		20° < θ[7] ≤ 30° (oblique)		30° < θ[7] ≤ 70° (oblique)		70° < θ[7] ≤ 90° (~orthogonal)	
							M1	M2	M1	M2	M1	M2	M1	M2	M1	M2
S20F7h-1	L/DL	U	**320.7**	**72.5**	**0.612**	**68.2**									**A**	
S20F7h-2	L/DL	U	320.7	93.5	0.548	47.2					B				A	
S23F31h-1	L/DL	SU	**221.7**	**66.1**	**0.609**	**24.4**			**A**						**B**	
S23F31h-2	L/DL	SU	221.7	58.0	0.607	16.3	A									
S23F30h-1	L/DL	SB	**203.9**	**55.4**	**0.584**	**31.5**	**A**									
S23F30h-2	L/DL	SB	203.9	26.7	0.633	2.8			A							
average						**31.7**										
S6F26h-1	DL	U	**245.5**	**72.6**	**0.552**	**7.1**	**A**									
S6F26h-2	DL	U	245.5	89.0	0.622	23.5							A		B	
S27F2h-1	DL	SU	**199.2**	**62.8**	**0.527**	**43.6**			**B**				**A**			
S27F2h-2	DL	SU	199.2	39.3	0.514	20.1					A					
S25F28h-1	DL	SU	**271.6**	**9.9**	**0.546**	**81.7**							**B**		**A**	
S25F28h-2	DL	SU	271.6	108.2	0.586	16.6	B						A			
S48F32h-1	DL	SU	**213.9**	**19.0**	**0.621**	**14.9**	**A**								**B**	
S48F32h-2	DL	SU	213.9	16.2	0.646	17.7			A				B			
S48F17h-1	DL	B	**234.4**	**52.6**	**0.540**	**1.8**			**A**	**B**						
S48F17h-2	DL	B	234.4	30.6	0.590	23.8			B					A		
S57F19h-1	DL	SB	**169.9**	**153.4**	**0.672**	**16.5**		**B**	**A**							
S57F19h-2	DL	SB	169.9	159.6	0.799	10.3	B				A					
S26F29h-1	DL	SB	**270.2**	**172.4**	**0.640**	**82.2**	**B**							**A**		
S26F29h-2	DL	SB	270.2	158.8	0.730	68.6			B			A				
S6F27h-1	DL	SB	**246.3**	**93.8**	**0.556**	**27.5**	**B**	**A**								
S6F27h-2	DL	SB	246.3	97.6	0.588	31.3		B			A					
S6F33h-1	DL	SB	**59.6**	**117.7**	**0.568**	**58.1**			**B**	**A**						
S6F33h-2	DL	SB	59.6	62.3	0.631	2.7					A			B		
S48F9h-1	DL	SB	**100.5**	**98.3**	**0.621**	**2.2**	**A**					**B**				
S48F9h-2	DL	SB	100.5	108.1	0.710	7.6	A							B		
S48F10h-1	DL	G	**73.4**	**58.9**	**0.552**	**14.5**					**A**		**B**			
S48F10h-2	DL	G	73.4	70.4	0.566	3.0					A					
average						**26.2**										
S60F13h-1	D	SU	**211.9**	**123.1**	**0.618**	**88.8**			**B**						**A**	
S60F13h-2	D	SU	211.9	143.7	0.614	68.2							B		A	
S60F14h-1	D	SB	**209.4**	**176.0**	**0.528**	**33.4**	**A**	**B**								
S60F14h-2	D	SB	209.4	11.1	0.665	18.3			A					B		
S60F11h-1	D	SB	**62.8**	**149.4**	**0.599**	**86.6**		**A**	**B**							
S60F11h-2	D	SB	62.8	34.8	0.645	28.0	A							B		
S60F15h-1	D	G	**22.0**	**139.6**	**0.615**	**62.4**									**A**	
S60F15h-2	D	G	22.0	137.6	0.563	64.4							B		A	
average						**56.3**										
S22F34h**-1**	G	SU	**285.0**	**131.2**	**0.683**	**26.2**					**A**				**B**	
S22F34h-2	G	SU	285.0	123.0	0.594	18.0	A							B		
S44F5h-1	G	G	**323.7**	**16.1**	**0.542**	**52.4**							**A**		**B**	
S44F5h-2	G	G	323.7	82.9	0.613	60.8			A						B	
average						**39.4**										

[1]Microfabics for grains <1 mm in apparent length are black; microfabrics for grains >1 mm in apparent length are grey.
[2]Diamicton genesis according to Neudorf (this study), where L/DL=lodgement or deformed lodgement, DL=deformed lodgement, D=deformation, and G=gravity flow.
[3]Macrofabric modality, where U=unimodal, SU=spread unimodal, B=bimodal, SB=spread bimodal, and G=girdled.
[4]Macrofabric principal eigenvector for all clasts in sample.
[5]Microfabric principal eigenvector (V_1) and principal eigenvalue (S_1).
[6]β=the acute (<90°) angle value between the horizontal microfabric principal eigenvector and the macrofabric principal eigenvector trend. (The macrofabric principal eigenvector used to determine β is for all clasts in the sample).
[7]θ=the acute (<90°) angle value range between microfabric cluster peaks (A=the peak of the tightest cluster, B=the peak of the second tightest cluster) and the principal eigenvector trend of the nearest macrofabric mode (M1=the primary/only mode, M2=the secondary mode).

~orthogonal to each other, they will not have microfabric clusters oriented ~orthogonal to one macrofabric mode without being oriented oblique, subparallel or parallel to the other mode. Therefore bimodal or spread bimodal macrofabrics tend to have microfabric cluster peaks oriented parallel, subparallel or oblique (20-30°) to macrofabric modes. A- and B-type cluster peaks are more likely to be oriented parallel or subparallel to M1 than to M2, and all clusters oriented 20-30° relative to M1 are A-type clusters.

Out of all 22 deformed lodgement till horizontal microfabrics, 12 have β values equal to or less than 17.7°. All seven microfabrics from deformed lodgement tills with A-type cluster peaks that are parallel or subparallel to M1 have β values that fall within this range. Out of the 12 microfabrics with β values in this range, four have A-type cluster peaks oriented 20-30° relative to M1, and only one has an A-type cluster peak oriented 30-70° relative to M1.

A-type cluster peaks in deformation tills with spread unimodal macrofabrics tend to be ~orthogonal to macrofabric principal eigenvectors. B-type cluster peaks are oriented either subparallel or oblique (30-70°) to macrofabric principal eigenvectors. A-type cluster peaks in deformation tills with spread bimodal macrofabrics are parallel to M2, parallel to M1, or subparallel to M1. Most B-type cluster peaks are oblique to M1 or M2. A-type cluster peaks in deformation tills with girdled macrofabrics are oriented ~orthogonal to M1.

Three horizontal microfabrics in deformation tills have β values less than or equal to 33.4°. These are associated with A-type cluster peaks oriented parallel or subparallel to M1. All other microfabrics have β values greater than or equal to 62.4°, and are associated with A-type cluster peaks oriented ~orthogonal to M1.

A-type cluster peaks in gravity flow diamictons are oriented subparallel or oblique to M1, or oblique to M2. Most B-type cluster peaks are oriented transverse to M1. The horizontal microfabric with the lowest β value (18.0°) is associated with an A-type cluster peak oriented 30-70° relative to M1, and a B-type cluster peak oriented parallel to M1. The microfabric with the highest β value (60.8°) has an A-type cluster peak oriented subparallel to M1, and a B-type cluster peak oriented ~orthogonal to M1.

Comparisons between diamicton types with regard to the above data yield the following general observations: 1) all diamicton types exhibit a wide range of values for β, however, all β values less than 18° are found only among the lodgement and deformed lodgement till types. 2) β values greater than 70° are restricted to deformed lodgement (S25F28h-1, S26F29h-1) and deformation tills (S60F11h-1, S60F13h-1), and

deformation tills have the highest average β value (56.3°) of all till types (Table 4.12-3). 3) Low β values are more likely to be associated with A- or B-type cluster peaks oriented parallel or subparallel to M1. 4) High β values are more likely to be associated with A- or B-type cluster peaks oriented oblique (30-70°) or ~orthogonal to M1.

The above general observations suggest that in *primary tills*, sand-sized grains are more likely to orient their long axes parallel or subparallel to shear (i.e. subparallel to pebble-sized clasts) during lodgement, ploughing, and (or) limited subglacial deformation processes than during deformation processes associated with a more saturated mobile substrate. It is also possible that microfabric and macrofabric consistency is influenced by diamicton clast concentration. Deformed lodgement and deformation tills in the study area, which have some of the highest β values, also have some of the highest clast concentrations measured in this study (see sites 48 and 60, Table 4.2-1). Therefore, sand-sized grain orientations in these diamictons may be less consistent with pebble orientations as a result of a higher likelihood of particle collisions during shearing events.

Gravity flow diamictons have either spread unimodal or girdled macrofabrics and β values ranging from 18.0-60.8°. A-type cluster peaks are oriented parallel, subparallel or oblique (20-70°) to M1, and most B-type cluster peaks are oriented ~orthogonal to M1. These results suggest that sand-sized grains do not necessarily follow pebble orientations, but rather respond to smaller scale extension and (or) compressive forces in a debris flow and collisions with other particles, and (or) rotate in a ductily deforming matrix.

Ring shear experiments on till with a Coulomb plastic rheology have shown that sand and pebble-sized grains along shear planes tend to orient themselves in the direction of shear, and that pebble-sized grains yield stronger fabrics than sand-sized grains (Hooyer and Iverson 2000b; Thomason and Iverson 2006). Some experiments also suggested that medium-coarse sand grains will yield stronger microfabrics than fine sand grains (Thomason and Iverson 2006). These observations have been attributed to the increased probability of small particles colliding with larger grains in plastically deforming sediment (Thomason and Iverson 2006). The relationship between grain size and grain orientation is explored in this study below and in Table 4.12-3. In general, data in this study seem to confirm the observations made by Thomason and Iverson (2006).

Principal eigenvalues (S_1) of horizontal microfabrics measured from primary tills are usually higher for grains greater than 1 mm in apparent length, than for grains less

than 1 mm in apparent length (Fig. 4.12-2). The average β value for primary till microfabrics from grains less than 1 mm in apparent length is 41.2°, while that for grains greater than 1 mm in apparent length is 27.5°. This data confirm the grain size-microfabric relationship observed by Thomason and Iverson (2006).

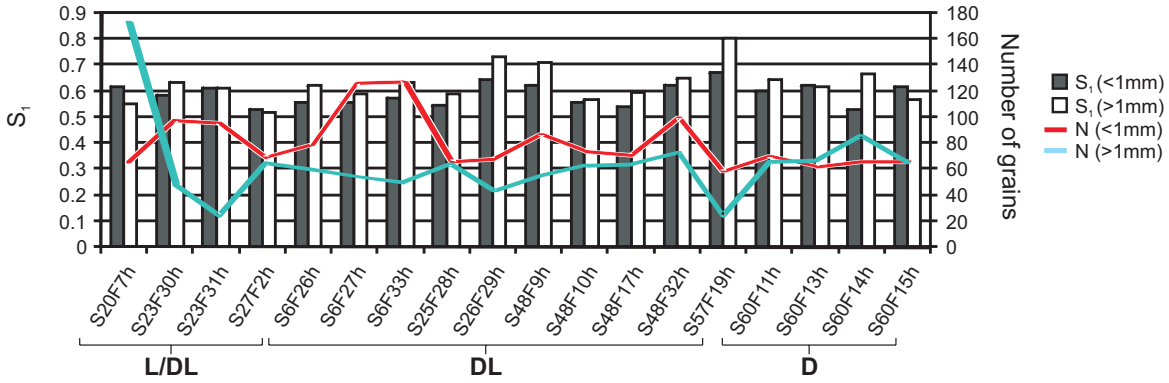

Figure 4.12-2. Primary till horizontal microfabric eigenvalues (S_1) for grains less than 1 mm in apparent length, and grains greater than 1 mm in apparent length. N=the total number of grains counted in a microfabric. Horizontal thin sections are sorted according to inferred genesis (this study), where L=mainly lodgement, DL=deformed lodgement, and D=deformation.

When primary till grain size-microfabric relationships are explored at the cluster level (Table 4.12-3), differences exist between till types. In Table 4.12-3, the microfabric statistics of grains less than 1 mm in apparent length are in black font, and those of grains greater than 1 mm in apparent length are in grey font in order to aid visual comparisons of cluster peak-mode relationships between grain size classes. For lodgement/deformed lodgement (L/DL) tills, both grain size classes have cluster peaks parallel, subparallel or orthogonal to M1, and deformation tills show no strong tendency for cluster peaks associated with the larger grain size class to align closer to M1 than cluster peaks associated with the smaller grain size class (Table 4.12-3). This suggests that the level of consistency between horizontal microfabrics and macrofabrics is not affected by the size of sand grains measured in these tills. It is also possible, however, that differences between grain size classes in these tills exist, but are not apparent due to the relatively low number of horizontal microfabrics measured (i.e., four microfabrics from lodgement/deformed lodgement tills, and four microfabrics from deformation tills).

For deformed lodgement tills, 9 out of 15 microfabric clusters that are parallel or subparallel to M1 belong to the smaller grain size class (<1 mm), and almost half of

these are B-type clusters. The larger grain size class has fewer clusters parallel/subparallel to M1, however it has many more clusters at a 20-30° angle relative to M1 than the smaller grain size class, and all of these clusters are A-type clusters. These results would explain the lower average β value associated with primary till microfabrics measured from the larger grain size class. If we assume that the orientations of the primary/only modes in the deformed lodgement tills in this study approximate the orientation of subglacial shear, than these data would appear to agree with ring shear experiments, and suggest that larger grains will align closer to the orientation of shear than smaller grains in deformed lodgement tills. The horizontal microfabric data collected in this study should, however, be interpreted with caution. In horizontal microfabrics, more grains were usually counted within the smaller grain size class than within the larger grain size class, because larger skeletal grains appeared less frequently in thin section (Fig. 4.12-2). Because, a larger sample size will lead to a higher statistical variance within grain trends, it is possible that differences in sample size (N) have contributed to the differences in microfabric statistics between grain size classes.

c) The origin of diamicton fissility

Fissility observed in lodgement or deformed (L/DL) tills at the macroscale (Table 4.2-1) was also observed in the form of subparallel planar voids at the micro-scale. Fissility has traditionally been considered to be a characteristic typical of lodgement tills (Hicock *et al.* 1996), but how fissility forms is not well understood. Past authors have attributed fissility to subglacial shear (van der Meer *et al.* 2003; Larsen 2006), but this is difficult to prove in the field. Microscopic examination of fissility planes does not support this interpretation. In some cases, a few relatively large skeletal grains are aligned with planar voids (e.g., site 23, Figs 4.2-5A, 4.2-6A), however, only three out of seven thin sections with parallel or subparallel planar voids had vertical microfabric principal eigenvectors and (or) peaks that were (sub)parallel to planar void orientations (Table 4.12-2). The misalignment between sand sized grains and fissility planes could be due to the following reasons: 1) the fissility planes are actually R_2 type Riedel shears that form ~75° angles relative to the shearing direction and have been observed to form in tills during ring shear experiments (Thomason and Iverson 2006), 2) the fissility planes develop as fractures in response to unloading of the sediment after ice retreat, and are only partly influenced by the orientation of grains in the diamicton, or 3) the fissility

planes are part of a platy structure that can develop in silty sediments or soils as a result of ice lens formation in the winter, where the orientation of the planes is controlled by the geometry of the downward migrating freezing front (van Vliet-Lanoë *et al.* 1984; Sveistrup *et al.* 2005). Given that fissility planes were best observed near the upper contacts of till units and within 1 m of the ground surface, explanations 2), 3), or a combination thereof, are considered to be most plausible.

Chapter 5: Intra- and inter-site micromorphological comparisons - a clustering approach

5.1 Purpose and methodology

> …specific microstructures and microfabrics are probably more likely to be found in certain glacial lithofacies types more than in others (Menzies 2000, p. 247).

In Chapter 4, microscale depositional and deformational processes were inferred from diamicton microstructures and microfabrics, and the relationship between diamicton micromorphology and macroscale sedimentology was explored through qualitative analysis. In that chapter, the relative proportion of discrete microstructure types (hereafter referred to as a 'microstructure association') is quantified for each vertical thin section, and illustrated using frequency histograms and microstructure maps. In this chapter, the microstructure associations of all diamictons are explored using hierarchical cluster analysis techniques to complete the following objectives:

1) to demonstrate that diamicton types in the study area, which have been classified here using macroscale sedimentological evidence and the definitions of the INQUA Commission on the Genesis and Lithology of Glacial Quaternary Deposits (Dreimanis 1989), have no diagnostic micromorphologies, (although the microstructures may support, or at least be explainable by the macroscale sedimentological interpretation, see Chapter 4); and
2) to investigate the relationship between diamicton micromorphology, and local environmental variables such as topographic position, diamicton texture, and local bedrock lithology.

Microstructure associations for all vertical thin sections are assembled into a single 23 x 5 matrix comprised of 23 vertical thin sections (unique compositions) and 5 microstructure types (variables) (Table 4.12-1). Because the microstructure associations are expressed as normalized relative frequencies with a constant sum of 100%, it is necessary to cluster them using techniques designed for compositional data (Aitchison 1986; Martın-Fernandez *et al.* 1998). The statistical protocol includes the following steps:

1) All zeros are removed from the dataset using the 'Multiplicative Replacement Strategy' proposed by Martín-Fernández *et al.* (2003). This is done to avoid undefined values that would result from the data

transformation in Step 2. Thus, if each composition with Z zeros (where Z>0), is expressed as a vector **x**, **x** is replaced by the composition *r* using the following expression:

$$r_j = \begin{cases} \delta_j, & \text{if } x_j = 0, \\ (1 - \frac{\sum_{k|x_k=0} \delta_k}{c}) x_j, & \text{if } x_j > 0, \end{cases} \qquad (1)$$

where δ_j is an imputed value equal to 65% of the rounding threshold, and *c* is the sum constraint equal to 100 (Martín-Fernández *et al.* 2003). Because all values in the dataset are rounded to the nearest percent, the rounding threshold value is 0.5%.

2) Aitchison's (1986) centred log-ratio transformation is applied to the dataset. This transformation removes the constant sum constraint from the data, so that multivariate statistics can be applied (e.g. Martin-Fernandez *et al.* 1998). The centred log-ratio transformation is calculated as follows:

$$\text{clr}(\mathbf{x}) = [\ln(x_1/g(\mathbf{x}),...,\ln(x_D/g(\mathbf{x}))], \qquad (2)$$

where D is the number of variables (microstructure types) in composition **x**, and g(**x**) is the geometric mean of composition **x** as calculated below:

$$g(\mathbf{x}) = (\Pi_{j=1}^{D} x_j)^{1/D} \qquad (3)$$

3) All variables in the dataset are standardized to a mean of 0 and a variance of 1 using the formula:

$$b_{ij} = (x_{ij} - X_j)/s_j \qquad (4)$$

where X_j and s_j are the arithmetic mean and standard deviation of the (j)th variable, respectively. This standardization allows all variables to contribute equally to the clustering process (Romesburg 1984).

4) A dissimilarity matrix ($ED_{i,h}$) is constructed from the data using Euclidean distances. This matrix is a square, symmetrical matrix where every (i,h)th element represents the Euclidean distance between the (i)th and (h)th composition, and is calculated as follows:

$$ED_{i,h} = \sqrt{\sum_{j=1}^{D} (b_{i,j} - b_{h,j})^2} \qquad (5)$$

5) Agglomerative hierarchical cluster analyses (Everitt 1993) are conducted using multiple linkage methods (i.e., Ward's, single, complete, average, McQuitty's, median and centroid).

6) The cophenetic correlation coefficient ($r_{x,y}$) is calculated for each linkage method in order to choose the method that best represents the inter-composition similarity structure inherent in the dissimilarity matrix (Romesburg 1984).

All statistical analyses were conducted using "R: A Language and Environment for Statistical Computing" (R Development Core Team 2007).

Initially, microstructure associations were clustered using the Ward, single, complete, average, McQuitty, median and centroid linkage methods. Because the dendrograms derived from the median and centroid methods contained inversions (Morgan and Ray 1995), they were left out of subsequent analyses. The dendrograms for the Ward, single, complete and McQuitty linkage methods are shown in Figures I-1 through I-4 in Appendix I. The results of these linkage methods are superimposed on maps of the study area so that the geographic distribution of clusters can be seen (Figs I-5, I-6, I-7, I-8, Appendix I). The linkage method that yielded the highest cophenetic correlation coefficient (0.86) was the average linkage method. Thus, the dendrogram and map displaying these results are presented in Figures 5.1-1 and 5.1-2, respectively and will be discussed in detail below.

As will be demonstrated in Section 5.2, the hierchical clustering protocol described above is useful for comparing diamictons in terms of their relative abundances of particular microstructures. However, the robustness of this technique is limited by the subjectivity involved in identifying turbates, necking structures, grain lineations, grain stacks, and crushed/broken grains (see subjectivity test results in Fig. 3.3-6). Therefore, cluster analysis results presented in this thesis should be interpreted with caution until further research on subjectivity in diamicton micromorphology is pursued.

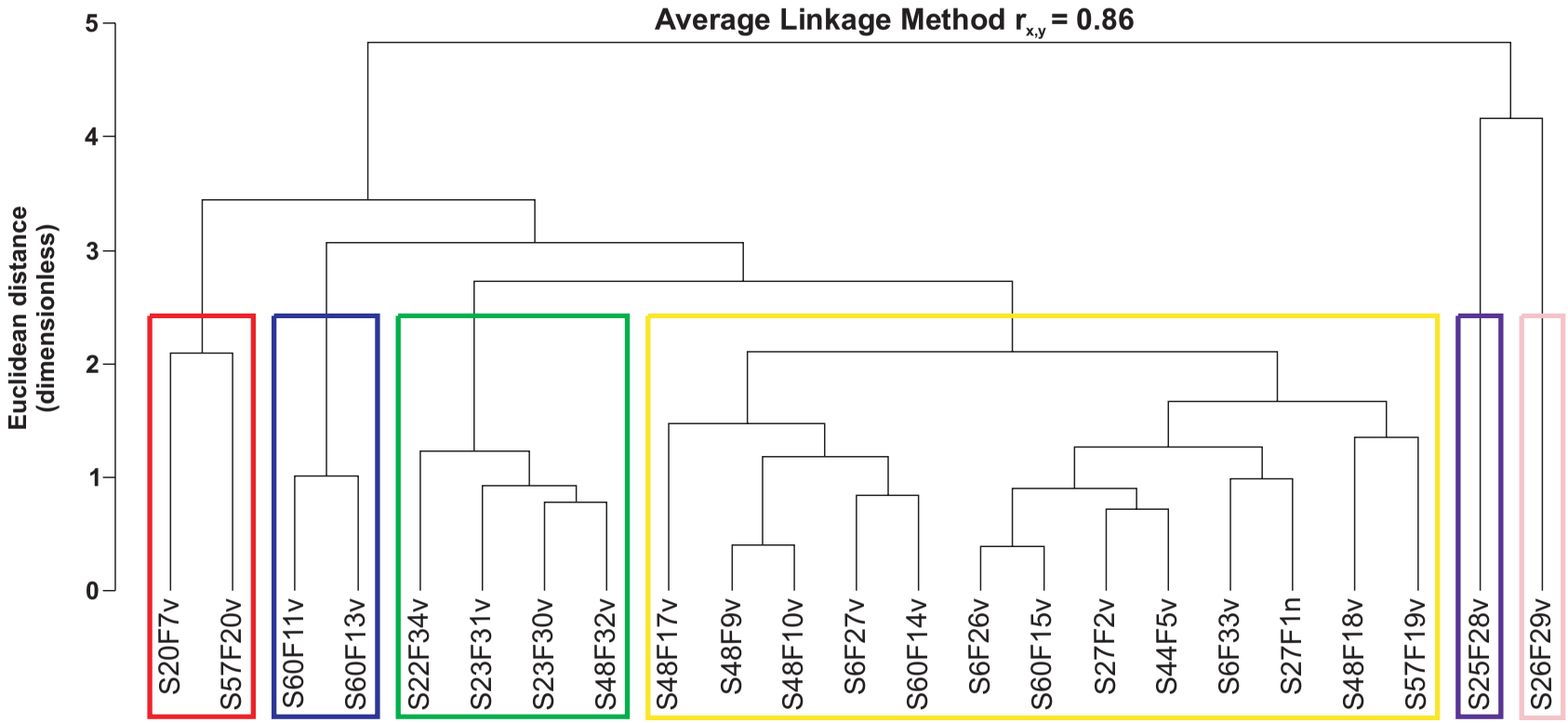

Genesis	L/DL	DL	D	D	G	L/DL	L/DL	DL	DL	DL	DL	DL	D	DL	D	L/DL	G	DL	L/DL	DL	DL	DL	DL
N	34	42	73	79	55	16	21	57	46	34	67	57	31	42	49	49	102	15	66	54	25	3	8
Clast c. (%)	8	6	24	25	15	9	18	21	25	8	19	6	17	7	26	13	8	3	9	18	10	3	5

Figure 5.1-1. A dendrogram showing the results of hierarchical cluster analysis of micromorphological data from all vertical thin sections using the average linkage method. $r_{x,y}$ = the cophenetic correlation coefficient. Coloured boxes delineate groups that have been superimposed on a map of the study area in Figure 5.1-2. Red = group 1, blue = group 2, green = group 3, yellow = group 4, purple = group 5, and pink = group 6. The inferred diamicton genesis (this study) and clast concentration (clast c.) associated with each thin section is included below the dendrogram. L/DL = lodgement or deformed lodgement, DL = deformed lodgement, D = deformation, and G = gravity flow. N is the absolute number of discrete microstructures counted in the thin section.

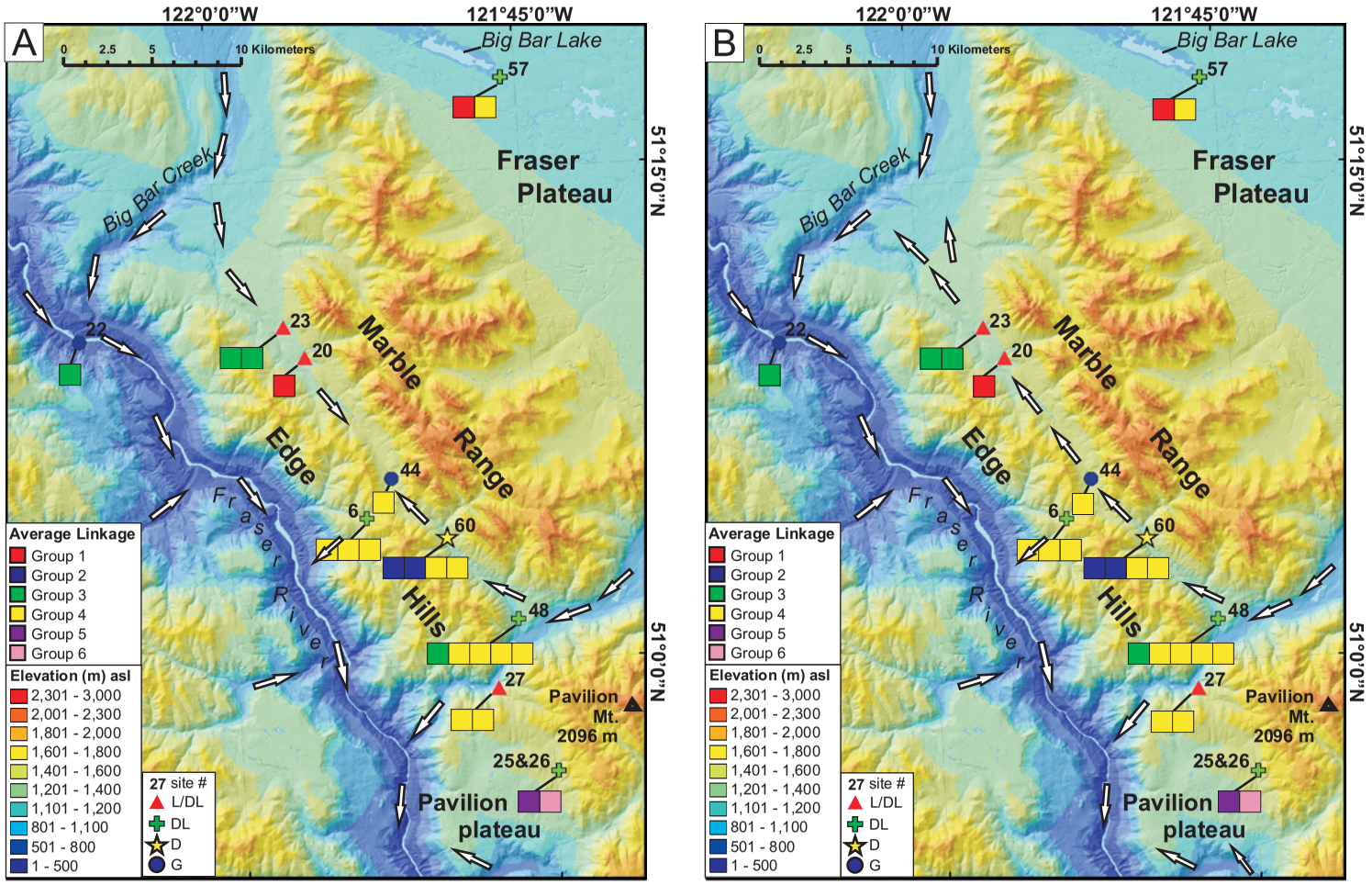

Figure 5.1-2. Geographic distribution of microstructure association clusters (groups) derived using the average linkage clustering method (see Figure 5.1-1 for dendrogram). Site locations are marked with symbols indicating the inferred diamicton genesis according to Neudorf (this study), where L/DL = lodgement or deformed lodgement (triangles), DL = deformed lodgement (crosses), D = deformation (star), and G = gravity flow (circle). Ice flow directions (white arrows) for the early part of the last glaciation (A), and the last glacial maximum (B) are from Lian and Hicock (2000). Both maps are superimposed on a hillshaded and classed TRIM I digital elevation model (Projection: Albers Conical Equal Area, Datum: NAD 83. Source: Government of British Columbia 2007. © Province of British Columbia).

5.2 Results and discussion

5.2.1 Microstructure association and diamicton type

When the microstructure association data is clustered down to six groups using the average linkage method, a spatial pattern emerges where sites in Cutoff Valley and the lower half of Jesmond valley (sites 44, 6, 60, 48, and 27) tend to have microstructure associations more similar to each other than to those of other sites (Fig. 5.1-2). Most microstructure associations from these sites belong to group 4, which is by far the largest cluster, and has a high amount of turbates (averaging 35% per thin section), moderate amounts of necking structures, grain lineations and crushed/broken grains, (averaging 26%, 19% and 15% per thin section, respectively), and small amounts of grain stacks (averaging 5% per thin section) (Fig. 5.2-1). The rest of the sites (sites 20, 22, 23, 25, 26 and 57) have microstructure associations that fall into groups 1, 3, 5 or 6, (with the exception of site 57, which also has one thin section that falls into group 4) (Fig. 5.1-2). These groups mainly contain 2-4 microstructures in association (Fig. 5.2-1). Two of them (groups 1 and 3) are dominated by turbates, one (group 5) has equal proportions of necking structures, grain lineations and crushed/broken grains, and one (group 6) is dominated by crushed/broken grains (Fig. 5.2-1).

Diamicton types do not have diagnostic micromorphological associations (Figs 5.1-1, 5.1-2). For example, when microstructural data are clustered using the average linkage method, thin sections from lodgement/deformed lodgement (L/DL) tills cluster closer to gravity flow (G) diamictons than other lodgement/deformed lodgement (L/DL) tills (e.g., notice proximity of L/DL sites 23 and 27, to G sites 22 and 44, respectively, Fig. 5.1-1). Thin sections from similar diamicton types are often separated by some of the largest cophenetic distances (e.g., compare L/DL sites 20 and 23, and G sites 44 and 22 in Fig. 5.1-1). (The cophenetic distance is the Euclidean distance, at which two thin sections are first joined in the dendrogram (Romesburg 1984)).

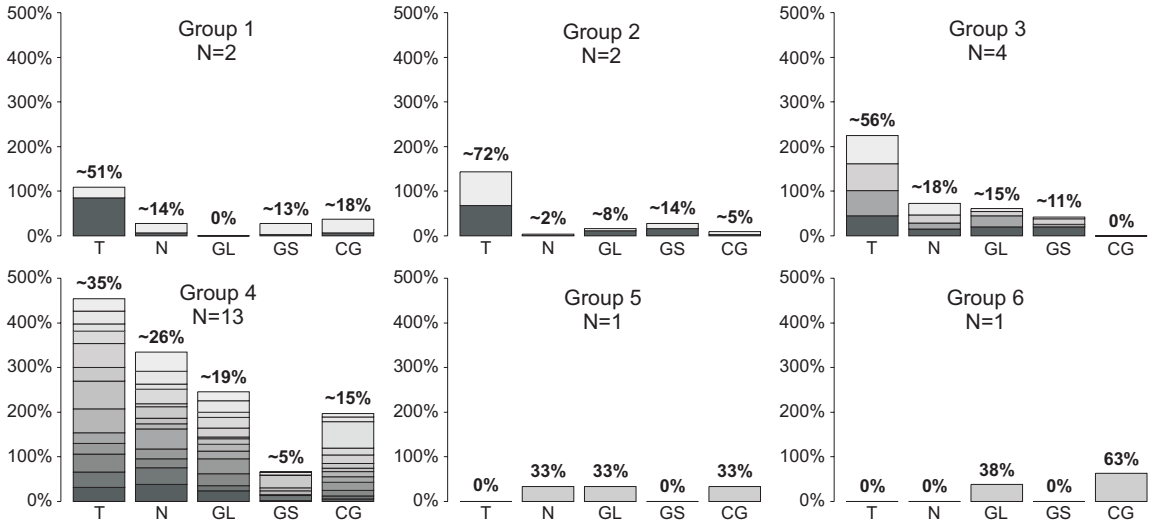

Figure 5.2-1. Stacked bar plots for each of the 6 groups identified by the average linkage clustering procedure. The microstructure association of each vertical thin section is represented by one layer in the stack. The value above each stack represents the average proportion (%) each microstructure represents in thin sections of that group. N is the total number of thin sections in each group.

5.2.2 Microstructure association and bedrock lithology

Two major formations lie on either side of the Jesmond valley, and meet at a fault line that follows Jesmond Road (Roddick *et al.* 1976) (Fig. 5.2-2). Most sites within Jesmond valley and on Pavilion plateau lie along this fault line, and consequently, the geography of these groups (microstructure associations) is not explained by bedrock lithology. Groups associated with sites that overlie a single bedrock type (e.g., sites 22, 57, 20, 23, 6 and 27) show no preference for any particular lithology.

5.2.3 Microstructure association and number of microstructures

In some cases, thin sections from the same diamicton unit at a site tend to cluster in close proximity to each other (e.g., thin sections from sites 23 and 27, Fig. 5.1-1). In other cases, the intra-unit cophenetic distances between thin sections are relatively high (e.g., site 57, Fig. 5.1-1). The large intra-unit cophenetic distance between thin sections sampled from the diamicton at sites 25 and 26 is likely a function of the low total number of discrete microstructures (N) that was counted (e.g., N=3 for S25F28v, N=8 for S26F29v, Fig. 5.1-1). The lower N is for a given thin section, the less likely a representative microstructure association is measured.

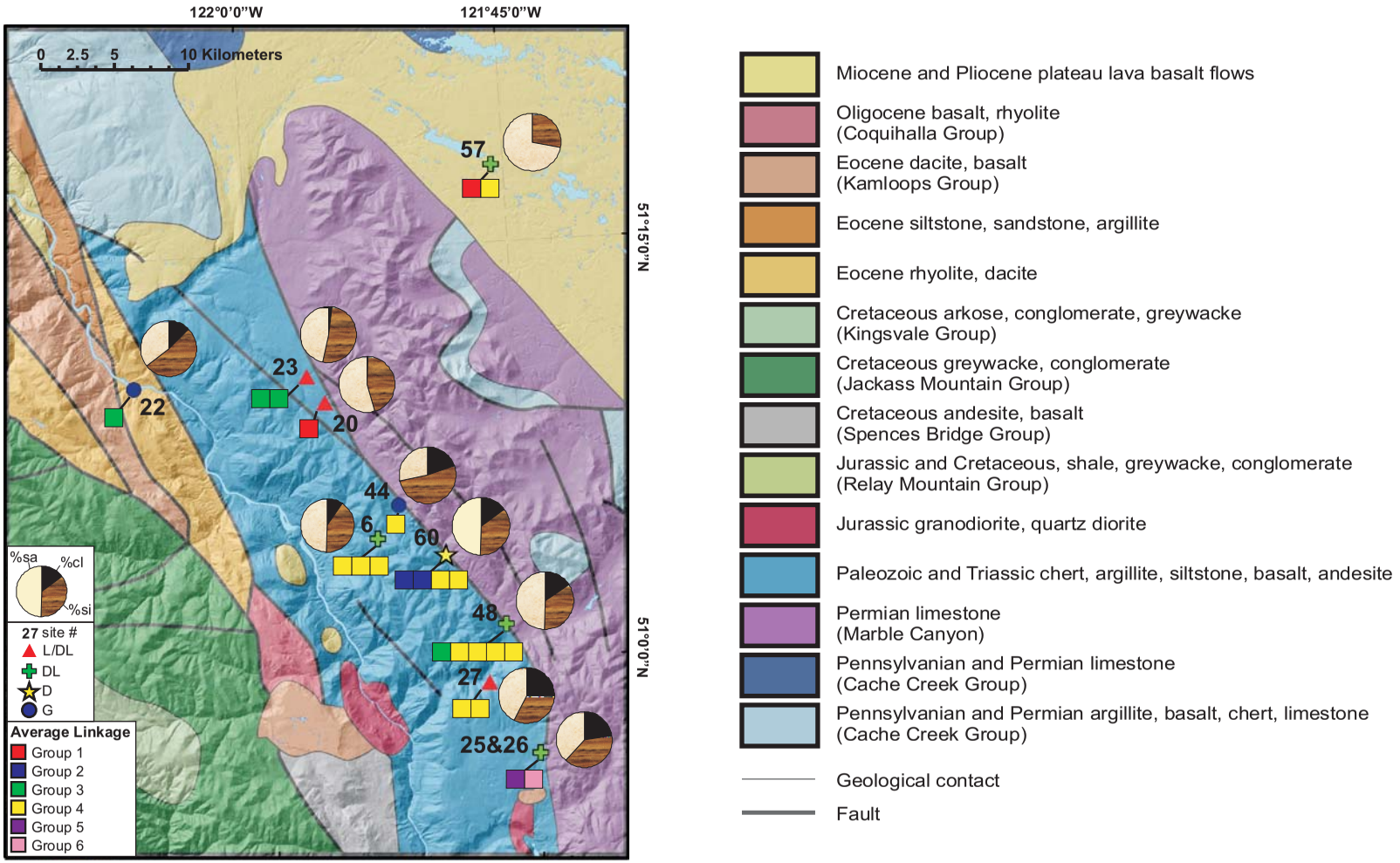

Figure 5.2-2. Average diamicton texture (pie charts, beige=sand, brown=silt, black=clay), and microstructure association clusters (average linkage clustering method) superimposed on a map of bedrock lithology (based on Roddick *et al.* 1976) overlaying a hillshaded TRIM I digital elevation model (Projection: Albers Conical Equal Area, Datum: NAD 83. Source: Government of British Columbia 2007. © Province of British Columbia). Site locations are marked with symbols indicating the inferred diamicton genesis according to Neudorf (this study), where L/DL = lodgement or deformed lodgement, DL = deformed lodgement, D = deformation, and G = gravity flow.

Another example where N seems to influence how thin sections are clustered appears at site 60. Thin sections S60F11v and S60F13v cluster together at the lowest clustering level, but are separated from S60F14v and S60F15v by a cophenetic distance of 3 (Fig. 5.1-1). For thin sections S60F11v and S60F13v, N=73 and 79 respectively, while N<50 for both thin sections, S60F14v and S60F15v.

Thin sections with a low absolute number of microstructures (N) tend to have more brittle-type structures than thin sections with a high absolute number of microstructures (Fig. 5.2-3). Thin sections with few microstructures are either poorly impregnated, exhibit lots of fractures and voids (e.g., S25F28v and S26F29v, Figs 4.9-4A, 4.9-5A), or have grains that are difficult to discern in the matrix (e.g., S57F19v and S57F20v, Figs 4.10-4A, 4.10-5A). Thus, ductile-type structures, such as turbates and necking structures, may be more difficult to identify in these thin sections. Differences in N leading to a difference in the relative abundance of ductile and brittle structures would explain the tendency for S57F19v and S57F20v to join different clusters (Fig. 5.2-3).

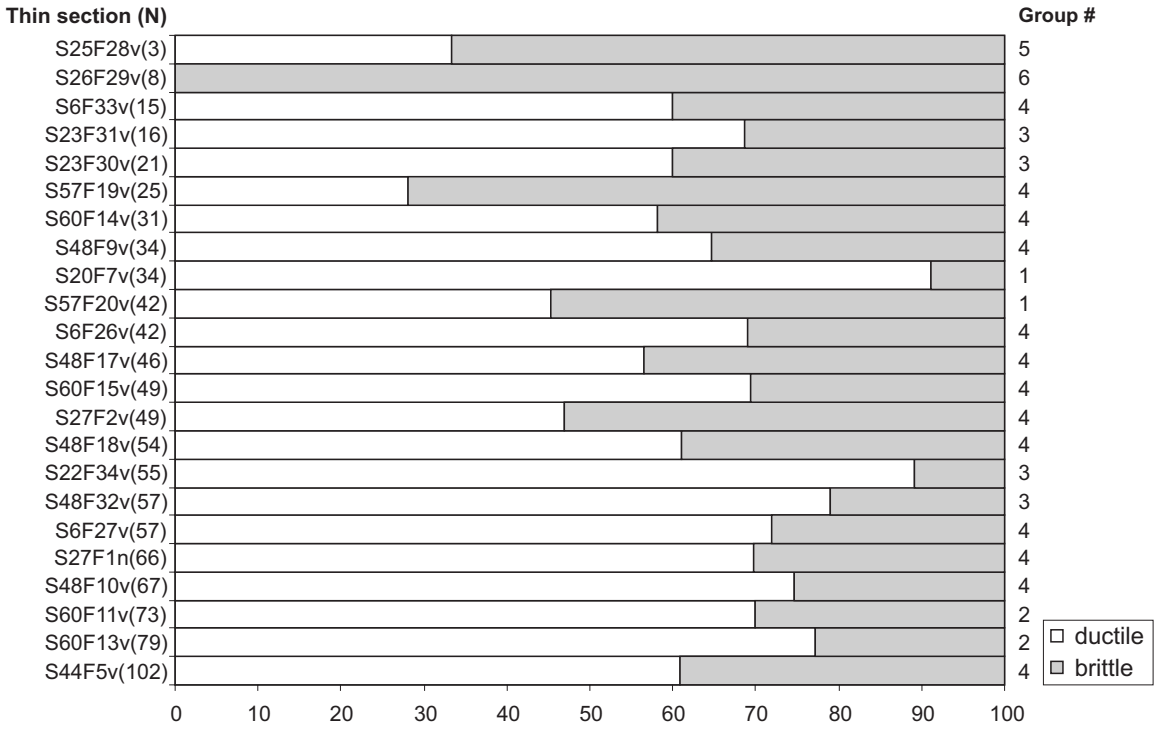

Figure 5.2-3. Proportion of brittle and ductile structures in each thin section, sorted by increasing number of microstructures (N) per thin section (top to bottom). The average linkage method group each thin section belongs to is indicated on the right side of the bar graph.

The above relationships do not explain all clusters, however. For example, thin section S48F10v clusters closer to sections S48F9v and S48F17v than to thin sections S48F18v and S48F32v despite the fact that N for S48F10 is closer to that of thin sections S48F18v and S48F32v than it is to that of sections S48F9v and S48F17v (Fig. 5.1-1). The relative proportion of ductile and brittle structures for thin section S48F10v (group 4) is also closer to that of thin section S48F32v (group 3) than it is to that of thin section S48F17v (group 4) (Fig. 5.2-3). Another explanation for the clustering pattern of site 48 may be linked to the location of diamicton sample sites relative to each other in the unit (Fig. 4.7-1). For example, thin sections S48F17v, S48F9v, S48F10v and S48F18v (group 4) cluster closer to each other, than to thin section S48F32v (group 3). The sample sites for thin sections S48F17v, S48F9v, S48F10v and S48F18v are also higher up in the unit and closer to each other than to the sample site of S48F32v (Fig. 4.7-1). This correlation between clusters and thin section sample positions may record intra-unit variations in diamicton depositional process, strain magnitude, and (or) porewater pressures. Thin section S48F32v has abundant turbates (60%), moderate amounts of necking structures, grain lineations and grain stacks (19%, 9% and 12% respectively), and no crushed/broken grains (Table 4.12-1). Thin sections S48F9v, S48F10v, S48F18v and S48F17v cluster together in group 4, and thus, are associated with more crushed grains (7-12%, Table 4.12-1, Fig. 5.2-1). The microstructure associations of the latter thin sections therefore could be interpreted to represent microscale depositional/deformational processes characterized by lower porewater pressures that caused higher inter-grain effective stresses leading to grain fracture (Hooke and Iverson 1995).

5.2.4 Microstructure association and diamicton texture

Figure 5.2-2 shows the average texture of the diamicton matrix at each site (Fig. 4.2-2, Table E-1, Appendix E). The particle size distribution of all sites is similar, except for sites 20, 23 and 57, which lack clay. Diamictons at sites 20 and 23, have markedly lower clay contents than sites in the lower half of Jesmond valley (containing microstructure association group 4). These diamictons may have been derived from preglacial sediments (perhaps advance glaciofluvial outwash) that also had low clay contents, or they may have experienced elutriation by subglacial and (or) proglacial meltwater as a result of better drained conditions in a less topographically constrained part of the valley (Lian and Hicock 2000). Diamictons in the lower half of Jesmond valley

may have been derived from preglacial sediments with higher clay contents. These preglacial sediments, in turn, may have been the products of the ponding of glacial meltwater in front of advancing ice flowing northward against the slope gradient (Section 4.6.4). Higher clay contents in diamictons in the lower part of Jesmond valley may also be a result of poor drainage conditions due to constricting topography (Lian and Hicock 2000), and limited subglacial and proglacial elutriation as a result.

There is, in general, no tendency for thin section microstructure associations to cluster according to the clast concentration of the diamicton they were measured from (Fig. 5.1-1). The exception is group 2, which contains two microstructure associations with similar clast concentrations. Despite the geographic relationship between microstructure association group 4 and finer grained diamictons (Fig. 5.2-2), plots of the proportion of each microstructure type against diamicton matrix texture show no clear relationship (Fig. 5.2-4, Table 5.2-1). Thus, these data suggest that microstructure development in these diamictons is not primarily controlled by diamicton texture, but rather by depositional processes that may have contributed to, or were influenced by diamicton texture.

5.2.5 Microstructure association and topographic position

Microstructure associations that form group 4 come from all diamicton types (Figs 5.1-1, 5.1-2), but their restricted geographic distribution might suggest that they correlate to specific depositional processes unique to that region. Lian (1997) and Lian and Hicock (2000) have suggested that the more topographically constrained, southern part of Jesmond valley was characterized by poorly drained subglacial conditions leading to the development of deformed lodgement and deformation till (sites 6, 48 and 60, Fig. 5.1-2), while the less topographically constrained, northern part of the valley consisted of better drained conditions allowing the preservation of lodgement till-like diamicton characteristics (sites 20 and 23, Fig. 5.1-2) (Lian and Hicock 2000). Microstructure associations in group 4 predominantly lie within the topographically constricted part of Jesmond valley. The small proportion of grain stacks and crushed grains (brittle-type structures) relative to necking structures and turbates (ductile-type structures) in primary tills in group 4 could be explained by elevated porewater pressures in a subglacial environment that reduce intergranular effective stress and friction during till deposition or emplacement (Hooke and Iverson 1995). These interpretations would thus, support Lian (1997) and Lian and Hicock's (2000) interpretation. However, primary

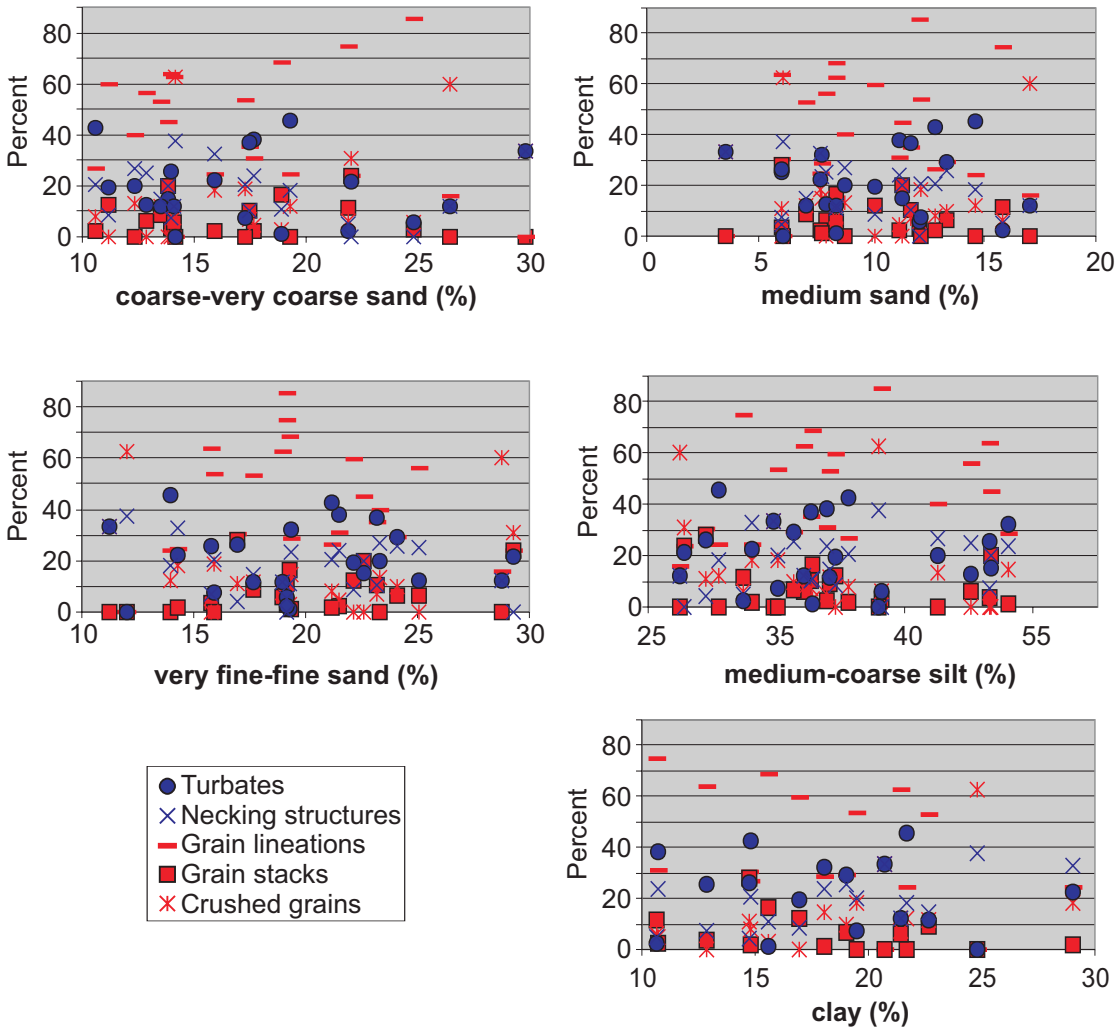

Figure 5.2-4. Scatterplots of microstructure relative abundance (%) against diamicton matrix texture. No clear correlation between and the size of sand, silt or clay fractions and the relative abundance of particular microstructures is discernable.

Table 5.2-1. Pearson-product moment correlation coefficients describing the strength and direction of the linear relationship between microstructure relative abundance and grain size fraction. See Figure 5.2-4 for scatterplots.

Microstructure	Clay	Medium-coarse silt	Very fine-fine sand	Medium sand	Coarse-very coarse sand
turbates	0.14	-0.02	-0.09	-0.06	-0.11
necking str.	0.49	0.40	-0.16	-0.22	-0.31
lineations	-0.26	0.20	0.28	0.27	0.21
grain stacks	-0.32	-0.32	0.13	-0.20	0.22
crushed/broken grains	0.08	-0.33	-0.27	-0.37	-0.10

tills in groups 1 and 3 located in the northern part of Jesmond valley (Fig. 5.1-2), *also* have low proportions of brittle-type microstructures and *even higher* proportions of ductile-type microstructures per thin section than group 4. Therefore, if drainage conditions in the valley, as described by Lian (1997) and Lian and Hicock (2000), did influence microstructure development in primary tills, then better drained subglacial conditions did not necessarily lead to high proportions of brittle-type microstructures and low proportions of ductile-type structures.

Ring shear experiments have shown that as till is sheared to a maximum strain magnitude of 7, the absolute number of turbates and grain lineations increases with shear strain, while the absolute number of grain stacks decreases with shear strain (Larsen *et al.* 2006). The relatively abundant turbates and grain lineations, and scarce grain stacks in groups 3 and 4 might suggest that the diamictons in the Jesmond valley, the Fraser River valley and on the Fraser Plateau have experienced higher strain magnitudes during deposition or emplacement than the diamictons on the Pavilion plateau. This inference, however, would require that all diamictons outside of groups 3 and 4 experienced strain magnitudes less than 7, and independent measurements of strain magnitude could not be obtained to verify this assumption.

5.2.6 Microstructure association and ice/sediment provenance

Paleo-ice flow directions for the early part of the last glaciation, converge on Jesmond valley from both ends (Lian and Hicock 2000) (Fig. 5.2-1A). During glacial maximum Jesmond valley is thought to have been dominated by northward flowing ice (Lian and Hicock 2000) (Fig. 5.2-1B). Northward flowing ice in the southern part of the Jesmond valley is supported in this study by sedimentological and structural evidence at sites 48 and 60 (Section 4.6). Southward flowing ice associated with the early part of the Fraser glaciation is supported by sedimentological and structural evidence from site 20, located in the northern part of Jesmond valley (Section 4.3). Southward flowing ice in the northern part of Jesmond valley, however, is *not* supported by clast fabrics and fissility planes at site 23 (Section 4.2). This evidence suggests, rather, ice flow from the S. The diamicton at site 23, therefore, may have been associated with subglacial deposition during the last glacial maximum after the deposition of the diamicton at site 20. If the deposition of the diamicton at site 20 did indeed occur under southward flowing ice, and the deposition of the diamicton at site 23 occurred under later,

northward flowing ice, then the textural and micromorphological similarities between sites 23 and 20 are not explained by ice/sediment provenance.

5.3 Summary

In this chapter hierarchical cluster analysis was used to explore the influence of environmental variables on microstructure development in diamictons, and to test the hypothesis that different diamicton types have unique microstructure associations. This has lead to the following conclusions:

1) glacigenic diamictons, which have been classified using macroscale sedimentological evidence and the definitions of the INQUA Commission on the Genesis and Lithology of Glacial Quaternary Deposits (Dreimanis 1989) do not have diagnostic micromorphologies,
2) discrete microstructure development in diamictons in the study area does not appear to be controlled by local bedrock geology, as many sites with contrasting microstructure associations lie along a similar fault line,
3) discrete microstructure development in diamictons is not primarily controlled by diamicton texture, but rather, may have been influenced by depositional processes that contributed to, or were influenced by diamicton texture,
4) the microstructure association of a thin section is partially influenced by the total number of microstructures that can be counted in thin section,
5) multiple microstructure associations within a single diamicton unit may record variations in diamicton depositional process, strain magnitude, and (or) porewater pressures,
6) discrete microstructure development in poorly drained substrates in topographically constricted areas may differ from that in better drained substrates in less topographically constricted areas. There is no evidence to suggest, however, that microstructure associations from diamictons deposited under well drained conditions will have a higher proportion of brittle-type microstructures than those deposited under poorly drained conditions, and
7) discrete microstructure development in diamictons in this area does not seem to be influenced by ice/sediment provenance.

Chapter 6: Discussion and conclusions

The three research objectives of this thesis were:

1) to investigate the relationship between diamicton micromorphology and macroscale sedimentology;
2) to test the hypothesis that diamictons classified using macroscale sedimentological criteria and definitions proposed by the INQUA Commission (Dreimanis 1989) contain diagnostic micromorphologies; and
3) to investigate the relationship between diamicton micromorphology and local environmental variables such as topography, diamicton texture, and local bedrock lithology.

This chapter summarizes the outcomes and implications of this research, and provides recommendations for future research.

6.1 Objective 1: The relationship between diamicton micromorphology and macroscale sedimentology

Qualitative micromorphological observations made from diamictons in the study area show differences between gravity flow diamictons and primary tills. Gravity flow diamictons observed in this study (sites 44 and 22) generally appear massive at the macroscale (Figs 4.4-2, 4.4-3, 4.11-2), but still seem to be more likely to exhibit evidence of water sorting or laminar flow at the microscale than primary tills (Figs 4.4-4A, 4.11-3A). Similar observations have been made by Lachniet (2001), Menzies and Zaniewski (2003) and Phillips (2006). Macroscopic and microscopic heterogeneities observed in the matrix of some primary tills (sites 48 and 27, Figs 4.7-4D, 4.8-3A) appear to be the result of the intermixing of diamictons from different sources through glaciotectonic deformation.

Microfabrics with subvertical peaks and eigenvectors with steep (70-90°) plunges seem to be restricted to deformed lodgement, deformation and gravity flow tills (see microfabrics S26F29v-1, S6F27v-1 and S60F14v-1, Table 4.12-2). This may reflect the increased likelihood of end-over-end grain rotation (i.e., rotation around grain b- or c-axes) within tills that have experienced post-depositional deformation or gravity flow. It may also record particle rotation as a result of a higher frequency of clast collisions in diamictons with relatively high clast concentrations (site 60, Table 4.2-1).

Comparisons between horizontal microfabric cluster orientations and macrofabric modes in primary tills suggest that sand-sized grains are more likely to align themselves

in the direction of shear (subparallel to pebble-sized clasts) in lodgement and (or) deformed lodgement tills than in deformation tills and gravity flow tills (Table 4.12-3). These observations are consistent with ring shear experiments, where the long axes of sand-sized grains point to the direction of shear along shear planes in plastically deforming till (Thomason and Iverson 2006) due to slip between grain surfaces and the surrounding diamicton. Therefore they may record lodgement of sand-sized grains at the ice-bed interface or non-pervasive plastic deformation within the diamicton. Deformation tills and gravity flow diamictons show less consistency between sand-sized grains and pebbles, as shown by their higher β values and fewer A-type cluster peaks oriented parallel or sub-parallel to macrofabric primary/only modes. Sand grain orientation in deformation tills may be influenced by periods of elevated subglacial porewater pressures leading to ductile deformation and Jeffrey-style rotation of grains, and (or) frequent clast collisions due to elevated clast concentrations (site 60, Table 4.2-1). Sand grain orientation in gravity flow diamictons may be influenced by rotation of grains in a ductily deforming matrix, particle collisions, and (or) small scale extension and compressive forces in a debris flow.

Macroscale and micro-scale observations would suggest that fissility, a feature observed at the macroscale often associated with lodgement tills, develops in response to unloading of the sediment after ice retreat, and (or) to freezing of the ground in winter (van Vliet-Lanoë *et al.* 1984; Sveistrup *et al.* 2005).

6.2 Objective 2: Do different diamicton types contain diagnostic micromorphologies?

All diamicton types classified in this study have turbates, necking structures, grain lineations, grain stacks, crushed grains, and clay and mineral precipitates. Cluster analyses for multivariate compositional data have revealed that the relative abundances of discrete microstructures are not unique to any diamicton type. There is evidence however, that some microscale sedimentological characteristics occur more frequently in specific diamicton types. As mentioned above, microfabrics may be less consistent with macrofabrics in deformation tills and gravity flow diamictons than in lodgement and (or) deformed lodgement tills, and evidence of water sorting or laminar flow may be more prevalent in gravity flow diamictons than in primary tills. These results suggest that though microstructures and microfabrics may not be *diagnostic* of any one diamicton type, depositional processes and conditions do express themselves at the microscale.

Therefore diamicton micromorphology may be used to elaborate on formational/depositional mechanics and post-depositional modification, however, interpretations are best made within the context of macroscale sedimentological inferences.

Macroscale sedimentological analyses revealed that, even after quantification of pebble morphological characteristics in the study area, unequivocal evidence for undeformed lodgement till could not be obtained. This is likely because glacigenic wear features on pebbles in the study area such as facets, keels, fractured ends and bullet noses, do not necessarily represent the most recent depositional process, and smaller sized clasts may be more susceptible to re-orientation during ploughing at the ice-bed interface and (or) after lodgement due to post-depositional deformation (Benn 1994; 1995). Previous studies have shown that glacigenic wear features recording lodgement are better preserved on larger clast sizes (Benn 1994; 1995), therefore quantification of clast wear features on cobbles and boulders may allow a more precise classification of diamictons in the study area.

6.3 Objective 3: The relationship between diamicton micromorphology and environmental variables

Diamicton microstructure associations do not appear to be influenced by underlying bedrock lithology (Fig. 5.2-2). However, the juxtaposition of diamictons of a different colour or susceptibility to weathering (e.g., sites 27 and 48, Figs 4.7-4D, 4.8-3A) provides evidence of ice flow over bedrock or sediments of variable composition.

No clear relationship between diamicton discrete microstructures and diamicton texture could be discerned in this study (Fig. 5.2-4, Table 5.2-1). However, the geographic distribution of microstructure association clusters (Fig. 5.1-2) suggests that discrete microstructure development may have been influenced by depositional processes that contributed to, or were influenced by diamicton texture.

Lian (1997) and Lian and Hicock (2000) have suggested that the more topographically constrained, southern part of Jesmond valley was characterized by poorly drained subglacial conditions leading to the development of deformed lodgement and deformation till, while the less topographically constrained, northern part of the valley consisted of better drained conditions allowing the preservation of lodgement till-like diamicton characteristics (Lian and Hicock 2000). The geographic distribution of microstructure association clusters (Fig. 5.1-2) suggests that discrete microstructure

formation may have been influenced by the drainage properties of the substrate that were, in turn, controlled by topography. There is no evidence to suggest, however, that microstructure associations from diamictons deposited under well drained conditions will have a higher proportion of brittle-type microstructures than those deposited under poorly drained conditions.

Microstructure associations should be interpreted with caution, because 1) the identification of microstructures is subjective, and 2) the relative amounts of brittle and ductile microstructures can be influenced by the total number of microstructures counted in a thin section.

6.4 Recommendations for future research

During the course of this project, it was discovered that identification of even the simplest microstructures is an extremely subjective exercise. As a result, a very detailed protocol containing strict definitions had to be developed in order to identify and quantify discrete microstructures and to ensure somewhat reproducible results (see Appendix F). Recent research has focused on developing quantitative image analysis methods and GIS techniques for the purpose of identifying and separating major components of a thin section image that show areas of diamicton matrix, void spaces, skeleton grains, and birefringent plasma (Zaniewski and van der Meer 2005). These techniques need to be further developed in order to automate the identification of turbates, necking structures, grain linations, grain stacks and crushed/broken grains. Until then, scientists intending to quantify diamicton microstructures would benefit from additional research on how to minimize observer bias and subjectivity. Additional tests for subjectivity have been performed, but are not included in this thesis. This data will be included in future publications.

This study assumes clast facets, bullet noses, fractured ends (observed on the upper-sides of clasts) and keels as features that develop on clasts when they are ploughed and (or) lodged into the substrate at the ice-bed interface. However, ring shear experiments (Iverson 2007, pers. comm.) and field studies (Mickelson *et al.* 1992; Benn 1995) suggest that clast abrasion and fracture may occur in plastically deforming till or within englacial ice. Future laboratory and (or) field research that compares the development of clast wear features at the ice-bed interface with those formed within shear zones in subglacially deforming till (or till that is sheared in a laboratory) or in deforming debris-rich ice, would benefit field scientists who seek to differentiate between

lodgement tills, melt-out tills, and tills that have experienced plastic deformation in the field.

Unlike previous studies (Lian 1997; Lian and Hicock 2000), unequivocal evidence for undeformed lodgement till was not obtained from glacigenic clast wear features in this study. This may be because many features on pebble sized clasts are inherited, and (or) they are more sensitive to re-orientation during ploughing at the ice-bed interface. Quantification of clast fabrics and clast wear features over a range of clast sizes in this study area may provide more insight concerning the depth of deformation (due to ploughing) within lodgement or deformed lodgement tills, and thus allow a more precise classification of these diamictons.

Appendix A

Site latitude and longitude coordinates

All coordinates were recorded by a hand held global positioning system (GPS) with a reported accuracy of 10 m or less.

Table A-1. Site latitude and longitude coordinates.

Site	Latitude North	Longitude West	Description
6	51° 4' 36.048"	121° 53' 22.56"	a logging road cut ~1.7 km west of Jesmond Road
20	51° 9' 34.992"	121° 55' 56.5674"	an excavated depression ~100 m east of Jesmond Road
22	51° 10' 25.212"	122° 6' 48.3474"	a gully on the west side of the Fraser River
23	51° 10' 32.7"	121° 56' 53.9874"	a logging road cut running perpendicular to Jesmond Road on its east side
25 & 26	50° 56' 35.232"	121° 44' 49.92"	a logging road cut on Pavilion plateau
27	50° 59' 13.3074"	121° 47' 28.5714"	a road cut at the corner of a switchback on Pavilion-Clinton Road
44	51° 5' 45.8514"	121° 52' 4.3314"	a logging road cut on the east side of Jesmond Road
48	51° 1' 17.1114"	121° 46' 20.3874"	a roadcut on the east side of Jesmond Road
57	51° 17' 47.6874"	121° 45' 40.3914"	an excavated hill on the east side of Big Bar Road on the Fraser Plateau
60	51° 3' 54.2514"	121° 49' 32.0514"	a roadcut on the east side of Jesmond Road

Appendix B

Clast shape data

The a, b, and c-axis lengths of each clast were measured in order to classify pebble shapes following the scheme of Sneed and Folk (1958). Shape data was then superimposed onto clast fabric scatterplots to visualize any trends between clast orientation and clast shape (Fig. B-1).

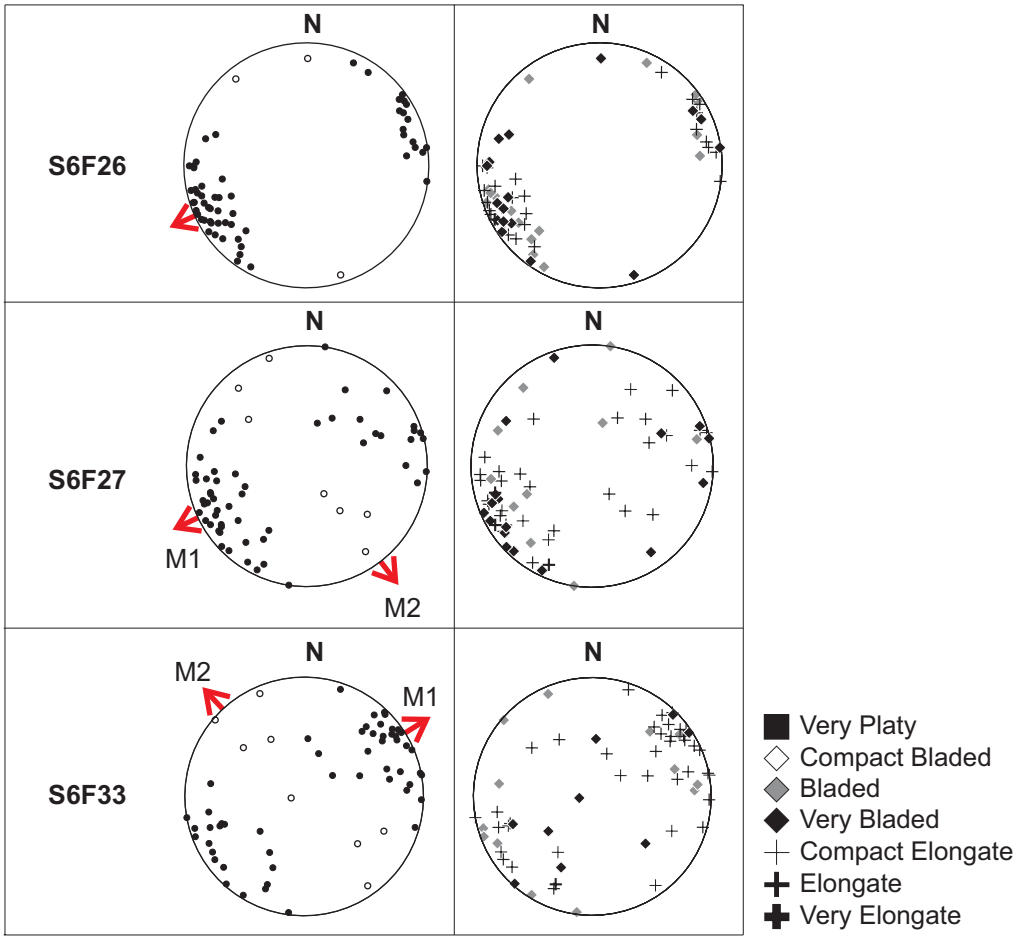

Figure B-1. Fabric scatterplots showing principal eigenvectors for all modes (left) adjacent to fabric scatterplots with symbols representing clast shapes according to Sneed and Folk (1958) (right). Sites are arranged in ascending numerical order (pages 204 to 209).

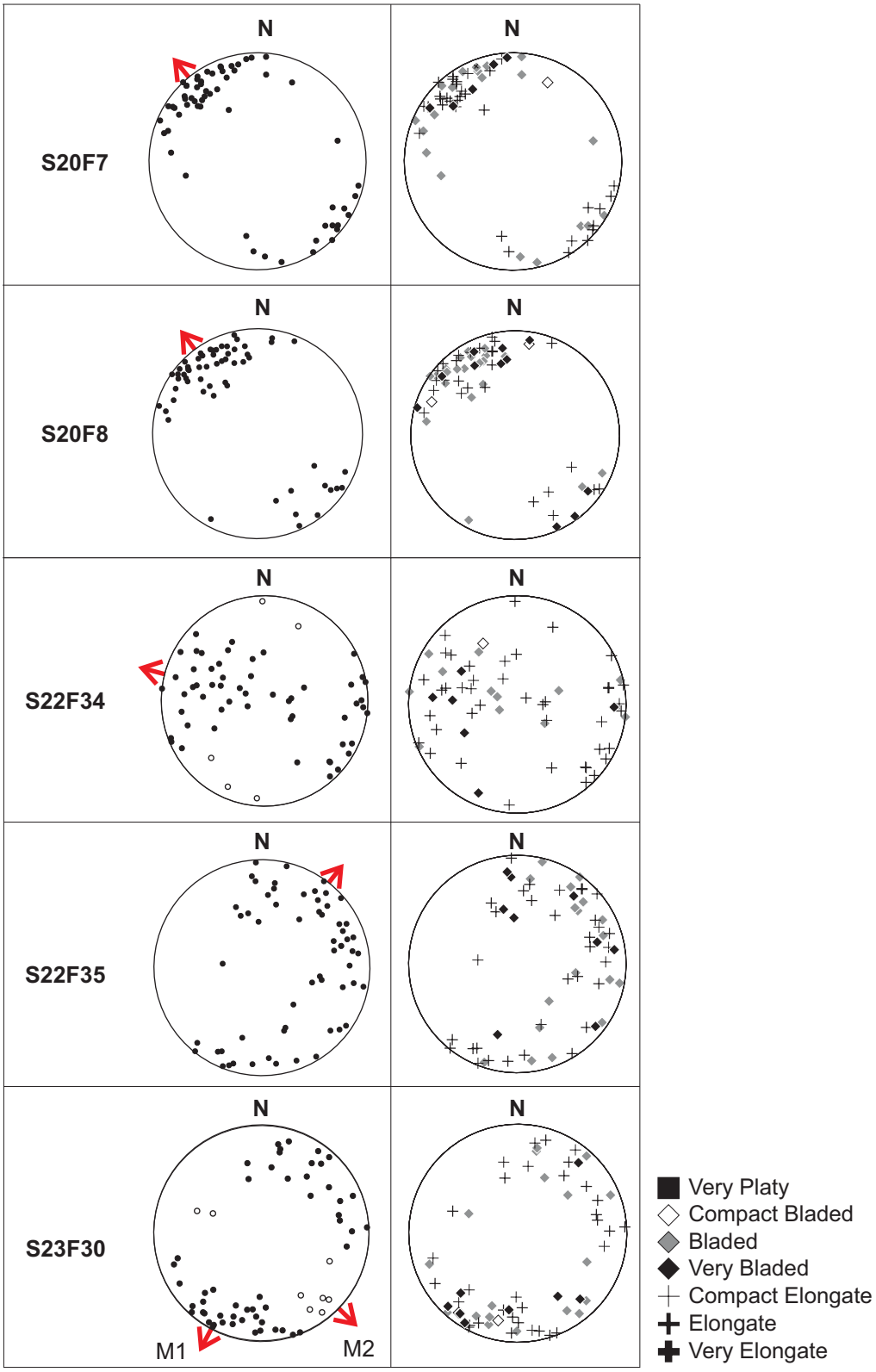

Figure B-1. Clast fabric and clast shape (continued).

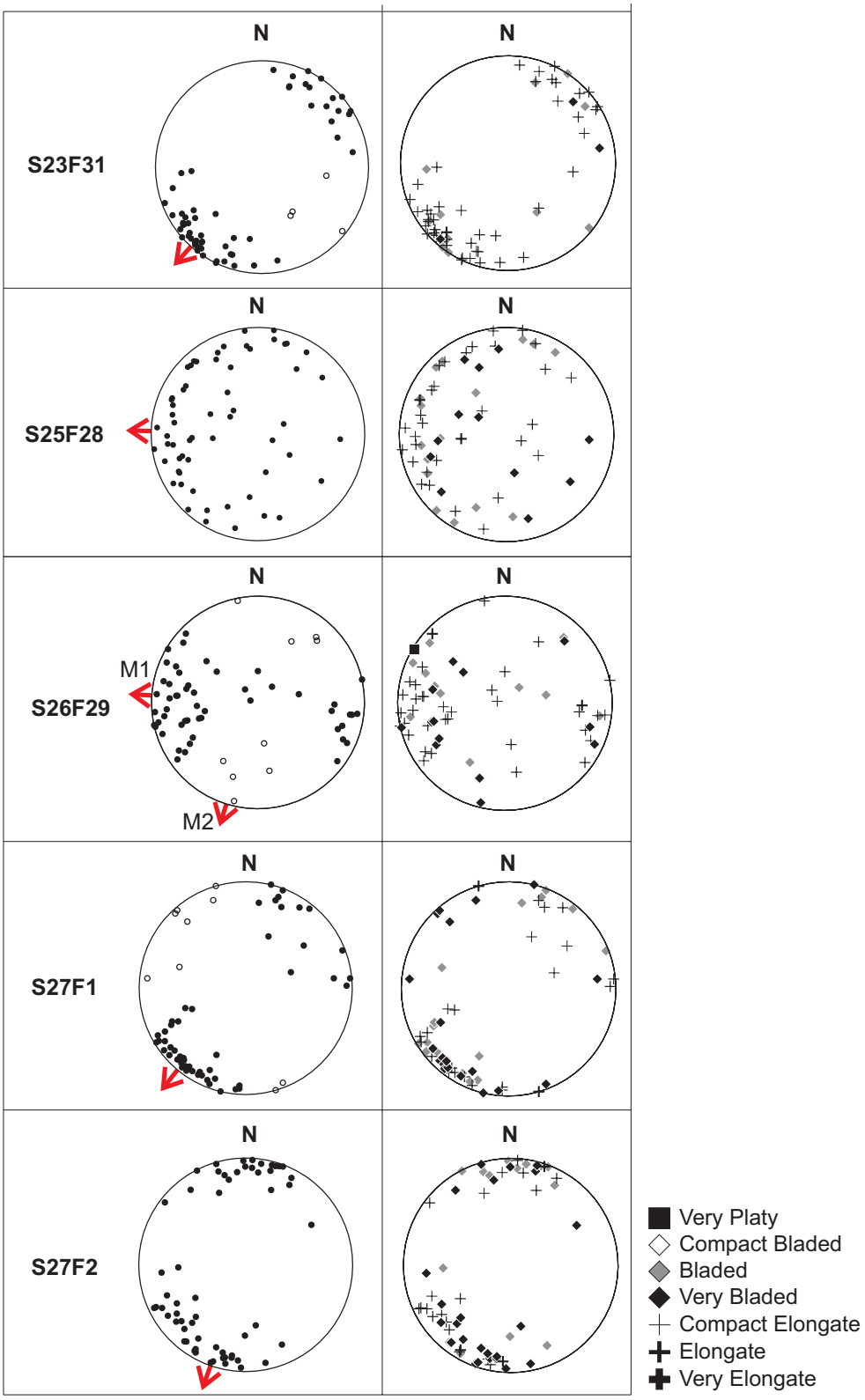

Figure B-1. Clast fabric and clast shape (continued).

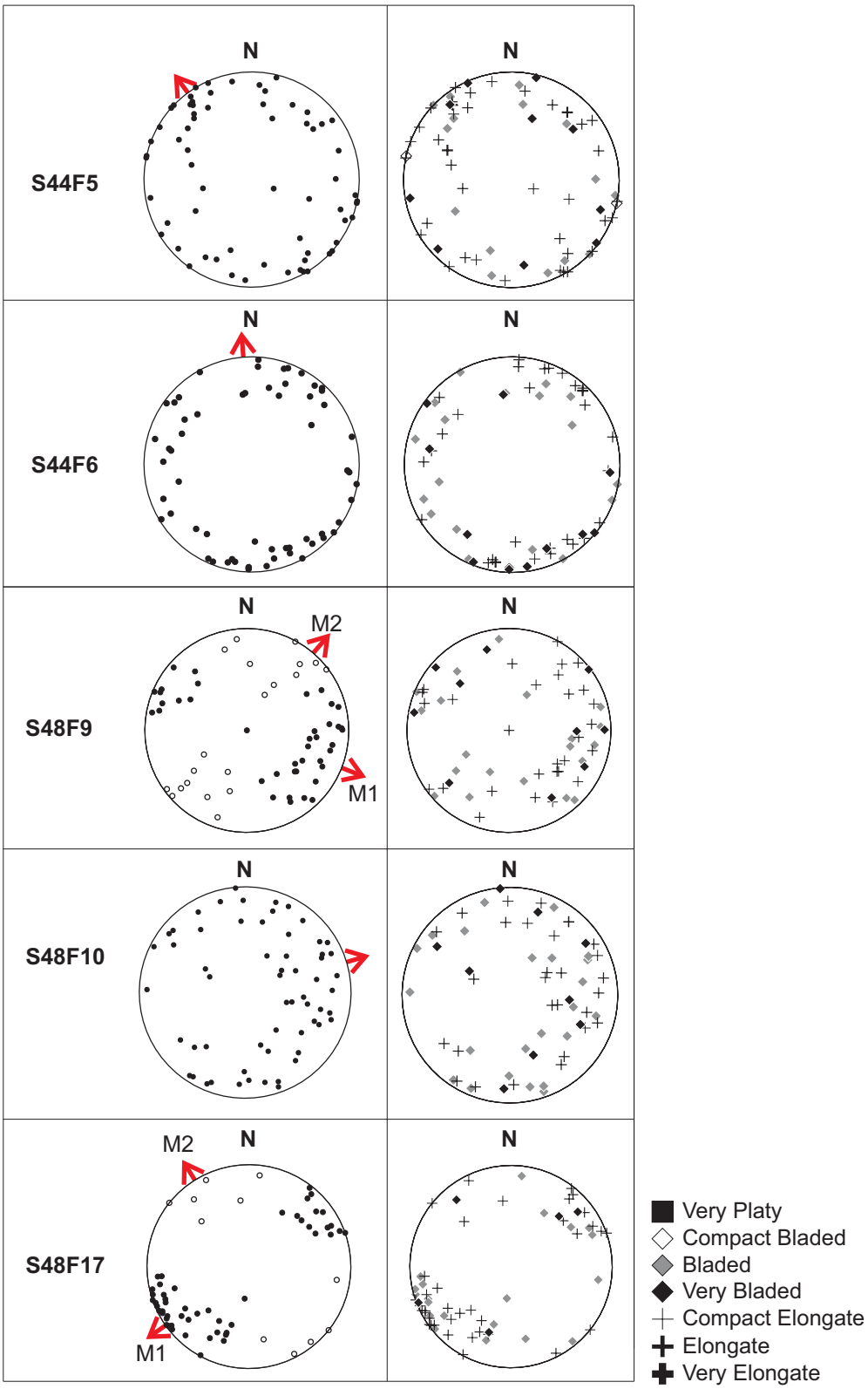

Figure B-1. Clast fabric and clast shape (continued).

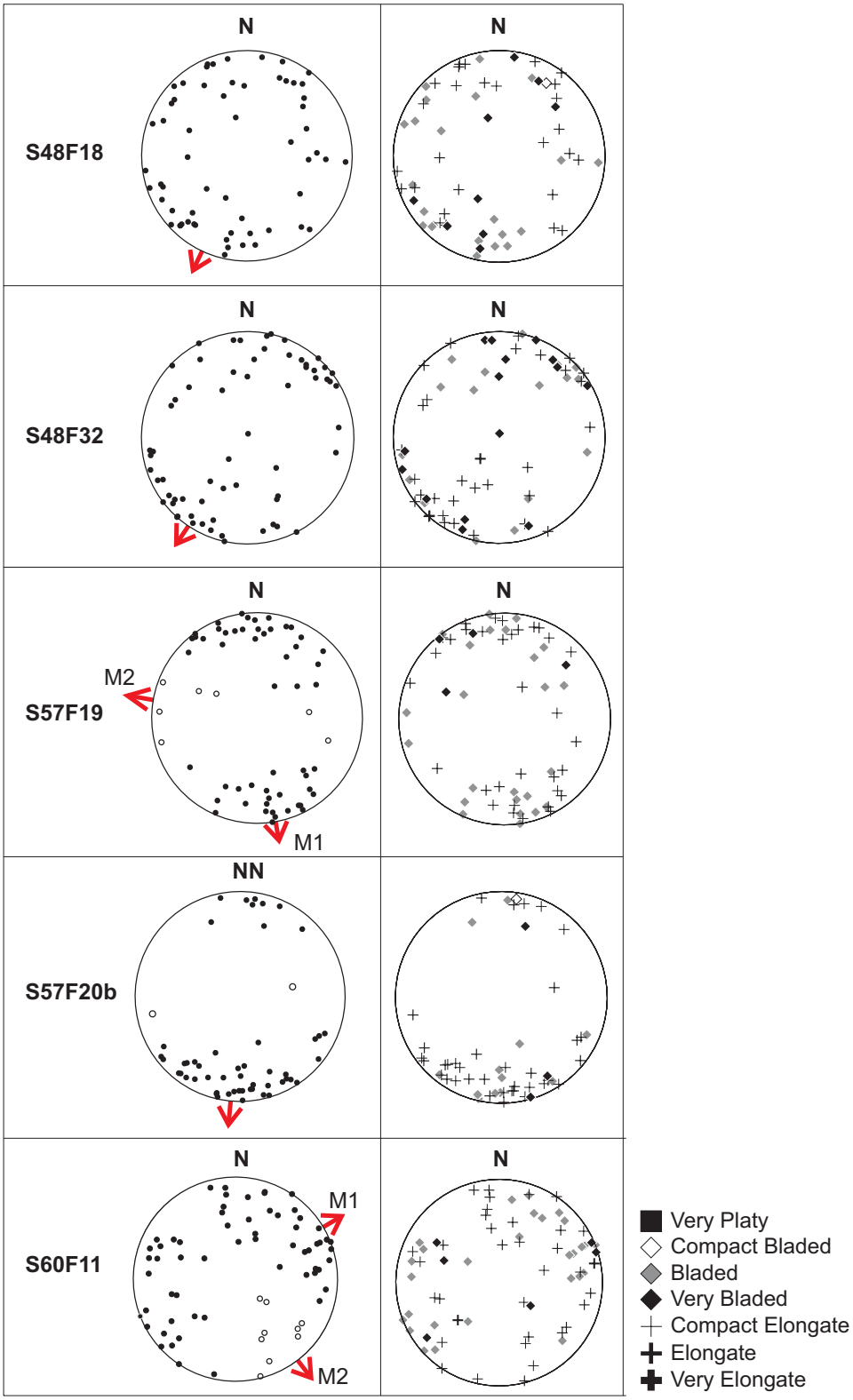

Figure B-1. Clast fabric and clast shape (continued).

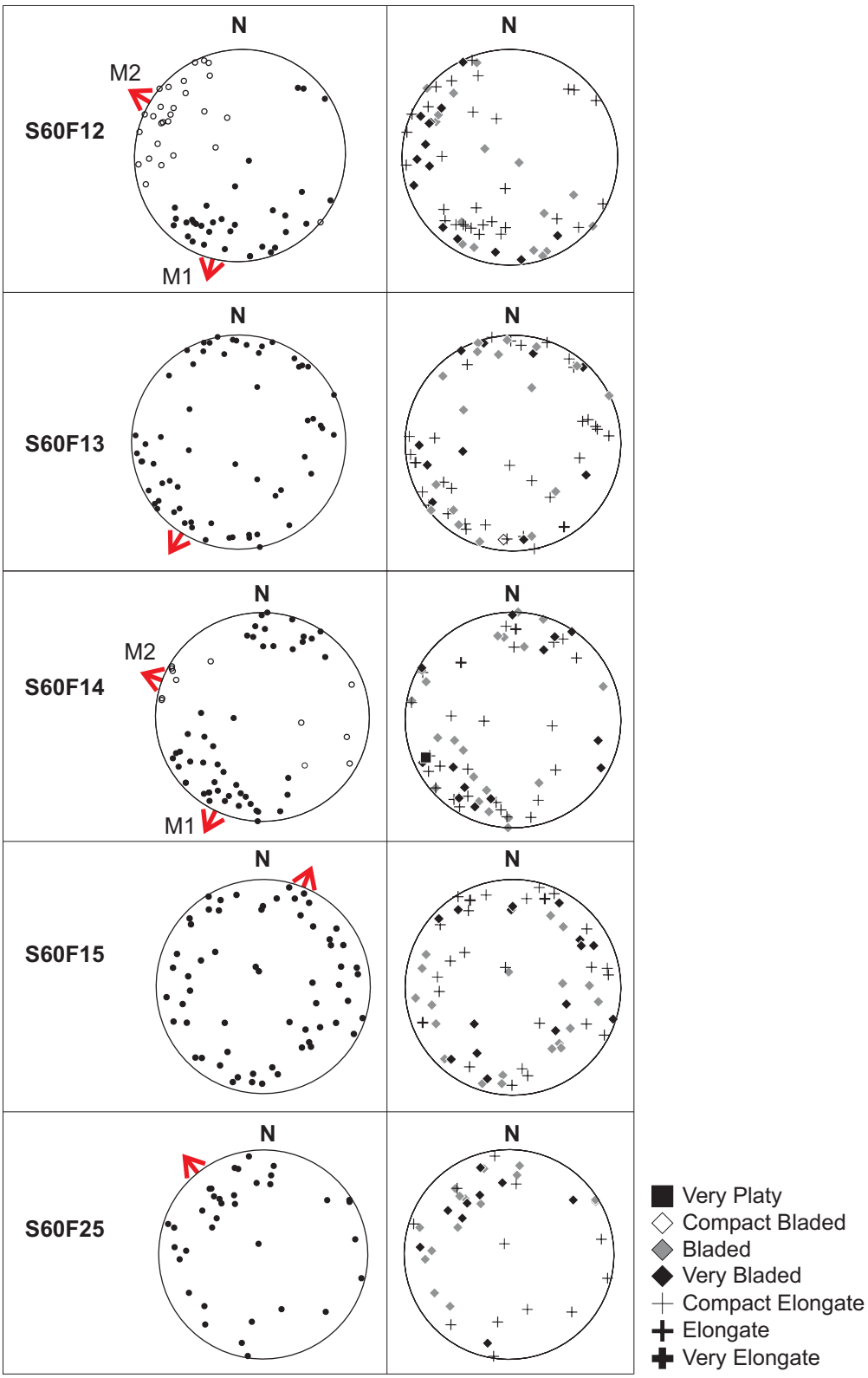

Figure B-1. Clast fabric and clast shape (continued).

Appendix C

Rectified photographs of diamictons for clast concentration measurements

A 45 cm x 35 cm grid was held against the face and photographed using a 4 megapixel digital camera. Photographs were rectified using GIS software to rid of parallax effects and are included on DVD 1 as TIFF files. These files can be opened by most image viewing or graphics applications. All clasts visible in the photographs (generally greater than or equal to 0.5 cm) were then digitally traced. The area of each clast was calculated using the image processing software package, "ImageJ" (Rasband 1997-2007) (Fig. 3.3-2). The sum of all clast areas was then divided by the total area of the face covered by the grid in order to calculate clast concentration in percent.

DVD 1:

- RectifyS6F26.tif 11,484 KB
- RectifyS6F27.tif 11,486 KB
- RectifyS6F33.tif 11,481 KB
- RectifyS20F7.tif 11,483 KB
- RectifyS20F8.tif 11,490 KB
- RectifyS22F34.tif 11,478 KB
- RectifyS22F35.tif 11,477 KB
- RectifyS23F30.tif 11,490 KB
- RectifyS23F31.tif 11,490 KB
- RectifyS25F28.tif 11,485 KB
- RectifyS26F29.tif 11,483 KB
- RectifyS27F1.tif 11,485 KB
- RectifyS27F2.tif 11,491 KB
- RectifyS44F5.tif 11,481 KB
- RectifyS44F6.tif 11,472 KB
- RectifyS48F9.tif 11,489 KB
- RectifyS48F10.tif 11,483 KB
- RectifyS48F17.tif 11,483 KB
- RectifyS48F18.tif 11,489 KB
- RectifyS48F32.tif 11,481 KB

- RectifyS57F19.tif 11,481 KB
- RectifyS57F20.tif 11,486 KB
- RectifyS60F11.tif 11,483 KB
- RectifyS60F12.tif 11,482 KB
- RectifyS60F13.tif 11,486 KB
- RectifyS60F14.tif 11,488 KB
- RectifyS60F15.tif 11,480 KB
- RectifyS60F25.tif 11,483 KB

Appendix D

Thin section preparation protocol

Thin sections were prepared at the Micromorphology Laboratory at Brock University. Diamicton samples were shaved down to more manageable sizes (~10 x 10 x 10 cm) and left to dry in the laboratory. The samples were then impregnated with acetone based polyester resin, cured, cut, mounted on glass and hand ground down to a thickness of 25-30 μm. Thin section preparation procedures for unconsolidated sediments are discussed in more detail by van der Meer et al. (2006), but a general outline of the protocol, after Lee and Kemp (1992) is presented in Figure D-1.

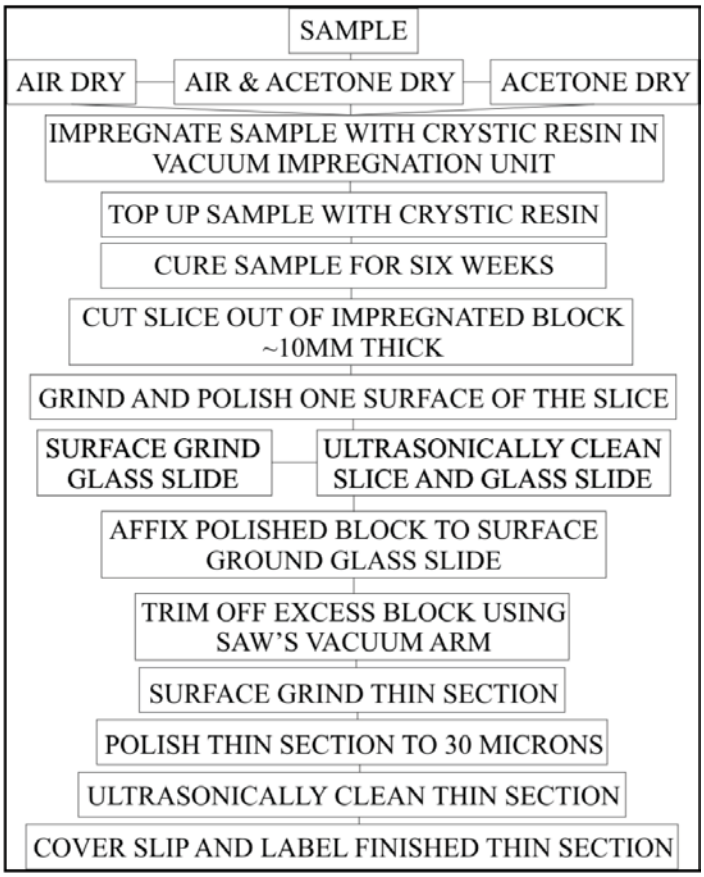

Figure D-1. General thin section preparation procedure based on protocol after Lee and Kemp (1992).

Appendix E

Grain size data

Grain size analysis was conducted on the diamicton matrix for the grain size range from clay to very coarse sand (Wentworth 1922). These samples were processed at the University of Calgary using laser diffraction (Mullins and Hutchison 1982; Anonymous 1998).

Table E-1. Grain size data for each diamicton matrix sample. Sites are arranged in numerical order.

Site/Fabric	clay (≤ 2 µm) (%)	med-fine silt (2-20 µm) (%)	coarse silt (20-50 µm) (%)	very fine sand (50-125 µm) (%)	fine sand (125-250 µm) (%)	medium sand (250-500 µm) (%)	coarse sand (500 µm – 1 mm) (%)	very coarse sand (1-2 mm) (%)
S6/F26	10.74	26.66	12.21	12.87	8.61	11.24	12.94	4.73
S6/F27	9.96	24.54	13.12	13.56	9.63	11.73	11.37	6.09
S6/F33	7.99	32.11	15.45	14.16	9.12	8.81	8.32	4.04
S20/F7	0.72	31.49	11.72	11.55	7.60	12.15	17.03	7.79
S20/F8	0.74	33.48	12.77	11.68	6.03	8.42	18.32	8.56
S22/F34	12.84	36.41	15.22	9.91	5.86	6.00	8.45	5.49
S23/F30	0.56	34.64	17.04	13.54	9.03	11.36	10.26	3.57
S23/F31	3.90	34.49	15.66	15.52	9.55	8.01	7.52	5.35
S25/F28	20.73	27.61	7.12	6.07	5.16	3.51	12.63	17.17
S26/F29	24.78	34.16	8.81	7.70	4.32	6.05	9.89	4.29
S27/F1	21.69	24.76	5.70	6.65	7.28	14.62	14.80	4.50
S27/F3	29.02	26.72	6.36	7.44	6.85	7.71	9.43	6.47
S44/F5	18.07	40.85	12.24	11.38	7.95	7.81	1.70	0.00
S44/F6	21.32	40.66	10.74	9.58	5.68	5.83	4.66	1.53
S48/F9	22.67	29.37	9.75	10.40	7.24	7.08	6.88	6.61
S48/F10	21.41	27.57	9.50	10.53	8.45	8.45	8.84	5.25
S48/F17	14.71	22.10	7.42	8.57	8.40	6.01	15.01	17.78
S48/F18	19.51	26.26	8.84	9.71	6.19	12.23	15.76	1.50
S48/F32	16.95	28.88	10.71	12.81	9.33	10.13	9.22	1.97
S57/F19	0.21	15.17	12.34	15.80	12.98	17.07	18.71	7.72
S57/F20	0.17	14.89	12.93	15.47	13.84	20.68	17.13	4.89
S60/F11	15.56	26.95	10.86	10.69	8.60	8.43	10.44	8.47
S60/F13	10.65	23.17	9.28	10.03	9.11	15.87	16.18	5.71
S60/F14	19.04	26.67	9.64	11.09	12.97	13.34	6.00	1.25
S60/F15	14.83	29.06	11.56	11.57	9.58	12.83	8.03	2.54

Appendix F

Criteria for identification of discrete microstructures

Turbates

The majority of elongate grains of a similar size must be subparallel to the edges of the core stone on a minimum of 3 out of 4 sides for the structure to be considered a turbate (Fig. F-1). Turbate structures without core stones were rarely observed, but those that were counted consisted of encircling grains, with inter-particle distances smaller than the dimensions of the particles along the path of the circle.

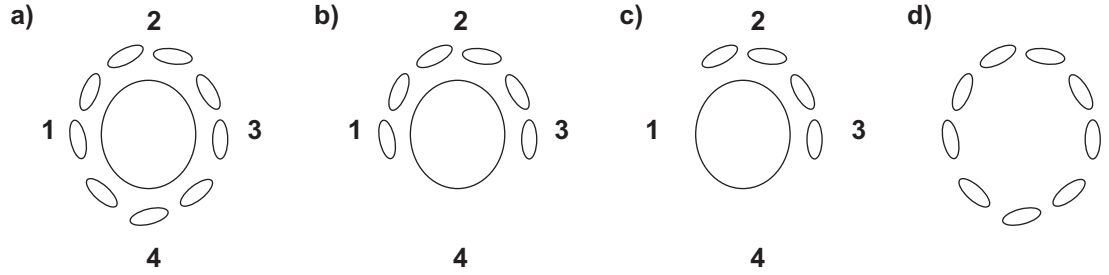

Figure F-1. Criteria for identifying turbates. 'a'-'c' have smaller grains surrounding a core stone with four sides labelled 1, 2, 3 and 4. 'a' and 'b' are counted as turbates, but 'c' is not because only 2 sides of the core stone (2 & 3) have grains oriented with their long axes subparallel to the core stone edge. 'd' is a turbate with no core stone.

Necking Structures

Includes preferred alignment of small grains between two adjacent large grains (sizes are relative) (Fig. F-2). Counted necking structures did not include aligned particles that were part of turbates.

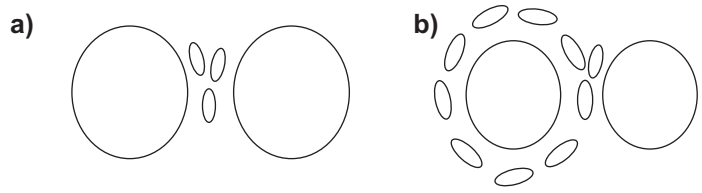

Figure F-2. Criteria for identifying necking structures. 'a' is considered to be a necking structure, 'b' considered to be part of a turbate.

Grain Lineations

Identified by minimum of three elongate grains aligned end to end. The distance between grains must be less than their lengths along the path of the lineation (Fig. F-3).

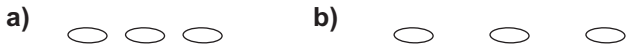

Figure F-3. Criteria for identifying grain lineations. 'a' is considered to be a grain lineation, 'b' is not.

Grain Stacks

Must include a series of a minimum of four grains forming a subvertical stack. Only the flat edges (as opposed to corners) of the grains face each other. The distances between these grains must be smaller than their 'along-path' dimensions (Fig. F-4).

Figure F-4. Criteria for identifying grain stacks. 'a' is considered to be a grain stack, 'b' is not.

Crushed grains

Evidence of crushing or breakage must include separate pieces of the same grain suspended in the matrix. Pieces of a broken grain on either side of a fracture in the matrix was not included to avoid counting grains that may have been fractured during thin section grinding (Fig. F-5). Under 40x magnification, edges of the separate pieces must match up, or where visible, birefringence or foliation patterns must be consistent between all pieces. Because the susceptibility of grains to fracture is influenced by their internal defects and hardness, the following letter scheme was used to record crushed/broken grain lithology: cr = crystalline, ms = metasedimentary, v = volcanic, ls = limestone, and u = unknown.

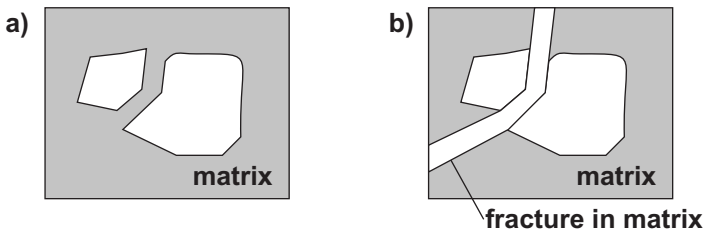

Figure F-5. Criteria for identifying crushed/broken grains. 'a' is considered to be a crushed/broken grain, 'b' is not.

Appendix G

Annotated 2400 dpi vertical thin section scans

All vertical thin section 2300 dpi scans are included on DVDs 2 and 3 as TIFF files. These files can be opened by most image viewing or graphics applications. There are two TIFF files for each thin section, one with annotation (including the 6 cell counting grid) and one without.

DVD 2:

- S6F26v.tif 121,455 KB
- S6F26v-annotated.tif 121,455 KB
- S6F27v.tif 121,653 KB
- S6F27v-annotated.tif 121,653 KB
- S6F33v.tif 121,561 KB
- S6F33v-annotated.tif 121,561 KB
- S20F7v.tif 120,786 KB
- S20F7v-annotated.tif 120,787 KB
- S22F34v.tif 121,242 KB
- S22F34v-annotated.tif 121,242 KB
- S23F30v.tif 120,846 KB
- S23F30v-annotated.tif 120,846 KB
- S23F31v.tif 122,958 KB
- S23F31v-annotated.tif 122,958 KB
- S25F28v.tif 121,616 KB
- S25F28v-annotated.tif 121,616 KB
- S26F29v.tif 123,312 KB
- S26F29v-annotated.tif 123,312 KB
- S27F1n.tif 123,410 KB
- S27F1n-annotated.tif 123,410 KB
- S27F2v.tif 119,808 KB
- S27F2v-annotated.tif 119,808 KB
- S44F5v.tif 120,142 KB
- S44F5v-annotated.tif 120,142 KB

- S48F9v.tif 119,537 KB
- S48F9v-annotated.tif 119,537 KB
- S48F10v.tif 121,554 KB
- S48F10v-annotated.tif 121,554 KB
- S48F17v.tif 120,400 KB
- S48F17v-annotated.tif 120,400 KB
- S48F18v.tif 120,006 KB
- S48F18v-annotated.tif 120,006 KB
- S48F32v.tif 122,126 KB
- S48F32v-annotated.tif 122,126 KB

DVD 3:

- S57F19v.tif 120,967 KB
- S57F19v-annotated.tif 120,967 KB
- S57F20v.tif 122,087 KB
- S57F20v-annotated.tif 122,087 KB
- S60F11v.tif 122,087 KB
- S60F11v-annotated.tif 122,087 KB
- S60F13v.tif 119,537 KB
- S60F13v-annotated.tif 119,537 KB
- S60F14v.tif 121,456 KB
- S60F14v-annotated.tif 121,456 KB
- S60F15v.tif 120,179 KB
- S60F15v-annotated.tif 120,179 KB

Appendix H

2400 dpi horizontal thin section scans

All horizontal thin section 2300dpi scans are included on DVD 1 as TIFF files. These files can be opened by most image viewing or graphics applications. Thin red lines mark grains measured for microfabric analysis. A blue grid, superimposed on each image, was used to select grains for microfabric measurements that are uniformly distributed over the thin section area

DVD 1:

- S6F26h-grid&lines.tif 116,119 KB
- S6F27h-grid&lines.tif 123,371 KB
- S6F33h-grid&lines.tif 121,592 KB
- S20F7h-grid&lines.tif 121,257 KB
- S22F34h-grid&lines.tif 120,376 KB
- S23F30h-grid&lines.tif 120,414 KB
- S23F31h-grild&lines.tif 119,514 KB
- S25F28h-grid&lines.tif 117,942 KB
- S26F29h-grid&lines.tif 117,942 KB
- S27F2h-grid&lines.tif 117,926 KB
- S44F5h-grid&lines.tif 108,897 KB
- S48F9h-grid&lines.tif 118,168 KB
- S48F10h-grid&lines.tif 104,312 KB
- S48F17h-grid&lines.tif 105,943 KB
- S48F32h-grid&lines.tif 106,149 KB
- S57F19h-grid&lines.tif 120,872 KB
- S60F11h-grid&lines.tif 120,439 KB
- S60F13h-grid&lines.tif 120,068 KB
- S60F14h-grid&lines.tif 107,294 KB
- S60F15h-grid&lines.tif 119,615 KB

Appendix I

Hierarchical clustered microstructure association data

Microstructural data are clustered using the hierarchical clustering technique and the Ward's, single, complete and McQuitty linkage methods. The resulting dendrograms are presented in Figures I-1 through I-4. The geography of the microstructure clusters are presented in Figures I-6 through I-10.

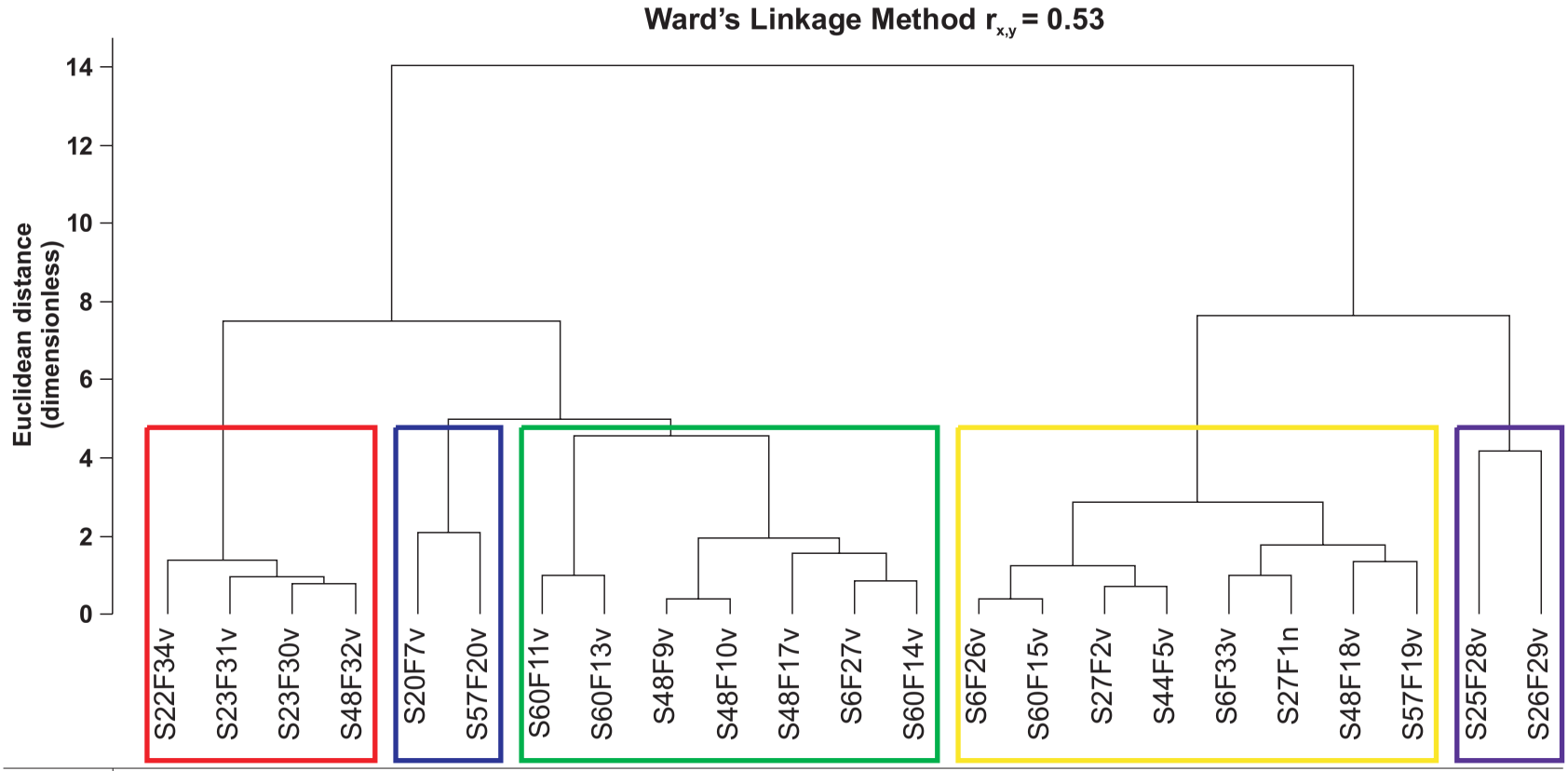

Genesis	G	L/DL	L/DL	DL	L/DL	DL	D	D	DL	DL	DL	DL	D	DL	D	L/DL	G	DL	L/DL	DL	DL	DL	DL
N	55	16	21	57	34	42	73	79	34	37	46	57	31	42	49	49	102	15	66	54	25	3	8

Figure I-1. A dendrogram showing the results of hierarchical cluster analysis of micromorphological data from all vertical thin sections using Ward's linkage method. $r_{x,y}$ = the cophenetic correlation coefficient. Coloured boxes delineate groups that have been superimposed on a map of the study area in Figure F-5. Red = group 1, blue = group 2, green = group 3, yellow = group 4, purple = group 5, and pink = group 6. The inferred diamicton genesis (this study) associated with each thin section is included below the dendrogram. L/DL = lodgement or deformed lodgement, DL=deformed lodgement, D=deformation, and G=gravity flow. N is the absolute number of discrete microstructures counted in the thin section.

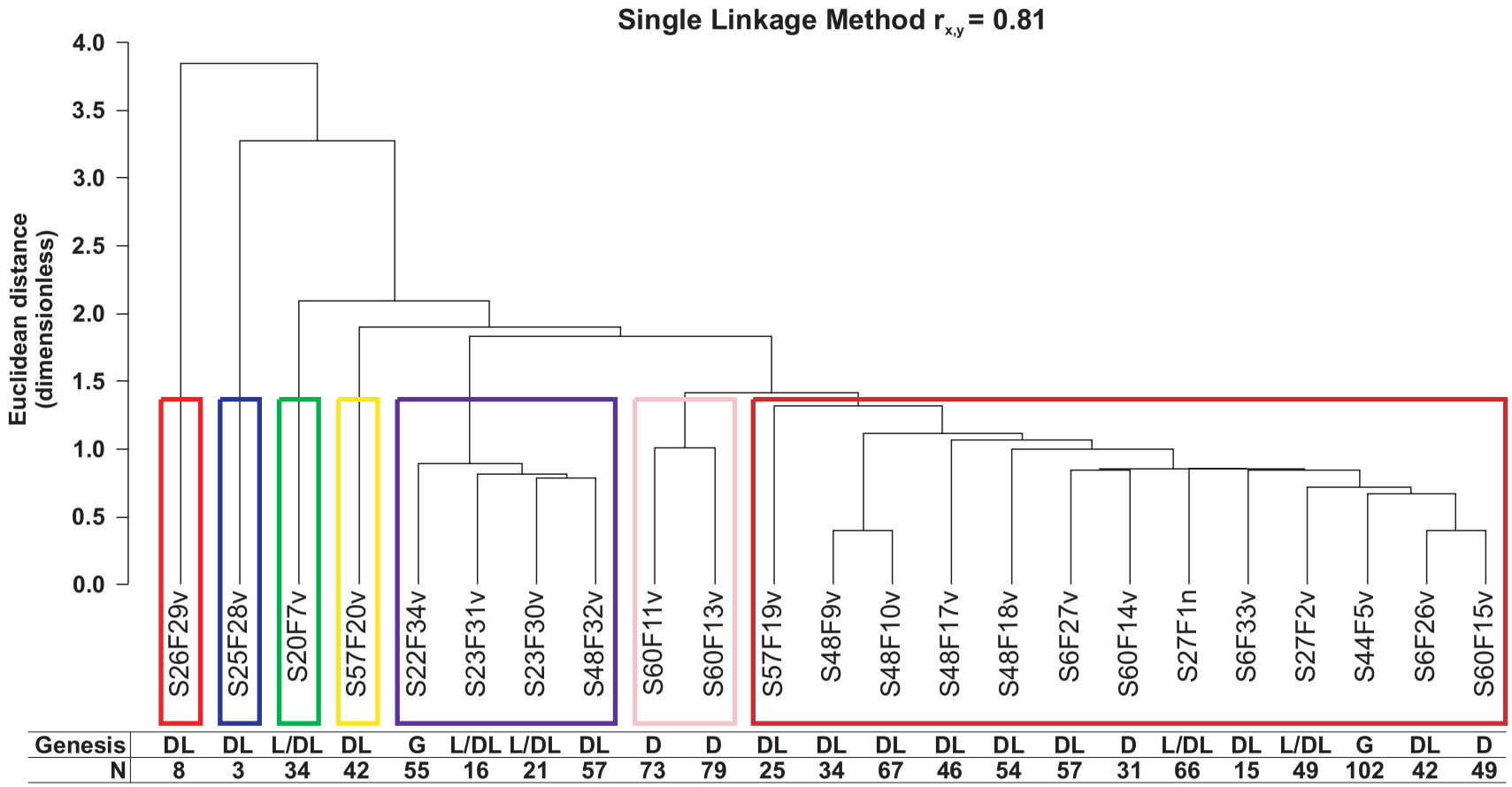

Genesis	DL	DL	L/DL	DL	G	L/DL	L/DL	DL	D	D	DL	DL	DL	DL	DL	DL	D	L/DL	DL	L/DL	G	DL	D
N	8	3	34	42	55	16	21	57	73	79	25	34	67	46	54	57	31	66	15	49	102	42	49

Figure I-2. A dendrogram showing the results of hierarchical cluster analysis of micromorphological data from all vertical thin sections using the single linkage method. $r_{x,y}$ = the cophenetic correlation coefficient. Coloured boxes delineate groups that have been superimposed on a map of the study area in Figure F-6. Red = group 1, blue = group 2, green = group 3, yellow = group 4, purple = group 5, and pink = group 6. The inferred diamicton genesis (this study) associated with each thin section is included below the dendrogram. L/DL = lodgement or deformed lodgement, DL = deformed lodgement, D = deformation, and G = gravity flow. N is the absolute number of discrete microstructures counted in the thin section.

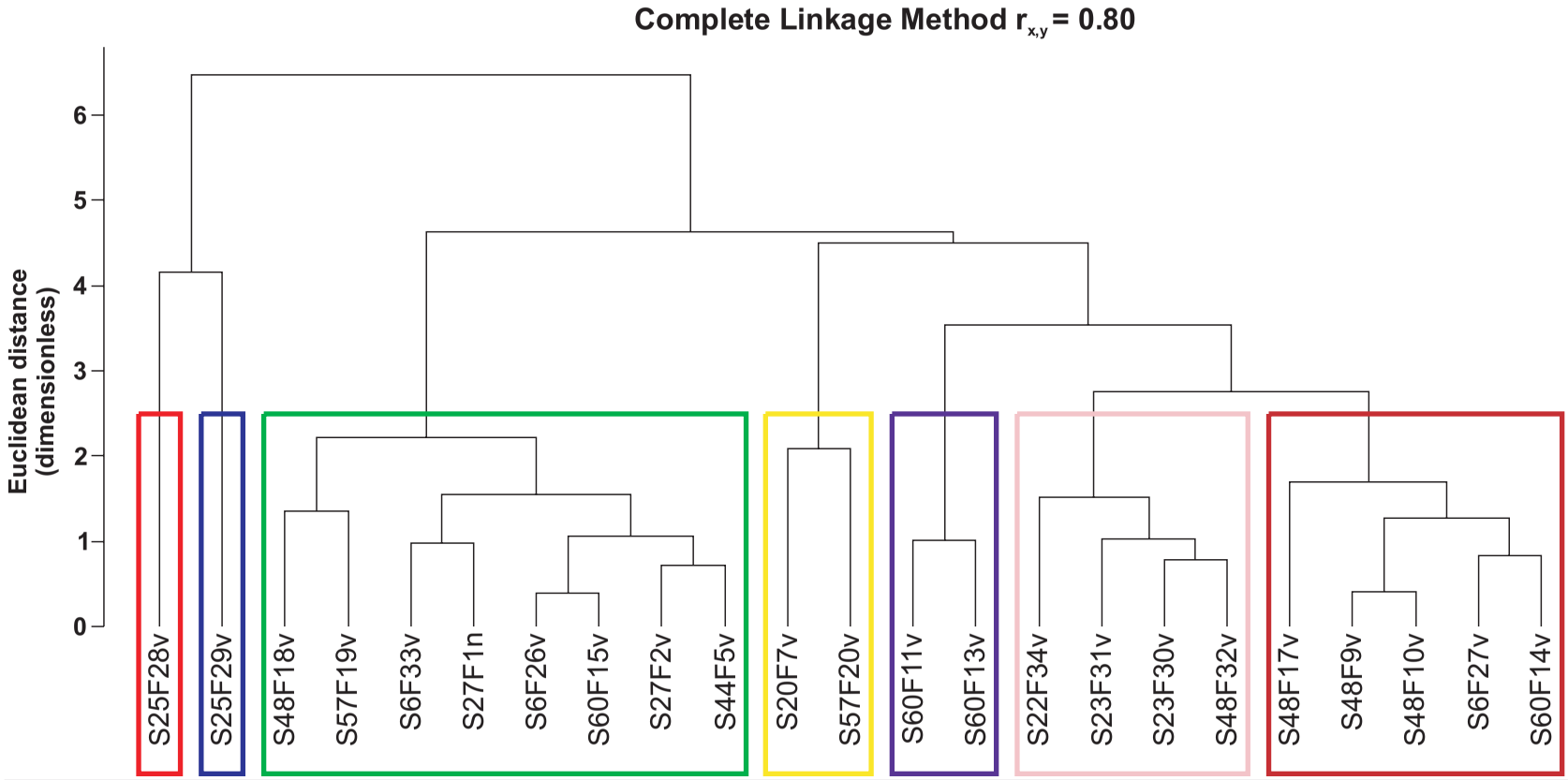

Genesis	DL	DL	DL	DL	DL	L/DL	DL	D	L/DL	G	L/DL	DL	D	D	G	L/DL	L/DL	DL	DL	DL	DL	DL	D
N	3	8	54	25	15	66	42	49	49	102	34	42	73	79	55	16	21	57	46	34	67	57	31

Figure I-3. A dendrogram showing the results of hierarchical cluster analysis of micromorphological data from all vertical thin sections using the complete linkage method. $r_{x,y}$ = the cophenetic correlation coefficient. Coloured boxes delineate groups that have been superimposed on a map of the study area in Figure F-7. Red = group 1, blue = group 2, green = group 3, yellow = group 4, purple = group 5, and pink = group 6. The inferred diamicton genesis (this study) associated with each thin section is included below the dendrogram. L/DL = lodgement or deformed lodgement, DL = deformed lodgement, D = deformation, and G = gravity flow. N is the absolute number of discrete microstructures counted in the thin section.

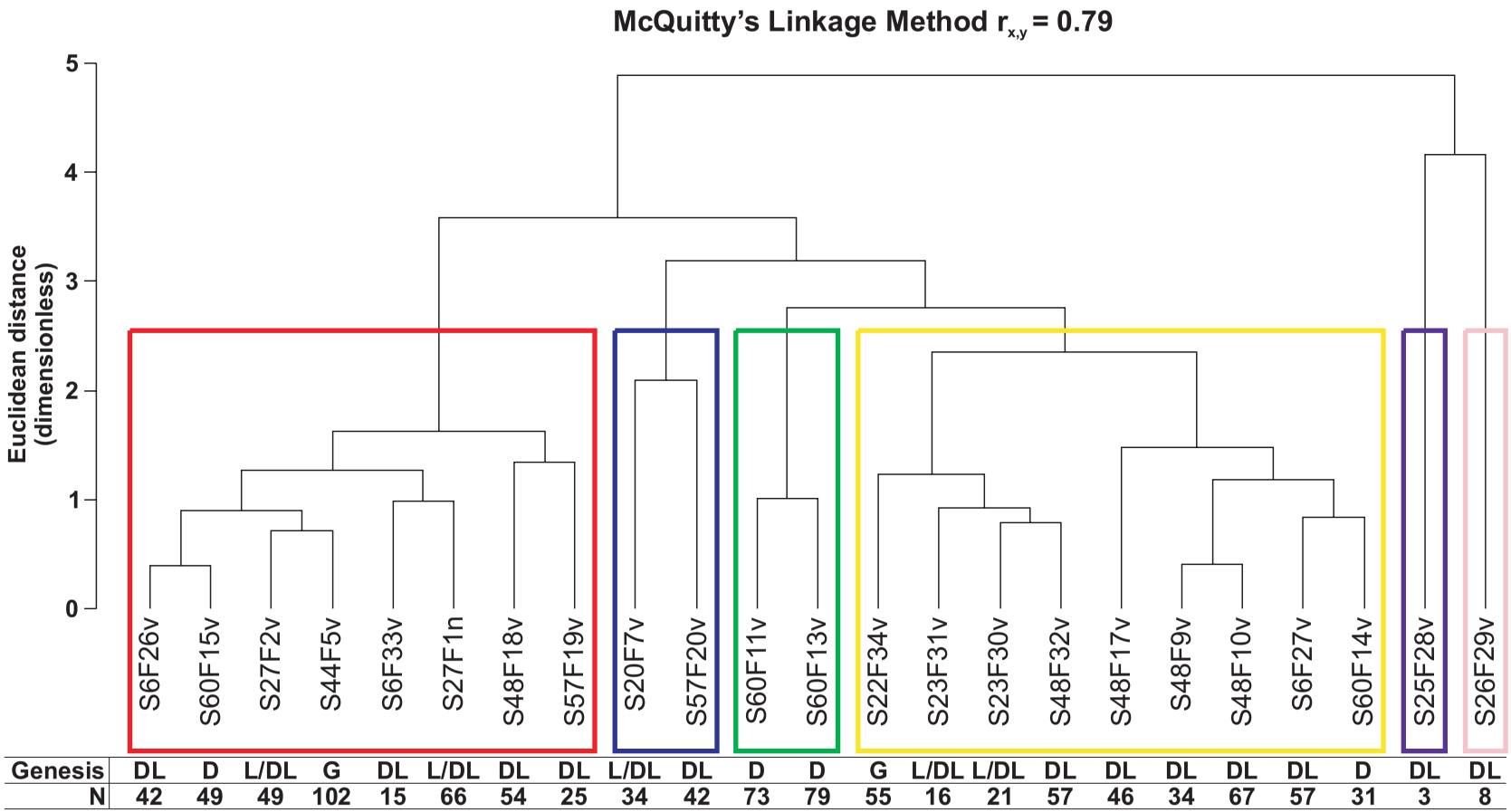

Genesis	DL	D	L/DL	G	DL	L/DL	DL	DL	L/DL	DL	D	D	G	L/DL	L/DL	DL	DL	DL	DL	DL	D	DL	DL
N	42	49	49	102	15	66	54	25	34	42	73	79	55	16	21	57	46	34	67	57	31	3	8

Figure I-4. A dendrogram showing the results of hierarchical cluster analysis of micromorphological data from all vertical thin sections using McQuitty's linkage method. $r_{x,y}$ = the cophenetic correlation coefficient. Coloured boxes delineate groups that have been superimposed on a map of the study area in Figure F-8. Red = group 1, blue = group 2, green = group 3, yellow = group 4, purple = group 5, and pink = group 6. The inferred diamicton genesis (this study) associated with each thin section is included below the dendrogram. L/DL = lodgement or deformed lodgement, DL = deformed lodgement, D = deformation, and G = gravity flow. N is the absolute number of discrete microstructures counted in the thin section.

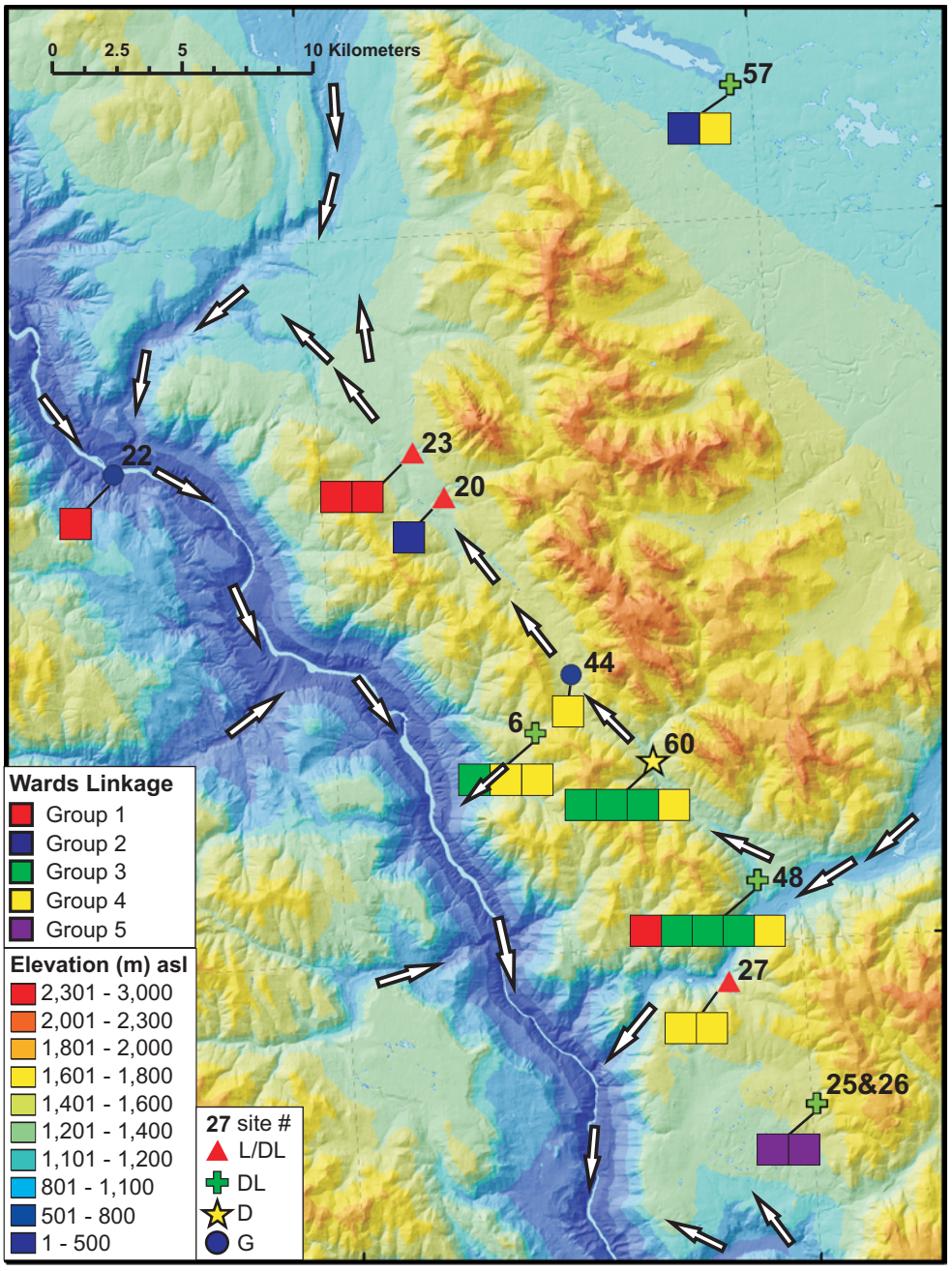

Figure I-5. Geographic distribution of microstructure association clusters (groups) derived using Ward's linkage clustering method (see Figure I-1 for dendrogram). Site locations are marked with symbols indicating the inferred diamicton genesis according to Neudorf (this study), where L/DL = lodgement or deformed lodgement (triangles), DL = deformed lodgement (crosses), D = deformation (star), and G = gravity flow (circles). Last glacial maximum ice flow directions (white arrows) are from Lian and Hicock (2000). The map is superimposed on a hillshaded and classed TRIM I digital elevation model (Projection: Albers Conical Equal Area, Datum: NAD 83. Source: Government of British Columbia 2007. © Province of British Columbia).

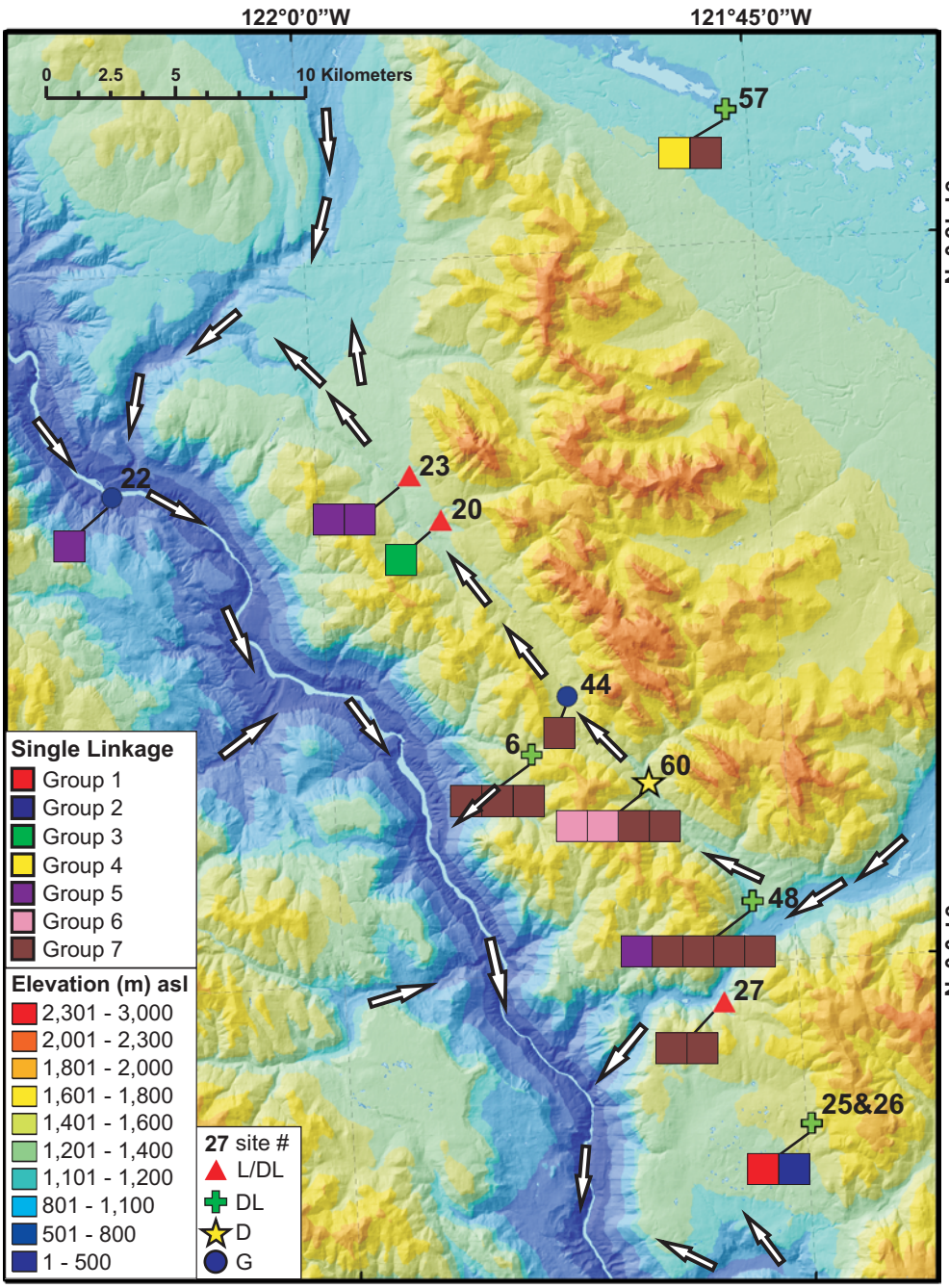

Figure I-6. Geographic distribution of microstructure association clusters (groups) derived using the single linkage clustering method (see Figure I-2 for dendrogram). Site locations are marked with symbols indicating the inferred diamicton genesis according to Neudorf (this study), where L/DL = lodgement or deformed lodgement (triangles), DL = deformed lodgement (crosses), D = deformation (star), and G = gravity flow (circles). Last glacial maximum ice flow directions (white arrows) are from Lian and Hicock (2000). The map is superimposed on a hillshaded and classed TRIM I digital elevation model (Projection: Albers Conical Equal Area, Datum: NAD 83. Source: Government of British Columbia 2007. © Province of British Columbia).

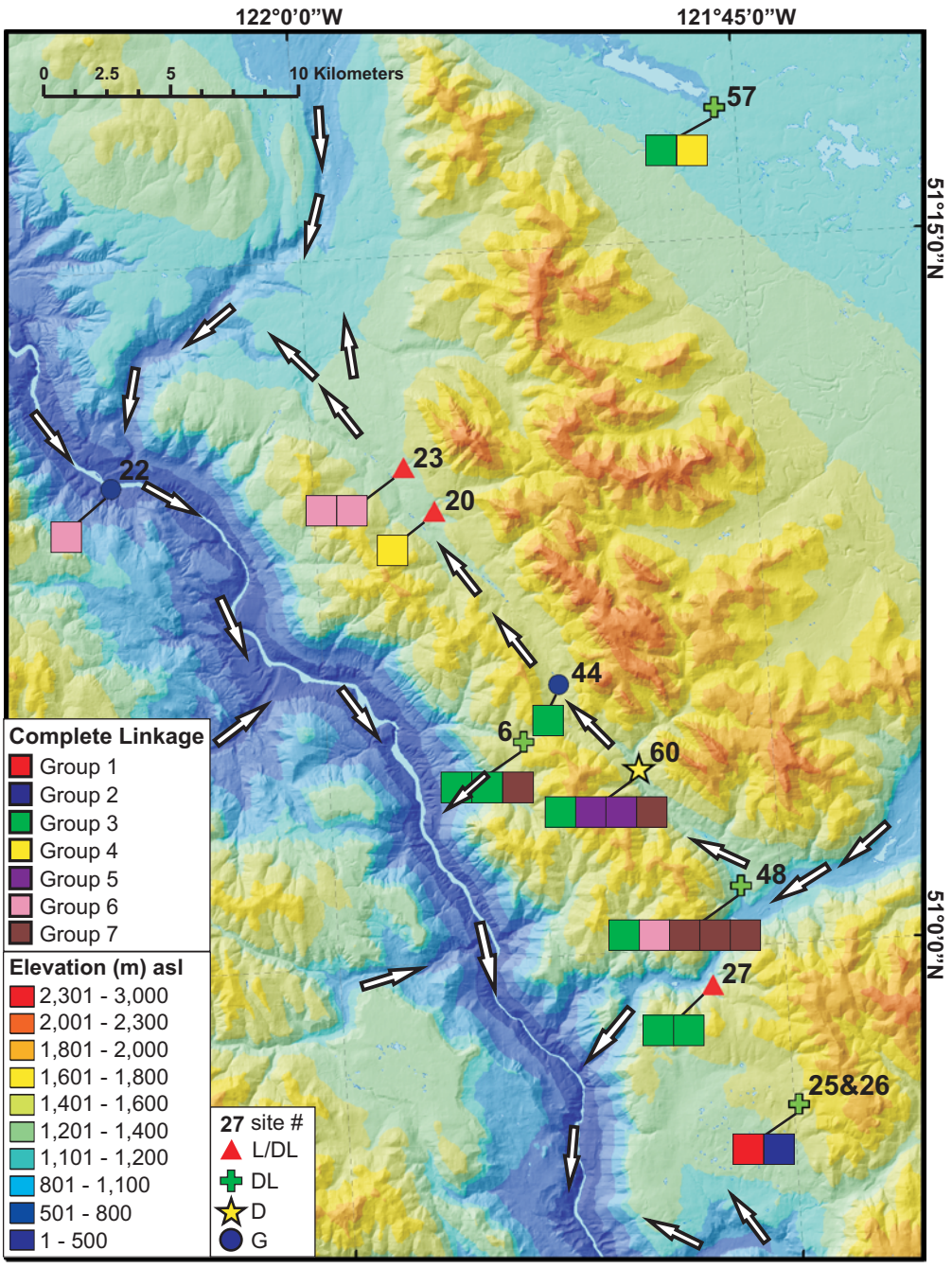

Figure I-7. Geographic distribution of microstructure association clusters (groups) derived using the complete linkage clustering method (see Figure I-3 for dendrogram). Site locations are marked with symbols indicating the inferred diamicton genesis according to Neudorf (this study), where L/DL = lodgement or deformed lodgement (triangles), DL = deformed lodgement (crosses), D = deformation (star), and G = gravity flow (circles). Last glacial maximum ice flow directions (white arrows) are from Lian and Hicock (2000). The map is superimposed on a hillshaded and classed TRIM I digital elevation model (Projection: Albers Conical Equal Area, Datum: NAD 83. Source: Government of British Columbia 2007. © Province of British Columbia).

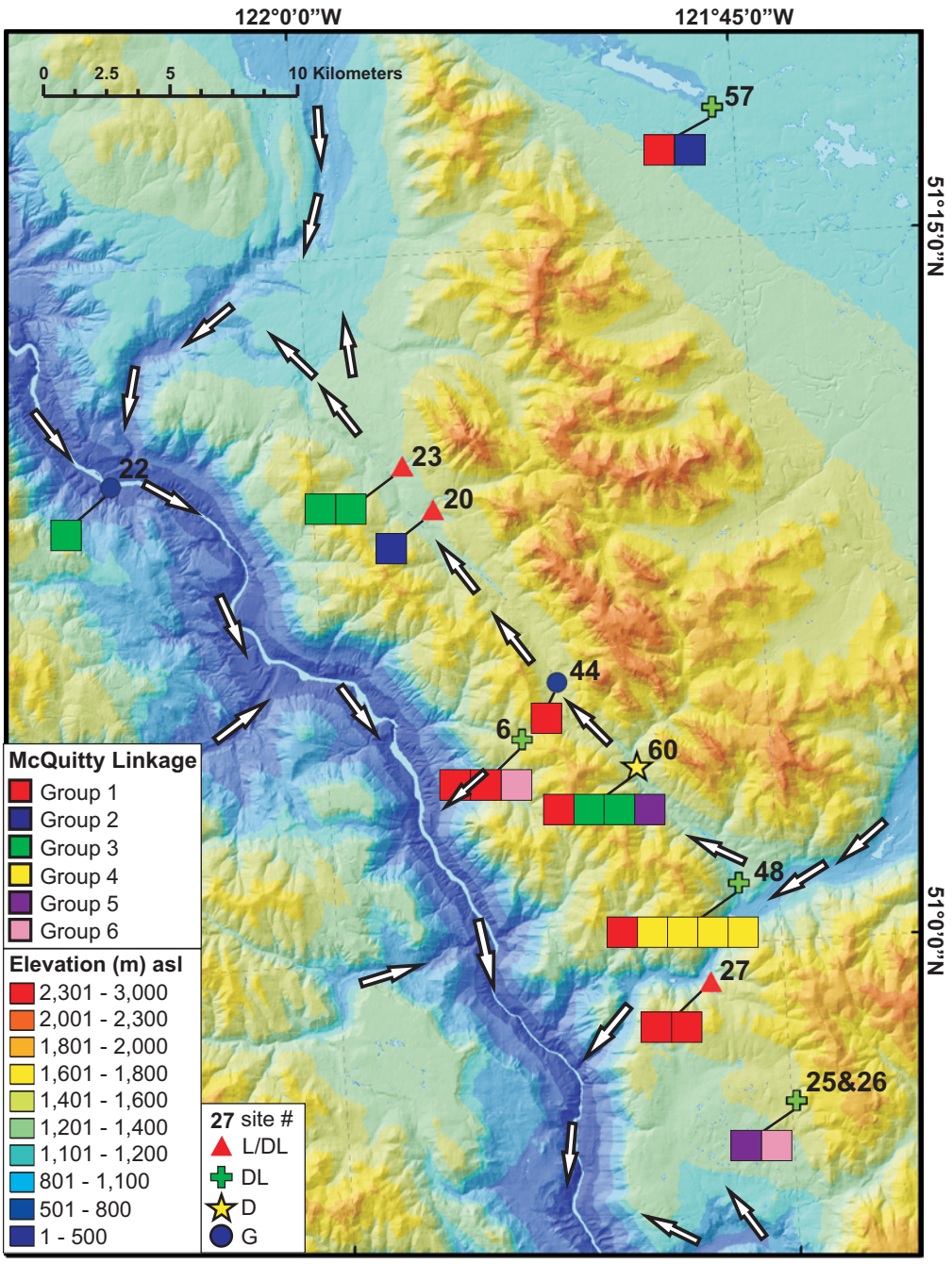

Figure I-8. Geographic distribution of microstructure association clusters (groups) derived using McQuitty's linkage clustering method (see Figure I-4 for dendrogram). Site locations are marked with symbols indicating the inferred diamicton genesis according to Neudorf (this study), where L/DL = lodgement or deformed lodgement (triangles), DL = deformed lodgement (crosses), D = deformation (star), and G = gravity flow (circles). Last glacial maximum ice flow directions (white arrows) are from Lian and Hicock (2000). The map is superimposed on a hillshaded and classed TRIM I digital elevation model (Projection: Albers Conical Equal Area, Datum: NAD 83. Source: Government of British Columbia 2007. © Province of British Columbia).

References

Aitchison, J. 1986. The statistical analysis of compositional data. Chapman and Hall, London, New York.

Anonymous 1998. Malvern Instruments Operators Guide. Malvern Instruments Ltd Worcestershire, United Kingdom.

Benn, D.I. 1994. Fluted moraine formation and till genesis below a temperate valley glacier; Slettmarkbreen, Jotunheimen, southern Norway. Sedimentology, **41**(2): 279-292.

Benn, D.I. 1995. Fabric signature of subglacial till deformation, Breidamerkurjokull, Iceland. Sedimentology, **42**(5): 735-747.

Benn, D.I. 2002. Clast-fabric development in a shearing granular material; implications for subglacial till and fault gouge; discussion and reply. Geological Society of America Bulletin, **114**(3): 382-384.

Benn, D.I., and Evans, D.J.A. 1996. The interpretation and classification of subglacially-deformed materials. Quaternary Science Reviews, **15**(1): 23-52.

Benn, D.I., and Evans, D.J.A. 1998. Glaciers and Glaciation. Arnold London, United Kingdom (GBR).

Benn, D.I., and Gemmell, A.M.D. 2002. Fractal dimensions of diamictic particle-size distributions; simulations and evaluation. Geological Society of America Bulletin, **114**(5): 528-532.

Bennett, M.R., and Glasser, N., F. 1996. Glacial Geology; Ice Sheets and Landforms. John Wiley & Sons, New York, NY.

Bennett, M.R., Waller, R.I., Glasser, N., F., Hambrey, M.J., and Huddart, D. 1999. Glacigenic clast fabrics: genetic fingerprint or wishful thinking? Journal of Quaternary Science, **14**(2): 125-135.

Boulton, G.S. 1996. Theory of glacial erosion, transport and deposition as a consequence of subglacial sediment deformation. Journal of Glaciology, **42**(140): 43-62.

Boulton, G.S., and Jones, A.S. 1979. Stability of temperature ice caps and ice sheets resting on beds of deformable sediment. Journal of Glaciology, **24**(90): 29-43.

Boulton, G.S., and Hindmarsh, R.C.A. 1987. Sediment deformation beneath glaciers; rheology and geological consequences. Journal of Geophysical Research, B, Solid Earth and Planets, **92**: 9059-9082.

Boulton, G.S., Dent, D.L., and Morris, E.M. 1974. Subglacial shearing and crushing and the role of water pressures in tills from south-east Iceland. Geografiska Annaler, Series A: Physical Geography, **56**(3): 135-145.

Boulton, G.S., Dobbie, K.E., and Zatsepin, S. 2001. Sediment deformation beneath glaciers and its coupling to the subglacial hydraulic system. Quaternary International, **86**(1): 3-28.

Boulton, G.S., van der Meer, J.J.M., Hart, J., Beets, D., Ruegg, G.H.J., van der Wateren, F.M., and Jarvis, J. 1996. Till and moraine emplacement in a deforming bed surge; an example from a marine environment. Quaternary Science Reviews, **15**(10): 961-987.

Brewer, R. 1976. Fabric and Mineral Analysis of Soils. Krieger, Huntington NY.

Broster, B.E., and Hicock, S.R. 1985. Multiple flow and support mechanisms and the development of inverse grading in a subaquatic glacigenic debris flow. Sedimentology, **32**(5): 645-657.

Carlson, A.E. 2004. Genesis of dewatering structures and its implications for melt-out till identification. Journal of Glaciology, **50**(168): 17-24.

Carr, S. 1999. The micromorphology of Last Glacial Maximum sediments in the Southern North Sea. Catena, **35**(2-4): 123-145.

Carr, S. 2001. Micromorphological criteria for discriminating subglacial and glacimarine sediments: Evidence from a contemporary tidewater glacier, Spitsbergen. Quaternary International, **86**(1): 71-79.

Carr, S.J., and Lee, J.A. 1998. Thin-section production of diamicts; problems and solutions. Journal of Sedimentary Research, Section A: Sedimentary Petrology and Processes, **68**(1): 217-220.

Carr, S.J., and Rose, J. 2003. Till fabric patterns and significance; particle response to subglacial stress. Quaternary Science Reviews, **22**(14): 1415-1426.

Carr, S.J., Haflidason, H., and Sejrup, H.P. 2000. Micromorphological evidence supporting late Weichselian glaciation of the northern North Sea. Boreas, **29**(4): 315-328.

Chadwick, O.A., and Graham, R.C. 2000. Pedogenic Processes. *In* Handbook of Soil Science. *Edited by* M.E. Sumner. CRC Press, Boca Raton: pp. E.41-E.75.

Clague, J.J., Ryder, J.M., Matthews, W.H., Hughes, O.L., Rutter, N.W., Jackson, L.E., Matthews, J.V., Jr., and MacDonald, G.M. 1989. Quaternary geology of the Canadian Cordillera. *In* Quaternary Geology of Canada and Greenland. *Edited by* R.J. Fulton and J.O. Wheeler. Geological Survey of Canada, Ottawa, **1**: pp. 15-96.

Clark, P.U., and Hansel, A.K. 1989. Clast ploughing, lodgement and glacier sliding over a soft glacier bed. Boreas, **18**(3): 201-207.

Dowdeswell, J.A., and Sharp, M. 1986. Characterization of pebble fabrics in modern terrestrial glacigenic sediments. Sedimentology, **33**(5): 699-710.

Drake, L.D. 1974. Till fabric control by clast shape. Geological Society of America Bulletin, **85**(2): 247-250.

Dreimanis, A. 1984. Till Work Group - Circular no. 25. INQUA Commission on Genesis and Lithology of Quaternary Deposits. p. 4.

Dreimanis, A. 1989. Tills; their genetic terminology and classification. *In* Genetic Classification of Glacigenic Deposits. *Edited by* R.P. Goldthwait and C.L. Matsch. A. A. Balkema, Rotterdam: pp. 17-96.

Dreimanis, A., and Lundqvist, J. 1984. What should be called till? *In* Ten years of Nordic till research. *Edited by* L.K. Königsson. Striae, **20**: pp. 5-10.

Elson, J.A. 1989. Comment on glacitectonite, deformation till, and comminution till. *In* Genetic classification of glacigenic deposits. *Edited by* R.P. Goldthwait and C.L. Matsch. A. A. Balkema, Rotterdam: pp. 85-88.

Evans, A.J. 1998. The causes and implications of microstructures in glacial sediments. Ph. D. thesis, University of Leeds, Leeds, West Yorkshire, UK.

Evans, D.J.A., Phillips, E.R., Hiemstra, J.F., and Auton, C.A. 2006. Subglacial till: Formation, sedimentary characteristics and classification. Earth Science Reviews, **78**(1-2): 115-176.

Evenson, E.B. 1971. The relationship of macro- and microfabric of till and the genesis of glacial landforms in Jefferson County, Wisconsin. *In* Till; a Symposium. *Edited by* R.P. Goldthwait. Ohio State Univ. Press: pp. 345-364.

Everitt, B. 1993. Cluster Analysis. Halsted Press, London, New York.

Eyles, N., and Kocsis, S. 1988. Sedimentology and clast fabric of subaerial debris flow facies in a glacially-influenced alluvial fan. Sedimentary Geology, **59**(1/2): 15-28.

Glen, J.W., Donner, J.J., and West, R.G. 1957. On the mechanism by which stones in till become oriented. American Journal of Science, **255**(3): 194-205.

Hampton, M.A. 1975. Competence of fine-grained debris flows. Journal of Sedimentary Petrology, **45**(4): 834-844.

Hart, J.K. 1994. Till fabric associated with deformable beds. Earth Surface Processes and Landforms, **19**(1): 15-32.

Hart, J.K. 1997. The relationship between drumlins and other forms of subglacial glaciotectonic deformation. Quaternary Science Reviews, **16**(1): 93-107.

Hart, J.K. 2006. An investigation of subglacial processes at the microscale from Briksdalsbreen, Norway. Sedimentology, **53**(1): 125-146.

Hart, J.K., and Boulton, G.S. 1991. The interrelation of glaciotectonic and glaciodepositional processes within the glacial environment. Quaternary Science Reviews, **10**(4): 335-350.

Hart, J.K., and Roberts, D.H. 1994. Criteria to distinguish between subglacial glaciotectonic and glaciomarine sedimentation; I, Deformation styles and sedimentology. Sedimentary Geology, **91**(1-4): 191-213.

Hart, J.K., Hindmarsh, R.C.A., and Boulton, G.S. 1990. Styles of subglacial glaciotectonic deformation within the context of the Anglian ice-sheet. Earth Surface Processes and Landforms, **15**(3): 227-241.

Hart, J.K., Gane, F., and Watts, R.J. 1996. Deforming bed conditions on the Danischer Wohld Peninsula, northern Germany. Boreas, **25**(2): 101-113.

Hart, J.K., Gane, F., and Watts, R.J. 1997. 'Deforming bed conditions on the Danischer Wohld Peninsula, northern Germany': Reply to comments. Boreas, **26**(2): 79-80.

Hart, J.K., Khatwa, A., and Sammonds, P. 2004. The effect of grain texture on the occurrence of microstructural properties in subglacial till. Quaternary Science Reviews, **23**(23-24): 2501-2512.

Hicock, S.R. 1990. Genetic till prism. Geology, **18**(6): 517-519.

Hicock, S.R. 1991. On subglacial stone pavements in till. Journal of Geology, **99**(4): 607-619.

Hicock, S.R., and Dreimanis, A. 1992. Deformation till in the Great Lakes region; implications for rapid flow along the south-central margin of the Laurentide ice sheet. Canadian Journal of Earth Sciences, **29**(7): 1565-1579.

Hicock, S.R., and Fuller, E.A. 1995. Lobal interactions, rheologic superposition, and implications for a Pleistocene ice stream on the continental shelf of British Columbia. Geomorphology, **14**(2): 167-184.

Hicock, S.R., and Lian, O.B. 1999. Cordilleran ice sheet lobal interactions and glaciotectonic superposition through stadial maxima along a mountain frontal in southwestern British Columbia, Canada. Boreas, **28**(4): 531-542.

Hicock, S.R., Goff, J.R., Lian, O.B., and Little, E.C. 1996. On the interpretation of subglacial till fabric. Journal of Sedimentary Research, **66**(5): 928-934.

Hiemstra, J.F., and van der Meer, J.J.M. 1997. Pore-water controlled grain fracturing as an indicator for subglacial shearing in tills. Journal of Glaciology, **43**(145): 446-454.

Hiemstra, J.F., and Rijsdijk, K.F. 2003. Observing artificially induced strain; implications for subglacial deformation. Journal of Quaternary Science, **18**(5): 373-383.

Hiemstra, J.F., Rijsdijk, K.F., Evans, D.J.A., and van der Meer, J.J.M. 2005. Integrated micro- and macro-scale analyses of last glacial maximum Irish Sea diamicts from Abermawr and Traeth y Mwnt, Wales, UK. Boreas, **34**(1): 61-74.

Hindmarsh, R. 1997. Deforming beds; viscous and plastic scales of deformation. Quaternary Science Reviews, **16**(9): 1039-1056.

Hooke, R.L., and Iverson, N.R. 1995. Grain-size distribution in deforming subglacial tills; role of grain fracture. Geology, **23**(1): 57-60.

Hooke, R.L., Hanson, B., Iverson, N.R., Jansson, P., and Fischer, U.H. 1997. Rheology of till beneath Storglaciaren, Sweden. Journal of Glaciology, **43**(143): 172-179.

Hooyer, T.S., and Iverson, N.R. 2000a. Diffusive mixing between shearing granular layers: constraints on bed deformation from till contacts. Journal of Glaciology, **46**(155): 641-651.

Hooyer, T.S., and Iverson, N.R. 2000b. Clast-fabric development in a shearing granular material; implications for subglacial till and fault gouge. Geological Society of America Bulletin, **112**(5): 683-692.

Iverson, N.R., and Iverson, R.M. 2001. Distributed shear of subglacial till due to Coulomb slip. Journal of Glaciology, **47**(158): 481-488.

Iverson, N.R., Baker, R.W., and Hooyer, T.S. 1997. A ring-shear device for the study of till deformation; tests on tills with contrasting clay contents. Quaternary Science Reviews, **16**(9): 1057-1066.

Iverson, N.R., Hooyer, T.S., and Baker, R.W. 1998. Ring-shear studies of till deformation; Coulomb-plastic behavior and distributed strain in glacier beds. Journal of Glaciology, **44**(148): 634-642.

Iverson, N.R., Moore, P.L., Hooyer, T.S., Thomason, J.F., and McLoughlin, M.P. 2003. Laboratory studies of till mechanical behavior and fabric evolution during shear. XVI INQUA congress; shaping the Earth; a Quaternary perspective. Reno, NV, United States. July 23-30, 2003. Congress of the International Union for Quaternary Research, Vol.16, p. 124.

Iverson, N.R., Hooyer, T.S., Thomason, J.F., Graesch, M., and Shumway, J.R. 2008. The experimental basis for interpreting particle and magnetic fabrics of sheared till. Earth Surface Processes and Landforms, **33**(4): 627-645.

Jeffery, G.B. 1922. The motion of ellipsoidal particles immersed in a viscous fluid. Proceedings of the Royal Society of London, Series A: Containing Papers of a Mathematical and Physical Character, **102**(715): 161-179.

Khatwa, A., and Tulaczyk, S. 2001. Microstructural interpretations of modern and Pleistocene subglacially deformed sediments; the relative role of parent material and subglacial processes. Journal of Quaternary Science, **16**(6): 507-517.

Kilfeather, A.A., and van der Meer, J.J.M. 2008. Pore size, shape and connectivity in tills and their relationship to deformation processes. Quaternary Science Reviews, **27**(3-4): 250-266.

Kruger, J. 1984. Clasts with stoss-lee form in lodgement tills: A discussion. Journal of Glaciology, **30**(105): 241-243.

Lachniet, M.S., Larson, G.J., Lawson, D.E., Evenson, E.B., and Alley, R.B. 2001. Microstructures of sediment flow deposits and subglacial sediments: a comparison. Boreas, **30**(3): 254-262.

Lachniet, M.S., Larson, G.J., Strasser, J.C., Lawson, D.E., Evenson, E.B., and Alley, R.B. 1999. Microstructures of glacigenic sediment-flow deposits, Matanuska Glacier, Alaska. Special Paper - Geological Society of America, **337**: 45-57.

Larsen, N.K. 2006. Sediment transport, deposition and deformaiton under soft-bedded glaciers and ice sheets. Ph.D. thesis, University of Aarhus, Aarhus, Denmark.

Larsen, N.K., and Piotrowski, J.A. 2003. Fabric pattern in a basal till succession and its significance for reconstructing subglacial processes. Journal of Sedimentary Research, **73**(5): 725-734.

Larsen, N.K., Piotrowski, J.A., and Kronborg, C. 2004. A multiproxy study of a basal till; a time-transgressive accretion and deformation hypothesis. Journal of Quaternary Science, **19**(1): 9-21.

Larsen, N.K., Piotrowski, J.A., and Christiansen, F. 2006. Microstructures and microshears as proxy for strain in subglacial diamicts: Implications for basal till formation. Geology, **34**(10): 889-892.

Larsen, N.K., Piotrowski, J.A., Menzies, J., Christiansen, F., Christoffersen, P., and Wysota, W. 2005. Subglacial sediment deformation revealed by microstructures from modern, Pleistocene and synthetic tills. International Conference on Glacial Sedimentary Processes & Products. University of Wales, Aberystwyth. 22-27 August 2005. Abstract, p. 78.

Lee, J.A., and Kemp, R.A. 1992. Thin sections of unconsolidated sediments and soils: a recipe, Report CEAM Report #2, University of London, Royal Holloway.

Lian, O.B. 1997. Quaternary geology of the Fraser Valley area, southcentral B.C. Ph.D. thesis, University of Western Ontario, London, Ontario.

Lian, O.B., and Hicock, S.R. 2000. Thermal conditions beneath parts of the last Cordilleran ice sheet near its centre as inferred from subglacial till, associated sediments, and bedrock. Quaternary International, **68-71**: 147-162.

Lian, O.B., and Hicock, S.R. 2001. Lithostratigraphy and limiting optical ages of the Pleistocene fill in Fraser River valley near Clinton, south-central British Columbia. Canadian Journal of Earth Sciences, **38**(5): 839-850.

Lian, O.B., Barendregt, R.W., and Enkin, R.J. 1999. Lithostratigraphy and paleomagnetism of pre-Fraser glacial deposits in south-central British Columbia. Canadian Journal of Earth Sciences, **36**(8): 1357-1370.

Lian, O.B., Hicock, S.R., and Dreimanis, A. 2003. Laurentide and Cordilleran fast ice flow: some sedimentological evidence from Wisconsinan subglacial till and its substrate. Boreas, **32**(1): 102-113.

Lundqvist, J. 1989. Glacigenic processes, deposits, and landforms. *In* Genetic Classification of Glacigenic Deposits. *Edited by* R.P. Goldthwait and C.L. Matsch. A. A. Balkema, Rotterdam: pp. 3-16.

March, A. 1932. Mathematische theorie der regelung nach der korngestalt bei affiner deformation. Zeitsschrift für Kristallographie, **81**: 285-297.

Mark, D.M. 1973. Analysis of axial orientation data, including till fabrics. Geological Society of America Bulletin, **84**(4): 1369-1373.

Martin-Fernandez, J.A., Barceló-Vidal, C., and Pawlowsky-Glahn, V. 1998. A critical approach to non-parametric classification of compositional data. Advances in Data Science and Classification. Proceedings of the 6th Conference of the International Federation of Classification Societies. Springer-Verlag Inc., pp. 49-56.

Martın-Fernandez, J.A., Barceló-Vidal, C., and Pawlowsky-Glahn, V. 1998. Measures of difference for compositional data and hierarchical clustering methods. The Fourth Annual Conference of the International Association for Mathematical Geology. Isola d'Ischia, Italy. De Frede Editore, Napoli, Vol.2, pp. 526-531.

Martín-Fernández, J.A., Barceló-Vidal, C., and Pawlowsky-Glahn, V. 2003. Dealing with zeros and missing values in compositional data sets using nonparametric imputation. Mathematical Geology, **35**(3): 253-278.

Menzies, J. 1990. Evidence of cryostatic desiccation processes associated with sand intraclasts within diamictons, southern Ontario, Canada. Canadian Journal of Earth Sciences, **27**(5): 684-693.

Menzies, J. 1998. Sedimentological and micromorphological examination of a late Devensian multiple diamicton sequence near Moneydie, Perthshire, east-central Scotland. Scottish Journal of Geology, **34**(1): 15-21.

Menzies, J. 2000. Micromorphological analyses of microfabrics and microstructures indicative of deformation processes in glacial sediments. *In* Deformation of glacial materials. *Edited by* A.J. Maltman, B. Hubbard, and M.J. Hambrey. Geological Society Special Publications, London, United Kingdom, **176**: pp. 245-257.

Menzies, J., and Maltman, A.J. 1992. Microstructures in diamictons - evidence of subglacial bed conditions. Geomorphology, **6**(1): 27-40.

Menzies, J., and Zaniewski, K. 2003. Microstructures within a modern debris flow deposit derived from Quaternary glacial diamicton; a comparative micromorphological study. Sedimentary Geology, **157**(1-2): 31-48.

Menzies, J., and Brand, U. 2007. The internal sediment architecture of a drumlin, Port Byron, New York State, USA. Quaternary Science Reviews, **26**(3-4): 322-335.

Menzies, J., Zaniewski, K., and Dreger, D. 1997. Evidence, from microstructures, of deformable bed conditions within drumlins, Chimney Bluffs, New York State. Sedimentary Geology, **111**(1-4): 161-175.

Menzies, J., van der Meer, J.J.M., and Rose, J. 2006. Till--as a glacial "tectomict", its internal architecture, and the development of a "typing" method for till differentiation. Geomorphology, **75**(1-2): 172-200.

Mickelson, D.M., Ham, N.R., and Ronnert, L. 1992. Comment and reply on "Striated clast pavements: products of deforming subglacial sediment?" Geology, **20**(3): 285-286.

Morgan, B.J.T., and Ray, A.P.G. 1995. Non-uniqueness and inversions in cluster analysis. Applied Statistics, **44**(1): 117-134.

Muller, B.U., and Schluchter, C. 2000. Influence of the glacier bed lithology on the formation of a subglacial till sequence -- ring-shear experiments as a tool for the classification of subglacial tills. Quaternary Science Reviews, **20**(10): 1113-1125.

Mullins, C.E., and Hutchison, B.J. 1982. The variability introduced by various subsampling techniques. Journal of Soil Science, **33**(3): 547-561.

O'Cofaigh, C., Dowdeswell, J.A., Allen, C.S., Hiemstra, J.F., Pudsey, C.J., Evans, J., and J.A. Evans, D. 2005. Flow dynamics and till genesis associated with a marine-based Antarctic palaeo-ice stream. Quaternary Science Reviews, **24**(5-6): 709-740.

Passchier, C.W., and Trouw, R.A.J. 2006. Microtectonics. Springer, Berlin, Federal Republic of Germany (DEU).

Passchier, S. 2000. Soft-sediment deformation features in core from CRP-2/2A, Victoria Land Basin, Antarctica. Terra Antartica, **7**(3): 401-412.

Phillips, E. 2006. Micromorphology of a debris flow deposit; evidence of basal shearing, hydrofracturing, liquefaction and rotational deformation during emplacement. Quaternary Science Reviews, **25**(7-8): 720-738.

Phillips, E., Merritt, J., Auton, C., and Golledge, N. 2007. Microstructures in subglacial and proglacial sediments: understanding faults, folds and fabrics, and the influence of water on the style of deformation. Quaternary Science Reviews, **26**(11-12): 1499-1528.

Piotrowski, J.A. 1994. Ice flow dynamics and subglacial bed conditions during the Weichselian glaciation in Schleswig-Holstein, Northwest Germany. Acta Universitatis Nicolai Copernici. Nauki Matematyczno-Przyrodnicze: Geografia, **27**: 141-160.

Piotrowski, J.A., and Tulaczyk, S. 1999. Subglacial conditions under the last ice sheet in northwest Germany: ice-bed separation and enhanced basal sliding? Quaternary Science Reviews, **18**(6): 737-751.

Piotrowski, J.A., Larsen, N.K., and Junge, F.W. 2004. Reflections on soft subglacial beds as a mosaic of deforming and stable spots. Quaternary Science Reviews, **23**(9-10): 993-1000.

Piotrowski, J.A., Larsen, N.K., Menzies, J., and Wysota, W. 2006. Formation of subglacial till under transient bed conditions: deposition, deformation, and basal decoupling under a Weichselian ice sheet lobe, central Poland. Sedimentology, **53**(1): 83-106.

Piotrowski, J.A., Doring, U., Harder, A., Qadirie, R., and Wenghofer, S. 1997. 'Deforming bed conditions on the Danischer Wohld Peninsula, northern Germany': Comments. Boreas, **26**(1): 73-77.

Piotrowski, J.A., Mickelson, D.M., Tulaczyk, S., Krzyszkowski, D., and Junge, F.W. 2001. Were deforming subglacial beds beneath past ice sheets really widespread? Quaternary International, **86**(1): 139-150.

Piotrowski, J.A., Mickelson, D.M., Tulaczyk, S., Krzyszkowski, D., and Junge, F.W. 2002. Were subglacial deforming beds beneath past ice sheets really widespread?; reply. Quaternary International, **97-98**: 173-177.

R Development Core Team 2007. R: A Language and Environment for Statistical Computing, Vienna, Austria.

Rasband, W.S. 1997-2007. ImageJ. U. S. National Institutes of Health, Bethesda, Maryland, USA.

Roberts, D.H., and Hart, J.K. 2005. The deforming bed characteristics of a stratified till assemblage in north East Anglia, UK: investigating controls on sediment rheology and strain signatures. Quaternary Science Reviews, **24**(1-2): 123-140.

Roddick, J.A., Muller, J.E., and Okulitch, A.V. 1976. Fraser River, British Columbia-Washington. Sheet 92. Geological Survey of Canada. Map 1386A.

Romesburg, H.C. 1984. Cluster analysis for researchers. Robert E. Krieger Publishing Company, Inc., Malabar, Florida.

Ruszczyńska-Szenajch, H. 2001. "Lodgement till" and "deformation till". Quaternary Science Reviews, **20**(4): 579-581.

Ruszczyńska-Szenajch, H., Trzcinski, J., and Jarosinska, U. 2003. Lodgement till deposition and deformation investigated by macroscopic observation, thin-section analysis and electron microscope study at site Debe, central Poland. Boreas, **32**(2): 399-415.

Seret, G. 1993. Microstructures in thin sections of several kinds of till; Glacial processes; stratigraphic, sedimentologic and proxy records. Quaternary International, **18**: 97-101.

Sneed, E.D., and Folk, R.L. 1958. Pebbles in the lower Colorado River, Texas; a study in particle morphogenesis. Journal of Geology, **66**(2): 114-150.

Starkey, J. 1977. The contouring of orientation data represented in spherical projection. Canadian Journal of Earth Sciences, **14**(2): 268-277.

Svard, N.M.M., and Johnson, M.D. 2003. Micromorphology and fabric of sandy loam till, west-central Wisconsin. Geological Society of America, North-Central Section, 37th annual meeting. Boulder, CO, United States. 2003. Geological Society of America (GSA), Vol.35, p. 20.

Sveistrup, T.E., Haraldsen, T.K., Langohr, R., Marcelino, V., and Kværner, J. 2005. Impact of land use and seasonal freezing on morphological and physical properties of silty Norwegian soils. Soil and Tillage Research, **81**(1): 39-56.

Thomason, J.F., and Iverson, N.R. 2006. Microfabric and microshear evolution in deformed till. Quaternary Science Reviews, **25**(9-10): 1027-1038.

Tipper, H.W. 1971. Multiple glaciation in central British Columbia. Canadian Journal of Earth Sciences, **8**(7): 743-753.

Tulaczyk, S. 2006. Scale independence of till rheology. Journal of Glaciology, **52**(178): 377-380.

van der Meer, J.J.M. 1987. Micromorphology of glacial sediments as a tool in distinguishing genetic varieties of till. Special Paper - Geological Survey of Finland, **3**: 77-89.

van der Meer, J.J.M. 1993. Microscopic evidence of subglacial deformation. Quaternary Science Reviews, **12**(7): 553-587.

van der Meer, J.J.M. 1996. Micromorphology. *In* Past Glacial Environments, Sediments, Forms, and Techniques, Glacial Environments II. *Edited by* J. Menzies. Butterworth-Heineman, Oxford: pp. 335-355.

van der Meer, J.J.M. 1997. Particle and aggregate mobility in till; microscopic evidence of subglacial processes. Quaternary Science Reviews, **16**(8): 827-831.

van der Meer, J.J.M., and Menzies, J. 2006. Sixth International Workshop on the Micromorphology of Glacial Sediments. Department of Geosciences, Hamilton College, Clinton, New York, pp. 1-83.

van der Meer, J.J.M., Menzies, J., and Rose, J. 2003. Subglacial till; the deforming glacier bed. Quaternary Science Reviews, **22**(15-17): 1659-1685.

van der Wateren, F.M., Kluiving, S.J., and Bartek, L.R. 2000. Kinematic indicators of subglacial shearing. *In* Deformation of glacial materials, London, United Kingdom. *Edited by* A.J. Maltman, B. Hubbard, and M.J. Hambrey. Geological Society Special Publications, United Kingdom (GBR), **176**: pp. 259-278.

van Vliet-Lanoë, B., Coutard, J.-P., and Pissart, A. 1984. Structures caused by repeated freezing and thawing in various loamy sediments: a comparison of active, fossil and experimental data. Earth Surface Processes and Landforms, **9**(6): 553-565.

Watts, R.J., and Carr, S.J. 2002. A laboratory simulation of the subglacial deforming bed (the deformation tank). Quaternary Newsletter, **98**: 1-9.

Wentworth, C.K. 1922. A scale of grade and class terms for clastic sediments. Journal of Geology, **30**(5): 377-392.

Woodcock, N.H., and Naylor, M.A. 1983. Randomness testing in three-dimensional orientation data. Journal of Structural Geology, **5**(5): 539-548.

Zaniewski, K., and van der Meer, J.J.M. 2005. Quantification of plasmic fabric through image analysis. Catena, **63**(1): 109-127.